UNIVERSIDAD PÚBLICA DE NAVARRA

DEPARTAMENTO DE CIENCIAS

Layered double hydroxides from aluminum saline slags applied in adsorption and photocatalysis processes for the removal of emerging pollutants

LETICIA SANTAMARÍA ARANA

Pamplona, 2020

https://doi.org/10.48035/Tesis/2454/41056

UNIVERSIDAD PÚBLICA DE NAVARRA

DEPARTAMENTO DE CIENCIAS

Memoria que presenta Dª. Leticia Santamaría Arana para optar al grado de Doctora con Mención Internacional por la Universidad Pública de Navarra.

En Pamplona a 2 de octubre de 2020

Leticia Santamaría Arana

Universidad Pública de Navarra
Nafarroako Unibertsitate Publikoa

ANTONIO GIL BRAVO, Catedrático, y SOPHIA A. KORILI, Profesora Titular de la Universidad Pública de Navarra, como Directores de la Tesis Doctoral titulada:

"Layered double hydroxides from aluminum saline slags applied in adsorption and photocatalysis processes for the removal of emerging pollutants"

Realizada en el Departamento de Ciencias de la Universidad Pública de Navarra por la doctoranda Dª. Leticia Santamaría Arana, licenciada en Ciencias Ambientales, autorizan la presentación de citada Tesis Doctoral, dado que reúne las condiciones necesarias para su defensa ante el tribunal designado.

Pamplona, a 2 de octubre de 2020

Fdo. Antonio Gil Bravo
Codirector de la Tesis Doctoral

Fdo. Sophia A. Korili
Codirectora de la Tesis Doctoral

AGRADECIMIENTOS

Esta Tesis Doctoral es la culminación de un trabajo que no se hubiera podido llevar a cabo sin la inestimable ayuda de muchas personas, algunas de las cuales quiero mencionar aquí.

Quiero expresar mi más sincero agradecimiento a mis directores de Tesis, el Dr. Andoni Gil Bravo y la Dra. Sophia Korili, por ofrecerme esta grandísima oportunidad, apoyarme en todo momento, confiar en mí, guiarme durante este proceso, saber calmarme en mis crisis… os estaré siempre agradecida.

Asimismo quisiera dar las gracias a la universidad Pública de Navarra por concederme el Contrato Predoctoral adscrito a Grupos e Institutos de Investigación, así como al Gobierno de Navarra por concederme la ayuda predoctoral de movilidad internacional y a Campus Iberus por la beca Erasmus +.

Extiendo mis agradecimientos al Departamento de Ciencias de los acebos, a todos los que me han ayudado a lo largo de estos años. A mis compañeros de grupo, Jonathan, Yaneth, a los que ya no trabajan en la UPNA: Edwin, Álvaro, Ekhine… y a los demás compañeros de fatigas: Nerea, Vigni, Karina, Maitane, Mikel, Guillermo… muchas gracias por apoyarme y ¡muchísimo ánimo con vuestro trabajo!

A María y Marcos, por la grandísima ayuda que me ofrecisteis, fuisteis unos compañeros geniales. Muchas gracias a Miguel Ángel, por todo tu esfuerzo, apoyo y gran compañía en congresos.

I would like to also thank Dr. Eric Gaigneaux for giving me the opportunity of working a few months in the Institute of Condensed Matter and Nanosciences of UCLouvain. I would also like to thank everybody that helped me during my stay, Françoise for her warm welcome and help throughout those months, François, for guiding me in the lab, helping me with the experiments and showing me a few Belgian delicatessen, Arnaud and Vijay for your great company in the office and Solène and Isaac for make me feel at home. I hope to see you again, s'il vous plaît prenez une T.K. à ma santé!

A Paula, tu sonrisa nos dejó demasiado pronto, tus cabras te echan de menos. A todas vosotras por estar siempre ahí, en todo lo que hemos pasado juntas, sois las mejores.

A mis chicas de Salamanca, allí empezó todo, qué suerte tuve de ir a la residencia Unamuno! Qué ganas tengo de veros, espero que nos podamos reunir pronto.

A mi familia, Lourdes y Miguel Ángel, Sandra y Cristian, por apoyarme en todo lo que hago, darme tanto cariño y energía, os quiero muchísimo.

A David, por la ayuda que me das cada día, por aguantarme todos estos años, y quererme tanto, espero que nuestro futuro sea tan bonito como lo que hemos pasado hasta ahora. A Toña y Luis, Jesús y Cristina por todo vuestro cariño y apoyo.

MUCHÍSIMAS GRACIAS!

A David,

a mi familia

y al que está por venir

INDEX

TABLE INDEX

I. INTRODUCTION

II.EXPERIMENTAL METHODOLOGY: MATERIALS AND EXPERIMENTAL TECHNIQUES DESCRIPTION

III. EFFECT OF THE SURFACE PROPERTIES OF Me^{2+}/Al LAYERED DOUBLE HYDROXIDES SYNTHESIZED FROM ALUMINUM SALINE SLAG WASTES ON THE ADSORPTION REMOVAL OF DRUGS

IV. Zn-Ti-Al LAYERED DOUBLE HYDROXIDES SYNTHESIZED FROM ALUMINUM SALINE SLAG WASTES AS EFFICIENT DRUG ADSORBENTS

V. EFFECT OF THE PREPARATION METHOD AND METAL CONTENT ON THE SYNTHESIS OF METAL MODIFIED TITANIUM OXIDE USED FOR THE REMOVAL OF SALICYLIC ACID UNDER UV LIGHT

VI. SALINE SLAG WASTE AS AN ALUMINUM SOURCE FOR THE SYNTHESIS OF Zn-Al-Fe-Ti LAYERED DOUBLE HYDROXIDES AS CATALYSTS FOR THE PHOTODEGRADATION OF EMERGING CONTAMINANTS

VII. OTHER MATERIALS AS DRUG ADSORBENTS

FIGURE INDEX

I. INTRODUCTION

II. EXPERIMENTAL METHODOLOGY: MATERIALS AND EXPERIMENTAL TECHNIQUES DESCRIPTION

III. EFFECT OF THE SURFACE PROPERTIES OF ME^{2+}/Al LAYERED DOUBLE HYDROXIDES SYNTHESIZED FROM ALUMINUM SALINE SLAG WASTES ON THE ADSORPTION REMOVAL OF DRUGS

IV. Zn-Ti-Al LAYERED DOUBLE HYDROXIDES SYNTHESIZED FROM ALUMINUM SALINE SLAG WASTES AS EFFICIENT DRUG ADSORBENTS

V. EFFECT OF THE PREPARATION METHOD AND METAL CONTENT ON THE SYNTHESIS OF METAL MODIFIED TITANIUM OXIDE USED FOR THE REMOVAL OF SALICYLIC ACID UNDER UV LIGHT

VI. SALINE SLAG WASTE AS AN ALUMINUM SOURCE FOR THE SYNTHESIS OF Zn-Al-Fe-Ti LAYERED DOUBLE HYDROXIDES AS CATALYSTS FOR THE PHOTODEGRADATION OF EMERGING CONTAMINANTS

VII. OTHER MATERIALS AS DRUG ADSORBENTS

Chapter I

Introduction

I.1. SALINE SLAG VALORIZATION

I.1.1. PRIMARY AND SECONDARY ALUMINUM PRODUCTION

Aluminum is the most abundant metal in the earth's crust and the second most used after iron. It has many industrial applications due to its different properties like low density, malleability, corrosion resistance, low melting point (933 K), its ability to alloy with other metals and recyclability.

Aluminum is too reactive with other elements to occur naturally and bauxite ore is the primary source of alumina (Al_2O_3). It became economically viable at the end of the 19th century when both the Bayer process and the Hall-Héroult process, still used nowadays, were invented (Ungureanu et al., 2004; Metson, 2011). The Bayer it's a costly process that, using different treatments such as grinding, absorption, solution and precipitation, allows the mass production of alumina from bauxite. The Hall-Héroult process refines the alumina to aluminum with an electrolytic process. Although the production approach has not changed, its efficiency with the use of cleaner technologies and renewable energy has been improved (Beck, 2013). To this day these energy improvements are not enough and there lies the importance of recycling aluminum.

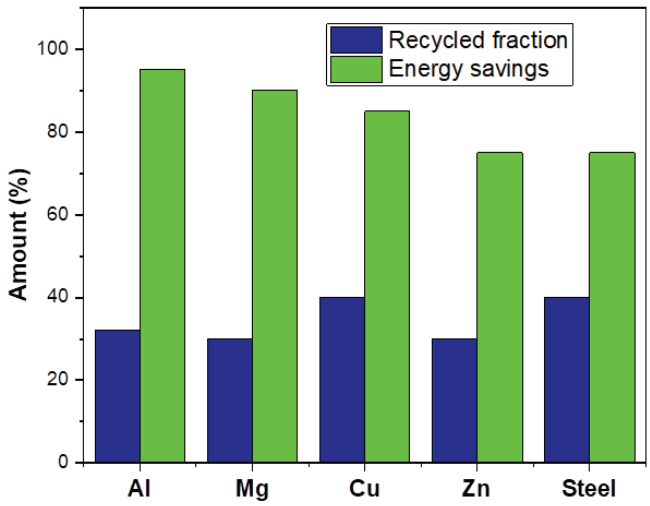

Figure I.1. Relative recycled fraction and secondary production energy saving of different metals with respect to primary production (Antrekowitsch et al., 2002; Bureau of International Recycling (BIR), 2020).

The recycling of aluminum is carried out without the loss of quality in the final product, it uses only between a 5 and a 20% of the energy needed in the primary production, generates less waste (Gil, 2005) and emits only a 5% of the greenhouse gas (Sevigné-Itoiz et al., 2014). When compared to other high-produced materials, it has the largest difference in terms of difference of energy saving between the primary and secondary productions (see Figure I.1) and their recycled fraction is in all cases between a 30 and a 40%.

I.1.2. TYPES OF WASTES GENERATED

Table I.1. shows the classification of the different hazardous wastes generated in the aluminum production industry according the European Commission (European Commission, 2018a).

Table I.1. Wastes from aluminum thermal metallurgy.

No.	Hazardous waste type	*Code*
1	Primary production slags	100304
2	Salt slag from secondary production	100308
3	Black drosses from secondary production	100309
4	Skimmings that are flammable or emit, upon contact with water, flammable gases in hazardous quantities	100315
5	Tar-containing waste from anode production	100317
6	Flue-gas dust containing hazardous materials	100319
7	Other particulates and dust (including ball-mill dust) containing hazardous substances	100321
8	Solid wastes from gas treatment containing hazardous substances	100323
9	Sludges and filter cakes from gas treatment containing hazardous substances	100325
10	Wastes from cooling-water treatment containing oil	100327
11	Wastes from treatment of salt slags and black drosses containing hazardous substances	100329

Between them the most important ones, as they are generated in larger quantities, are items 1, 2 and 3, generated both in the primary and the secondary production methods as can be seen in the aluminum production scheme (Figure I.2).

The transformation of bauxite into alumina produces *red mud*, the most important waste produced in the primary route. Depending on the type of bauxite used, the amount generated varies from 1.0 to 1.6 tons per ton of alumina (Tsakiridis, 2012) and its chemical composition is also different. It usually contains acidic oxides with iron, silicium and titanium oxides as major components but also with zinc, nickel and phosphorous oxides. These substances cannot be dissolved in the reaction conditions of the Bayer process and are usually managed by disposal in a controlled landfill as there is not an economically viable application reported.

Materials with more than 45% Al are called *skimming* and residues containing less than 45% Al are called *dross*. If the dross comes from the primary smelters is called *white dross* whereas the *black dross* comes from the secondary smelter. The difference in color is due to the aluminum source. While the raw material in the Halt-Héroult process is alumina, the remelting process uses aluminum wastes and scraps. The secondary smelter also produces *salt cake*, *salt slag* or *saline slag* as the re-melting process requires fluxing of salt. Their different compositions are shown in Table I.2. Salt fluxes are used as they have multiple functions (Gil, 2005):

- They disperse mechanically the oxides and metals or solid nonmetal substances present.

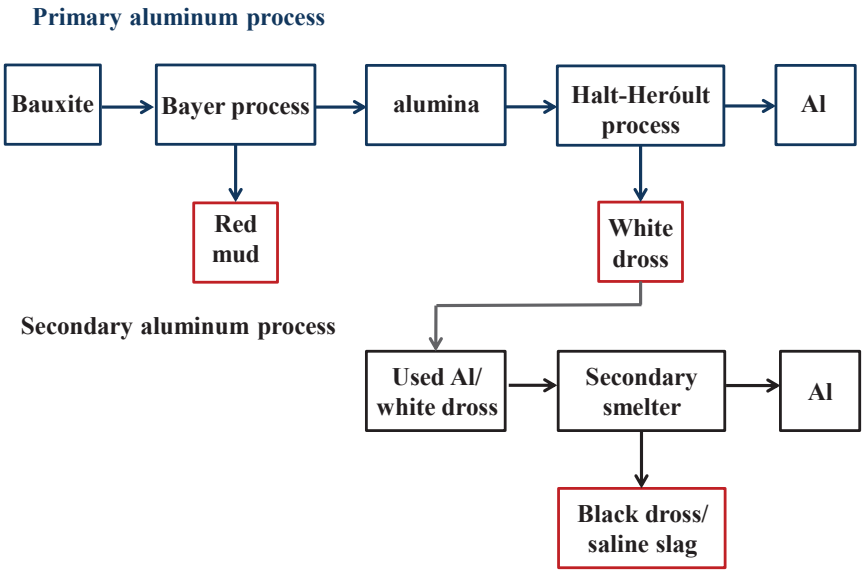

Figure I.2. Aluminum recycling process scheme.

- They isolate the metal from the atmosphere and pass the heat to the metal so the furnace reaches a temperature that melts the brine.
- In some cases they can chemically react with the aluminum oxides present and dissolve them.

Table I.2. Types and composition of aluminum dross (Meshram and Singh, 2018).

Type of dross	% Metallic aluminum	*% Aluminum Oxide*	% Salt Flux
White dross	15-80	20-85	< 5
Black dross	7-50	30-50	30-50
Saline slag	3-10	20-60	20-80

I.1.3. SALINE SLAG MANAGEMENT

Due to its harmful properties (Table I.3), saline slag must be properly managed. There are some significant problems associated with the a controlled landfill disposal such as the large area required, the elevated cost that road transportation implies or the toxicity associated to a possible leachate to groundwater or air contamination. This, together with the increasing number and strictness of environmental regulations (Gil and Korili, 2016), make the recovery of the saline slag an attractive alternative to managing the waste.

Table I.3. Hazardous properties of aluminum saline slag according to the European waste catalogue and hazardous waste list (Environmental Protection Agency, 2002).

Title	Meaning	Code
Highly flammable	Substances and preparations which, in contact with water or damp air, evolve highly flammable gases in dangerous quantities	H3-A
Irritant	Non-corrosive substances or preparations which through immediate prolonged or repeated contact with the skin or mucous membrane can cause inflammation	H4
Harmful	Substances and preparations which, if they are inhaled or ingested or if they penetrate the skin, involve limited health risk	H5
Leachable	Substances and preparations capable by any means, after disposal, of yielding another substance	H13

The valorization of aluminum saline slags means that a disposal is not required and present and future landfills are not needed creating at the same time economic opportunities.

Potential applications for aluminum saline slags as a raw material are being studied over the last years in construction, polymer composites, adsorbents or salts but another interesting strategy is to solve the available Al and use it to synthesize useful materials.

I.1.3.1. Saline slag characterization and Al extraction procedure

Aluminum was extracted from a saline slag coming from Iberica de Aleaciones Ligeras S.L. (IDALSA) a Spanish company specialized in the recycling of aluminum. The aluminum saline slag generated is a powdered solid composed, in more than 50 wt.%, of particles smaller than 23 mm in diameter.

Yoldi et al.(2019) studied different alkaline extraction procedures in order to obtain the best aluminum recovery efficiency. Saline slags were treated under reflux and stirring together with a NaOH solution and the best conditions determined were with a single extraction step with NaOH 2 mol/dm^3 for 1 h (see Figure I.3).

Figure I.3 Alkaline extraction of aluminum from saline slags.

The quantity of aluminum extracted to the solution was determined with ICP and it is over 7g/dm^3. An alkaline extraction was more appropriate in this work as the aluminum obtained is going to be employed for the synthesis of layered double hydroxides (LDH). This synthesis procedure requires a pH of 9-10 and, as the aluminum solution obtained in the extraction in very alkaline, there is not a need for adding NaOH during the LDH synthesis. Saline slag before and after Al extraction are showed in Figure I.4 together with the SEM micrographs.

The chemical composition of the residue before and after Al extraction with NaOH was calculated from the analysis with X-ray fluorescence (XRF) and powder X-ray diffraction (PXRD) and the results are shown (wt.%) in Figure I.5. All the deliverable aluminum, as metallic Al and AlN present in the original slag (19.2 wt.%) is extracted to the solution and there is none left after the extraction process. The percentage of non-crystalline components is expressed together with the loss of ignition and is higher after the Al extraction because of the removal of volatile components. Corundum (+ 3.4 wt.%) and spinel (− 0.5 wt.%) have limited change as they are not solved with the NaOH extraction. The slight increase on the percentage of corundum could be due to an Al oxidation in the extraction/purification process. XRF comparisons (Yoldi et al., 2019) also show that that NH_3 and other toxic elements are not determined after the extraction and they are removed in the process. Na quantity in the waste (after cleaning it with deonized water and drying it at 393 K for 4 hours) is very low, in the same order than the original waste, transforming the saline slag after extraction to a non-hazardous waste.

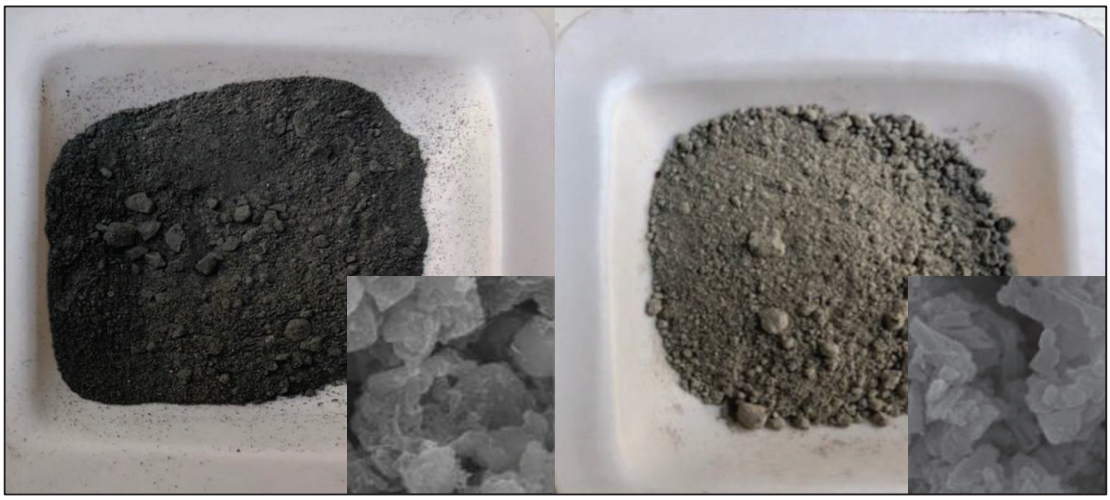

Figure I.4. Saline slags before (left) and after extraction (right).

I.2. POLLUTANTS IN WATER: LEGISLATION

Fresh water is a scarce resource and a fundamental element for life that has undergone a constant deterioration mainly due to the rapid economic development and its inappropriate use. Water pollution problems started being perceptible with the start of the industrial revolution, in the early nineteenth century. For a long time, biologically active substances with agricultural or industrial uses have been inadequately discharged into the environment without any further treatment. Water pollution problem has been exacerbated by the escalating desertification that the climate change generates and the global increase in population. Legislative and policy measures have been gradually adopted to try to palliate the problem. However, the increasing demand for water and the constant detection of new contaminants highlights the need for further research to be carried out.

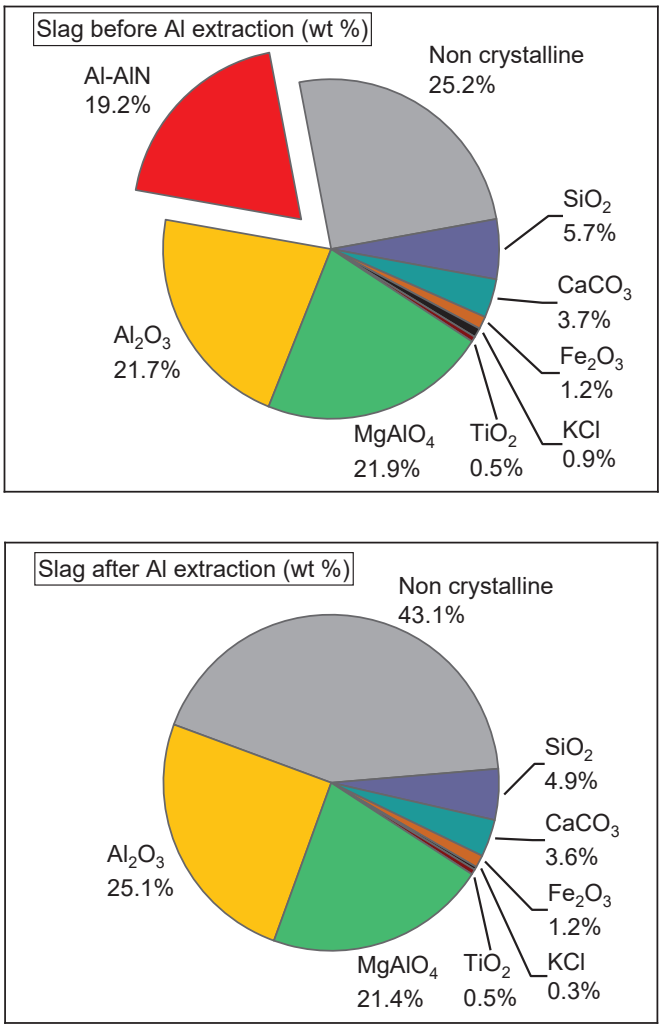

Figure I.5. Chemical composition of the slag before and after Al extraction.

On a national level, Spain established in 1879 its first water law ("ley de aguas") that considered water as a natural resource to be preserved of an improper use or privatization. It was mainly focused on the quantitative and consumption fields. This law was repealed over a hundred years afterwards by the law 25/1985. This water law established a new legal regime for the public hydraulic domain in the framework of the constitution. It also installed the distribution of competencies between the central and regional governments. With the entry of Spain in the European Union, the transposition of the dispositions coming from Europe onto our regulations was mandatory. In this respect, the European Water Framework Directive, published on October 2000 (European Union, 2000) is one of the most important international instruments to be instituted in the water field. The aim of this Directive was for the waterbodies of Europe to achieve a good ecological and chemical status by 2015. This meant that an action program had to be established, updated and implemented to the water management model through hydrological planning. The assessment of the quality of surface waterbodies is based on the use of ecological quality status and, to have a good ecological status, concentrations of specific pollutants must not exceed the environmental quality standards set at member state level (Mandaric et al., 2016). The directive 2008/105/EC later amended by the Directive 2013/39/EU (The European Parlament and the Council of the European Union, 2013) proposed two types of legally binding European environmental quality standards for selected chemical pollutants or priority substances: the annual average and the maximum allowable concentration of the substance. This directive also includes a list of 45 priority substances and provisions to improve the functioning of the legislation.

I.2.1. EMERGING CONTAMINANTS

Although the measures taken have improved drastically the presence of known pollutants in water, there are a great number of potentially dangerous chemical substances that can harm the environment. Emerging contaminants are synthetic or naturally occurring chemicals or any microorganisms that are not usually monitored in water bodies but have the potential to enter the environment and cause known or suspected adverse ecological and/or human health effects (Rosenfeld and Feng, 2011). They consist of pharmaceuticals, pesticides, fire retardants, industrial chemicals, surfactants, and personal care products that are consistently being found in groundwater,

surface water, municipal wastewater, drinking water and food sources. Among the pharmaceutical compounds, they include endocrine-disrupting compounds, analgesics, antibiotics, hormones, and a whole range of other pharmaceutical compounds including anti-inflammatory, antidiabetic, and antiepileptic drugs. These compounds are usually present in the water bodies in concentration ranges that go from μ/dm^3 to ng/dm^3 and, in general, these compounds do not represent acute risks. There is, however, a lack of knowledge concerning their long-term effects as well as their synergistic effects or those that come from their metabolites. There is not enough information about them to assess their potential damage and, thus, further research is needed to decipher their potential environmental toxicity and include them in future regulations. Their presence on water has been proven in numerous studies (Machado et al., 2016; Noguera-Oviedo and Aga, 2016; Wilkinson et al., 2017; Gogoi et al., 2018) and they usually end up in water following different pathways as seen in Figure I.6. As routine monitoring programs in the EU do not include emerging pollutants, the directive 2013/39/EU discusses that high-quality monitoring information targeted on emerging contaminants with a new mechanism is needed. This mechanism is focused on a limited number of compounds, to keep the costs at acceptable levels. Thus, a watch list, where these substances are temporarily included, is created and representative data is collected from a limited number of monitoring sites. This watch list has a restricted number of compounds and periodic controls are performed so the substances are not on the list longer than necessary (up to 4 years).

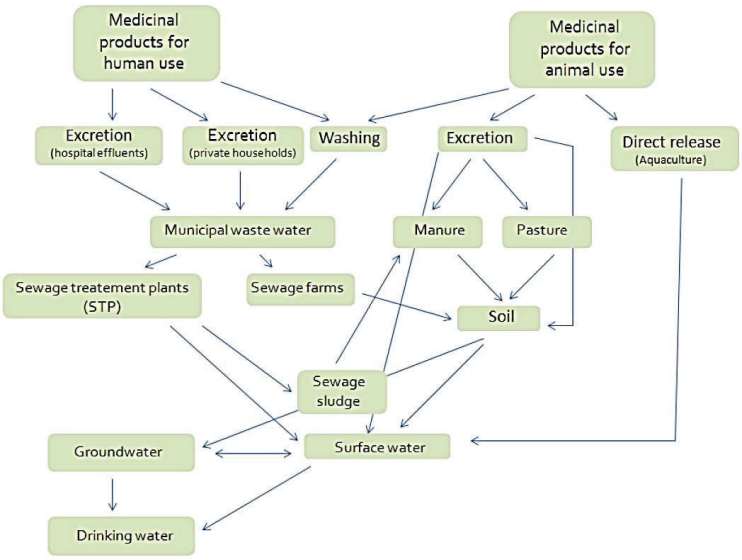

Figure I.6. Emission pathways related to the use-phase of pharmaceutical compounds (Executive Agency for Health and Consumers, 2013).

Those with a considerable risk at EU level will be labeled as candidate priority substances as soon as possible. Three pharmaceutical compounds were selected in the first watch list: 17-alpha- ethinylestradiol and 17-beta-estradiol (steroidal oestrogens) and diclofenac. These three substances were monitored and the high-quality data was obtained in the case of diclofenac, so it was taken from the watch list in 2018. The other two substances are still being monitored along with the antibiotics azithromycin, amoxicillin and ciprofloxacin (European Commission, 2018b; Loos et al., 2018).

I.3. WATER POLLUTION CONTROL PROCESSES/METHODOLOGY

Wastewater plant treatments usually employ conventional methods that, in general, are not appropriate for the elimination of emerging contaminants, as many of them remain without any transformation in the effluents of the wastewater treatment plant (aus der Beek et al., 2016). This is why is important to determine and asses the efficiency of alternative water treatment processes, to try to identify valuable alternatives with good results in the removal of emerging contaminants at an affordable cost. It is not an easy task as some of these pollutants (among them pharmaceutical compounds or endocrine disruptors) possess a wide variety of chemical properties which are responsible for the achievement of good removal rates (Mompelat et al., 2009). The most important technologies for water treatment are described hereunder.

I.3.1. COAGULATION-FLOCCULATION METHODS

Physico-chemical treatments are regarded as one of the most important and broadly used treatment processes for wastewater due to their effectiveness and simplicity. They have, however, several drawbacks such as the production of large amount of toxic sludge, complexity of scaling up the procedure or the inefficient removal of pollutants using natural coagulant. Furthermore, they are ineffective when it comes to the removal of heavy metals and emerging contaminants (Teh et al., 2016). A study on hospital wastewater (Suarez et al., 2009) containing heavy metals, toxic chemicals, microorganisms and radioactive elements confirmed that the coagulation-floculation process using alum was not effective as there was an increase in the total suspended solids at the end of the treatment. *Acero et al.* (2012) studied the removal capacity of 11 different emerging contaminants using ferric chloride or alum. Coagulation alone was capable of removing only less than 3% of them. In addition, a combination of

ultrafiltration with coagulation did not improve significantly the removal of emerging pollutants when compared to ultrafiltration alone.

I.3.2. MEMBRANE PROCESSES

Another possibility to try to eliminate emerging pollutants is the application of a treatment that operates with membranes such as membrane bioreaction, micro and ultrafiltration, nanofiltration or reverse osmosis.

Micro and ultrafiltration are capable of removing pathogens or heavy metals although they have low removal percentages of pharmaceutical compounds, as the pore size of the membrane is from 100 to 1000 times larger than the emerging pollutants (Deegan et al., 2011). Nanofiltration is more effective in the removal of organic (dyes, pharmaceuticals, pesticides) and inorganic (heavy metals) pollutants although they have high operational costs, and also an important energy demand apart from the problems with membrane fouling and disposal of the concentrate (Ahmed et al., 2017). Reverse osmosis technologies have also problems with the membrane fouling, high energy costs and the handling of the residual concentrate. However they remove more than 90 % of the endocrine disrupting compounds and have in general good removal percentages of pharmaceuticals and personal care products (Ahmed et al., 2017). In the last years, new types of reverse osmosis membranes have been developed that improve the separation process. Electrodialysis, which consists on the application of an electric current throughout the membrane, allows for the separation of some compounds from wastewater. This technique, commonly used in desalination plants, creates a faster ion transport through the membrane.

Membrane bioreactor is the combination of a membrane process (usually microfiltration or ultrafiltration) with the activated sludge process. It also has the problems related to membranes like fouling and also high energy consumption. The efficiency in removal of organic compounds depends on the compound characteristics. Hydrophilic and moderately hydrophobic compounds possessing strong electron withdrawing functional groups presented low removal efficiencies (<20%) and compounds with electron donating functional groups such as hydroxyl and primary amine groups showed high removal efficiencies (Tadkaew et al., 2011).

Some of the problems that these technologies present could be solved by the combination of two or more processes. One interesting possibility could be an activated carbon/ultrafiltration combo. Activated carbon has great adsorption capacity and the ability of the ultrafiltration process to retain high molecular weight compounds could enable the removal of low molecular weight compounds (Acero et al., 2012). However, this would imply higher operational and energy costs.

I.3.3. BIOLOGICAL PROCESSES

The basic sewage treatment system with biological trickling filters or activated sludge is able to quickly transform organic compounds into biomass, separated after of the aqueous phase by clarifiers. Still, this does not work for all compounds and, for example, steroids or estrogens are not completely broken down (Johnson and Sumpter, 2001). In addition, biological treatments at their best are only capable of removing certain emerging pollutants, particularly the polar ones (Bolong et al., 2009).

I.3.4. ADVANCED OXIDATION PROCESSES

Advanced oxidation processes are water treatments (that work at near ambient temperature and pressure) based on the generation of hydroxyl radicals to start the oxidative destruction of organic compounds. Hydroxyl radicals are strong and non-selective chemical oxidants which react a billion times faster than hydrogen peroxide or ozone, thus reducing system size and costs (Vogelpohl and Kim, 2004). These processes have emerged in the last years as a valuable class of technologies capable of accelerating the destruction of a wide range of organic pollutants in wastewater, which cannot be eliminated biologically. Under adequate conditions, the non-desired organic components are converted completely to CO_2, mineral salts and water. One of the main advantages of this method is that secondary pollutants are not generated in the process, which is commonly associated with conventional treatment techniques.

There is a variety of processes that can be adopted for the generation of hydroxyl radicals, the most important among them are:

- Ozone. In the presence of O_3, besides the straight ozonation of contaminants, the primary radicals of water radiolysis can react rapidly with ozone and hydroxyl radicals are formed. The reaction steps are described by *Wang and Xu* (2012). This

process achieves a great efficient degradation of organic pollutants based on the combination of hydroxyl radicals formed and the non-reactant ozone.

- Hydrogen peroxide. In advanced oxidation processes hydrogen peroxide is usually used in combination with UV radiation, metal compounds (particularly iron) or ozone to form hydroxyl radicals.
- Fenton's reaction. The use of hydrogen peroxide on its own is not effective for high concentrations of emerging contaminants as it has low rates of reaction. The use of transition metal salts such as iron salts can activate hydrogen peroxide to form hydroxyl radicals, as seen in the following reaction (Wang and Bai, 2017).

$$Fe^{2+} + H_2O_2 \rightarrow Fe^{3+} + OH\bullet + OH^- \qquad \text{Eq. I.1}$$

- Photocatalysis. This term refers to a catalytic reaction that involves the absorption of light by a catalyst. The ability of the catalyst to create electron-hole pairs, which generate free hydroxyl radicals, is defined as photocatalytic activity. In this process both oxidation and reduction reactions occur. Both light and a catalyst (a semiconductor) are needed for the reaction to happen. In the process first an electron-hole pair is generated in the semiconductor particle. A photon with energy $E = hv$ that meets or exceeds the break energy (band gap) between the valence and the conduction band is absorbed by the semiconductor and an electron is excited from the valence to the conduction band, generating a positive hole in the valence band. The excited electron then reacts with oxidants to form reduced products and the generated hole also reacts to produce oxidized products. That is, both oxidation and reduction reactions take place on the surface of the catalyst. The major problem that arises in this type of processes is recombination of the hole and the excited electron, which releases the energy acquired by the excited electron as heat. The development of functional photocatalysts is focused on prevent the electron-hole recombination using different approaches such as noble-metal nanoparticles or substitutional cation doping. In this work photocatalysts were synthesized and tested for degradation of emerging contaminants in chapters V and VI.

I.3.5. ADSORPTION PROCESSES

Adsorption is a matter transferring process that involves the concentration of a liquid or gaseous compound in the surface of a porous solid. On the other hand, desorption is the opposite process by which the molecule adsorbed on the surface of the solid returns to the fluid. If the solid-molecule interaction is of physic nature, the process is named physisorption. On the other hand, chemisorption involves the formation of covalent forces. Although physisorption can happen on its own, in favorable conditions, both processes occur simultaneously, and thus, it is usually difficult to distinguish between the two of them. The main characteristics of both processes are resumed in Table I.4.

Table I.4. Main characteristics of physisorption and chemisorption.

Physisorption	**chemisorption**
Non-specific in nature	Highly specific in nature
Fast, reversible	It can be slow and irreversible
Enthalpy of adsorption is low	Enthalpy of adsorption is high
It arises due to van der Waal's forces	It arises due to chemical bond formation
Monolayer or multilayer	Monolayer only
exothermic	Endothermic or exothermic

I.3.5.1. Adsorbent materials

There are different characteristics desired for an effective adsorbent such as high adsorption capacity and adsorption kinetics, good renewal capacity, high thermal, mechanic and chemical stability or low cost. The most employed adsorbents for emerging contaminants are carbonaceous materials, metal organic frameworks and clays which are described below.

I.3.5.1.1. Clays

Clay materials represent a good choice because of their low cost, high surface area and porosity and low toxicity. There are different types of clays such as smectites (saponite, montmorillonite), kaolinite, sepiolite or hydrotalcites (layered double hydroxides). Their adsorption capacities depend on the charge of the surface, which gives clays the capability to adsorb either positively or negatively charged species. In

this work, a variety layered double hydroxides have been synthesized, using always aluminum extracted from saline slag as aluminum source, and tested for the adsorption of emerging contaminants (chapters III and IV).

Several clays have been tested for the adsorption of emerging contaminants from aqueous media: propranolol was adsorbed by montmorillonite (del Mar Orta et al., 2019), ibuprofen was adsorbed by a sepiolite/zeolite combination (Li et al., 2019) or Congo red dye by kaolinite (Zhang et al., 2018).

I.3.5.1.2. Carbonaceous materials

This group of materials involves basically activated carbon, one of the most used adsorbents, and carbon nanotubes.

- Activated carbon. This material refers to porous carbon materials synthesized by different methods in order to reach a high porosity. The possibility of a size and pores distribution control are responsible for its adsorbent properties. It is produced by pyrolizing a raw material followed by the activation with oxidizing gases. The product obtained usually has a large surface area that ranges from 600 to 2000 m^2/g. They are used in a wide variety of applications in both aqueous and gas phases. The final properties of the activated carbon can be controlled and adapted with an appropriate selection of the precursor, the activation method or the synthesis process variables (such as temperature, gas flow…) (Grassi et al., 2012). These factors largely condition its physic-chemical, structural, electrochemical, redox and hydrophilic/phobic properties and, consequently, its area of application. These adsorbents were used for comparison purposes in chapter VII.
- Carbon nanotubes. They are the result of rolling a single graphite layer (graphene). Carbon nanotubes can have between 2 and 50 layers and they maintain their characteristic tubular shape via van der Waal's forces. As such, they are classified as multi-walled (MWCNTs) or single-walled (SWCNTs). In this work MWCNTs were used for comparison purposes in chapter VII.

I.3.5.1.3. Metal organic frameworks (MOFs)

MOFs are crystalline porous materials that also have interest in the field of adsorption due to the easy tunability of their pore size and shape in the range of microporous to mesoporous by changing the connectivity of the inorganic moiety and the nature of organic linkers (Hasan et al., 2012). They have been studied for the

removal of naproxen, clofribic acid and bisphenol A (Qin et al., 2015) or dyes (Haque et al., 2011). In this work MOF Basolite A100 was used for comparison purposes in chapter VII.

I.4. REMOVAL OF PHARMACEUTICAL COMPOUNDS FROM AQUEOUS SOLUTION USING LAYERED DOUBLE HYDROXIDES AS ADSORBENTS

I.4.1. INTRODUCTION

A wide range of emerging contaminants is being currently detected in worldwide aqueous environments. These include pesticides, industrial additives, pharmaceutical compounds, caffeine and nicotine metabolites flame retardants, surfactants, hormones, personal care products and fragrances (N. A. Khan et al., 2020b, 2020a). These pollutants are not appropriately regulated by law although they have been detected in both surface and groundwater. Although it is clear that they are a risk to water and soil environments, they are not presently being monitored because of a lack of information regarding their effects (Stuart et al., 2012). Thus, more research has to be performed on the prevalence, fate and treatments of emerging contaminants and human originated metabolites to try to develop risk based screening models and an appropriate framework (Gogoi et al., 2018). Among the wide range of emerging contaminants, the most commonly detected are pharmaceuticals like carbamazepine, ibuprofen or diclofenac (Stuart et al., 2012; aus der Beek et al., 2016; Riva et al., 2018).

Several treatment processes like membrane bioreactors (Besha et al., 2017), microfiltration - reverse osmosis (Rodriguez-Mozaz et al., 2015), ozonation – photocatalysis (Quiñones et al., 2015; A. H. Khan et al., 2020) or adsorption can be selected for the removal of emerging contaminants. Each of them has a number of advantages and disadvantages well described by *Patel et al.* (2019). In general the main problems of these techniques involve their high operational/energy costs, their difficulty to be applied on a large scale or their low removal rates. Adsorption technology has none of these issues as it is capable of obtaining a high percentage removal, needs low energy and mild operation conditions, and byproducts are not added to the system. There are, however, several concerns with adsorption that need to be tackled: mainly the regeneration and sludge management and the selection of an efficient adsorbent.

Layered double hydroxides (LDH), also called hydrotalcites or anionic clays, are a family of layered materials with hydrotalcite structure, derived from that of brucite ($Mg(OH)_2$), in which a partial substitution of Mg^{2+} by Al^{3+} takes place and the electric charge is balanced by anions in the interlayer space. Their general formula is $Mg_6Al_2(OH)_{16}CO_3{\cdot}4H_2O$, water being located with the anions in the interlayer. These materials are usually easy to prepare, not expensive and offer a wide range of variants within the family. Their divalent and trivalent cations choice is almost entirely restrained only by their charge and size and a combination of more than one divalent or trivalent cation can be also made. The interlayer anion choice has nearly no limits: simple or complex, organic or inorganic anions can be selected.

These features are responsible for the selection of LDH as adsorbents in recent studies. Although they have been largely studied as adsorbents for the release of drugs in animals and humans (Rives et al., 2014), the recent discoveries highlighting the need for an effective emerging contaminant collector have increased the interest of these compounds as adsorbents (Dias and Fontes, 2020; Lazaratou et al., 2020). In this review work, a compilation of the recent studies that use LDH as adsorbents of pharmaceutical compounds, an important group of emerging contaminants, taking into account several factors such as kinetic and isotherm studies, the use of support, synthesis strategies and recovery techniques has been carried out. At the end of the review, the main conclusions and perspectives regarding some of the main scientific challenges remaining in this field are also summarized.

I.4.2. PHARMACEUTICAL COMPOUNDS

Among the adsorbates studied (described in Table I.5), there are two main groups of compounds: antibiotics and Non-Steroidal Anti-Inflammatory Drugs (NSAID). Both cause great concern due to their environmental impact. Although caffeine is considered a central nervous system drug, it was also considered in this work, as is commonly added to over-the-counter medications. At present, there is a general rise in the production and consumption of pharmaceutical compounds all over the world. Several factors are responsible: the increase of the worldwide population and life expectancy, the great prevalence of chronic diseases or a steady input of new compounds entering the market every year (Patel et al., 2019). *Van Boeckel et al.* (2014) analyzed the global antibiotic consumption from 2000 to 2010 (see Figure I.7); in this decade, global

Table I.5. Chemical structure of the pharmaceutical compounds studied.

Name	Structure and characteristics		Name	Structure and characteristics	
Caffeine (CAF)	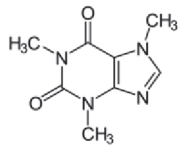	$C_8H_{10}N_4O_2$ m=194.19 Pk_a=10.4	Tetracycline (TCY)	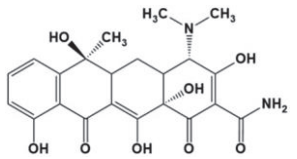	$C_{22}H_{24}N_2O_8$ m=444.15 Pk_a=7.38*
Diclofenac sodium (DCF)	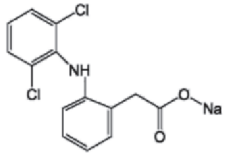	$C_{14}H_{10}Cl_2NNaO_2$ m=296.15 Pk_a=4.15	Metrodinazole (MTD)	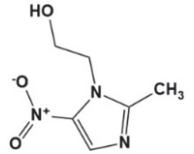	$C_6H_9N_3O_3$ m=171.06 Pk_a=13.41
Salicylic acid (SLC)	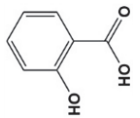	$C_7H_6O_3$ m=138.03 Pk_a=13.04, 2.98	Amoxicillin (AMX)	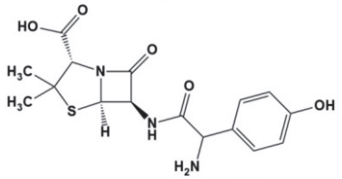	$C_{16}H_{19}N_3O_5S$ m=365.10 Pk_a=6.52*
Ibuprofen (IBP)	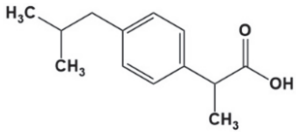	$C_{13}H_{18}O_2$ m=206.13 Pk_a=4.37	Norfloxacin (NFX)	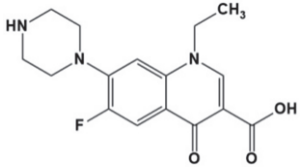	$C_{16}H_{18}FN_3O_3$ m=319.13 Pk_a=8.39, 2.63
Ketoprofen (KTP)	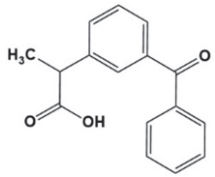	$C_{16}H_{14}O_3$ m=254.09 Pk_a=4.13	Sulfamethoxazole (SFM)	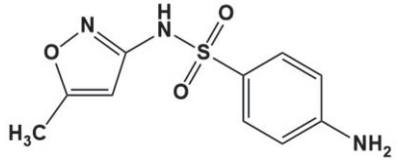	$C_{10}H_{11}N_3O_3S$ m=253.05 Pk_a=--
flurbiprofen (FBP)	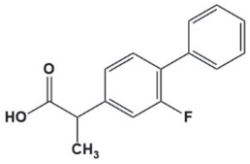	$C_{15}H_{13}FO_2$ m=244.09 Pk_a=4.15			

m=molecular mass
*molecule with more than 2 pk_a

antibiotic sales raised by 35%, such an increase was mainly due to developing countries such as Brazil, India, China and Russia. An increment in the antibiotic consumption has a synergic effect, as is a major driver for antibiotic resistance. The prevailing pathway of pharmaceuticals into the environment starts with their excretion by humans or animals, the release into raw sewage and the management in a WasteWater Treatment Plant (WWTP) followed by a discharge into water environment. However WWTP procedures are usually not effective for pharmaceutical compounds, with very different removal rates (Martín et al., 2012; Verlicchi et al., 2012). As an example, *He et al.* (2017) reviewed the potential adverse effect of NSAID residues on terrestrial and aquatic ecosystems and showed that concentrations as low as 1µg/dm^3 of diclofenac can cause tubular necrosis in the kidneys and histological changes in the liver and gills of the rainbow trout. Diclofenac has been detected in groundwater, surface water or drinking water in 50 countries and concentrations higher than 1 µg/dm^3 usually occur downstream of sewage-treatment plants in densely populated areas (aus der Beek et al., 2016).

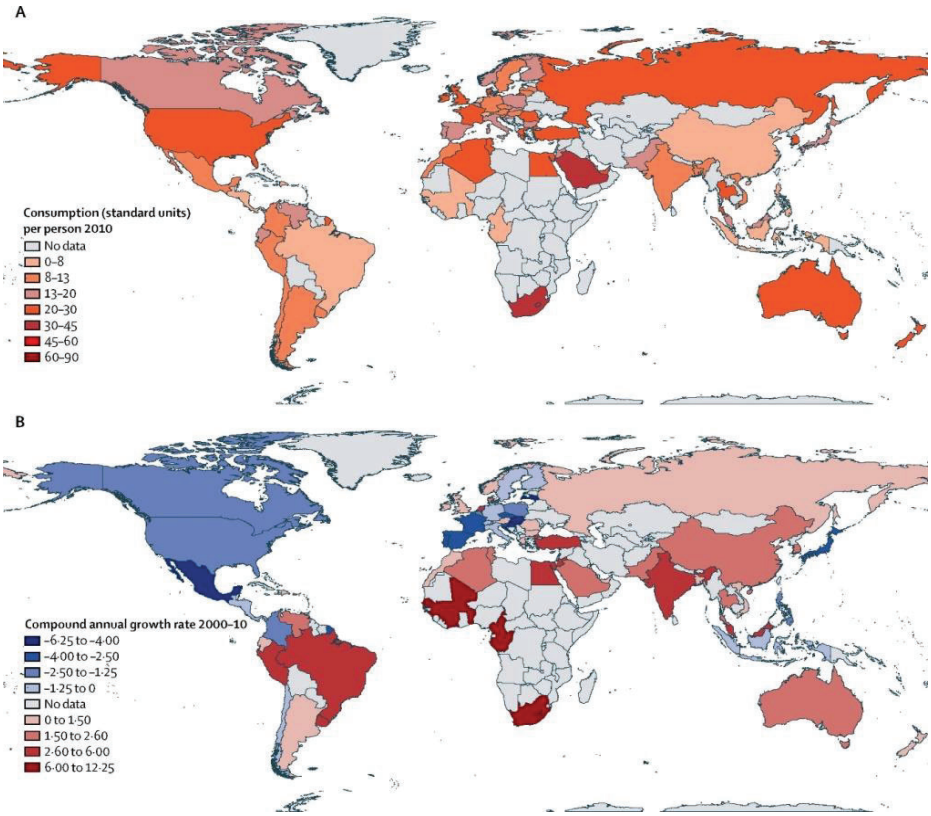

Figure I.7. Consumption of antibiotics in 2010. Expressed as pill, capsule or ampoule per person (A), and compound annual growth rate of antibiotic drug consumption between 2000 and 2010 (B). (Reproduced with permission from *Van Boeckel et al.* (2014)).

Antibiotic sulfamethoxazole was found in the surface water of 47 countries and had an average concentration of 2.53 μg/dm^3 in African countries (aus der Beek et al., 2016) (see Figure I.8). Its risk quotient values indicated that this antibiotic has a high ecological risk in soils of Kenya (Yang et al., 2016).

I.4.3. SYNTHESIS CONDITIONS, RATIOS AND COMPONENTS

The synthesis of LDH can be performed using various metals, the most used for the preparation of LDH destined to the adsorption of pharmaceutical compounds are Mg^{2+} and Zn^{2+} as divalent cations, and Al^{3+} as the trivalent one. These metals can be combined in different molar ratios and the resulting LDH can also be calcined at different temperatures, usually between 573 and 883 K. A calcination step is essential; its purpose is the elimination of the anions, usually carbonates, from the interlayer. When the calcined LDH is placed in an aqueous environment, it can recover its original structure, thanks to the memory effect, and "trap" the adsorbate in its interlayer. In the case of MgAl LDH, a calcination process above 653 K guarantees the formation of the metal oxide but a calcination above 1073 K leads to the formation of stable MgO and spinel phases, thus preventing the memory effect from occurring (Rives, 2002).

Xu et al. (2009) synthesized MgAl LDH with 2:1, 3:1 and 4: 1 Me^{2+}:Me^{3+} molar ratios via the hydrothermal method and their tetracycline (TCY) adsorption capacity

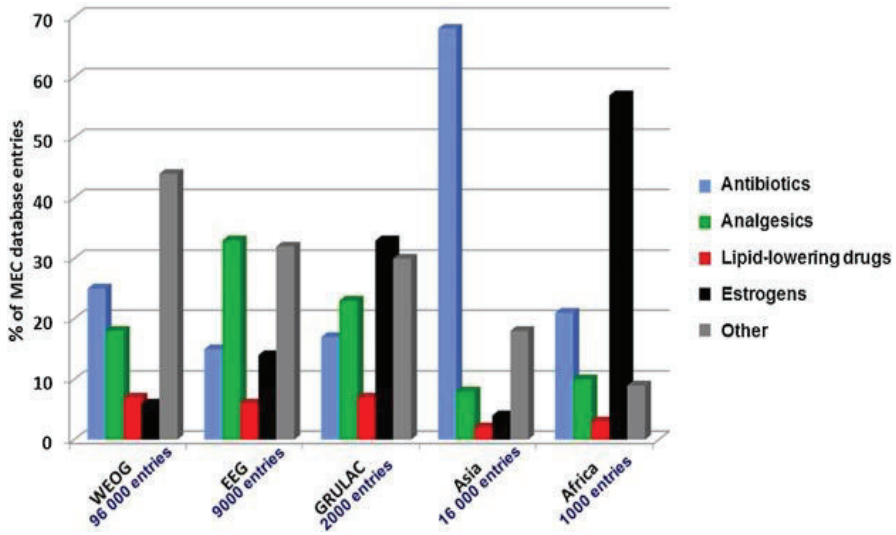

Figure I.8. Regional patterns of pharmaceutical therapeutic groups analyzed in each United Nations region. MEC = measured environmental concentration; WEOG = Western Europe and Others Group; EEG = Eastern Europe Group; GRULAC = Latin American and Caribbean States. (Reproduced with permission from *aus der Beek et al*. (2016)).

was investigated. The reconstruction of the LDH in water by the memory effect was only partial. Calcined LDH had a better performance than the non-calcined counterpart. These authors concluded that the adsorption of aqueous TCY by calcined LDH could occur by (i) adsorption in the interlayers of structurally restored LDH, (ii) adsorption on the external surfaces of structurally restored LDH, and (iii) adsorption on MgO surfaces as not all the LDH was restored. When comparing the samples fabricated with various ratios, all of them showed similar performances at low TCY concentrations and TCY was mostly adsorbed in the interlayer of the LDH. With greater drug concentration, the adsorption capacity of the 4:1 sample was the best one. In the 3:1 ratio sample the adsorption process followed a crystal-growth model, suggesting that the drug adsorption was controlled by the reconstruction of the LDH. Tetracycline adsorption by the calcined LDH fitted better a pseudo-second-order kinetics model and the isotherm was adjusted to the Langmuir model.

The removal capacity of, in this case, ZnAl LDH synthesized with various ratios (1:1, 3:1 and 5:1) and calcined at four temperatures (573, 673, 773, and 883 K) over salicylic acid (SLC) as a model of pharmaceutical pollutants was studied by *Elhalil et al.* (2018). Both molar ratios and calcination temperature were proven to have a great effect over the adsorption capacity of the adsorbent. The LDH with 3:1 Zn:Al ratio calcined at 573 K gave the best results. The adsorption process took place in two steps: first, a rapid process due to the adsorption on the external surface of the crystallites, followed by a slower process when the reconstruction of the LDH took place (see Figure I.9).

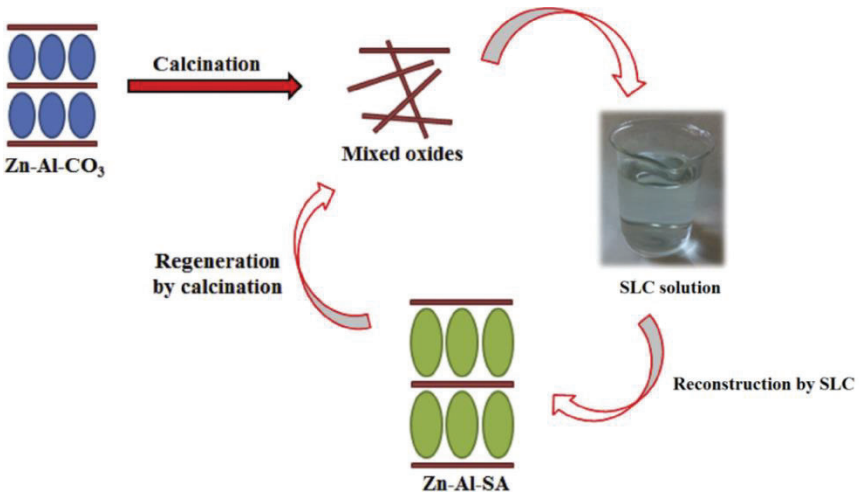

Figure I.9. Schematic illustration of the adsorption phenomenon of salicylic acid (SLC) onto LDH structure. (Reproduced with permission from *Elhalil et al.* (2018)).

Not all the LDH show the memory effect; as seen above, it depends greatly on the calcination temperature and the molar ratio used in the synthesis process. The divalent metal chosen is also of great importance, Mg^{2+} and Zn^{2+} LDH can recover their structure when placed in water if they had been calcined at the correct temperature, however metals like Co^{2+} or Ni^{2+} do not show the memory effect under normal circumstances, cobalt forms a highly stable Co_3O_4 spinel even when the calcination has been performed at low temperatures (Benito et al., 2008), while nickel would need both high pressure and temperature to recover its original structure (Sato, 1988). This was verified by *Rosset et al.* (2019) by synthesizing LDH with Mg, Ni or Zn as Me^{2+} and Al as Me^{3+} (2:1 ratio, continuous co-precipitation method) as adsorbents for the removal of sodium diclofenac (DCF). The structure of the LDH was regenerated, due to the "memory effect of the LDH", in the case of ZnAl and MgAl LDH but not in the sample with NiAl, which gave the poorest results (see Figure I.10).

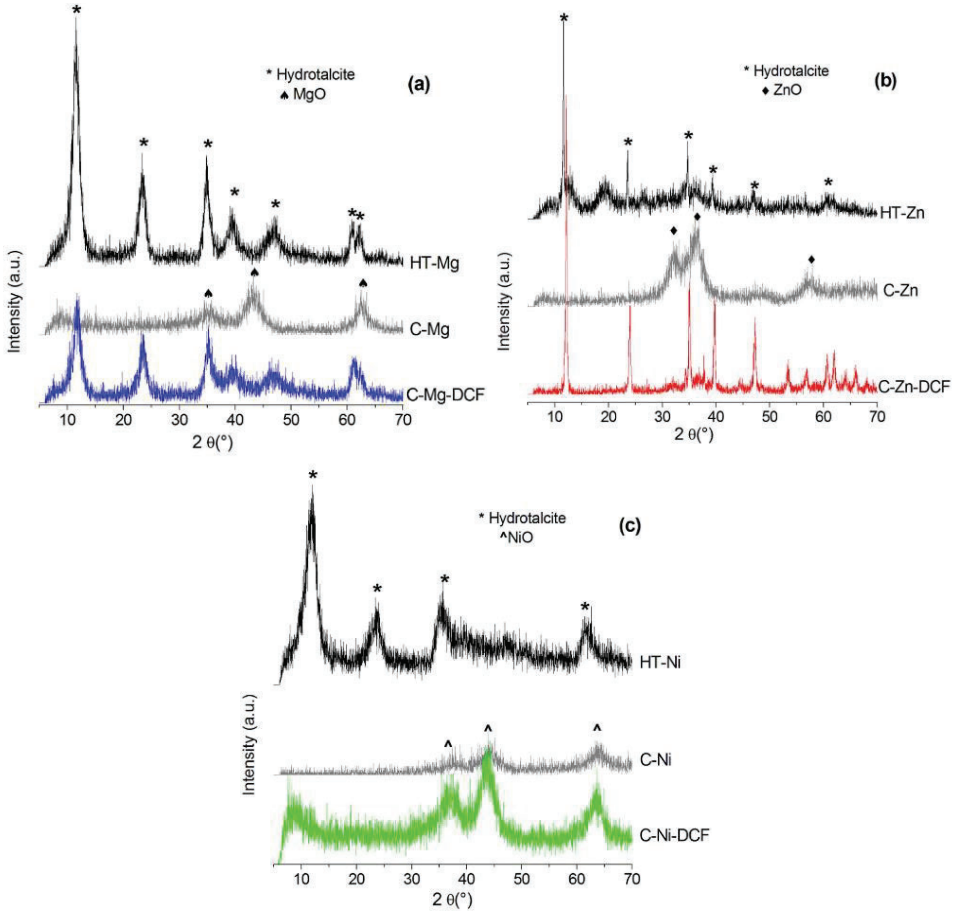

Figure I.10. XRD patterns of the solids before and after the calcination and after the adsorption of diclofenac sodium (DCF). Samples based on Mg (a), Zn (b) and Ni (c). (Reproduced with permission from *Rosset et al.* (2019)).

Although usually carbonates are used as interlayer anions in the synthesis of LDH, other anions can be present. Carbonates are the most common because the synthesis process is easier as they do not require an inert atmosphere to prevent the influence of atmospheric CO_2 and they are going to disappear anyway in the calcination process. However, the use of different interlayer anions can greatly influence the interlayer distance (Liu et al., 2020) and, thus, change the adsorption capacity of the LDH. *Sui et al.* (2012) synthesized MgAl LDH and studied their capacity to adsorb the antibiotic norfloxacin (NFX) in aqueous solution. MgAl LDH were fabricated with three Mg^{2+}/Al^{3+} molar ratios (2:1, 3:1 and 4:1) and with two anions in the interlayer (Co_3^{2-} and Cl^-) (see Figure I.11).

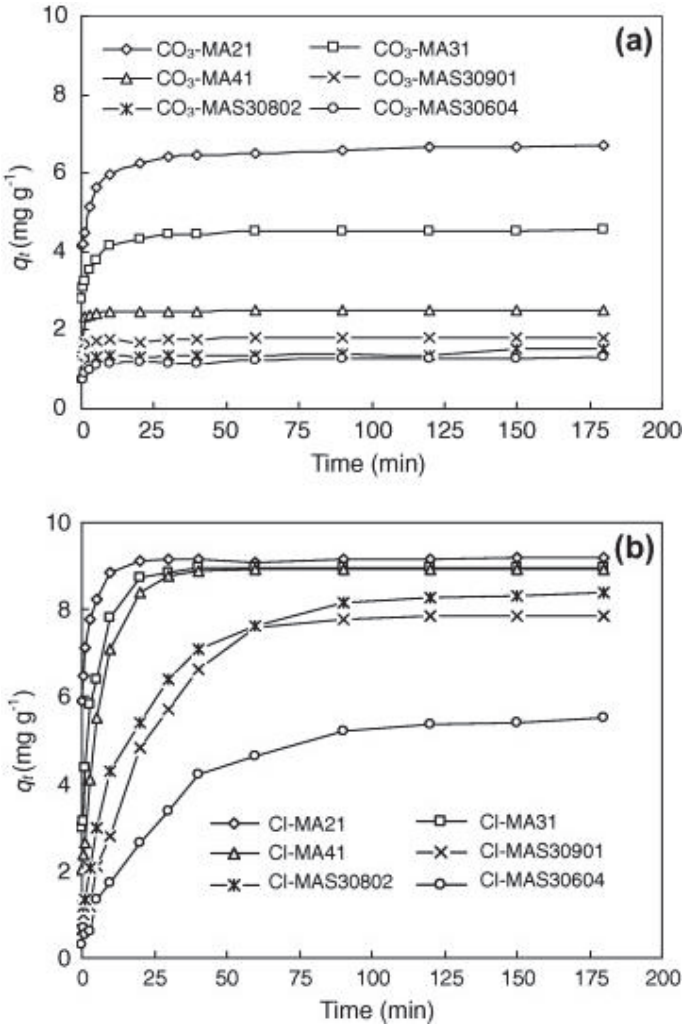

Figure I.11. Adsorption kinetics of NOR on: (a) CO_3-MA-LDH and CO_3-MAS-LDH, (b) Cl-MA-LDH and Cl-MAS-LDH (MAS denotes Mg, Al and Sn, respectively). Experimental conditions: initial concentration of NOR: 20 mg/dm^3, dose of LDH: 2 g/dm^3, initial pH: 6.7, and T: 298 K. (Reproduced with permission from *Sui et al.* (2012)).

The samples with greater Al^{3+} content showed a better performance and Cl^- as interlayer anion increased the adsorption capacity of the LDH. In the case of Cl^-–LDH both the anion exchange process and the electrostatic attraction contributed to the adsorption of the antibiotic while only the electrostatic attraction was responsible for the adsorption in CO_3^{2-}–LDH. The pseudo-second rate model fitted well the kinetic data and the Freundlich model fitted better the equilibrium data than the Langmuir model. The initial pH value (3.0 to 11.0) did not significantly influence the adsorption, proving the pH buffering ability of the LDH. In the same work, the change of the adsorption capacity of the samples with the incorporation of various cations in the structure of the LDH was also studied. The authors incorporated Sn^{4+} as an attempt to increase the charge density; however this only resulted in a reduction of the adsorption capacity of the LDH.

I.4.4. COMBINED ADSORPTION AND INFLUENCE OF FOREIGN SUBSTANCES

Studies that involve the adsorption of different substances at the same time, or in real water samples with the presence of other substances that can deter the adsorption process have also been performed. The simultaneous adsorption of two substances can lead to different results (Lu et al., 2016; Li et al., 2017).

Chen et al. (2019) studied the combined adsorption of TCY and Cd^{2+} on MgMn LDH. The adsorbents were synthesized by the hydrothermal method at a 2:1 ratio and activated with persulfates. The presence of TCY increased the adsorption of cadmium and the presence of cadmium sharply increased TCY adsorption. The authors credited the synergistic effect to the strong complex formation between the adsorbates as both the oxygen atoms and naphthamide group on the tetracene structure could bind to Cd^{2+}. They also compared the results between a calcined and non-calcined MgMn LDH. The kinetic experiments showed a betterr adjustment to the pseudo-second-order model in TCY adsorption and the isotherm data fitted better the Langmuir than the Freundlich model.

Real water samples coming from a dam, a river, three lakes and a wastewater plant were used by *Panplado et al.* (2019) when studying the adsorption capacity of calcined MgAl LDH, synthetized by the co-precipitation method with a 3:1 mole ratio, over

TCY. The removal capacity of TCY was superior to 90% in all cases. The process involved the utilization of the LDH components to initiate the precipitation of mixed metal hydroxides to act as sorbents. Hydrogen bonding and electrostatically induced attraction were responsible for a removal accomplished within 4 min. The recovery of TCY was tested by dispersing the adsorbents with the antibiotic in several solutions with common anions PO_4^{3-}, CO_3^{2-}, SO_4^{2-}, NO_3^-, CH_3COO^-, and Cl^-, phosphates giving a 98% recovery due to their high charge density.

Boukhalfa et al. (2017) concluded that the adsorption capacity of both ZnAl LDH and a K10 montmorillonite on DCF decreased when background electrolytes were present while pH did not have a significant effect. LDH was synthesized with a 2:1 ratio and the co precipitation method. Kinetic studies revealed that a pseudo-second-order model fitted better the experimental results and isotherm experiments fitted better the Langmuir over the Freundlich model. Maximum adsorption capacities were 55.46 mg/g for the montmorillonite and 737.02 mg/g for the LDH with equilibrium achieved after 5 and 20 min, respectively.

The influence of foreign ions such as nitrate, sulfate, carbonate and a hardness agent greatly affected drug adsorption in the experiments performed by *Sepehr et al*. (2017), (see Figure I.12). They synthesized MgAl LDH with the urea method (ratio 2:1) and

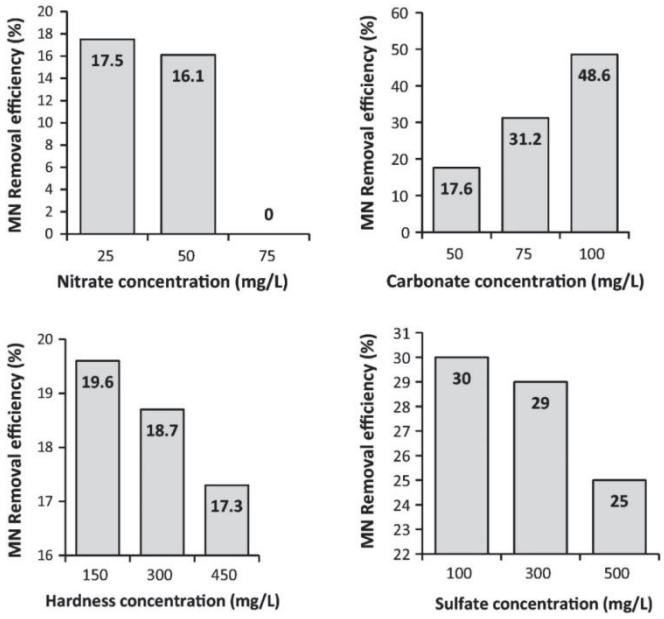

Figure I.12. Effect of increasing concentration of nitrate, sulfate, carbonate and hardness on metronidazole (MN) removal efficiency (pH = 9; LDH dose = 6 g/dm^3; MN conc. = 40 mg/dm^3; contact time = 2 h). (Reproduced with permission from *Sepehr et al.* (2017)).

used them to remove metronidazole (MTD) from water. Sulfate, nitrate and the hardness agent decreased the removal efficiency of the LDH. This may be due to the competing effect that they had with the MTD molecules for adsorption. In the case of carbonate-LDH, the opposite effect was observed; the removal efficiency was decreased at lower concentration of carbonate, and was increased with the increment of carbonate concentration. This could be due to the buttering effect of carbonate anions in solution. A higher final pH gave better removal results. The adsorption isotherm was described with Langmuir, Freundlich, Redlich-Peterson and Sips equation, the latter giving the best fit. The maximum adsorption capacity was of 62.8 mg/g.

Rosset et al. (2020) studied the adsorption capacity of ZnAl LDH (ratio 2:1, co-precipitation method) over acetylsalicylic acid. The effect of excipient present in 2 commercial aspirins was tested suggesting that a probable competition existed between the SLC and the other components. SLC removal was lower for both samples (62 and 73%) than for pure SLC sample (92% removal). The first sample had the lowest removal, which was probably related to the presence of sodium carbonate, since this compound effortlessly occupies the interlayer spacing facilitating the LDH reconstruction and thus decreasing the acetylsalicylic acid removal. The adsorption kinetics were better adjusted to the pseudo-second order model and the Sips equation was more precise in describing the isotherms' behavior showing that the adsorption occurs mainly by chemisorption in a monolayer (maximum adsorption capacity 198 mg/g).

I.4.5. USE OF SUPPORTS

Much effort has been put in the development of a composite LDH + support when trying to improve the adsorption capacity of the LDH. Immobilizing the adsorbent into a 2D or 3D structure aims at reducing the aggregation of the LDH. Their characteristics, adsorption conditions and performances are summarized in Table I.6.

Wu et al. (2018) prepared MgFe LDH (ratio 3:1, co-precipitation method) supported on chitosan to study its removal capacity of both TCY and methyl orange from water. Various calcination temperatures were tried (573, 673 and 773 K) and 673 K gave the best results, with a maximum adsorption capacity of TCY 195.31 mg/g. The pH change

Table I.6. Adsorption conditions of supported LDH.

LDH	Support	adsorbate	Adsorption conditions	q_{max}	Adsorbent concentration	Ref
MgAl	Syagrus coronata biochar	DCF	50-1000 mg/dm^3, 333 K, pH 5.65, 6 h	168 mg/g	4g/dm^3	(de Souza dos Santos et al., 2020)
CaAl	Polymer ionomer	DCF	0.5-200 mg/dm^3, pH=9, 2 min, room temperature	268 mg/g	1g/dm^3	(Hossein Beyki et al., 2017)
MgAl	Poly (m-Phenylenediamine)	DCF	50-400 mg/dm^3, 313 K, pH=7, 2 min	589 mg/g	0.125 g/dm^3	(Xiong et al., 2019b)
MgAl	Bovine bone biochar	CAF	5-200mg/dm^3, 313 K, pH=12, 30 min,	26 mg/g	4g/dm^3	(dos Santos Lins et al., 2019)
NiAl	Cotton fiber	KTP	200 mg/dm^3, 30 min, room temperature,	714 mg/g	3g/dm^3	(Wang et al., 2018)
NiMgAl	Copper ferrite	TCY	250 mg/dm^3, 303 K, pH =4, 6 h	192mg/g	1 g/dm^3	(Eniola et al., 2020)
NiAl, ZnAl, CuFe MgFe	Polypropylene chip	KTP, FBP	1mg/dm^3, 303 K, 20 min			(Zhou et al., 2017)
MgAl	SiO_2 spheres	DCF, IBP	10 mg/dm^3, room temperature, 5 min	758 mg/g, 400 mg/g	0.11g/dm^3	(Chen et al., 2013)
MgAl	cellulose	AMX	60 mg/dm^3, 318 K, natural pH, 24 h	138 mg/g	0.1g/dm^3	(Yang et al., 2020)
MgAl	γ-AlO(OH) nanowires	TCY	200 mg/dm^3, pH=7	302 mg/g	0.5g/dm^3	(Li et al., 2015)

did not greatly affect the adsorption processes; the results from initial pH 5 to 9 were similar. The presence of different anions in the water sample was studied and the monovalent anions had almost no effect while divalent and trivalent had a great effect in the adsorption capacity of chitosan-LDH against TCY. The kinetics of both adsorbates showed a better fit with the pseudo-second order model and TCY isotherm experiments fitted better the Langmuir than the Freundlich model.

The adsorption capacity of the LDH and the support separately and together has been compared by *Xiong et al.* (2019). They synthesized MgAl LDH (ratio 2:1, urea method synthesis) along with Poly(m-Phenylenediamine) (PmPD) to remove DCF from actual medical wastewater. The composites were prepared via a chemical oxidation polymerization method. The composite had a maximum adsorption capacity of 588.9 mg/g, while PmPD and LDH on their own had 272 and 104 mg/g, respectively. PmPD particles tend to aggregate and a combination with LDH weakened the accumulating density of PmPD and increased the specific surface area, which favored diclofenac adsorption on LDH-PmPD surface. Its removal efficiency in medical wastewater was almost 100% in only 2 minutes with 0.125 g/dm^3 of adsorbent. The presence of electrostatic attraction, π-π electron-donor-acceptor interaction and N···HO hydrogen bonding between diclofenac and LDH-PmPD were responsible for the good adsorbent performance. The adsorption kinetics was described with the pseudo-second-order model and the isotherm data fitted better the Langmuir model than the Freundlich one. Humic acids present in water decreased the adsorption capacity of the samples.

Eniola et al. (2020) studied the separated and combined adsorption performances of a modified copper ferrite/NiMgAl LDH composite over oxytetracycline hydrochloride. The adsorption capacities went from 106 mg/g ($CuFe_2O_4$) and 116 mg/g (NiMgAlLDH), to 192 mg/g for the composite. Anionic exchange, electrostatic attraction and hydrogen bonding were responsible for the adsorption process. The kinetics and isotherm data followed a pseudo-second-order and Langmuir models. Three temperatures were tested (303, 313, 323 K) with the last one giving the best results, that is, the process was endothermic and spontaneous. In all the cases, adsorption performance was better at an acidic pH. The co-adsorption results with various salts showed synergistic ($CuSO_4$), neutral ($NaHCO_3$) and antagonistic effect (NaCl) on the antibiotic adsorption.

Zhou et al. (2017) considered different methods to immobilize the LDH into different surfaces such as polypropylene chip, glass slides and metal coins (see Figure I.13). Although methods like colloid deposition, sol-gel spin coating and solvent evaporation have been previously used, they often suffer from an uncontrollable formation of multiple layers due to strong aggregation. For this reason, they used the in situ growing strategy to immobilize a LDH film in one step. NiAl, ZnAl, CuFe and MgFe LDH (ratio 2:1, urea method) were prepared, and polydopamine was used to immobilize the LDH film and study the adsorption capacity of the samples over both pharmaceutical compounds and organic dyes. NiAl LDH showed the best adsorption capacity for rhodamine B. Further adsorption experiments were performed with NiAl LDH. The LDH were immobilized onto the inner wall of the 1.5 mL polypropylene centrifuge tube and a dense and homogeneous LDH film with a thickness of 400 nm formed onto the tube's surface. The aqueous solutions containing pharmaceuticals (ketoprofen, flurbiprofen) or acid organic dyes (rhodamine B or congo red) were put into the tube, obtaining a good adsorbance performance of the immobilized LDH.

Yang et al. (2020) also used and in-situ method to synthesize MgAl LDH/cellulose nanocomposite beads and study their amoxicillin adsorption capacity. Cellulose beads were produced with an optimal extrusion dropping technology. The synthesis of MgAl LDH/cellulose was carried out by the co-precipitation method using urea with no calcination afterwards. The maximum adsorption capacity of the composite was of

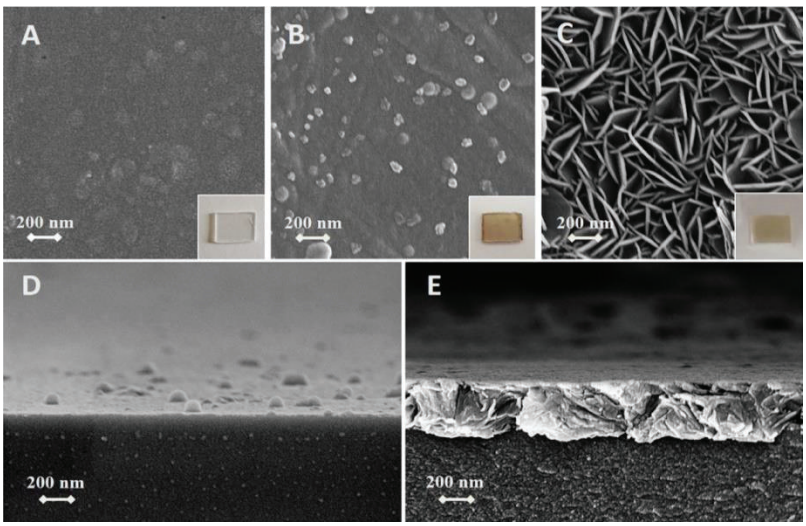

Figure I.13. Photographs and SEM images of the bare and modified polypropylene chip, (A) Bare chip, (B) polydopamine (PD) modified chip, (C) NiAl-LDH modified chip, (D) SEM cross-sectional view of PD layer, and (E) SEM cross-sectional view of NiAl-LDH film. (Reproduced with permission from *Zhou et al.* (2017)).

138.3 mg/g. The kinetics of the adsorption process followed better a pseudo-second-order than a pseudo-first-order model. The isotherms fitted better the Freundlich than the Langmuir model which suggested that the antibiotic removal process was mainly controlled by chemical adsorption and involved a multiple surfaces system. The adsorption mechanism suggested by the authors was an electrostatic interaction that drove the combination of anionic amoxicillin group and the positively charged LDH particles.

Chen et al. (2013) fabricated 3D hierarchical MgAl LDH on the surface of SiO_2 spheres and studied the LDH adsorption capacity with and without support. A good dispersion of the adsorbent particles maximized the contact between the solid surface and the water, as shown in a previous study were LDH nanosheets were synthesized on a 2D structure (Xu et al., 2006). This planar structure would however encounter difficulties in practical operations such as high pressure drop when filled in a column for continuous adsorption or inefficient separation from water due to small particle sizes. That is why LDH mobilized into SiO_2 spheres were more attractive for practical operations. The spheres were synthesized with a modified Stöber method and the dispersed SiO_2-LDH composite was fabricated by a slow co-precipitation method. An ultrasound treatment during growth and aging of the LDH and the removal of free electrolytes after precipitation were the two main factors that influenced the formation of well dispersed spheres. The adsorption capacity of SiO_2-LDH spheres could reach 758 mg/g for DCF compared to 489 mg/g for the LDH without support and the same drug. The adsorption capacity of SiO_2-LDH spheres onto ibuprofen and folic acid was also tested and found to be around 400 mg/g and 332 mg/g, respectively.

Li et al. (2015) also used the 3D support strategy to synthesize a structure composed of stacks of MgAl LDH with different Mg/Al ratios (3, 2 and 1) arranged directionally over γ-AlO(OH) nanowires and amorphous carbon by a biotemplate method (see Figure I.14). Carbon was removed through hydrothermal treatment followed by calcination. Both the molar ratio and the pH during the hydrothermal process had an important role in the formation of the 3D structures. They studied the composite adsorption capacity over minocycline and Congo Red with maximum values of 302 and 447 mg/g, respectively. The isotherms were best described by the Langmuir model and the kinetics by the pseudo-second-order model. The main adsorption mechanisms were ion exchange, electrostatic adsorption and π−π interaction. A change in pH did not have a

significant effect on the adsorption capacity of the composite, due to the amphoteric nature of minocycline.

Hossein Beyki et al. (2017) synthetized a polymeric ionomer together with a CaAl LDH (2:1 ratio) by means of the urea method. The magnetic polymer ionomer was prepared in several steps that involved the addition of iron, pyridin and epichlorohydrin to the cellulose. The magnetite cellulose – LDH (MCL) and the ionomer were used for efficient adsorption of diclofenac sodium. The equilibrium time of the magnetic ionomer was only of 2 minutes with an uptake of up to 268 mg/g. The kinetic models showed a better pseudo-second order fit. In the isotherm studies, the Freundlich model was better at a high concentration of diclofenac. The study of the pH effect on the removal efficiency showed that the adsorption capacity of the adsorbates went up progressively from 3 reaching a maximum removal capacity at 9.

The use of environmental friendly materials such as biochar or cotton fiber as support has also been studied. *de Souza dos Santos et al.* (2020) fabricated a composite with MgAl LDH supported on syagrus coronata biochar that achieved a great efficiency in DCF adsorption (see Figure I.15). The biochar was produced by pyrolysis of the endocarp of the palm tree at 673 K. The LDH was synthesized with a 2:1 ratio and the co-precipitation method and the biochar was added after the dissolution of the salts. The kinetic studies showed that different mechanisms worked depending on the adsorbate initial concentration. Low concentrations favored physisorption, equilibrium time was

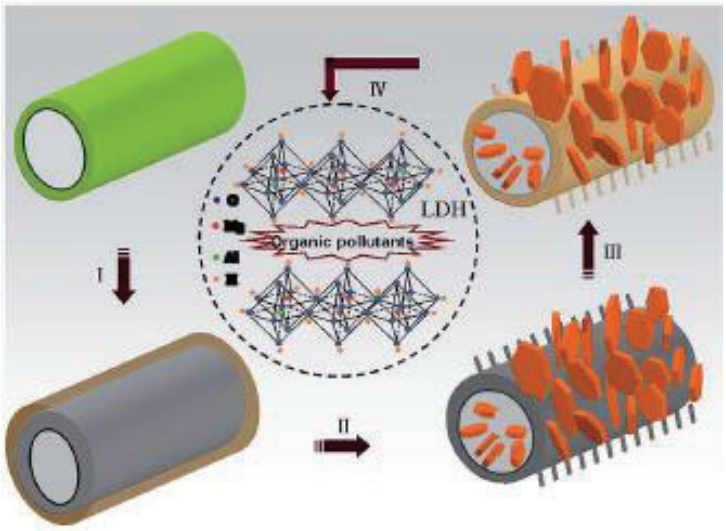

Figure I.14. Schematic representation of the formation process of MgAl LDH arranged over γ-AlO(OH) nanowires. (Reproduced with permission from *Li et al.* (2015)).

reached in less than 1 h and data were better fitted to the pseudo-first order model. At greater concentrations equilibrium time took up to 6 hours as the adsorption was more complex with chemisorption also taking place, and data were better fitted to the pseudo-second order model. Several isothermal models were used; Sips model gave the best results. The effect of the initial pH was also tested with maximum removal efficiency at a pH between 6 and 12.

dos Santos Lins et al. (2019) synthesized MgAl LDH (3:1 ratio, coprecipitation method with bovine bone biochar as support for the LDH. The composite was used as adsorbent for caffeine removal from water. Kinetic studies showed that the adsorption mechanism was better fitted the pseudo-first-order model suggesting a physical adsorption. The equilibrium was reached in 20 min achieving a 26.22 mg/g adsorption capacity. The isotherm models that better adjusted the experimental data were Redlich–Peterson and Sips.

Wang et al. (2018) immobilized NiAl LDH onto cotton fiber via a polydopamine functionalization procedure, thus upgrading the adsorption performance of free-standing LDH. Its performance on the adsorption of ketoprofen and Congo Red (in addition to flurbiprofen, ciprofloxacin, enrofloxacin and bromophenol blue) was tested. Several ratios (3:1, 2:1, 1:1, 1:2 and 1:3) were considered, finally choosing 2:1 due to its better effectiveness. The kinetics was studied with the pseudo-second order model and the

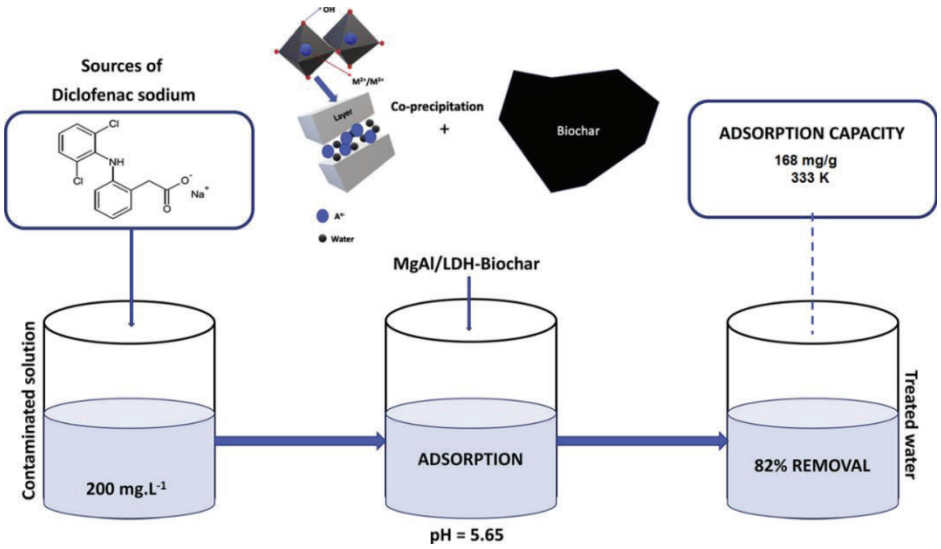

Figure I.15. MgAl LDH supported on biochar as adsorbent of diclofenac sodium (DCF). (Reproduced with permission from *de Souza dos Santos et al.*(2020)).

isotherms were better fitted to the Langmuir model vs the Freundlich one. The maximum adsorption capacities of the composite were 625 and 714 mg/g for ketoprofen and Congo red, respectively. The authors also adjusted the adsorbent into different devices such as micropipettes, a precolumn or a syringe-driven filter obtaining good results in all cases.

I.4.6. KINETIC AND ISOTHERM STUDIES

The 82% of the works reviewed in this study used kinetics and isotherm studies to describe the adsorption processes. The most common expressions used to try to adjust the experimental data are shown in Table I.7.

Kinetic experimental results are in all cases fitted to pseudo-first and pseudo-second order models. When only these models were used, the 83% of the studies were better adjusted to the pseudo-second order model and only one work (de Souza dos Santos et al., 2020) changed the best fit model depending on the adsorbate concentration, the authors suggested that a better fit to the pseudo-first order model was due to physisorption, and the pseudo-second order model fitted better when chemisorption also took place. The fact that the pseudo-second-order model is usually seen as the best fit model can be however due to the introduction of an excess data close to, or at, equilibrium. This creates a methodological bias which has promoted it as the number one model (Simonin, 2016).

The results in the isotherm studies show that a 63% of the works analyzed fit the experimental results to only the Langmuir and Freundlich models. Of them, a 67% of the works considered that their data fitted better the Langmuir model. One of the studies that considered that the Freundlich model gave a better fit of the results was from *Mourid et al.* (2019). They investigated the removal of sulfamethoxazole by a ZnAl LDH with a Zn^{2+}/Al^{3+} ratio of 1:1, prepared by the co-precipitation method and calcined at 773 K. The kinetic results fitted better the pseudo-second-order model and the thermodynamic parameters (298, 318 and 333 K) showed that the adsorption was governed by physisorption; the process was spontaneous and exothermic. The LDH adsorption capacity for the drug reached 4314 mg/g. The recovery of the adsorbents with Na_2CO_3 solution, selected because of the high affinity of carbonate for LDH, meant a decrease in their adsorption capacity from 93% to 71% after six cycles. When

studying the effect of the pH, the low retention values observed in acidic solutions may be explained by partial dissolution of the solid by hydrolysis. The maximum retention was obtained for a pH value between 7 and 8. The low retention capacity of the calcined LDH at higher pH values may result from competition with the carbonate anions, for which the LDH matrix has a very high affinity.

Studies that used three and even four parameter models to fit their isotherm experimental data almost always preferred their adjustments to those given by the Langmuir and Freundlich two parameter models. One of the works that most isotherm models used was *Younes et al*. (2019) (see Figure I.16). They synthesized ZnFe LDH with a 4:1 molar ratio by the co-precipitation method and studied its efficiency as adsorbent for the removal of DCF. The equilibrium was achieved in 30 min with an adsorption capacity of 74.5 mg/g, a pseudo-second order kinetic model gave the best adjustment results and the best-fitted isothermal models were those with three and four parameters (Sips, Langmuir-Freundlich and Baudu). They also studied the adsorption mechanism between the DCF and the LDH with molecular dynamic simulations, suggesting both a physisorption, due to the formation of H-bonds between the diclofenac and the hydroxyl groups of the LDH, and chemisorption, due to the presence of free-bond metal atoms in the LDH surface, took place. In addition, a LDH toxicity study was performed in mice showing no toxic symptoms or mortality and, thus, concluding that these LDH could be used on different body organs safely.

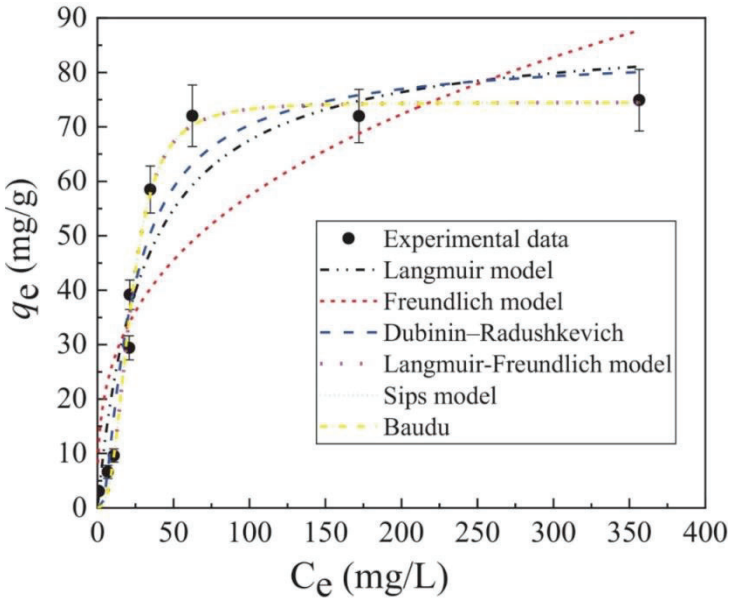

Figure I.16. Equilibrium adsorbed amount of diclofenac sodium (DCF) on ZnFe LDH. (Reproduced with permission from *Younes et al*. (2019)).

Table I.7. Most used Isotherm, kinetic and thermodynamic equations.

Isotherm model	Expression	Kinetic model	Expression
Two parameter isotherm			
Langmuir	$q_e = \frac{k_L \cdot q_L \cdot C_e}{1 + k_L \cdot C_e}$	**Pseudo-first order**	$\frac{dq}{dt} = k_1 (q_e - q_t)$
Freundlich	$q_e = k_F \cdot C_e^{1/m_F}$	**Pseudo-second order**	$\frac{dq}{dt} = k_2 (q_e - q_t)^2$
		Intraparticule diffusion	$\frac{dq}{dt} = k_3 t^{1/2} + C$
Three parameter isotherm		**Thermodynamic equations**	
Toth	$q_e = \frac{k_T \cdot q_T \cdot C_e}{[1 + (k_T \cdot C_e)^{m_T}]^{1/m_T}}$	**Van't Hoff**	$\ln\left(\frac{q_e}{C_e}\right) = \frac{\Delta S^\circ}{R} - \frac{\Delta H^\circ}{RT}$
Sips	$q_e = \frac{q_s (K_S C_e)^{1/m}}{1 + K_S C_e^{1/m}}$	**Gibbs**	$\Delta G^\circ = -RT \ln(K_d)$
Langmuir-Freundlich	$q_e = \frac{q_{max} (K_{LF} C_e)^{\beta}}{1 + (K_{LF} C_e)^{\beta}}$	q_e: equilibrium capacity, C_e: equilibrium conc, q_L: Langmuir capacity K_L:Langmuir constant, K_F, n: Freundlich constants	
Redlich -Petersson	$q_e = \frac{C_e K_{rp}}{(1 + a_{rp} C_e^{b_{rp}})}$	q_T, K_T, m_T : Toth constants, q_S: Sips capacity, K_S, m: sips constants; K_{LF}, β, qmax: Lanmguir-Freundlich constants; a_{rp}, K_{rp}, b_{rp}: redlich-Petersson constants	
		qt: capacity at t, K_1: adsorption rate constant, t:adsorption time, K_2: adsorption rate constant, K_3: diffusion rate constant, C: indicates thickness of the boundary layer,	
		R: gas constant, T: temperature, ΔG: change in free energy, ΔH: enthalpy, ΔS: entropy	

I.4.7. ADSORPTION THERMODYNAMICS

Several works have collected the thermodynamic data for adsorption systems of LDH over pharmaceutical compounds. In order to do so, they have performed a series of experiments at various temperatures. Most used thermodynamic equations involving enthalpy (ΔH), entropy (ΔS) and Gibbs free energy (ΔG), shown in Table I.7. Thermodynamic results for various drugs and LDH are shown in Table I.8.

Boukhalfa et al. (2017) studied the adsorption of diclofenac on ZnAl LDH. The adsorption process was spontaneous and inversely proportional to the temperature as the ΔG° values at various temperatures were negative and decreased with an increase of temperature. The negative value of ΔS° implied that an associative mechanism was involved in the adsorption process and that the adsorbent did not have significant changes in its internal structure. The process was exothermic as revealed by the negative values of ΔH°. *Wu et al.* (2018) also found the process of TCY adsorption over MgFe LDH to be spontaneous; however, the nature of the adsorption process was endothermic as it implied positive enthalpy changes. Positive entropy values showed an increase in randomness of the irreversible adsorption process and, thus, a good adsorbate-adsorbent affinity. *Sepehr et al.* (2017) found the metrodinazole adsorption over MgAl LDH to be non-spontaneous in nature as indicated by the positive values of free energy (ΔG°, temperatures from 283 to 303 K). The process was exothermic; ΔG° values went up with increasing temperature and the negative values of ΔS° showed that during the adsorption process a decrease in the randomness at the solid/liquid interface occurred.

Xiong et al. (2019) used the Hill model to estimate the number of bonded molecules and the adsorption energy at various temperatures to study diclofenac adsorption over MgAl LDH. The number of molecules linked per adsorbent site was inferior to one indicating a parallel adsorbate position. At higher temperature this number was above one showing a change in the diclofenac adsorption geometries, possibly due to the thermal agitation effect. The adsorption energy decreased with an increase of temperature, which may be associated with a decrease of the adsorbed quantity.

Table I.8. Thermodynamic parameters of NSAID/antibiotic adsorption onto LDH.

LDH	adsorbate	ΔH° (J/mol)	ΔS° (J/mol·K)	−ΔG° (J/mol)			Adsorption nature	Ref
				303 K	313 K	323 K		
MgAl on tree biochar	DCF	−111.61	−0.271	−29.6	−28.57	−20.09	Spontaneous, exothermic	(de Souza dos Santos et al., 2020)
MgAl on bovine bone biochar	CAF	−10.37	−0.0195		−16.93	−15.74	Spontaneous, exothermic	(dos Santos Lins et al., 2019)
MgAl	MTD	−4.36	−34.669	6073			Non spontaneous, exothermic	(Sepehr et al., 2017)
NiMgAl on copper ferrite	TCY	21.48	5.8	−2.089	−2.818	−2.978	Spontaneous, endothermic	(Eniola et al., 2020)
				298 K	**308 K**	**318 K**		
ZnAl	DCF	−13.11	−23.25	11.13	9.42	9.00	Non spontaneous, exothermic	(Boukhalfa et al., 2017)
MgAl CO_3	NFX	−3.03	45.87	−16.70	−17.16	−17.61	Spontaneous, exothermic	(Sui et al., 2012)
MgAl Cl	NFX	−27.65	−22.21	−21.03	−20.80	−20.50	Spontaneous, exothermic	(Sui et al., 2012)
MgFe	TCY	1.493	6.13	−0.334	−0.395	−0.456	Spontaneous, endothermic	(Wu et al., 2018)
ZnAl	SLC	−33.76	103.17	−29.68	−30.71	−31.74	Spontaneous, exothermic	(Rosset et al., 2020)
ZnAl	SFM	−15.586	−30.827	−3.962		−3.381	Spontaneous, exothermic	(Mourid et al., 2019)

I.4.8. RECOVERY OF THE ADSORBENT

One of the main problems of adsorption technology, due to its difficulty and cost, is the regeneration of the adsorbents. It may account for more than 70% of the total operating and maintenance costs of an adsorption system (Goh et al., 2008). A regeneration process is successful if it restores the adsorbent to performances similar to its initial ones for effective reuse. Several strategies can be followed when trying to regenerate the adsorbate, like and oxidation method, washing with and organic solvent or basic solution or thermal treatment. Table I.9 describes several adsorbent reuse strategies followed when adsorbing pharmaceutical compounds.

Thermal decomposition (773 K for 12 hours) was used by *Rosset et al.* (2019) in the regeneration of three different samples synthesized: NiAl, MgAl and ZnAl. This strategy did not work for neither NiAl nor MgAl samples, were the loss in their DCF removal capacity was important in the third and fourth cycle, respectively. ZnAl removal capacity, however, did not significantly lower until the eighth cycle. After characterizing the samples with XRD and FITR techniques, the authors associated NiAl and MgAl problem to both the progressive loss of crystallinity of the samples during the reconstruction process of the material (memory effect) and the incorporation of organic species (dos Santos et al., 2013). *Chen et al. (2013)* used an advanced oxidation method (Hasan et al., 2012) to decompose the adsorbed drugs using oxone as oxidant and Co^{2+} as catalyst. Their results were excellent as DCF was eliminated by the oxidation process in less than 1 minute and the LDH efficiency did not suffer any apparent loss of removal capacity for four consequent cycles (above 90% in the four cases). The use of organic solvents like methanol or salts such as NaCl as desorption agents was tried by *dos Santos Lins et al. (2019)*. After 6 cycles, their results show no loss in the adsorption capacity when methanol was employed and a 35% loss with the use of NaCl. The latter lower efficiency could be due to the loss of solubility that caffeine suffers when NaCl is present in the solution, which hinders its desorption form the adsorbent. The drug is better extracted with methanol because its affinity to the solvent is higher than the adsorbent phase. *Wang et al.* (2018) tested the use of an alkaline solution (NaOH 1 M) in cotton supported LDH. The theory supporting this method is the strong affinity that OH^- has towards the highly positive layers of the LDH. The pipette tip packed with the ketoprofen-cotton-LDH was rinsed with the NaOH solution and deionized with water.

Table I.9. LDH regeneration strategies and performance.

LDH	Adsorbate	Regeneration conditions	Regeneration performance	Reference
CaAl on Polymer ionomer	DCF	Basic solutions and organic solvents	Reduction of 11% after 3 cycles	(Hossein Beyki et al., 2017)
MgAl on a biochar	CAF	NaCl or methanol	6 cycles	(dos Santos Lins et al., 2019)
NiAl on cotton fiber	KTP	NaOH 1 M rinse	Close to 100% after 8 cycles	(Wang et al., 2018)
NiMgAl on copper ferrite	TCY	NaOH, acetone and ethanol	42.5% reduction after 3 cycles	(Eniola et al., 2020)
MgAl on SiO_2 spheres	DCF, IBP	Oxidation method	Above 90% in four cycles	(Chen et al., 2013)
MgAl on γ-AlO(OH) nanowires	TCY	Thermal decomposition at 823 K for 3 hours	Adsorption capacity of 88% after 3 cycles	(Li et al., 2015)
ZnAl	SLC	Thermal regeneration at 573 K	Second adsorption lowered adsorption by 16.7%	(Elhalil et al., 2018)
ZnAl	DCF	Ethanol	4 cycles reduction less 10%	(Boukhalfa et al., 2017)
ZnAl, MgAl, NiAl	DCF	Thermal treatment at 773 K for 12 hours	8 cycles, ZnAl stable for 7 cycles	(Rosset et al., 2019)
MgFe on chitosan	TCY	$NaCO_3$ solution + thermal treatment 673 K for 2 hours	Good results	(Wu et al., 2018)
ZnAl	SLC	Thermal regeneration at 673 K	In 5 cycles, reduction of 22%	(Rosset et al., 2020)
ZnAl	SFM	Na_2CO_3	Reduction from 93 to 71% in 6 cycles	(Mourid et al., 2019)

There was no apparent loss on the removal capacity of the cotton supported LDH after 8 cycles. The authors found no differences in the morphology or crystal structure of the immobilized LDH in the SEM and XRD analysis made after regeneration.

I.5. HYDROTALCITE-LIKE COMPOUNDS AND RELATED MATERIALS AS CATALYSTS FOR THE PHOTODEGRADATION OF PHARMACEUTICAL COMPOUNDS: SYNTHESIS AND CATALYTIC PERFORMANCES

I.5.1. INTRODUCTION

At present, large amounts of pharmaceutical compounds are used in several areas, as medicine, industry and cosmetics (Michael et al., 2013). This large intake may cause an increase in the presence of these compounds in natural environments, due to their discharge in untreated wastes or partially treated wastewater. This can hardly be avoided; for example, some medicines are excreted unmetabolized by living organisms in percentages that can reach even the 90% of the ingested dose. Obviously, this may led to the contamination of surface or underground waters (Bethi et al., 2016). Water is one of the more abundant compounds in Nature, covering about three quarters of Earth surface. However, several factors limit its availability for human intake. Human activities strongly affect the quality of water, mainly by the discarding of pollutants, which can provoke very negative effects on vegetal and animal species in the ecosystems, and on humankind itself (Qadir et al., 2010). In the last years, new contaminants have been detected in the environment, being denoted as Emerging Organic Pollutants (EOPs), listed by NORMAN Network (NORMAN, 2019) and defined as synthetic or naturally occurring chemicals that are not commonly monitored in the environment, but which have the potential to enter the environment and cause known or suspected adverse ecological and (or) human health effects. More than 700 EOPs pollutants, and their metabolites and transformation products, have been reported in European aquatic environments, among them are pharmaceutical products, drugs, pesticides, personal care products and industrial additives, and some of them can also be considered as anthropogenic markers for wastewater contamination (Geissen et al., 2015). In the case of medicines, particularly antibiotics, their increasing propagation in the environment is causing the development of strongly resistant bacteria, which is an additional and very important health problem

(Marti et al., 2014). It is expected that in the next years the main cause of death, surpassing those produced by cancer, will be the presence of bacteria multiresistant to several families of antibiotic molecules. This situation has been generated by the abuse of antibiotics in human medicine and environmental pollution derived from agricultural and livestock production.

Thus, the removal of these pollutants becomes mandatory. Several procedures have been proposed, and are being used, for such removal, as solvent extraction, reverse osmosis or adsorption (Williams et al., 1999; Park et al., 2009). Adsorption using materials from various porous families is probably the most popular method, as these materials have low cost, their use is simple and versatile, and they adsorb several types of pollutants (Khenniche and Aissani, 2010). The adsorption process is mainly controlled by the pH of the aqueous solution, the ionic characteristics of the adsorbent and the pollutants, and the ionic strength of the medium. However, this process is based on the change of the pollutants from one phase (water) to the other (adsorbent), but does not destroy them.

In this context, Advanced Oxidation Processes (AOPs) constitute a group of techniques very attractive for the elimination of these pollutants. They cover chemical, photochemical, sonochemical, and electrochemical procedures, including Fenton, ozonation, plasma, photocatalysis, and wet air oxidation reactions, among others, but almost all the processes are based in the production of •OH radicals (sulfate and chlorine radicals can also be used). Other common characteristics are the operation at ambient temperature and pressure conditions (or very close to them) and that they attack all the organic compounds, that is, as they are based on the generation of strong radicals, they are not selective to the pollutants. Under optimal conditions, the process may lead to the complete mineralization of the pollutants (Miklos et al., 2018).

Several materials have been used for assisting heterogeneous photocatalytic processes. Titanium dioxide, TiO_2 under anatase structure, is the most used, functional, versatile and effective photocatalyst, based on its excellent photoelectric properties, low cost, corrosion resistance and non-toxicity for living organisms (Papoulis et al., 2013). However, TiO_2 has an important limitation, its energy band gap is 3.2 eV, and this limits its efficiency to the ultraviolet wavelength of 387.5 nm, only 3 - 5% of the solar radiation that reaches the Earth surface (Deng et al., 2016). This can be partially solved by

dispersing TiO_2 on inorganic matrices, or by modifying it with several dopants as noble metals, transition metal or non-metals, etc., which can decrease the energy required for its activation.

A different strategy is to substitute TiO_2 by other catalyst. For example, clay minerals have received large attention (Garrido-Ramírez et al., 2010; Herney-Ramirez et al., 2010; Praneeth and Paria, 2017) However, hydrotalcites have received very little consideration, although these solids, also called Layered Double Hydroxides, are structurally related to clays and exist with a great variety of compositions. The use of these solids for photocatalytic removal of organic compounds has been recently reviewed (Mohapatra and Parida, 2016) but their use for the degradation of pharmaceutical pollutants has been scarcely reported. In this context, the application of this family of solids for catalytic photodegradation of pharmaceutical pollutants is reviewed in this chapter. Before, the structure and methods of preparation of these materials are briefly presented.

I.5.2. STRUCTURE OF HYDROTALCITES

The hydrotalcite-like materials, or simply hydrotalcites, are a group of solids whose structure and composition are related to the mineral Hydrotalcite, $Mg_6Al_2(CO_3)(OH)_{16}{\cdot}4(H_2O)$. These solids have a lamellar structure, with a form similar to that of brucite, $Mg(OH)_2$. As they are hydroxides of two cations, they are also called Layered Double Hydroxides, and abbreviated LDH.

The structure and chemical composition of hydrotalcites can be considered derived from brucite. Brucite is formed by a hexagonal compact packing of hydroxyl anions, with Mg^{2+} cations occupying all the octahedral holes each two layers, thus generating a layered structure. Mg^{2+} can be substituted by trivalent cations, and each time that this substitution occurs, a positive charge is generated, that must be balanced by the incorporation of compensating anions in the interlayer region. Thus, the layers are positively charged, and compensating anions are located in the interlayer region, just the opposite than in clays, reason why hydrotalcites are also known as Anionic Clays, and can be seen as a *mirror* of clays. In the case of Hydrotalcite, one fourth of Mg^{2+} cations are substituted by Al^{3+}, that is, two of eight in the formula given before, and consequently two positive charges are generated, compensated by the incorporation of a carbonate anion. So, the hydroxyl anions in the formula are *structural*, that is, they form the

octahedral of the structure, while carbonate anions are charge-balancing, and located in the interlayer. Besides, a certain amount of water also incorporates to the interlayer region, this amount depending on the ambient conditions (Rives and Ulibarri, 1999; Rives, 2001; Nalawade et al., 2009; Rives et al., 2013; Mishra et al., 2018). The resultant structure is that shown in Figure I.17.

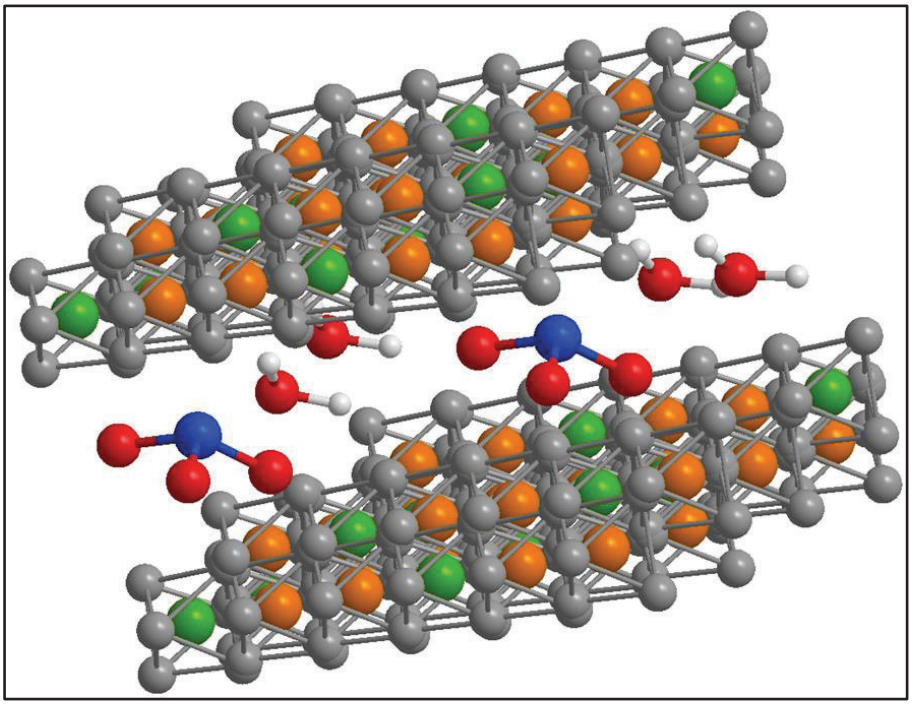

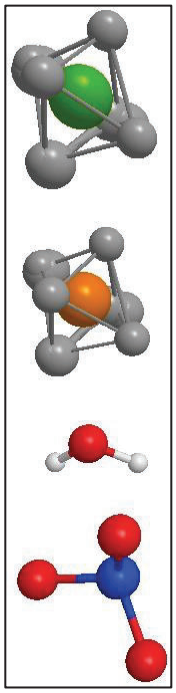

$[M^{III}(OH)_6]^{3-}$

$[M^{II}(OH)_6]^{4-}$

H_2O

Anion (CO_3^{2-})

Figure I.17. Structure of hydrotalcites.

It is remarkable that hydrotalcite layers can stack on different ways, giving up to different polytypes (rhombohedral and hexagonal). More interesting for the application of these solids is the large variety of chemical composition that they can show. Thus, a large amount of divalent and trivalent cations can occupy the positions that in the parent compound are occupied by Mg^{2+} and Al^{3+}, respectively. Strictly, *Hydrotalcite* is the mineral above referenced, and *hydrotalcites* are the solids derived from it, considering the changes in composition we are commenting on now. Almost all the cations, both divalent and trivalent, with size similar to Mg^{2+} can occupy the octahedral holes maintaining the hydrotalcite structure, and hydrotalcites containing a large variety of cations have been prepared in the laboratory. Divalent: Ca, Mn, Co, Ni, Cu, Zn, Pd, Pt; Trivalent: Ga, In, Y, V, Cr, Mn, Fe, Co, Rh, Ir, Ru, lanthanides, among others. The structure is maintained if two or more divalent cations, and/or two or more trivalent cations enter the composition. Even more, when monovalent or tetravalent cations that can isomorphically occupy the octahedral positions, as Li^{+} or Zr^{4+}, are incorporated into the composition, the structure is also maintained. (Rives and Ulibarri, 1999; Rives, 2001; Nalawade et al., 2009; Rives et al., 2013; Mishra et al., 2018).

Besides of the size of the cations, other limiting structural factor is the degree of substitution, that is, beginning from an ideal brucite structure the amount of trivalent cations that can substitute the divalent ones. The molar fraction of the trivalent cation must be ranged between 0.20 and 0.33; in other words, the ratio Me^{2+}/Me^{3+} must range between 2-4. Theoretical calculations have found that the maximum stability is found when the degree of substitution is 0.25 (Me^{2+}/Me^{3+} = 3.0), that is exactly the value present in the natural hydrotalcite. If the substitution degree is higher than 0.33, charged $[Al(OH)_6]$ octahedral must be neighbor among them, creating a repulsion that desestabilizes the structure, while for a substitution degree lower than 0.25 the amount of compensating anions is very low and their distance very large, also destabilizing the structure (Rives and Ulibarri, 1999; Rives, 2001; Nalawade et al., 2009; Rives et al., 2013; Mishra et al., 2018).

As indicated before, the degree of substitution directly determines the charge of the layers, so it conditions the amount of compensating anions. This allows to define the *anion exchange capacity, AEC* as the amount of anions that can be exchanged by a determined amount of hydrotalcite, by analogy with the well-known *cation exchange capacity, CEC* of clays. In the natural hydrotalcite the compensating anion is carbonate,

and due to its divalent charge, its amount is logically half of the substitution degree. When the hydrotalcites are prepared in the laboratory, other compensating anions can be incorporated to the structure, as nitrate, halides, borates, hydroxyl (i.e., hydroxyls as compensating cations, besides of structural hydroxyls, the resultant hydrotalcite being known as meixnerite variety), phosphate, arsenate, sulfate, sulfonates, carboxylates (lactate, terephthalate, acrylate, etc.), but also coordination compounds and polyoxometalates (polyvanadates, polymolibdates, polywolframates, etc.). In these last cases, a new metal is incorporated to the structure, besides of those composing the layers.

With all these considerations, the general formula of the hydrotalcite family can be expressed as $[Me^{2+}_{1-x}\ Me^{3+}_{x}\ (OH)_2]^{x+}\ (A^{n-})_{x/n} \bullet mH_2O$, where x is the degree of substitution of the divalent Me^{2+} cations by the trivalent Me^{3+} cations and consequently the charge of the layer, n is the charge of the anion A, and m is the degree of hydration (Rives and Ulibarri, 1999; Rives, 2001; Nalawade et al., 2009; Rives et al., 2013; Mishra et al., 2018).

When calcined, hydrotalcites tend to transform into oxides. As hydrotalcites are composed of divalent and trivalent cations, the calcination tends to form the spinels $Me^{2+}_{1-x}\ Me^{3+}_{x}\ (OH)_2]^{x+}$, with an excess of the divalent oxide, due to the ratios of both cations in the hydrotalcites and in the spinels. The degree of substitution allows to tailor the amount of spinel in the final oxide mixture, and if in the compensating anions coordination compounds or polyoxometalates, other metal is incorporated to the final mixtures of oxides, this strongly influencing their catalytic performance.

I.5.3. PREPARATION OF HYDROTALCITES

The preparation of hydrotalcites is a relatively simple laboratory procedure, as the thermodynamic tendency to form these compounds is high when the adequate amount of cations and anions are present. Thus, the following preparation procedures can be listed (Rives, 2001).

- Coprecipitation: it is the simplest procedure (see Figure I.18). In summary, it consists in the preparation of aqueous solutions of the desired metal cations in the desired ratios, their mixture, and the increase of the pH up to the precipitation of the hydrotalcite. Usually, the pH is increased by adding NaOH, Na_2CO_3 and/or $NaHCO_3$ solutions (or the metallic solutions are added over the alkaline solution).

If not special precautions are taken, the interlayer anions should be carbonate, even if nor carbonate neither bicarbonate are used for the increase of pH; the reacting mixture, due to its strong alkaline pH, reacts with atmospheric CO_2 and the formed carbonate has a strong tendency to enter into the interlayer. With special precautions and selecting adequately the metallic salts used at the beginning of the process, nitrates, chlorides, etc., these anions can be incorporated into the interlayer.

This method has small modifications, which try to avoid the abrupt precipitation of the solid. The use of automatic titrators allows to modify the pH very slowly and to fix it very precisely to a predetermined value. Other possibility, widely used in the preparation of other families of solids, is to carry out the synthesis assisted by the hydrolysis of urea. A certain amount of urea is added to the mixture, and this is slowly heated, provoking the hydrolysis of the urea, what leads to the formation of ammonium carbonate, thus increasing the pH. Therefore, the increase of the pH can be controlled by the intensity of the heating, with the advantage that the hydrolysis of urea is homogeneous in all the solution, and thus the precipitation leads to more uniform and smaller particles.

Figure I.18. Laboratory procedure for the preparation of hydrotalcites by the coprecipitation method.

- Anion Exchange: this method allows to obtain a hydrotalcite with a certain interlayer anion from the solid containing other anion. The parent solid is put into a highly concentrated solution of the second anion, and the exchange proceeds. Carbonate-hydrotalcite cannot be used as precursor, since the high affinity of this anion to the hydrotalcite interlayer avoids its exchange with other anions. The method is applicable for the intercalation of polyoxometallates and other large anions, and also if the desired anion is not stable in the initial alkaline conditions needed for the precipitation of the hydrotalcite.
- Reconstruction: as indicated before, hydrotalcites are usually calcined to obtain mixtures of oxides. If this calcination is carried out at moderate temperatures, usually ≤ 773 K, the solids obtained show memory effect, that is, the solids are able to recover the hydrotalcite structure if they are dispersed in an anionic solution. Thus, a normal hydrotalcite is obtained, usually containing carbonate and prepared by coprecipitation, and calcined. The calcined solid is then dispersed in a solution containing the final desired anion and the hydrotalcite structure is now reconstructed with this desired anion in the interlayer. As in the previous method, this method is especially indicated for the preparation of hydrotalcites containing polyoxometallates and other large anions, or if the desired anions are not stable under the conditions for coprecipitation synthesis.

In some cases, the hydrotalcite synthesis is assisted by hydrothermal conditions, in recent years microwave treatments being frequent, allowing improvement in the crystallinity and homogeneity of the solids.

I.5.4. HYDROTALCITES IN THE PHOTODEGRADATION OF PHARMACEUTICALS

As indicated before, although the use of hydrotalcites as photocatalysts has been recently reviewed (Mohapatra and Parida, 2016), the use of these materials for the degradation of pharmaceutical pollutants has not been revised. A summary of the main conditions and results is included in Table I.10.

Table I.10. Applications and use conditions of hydrotalcite-like materials as catalysts for the photodegradation of pharmaceutical compounds.

Composition of the LHD	Preparation method	Calcination temperature	Pharmaceutical pollutant	Radiation	Reference
Cu-Ni-Zn-Cr nitrate and carbonate	Mixture, colloid mill and aging (nitrate solids) Anion exchange (carbonate solids)	NO (drying at 333 K)	Salicylic acid	Visible	(Zhao et al., 2011)
Mg-Al carbonate	Co-precipitation	723 K	Sodium naproxen, Oxytetracycline hydrochloride	UV	(Jácome-Acatitla et al., 2014)
Ce-Zn-Al carbonate	Co-precipitation	723, 873, 1023, 1173 K	Paracetamol	Solar simulated	(Zhu et al., 2016)
Zn-Al carbonate	Co-precipitation	473, 573, 673, 773 K	Ibuprofen	Solar simulated	(Di et al., 2017)
Zn-Fe carbonate	Co-precipitation	573, 673, 773, 873, 1073, 1273 K	Caffeine	UV	(Elhalil et al., 2017)
Zn-Fe	Co-precipitation	823, 973 K	Tetraclycine	Visible	(Yang et al., 2017)
Zn-Al chloride	Co-precipitation and anionic exchange	NO (drying at room temperature)	Tetracycline, Oxytetracycline	UV	(Bouaziz et al., 2018)
Zn-Fe*	Hydrothermal	723 K	Paracetamol	Solar simulated	(Zhu et al., 2018)
Zn-Al-La carbonate**	Co-precipitation	573, 673, 773, 873, 1073, 1273 K	Caffeine	UV	(Elhalil et al., 2019)

* Forming composites with graphene oxide. ** Forming composites with Ag

The catalytic photodegradation of salicylic acid sodium under visible-light irradiation has been studied by *Zhao et al.* (2011). Other pollutants, although not pharmaceutical compounds, were also photodegraded, namely sulforhodamine-B, Congo Red and chlorinated phenol. The catalysts were a series of $Me^{2+}Cr$ hydrotalcites (Me^{2+} = Cu, Ni, Zn), prepared by mixing a solution containing the metallic nitrates with a NaOH solution, and submitting the mixture to a colloid mill rotating at 3000 rpm for a short time, followed by a separate aging process at 373 K. Nitrate-containing hydrotalcites were thus obtained, the corresponding carbonate-counterparts being obtained by anion exchange. These catalysts exhibited 20-times higher photocatalytic performance than Degussa P25, attributable to their low band gap (1.6 eV) and their abundant surface OH groups. The authors claimed that the high dispersion of CrO_6 octahedron in the LDH layer played a key role in responding to visible light and photogenerating charge carriers. The LDH matrix provided an ordered dispersion of the CrO_6 octahedron in the layer; which promoted the efficiency of the excited electron and avoided the recombination of electron and hole. The solids showed high recyclable stability for three cycles.

Jácome-Acatitla et al. (2014) prepared MgAl hydrotalcites, with Mg/Al ratios of 2.0, 2.5, 3.0 by the coprecipitation method (K_2CO_3/KOH, pH = 9). The resulting hydrotalcites were calcined at 723 K. The calcined solids were employed for the catalytic photodegradation of sodium naproxen and oxytetracycline hydrochloride, under 254 nm UV irradiation. About 90% of sodium naproxen and 70% of oxytetracycline hydrochloride were mineralized by the best catalyst (Mg/Al = 2.5) after 5 h of reaction, showing better behavior than that of commercial Degussa P25 TiO_2. Fluorescence spectroscopy study suggested the generation of hydroxyl radicals as the oxidative species, and band gap energies were 3.054 – 3.083 eV.

Catalysts based on Zn-Al-Ce were prepared by calcination of Ce-doped Zn-Al hydrotalcite precursors and used in the photodegradation of paracetamol and rhodamine B dye in aqueous solutions under simulated solar light irradiation (Zhu et al., 2016). The results showed an increase of the catalytic photoactivity due to the presence of Ce. The optimal Ce content was studied and found to be of 5% mole ratio ($n_{Ce}/n_{(Zn+Al+Ce)}$), which could be attributed to the increase in the separation efficiency of electrons and holes. The most effective calcination temperature was also examined and found to be 1023 K, which was attributed to the formation of well-crystallized metal oxides. After 240 min,

a 98.9% of paracetamol degradation efficiency was achieved (97.8% for rhodamine B) and the authors suggested the importance of holes, superoxide radicals and hydroxyl radical roles during the photocatalytic process. These catalysts were also proven to be stable and reusable up to 10 cycles.

Di et al., (2017) prepared Zn-Fe carbonate hydrotalcite by coprecipitation, and calcined it at several temperatures, using the resultant solids for the degradation of ibuprofen. The solid with Zn/Fe ratio of 4 and calcined at 573 K exhibited the best efficiency in the degradation of the pharmaceutical compound (the amount degraded was not given, although from the plot seems to be c.a. 95%, the rate constant was 1.584 x 10^{-2} 1/min). The solids were also used for the adsorption removal of As(III) (arsenite), obtaining a maximum adsorption capacity of 176.3 mg/g, and for the simultaneous removal of ibuprofen and arsenite, finding that the presence of ibuprofen did not affect the adsorption of arsenite but, in contrast, the presence of arsenic strongly influenced the degradation of ibuprofen, depending on the arsenic species and concentrations. The authors indicated that photogenerated h^+ played a major role in the process of ibuprofen degradation, while arsenic was removed by combined oxidation and adsorption. The reusability was also studied for six runs, with excellent behavior. Although the authors claimed that the process was effective using other pharmaceuticals, namely acetaminophen and diclofenac, but no data on their degradation were given.

The degradation of caffeine using the solids derived from Zn-Al carbonate hydrotalcites has been studied by *Elhalil et al.* (2017). Various Zn/Al molar ratios were considered, namely 1, 3 and 5, and the resulting hydrotalcites were calcined at 573, 673, 773, 873, 1073, 1273 K for 6 h. As this calcination led to ZnO-$ZnAl_2O_4$ mixture, a pure ZnO sample was also prepared, and Degussa P-25 TiO_2 was also used as reference. The best caffeine removal efficiency (97.32%) was shown by the sample with Zn/Al = 3 calcined at 773 K, and caffeine photodegradation reaction always followed a pseudo-first-order kinetics. The catalytic efficiency of the solids derived from the hydrotalcites, composed of mixtures ZnO-$ZnAl_2O_4$, strongly depended on the calcination temperature, attributed to the progressive formation of the active phase ZnO. These solids showed better behavior than pure ZnO and also than standard Degussa P25. The authors proposed that the crystallinity and good dispersion of ZnO on the surface of the solids were important factors in the catalytic performance.

The same authors (Elhalil et al., 2019) have used as photocatalysts composites Ag-ZnO-$La_2O_2CO_3$ derived from hydrotalcites. The hydrotalcites were formed by the coprecipitation method, considering the ratios Zn/(Al+La) of 3 and La/Al of 0, 0.25 and 0.5. The pH was increased with Na_2CO_3/NaOH up to 8.5 when only Zn and Al formed the hydrotalcite and to 10 for the two samples containing La. The resulting hydrotalcites were calcined at 573, 673, 773, 873, 1073, 1273 K. The dried solids were composed of LDH and $LaCO_3OH$ phases, while ZnO, $ZnAl_2O_4$, $La_2O_2CO_3$ and $LaAlO_3$ were observed, in function of the temperature, in the calcined samples. Ag was deposited by a solvent-free ceramic process, grinding $AgNO_3$ and LDH in an agate mortar, and then calcining them in air at 773 K for 6 h; 1, 3 and 5% Ag contents were considered. The solids were applied in the degradation of caffeine under an UV mercury lamp. The Ag-containing solids were much more active than undoped composites, and also than reference ZnO and Degussa P-25 TiO_2. The best degradation result, 99.4% after 40 min of irradiation, was shown by the solids with La/Al= 0.25 and 5% Ag. The optimal catalyst dosage for the degradation of a 20 mg/dm^3 of caffeine solution was 0.3 g/dm^3. The catalytic activity was mainly attributed to the interfacial heterostructure in the Ag-ZnO-Al_2O_3 surface, and was observed depending on the pH, 9.5 being the optimal value. The reusability was evaluated for the best catalyst, being excellent as it showed a degradation of 92.98% in the third cycle.

Yang et al. (2017) prepared a Zn/Fe hydrotalcite by the co-precipitation method, with molar ratio of Zn/Fe = 2.0. The anions should be nitrate and carbonate, as the nitrates were used as source of the cations, and the pH was increased with NaOH, but no special precautions to avoid the carbonate incorporation were reported. The hydrotalcite was calcined at 823 and 1023 K to form the photocatalysts, denoted as Zn/Fe mixed metal oxide (Zn/Fe-MMO) nanocomposites by the authors, which were used for the degradation of the antibiotic tetracycline, and also of the dye methylene blue, under visible light irradiation. The catalysts were composed of wurtzite-ZnO and spinel-$ZnFe_2O_4$ phases. The hydrotalcite, not calcined, was also tested as catalyst, showing lower activity than the calcined composites. The degradation reached 90% after 60 minutes for the solid calcined at 973 K, following pseudo-first order kinetics. The improved catalytic performance of this solid was attributed to the visible-light adsorption and more production of photogenerated electron-hole pairs. Based on the

trapping radical tests and ESR analysis, the authors suggested that the photodegradation occurred with the generation of active radicals ($\bullet O_2^-$ and •OH).

The preparation of ZnAl-chloride hydrotalcite (Zn/Al = 2) and its interaction with the antibiotics tetracycline and oxytetracycline was considered by *Bouaziz et al.* (2018). In this case, nor the hydrotalcite neither the oxides derived from its calcination were used for the degradation of the antibiotics, but the interaction between them was studied in a different way. First, the antibiotic were intercalated into the interlayer of the hydrotalcite, and two methods were considered, the anionic exchange of the chloride anions of a previously prepared sample of the hydrotalcite by the antibiotics or the preparation of the hydrotalcite in the presence of the antibiotics. That is, having the antibiotics in the solution of the cations before increasing the pH for the coprecipitation process. Unfortunately, intercalation was not successful, and the antibiotics were located on the external surface of the hydrotalcite. The antibiotics were released after 10 hours. The antibacterial activity of the solids was tested against *Escherichia coli* and *Staphylococcus epidermidis*, finding lower activity than for the free antibiotics. It is proposed that the antibiotics partially degraded in contact with the hydrotalcite. The degradation was confirmed under exposure of the solids to UV radiation or under storage at increasing temperatures (303, 333 and 393 K).

Zhu et al. (2018) prepared ZnFe carbonate hydrotalcite (Zn:Fe = 3) by the urea assisted coprecipitation. Composites graphene oxide/hydrotalcite was prepared by carrying out the hydrotalcite synthesis under the same conditions but in the presence of various amounts of graphene oxide, previously submitted to sonication for its delamination. The process was completed by hydrothermal treatment for 24 h at 393 K, centrifugation, drying and calcination at 723 K under nitrogen atmosphere. The structure of well-crystallized hydrotalcite was observed in all the X-ray diffractograms. The calcined samples showed the presence of ZnO and $ZnFe_2O_4$. These composites were used towards the degradation of paracetamol under simulated solar light irradiation and exhibited a 3.5 times improved catalytic performance as compared to pristine ZnFe hydrotalcite sample. This behavior was attributed to the graphene oxide, which may increase pollutant adsorption capacity and enhance charge separation efficiency. These composites were also applied to the catalytic photooxidation of As(III) to As(V). Interestingly, paracetamol degradation was more efficient in the mixed system paracetamol/As(III) than in the single paracetamol system, while arsenic was also

efficiently removed. The catalysts showed excellent reuse properties, showing a slight decrease of performance, 8.1%, after five successive experimental runs, with the advantage that can be easily separated and recovered by an external magnet.

I.6. CONCLUSIONS AND FUTURE PERSPECTIVES

The presence of pharmaceutical compounds in natural water is an increasing problem as these compounds have environmental effects even at low concentrations. This is why the need for efficient systems to clean water from emerging contaminants is of considerable importance.

Hydrotalcite-like compounds, also known as Layered Double Hydroxides (LDH), are strong contestants as both photocatalysts and adsorbents because of their high versatility in chemical composition, the easiness of their synthesis and their good properties. LDH effectiveness in the removal of different antibiotics (tetracycline, metrodinazole, amoxicillin, norfloxacin, sulfamethoxazole) and NSAID (diclofenac, salicylic acid, ibuprofen, ketoprofen, flurbiprofen) from water has been reviewed. Several factors such as preparation procedures, structure, the memory effect, and the use of support or foreign substances have been described and analyzed. In adsorption, Kinetics and isotherm models highlighted the prevalence of pseudo-first and pseudo-second-order models and Langmuir and Freundlich model, respectively. The temperature seems to have a greater effect than the initial pH, with the majority of the processes being exothermic and spontaneous. As is one of the main drawbacks of the adsorption technique, different strategies to recover the adsorbents in a simple yet effective way have also been described.

Even though much effort has been put into the study of LDH as photocatalysts and adsorbents for pharmaceutical compounds over the last years, there are several factors that need to be further studied and implemented, such as further study of green supports, the use of real water effluents with more than one contaminant, adsorption in continuous mode (fixed-bed experiments) or the search for low cost and environmentally friendly regeneration methods. Thus, the removal process should be studied using larger-scale processes to check its feasibility in full-scale installations at an industrial level.

There are still many interesting areas to explore for LDH applications. The particular structure of these materials can be designed, controlled and adapted to the desired purpose, such as the immobilization of enzymes and microorganisms and their possible applications as biocatalysts. The synthesis of LDH from industrial metal wastes may also be of relevant interest because this method achieves the loop closure of a circular economy system.

I.7. SCOPE AND OBJECTIVES OF THIS THESIS

The objective of the work studied here was to synthesize Layered Double Hydroxides (LDH) with aluminum extracted from saline slags and test their function once calcined into adsorbents/catalysts for use in the removal of emerging contaminants (pharmaceutical compounds) from aqueous media.

Two different techniques for the removal of contaminants were tested, adsorption and photocatalysis. The work carried out has been divided into the different chapters of this written report.

For the use of LDH as adsorbents, different metals were chosen as Me^{2+} (Co, Mg, Ni and Zn) and Al extracted from saline slags always as Me^{3+} to synthesize 4 different adsorbents and test their adsorption capacities of diclofenac and salicylic acid as example of emerging contaminants (chapter III). The pH, mass of adsorbent, contact time and concentration of pollutant were the parameters used to compare their adsorption capacities. The results showed that, in general, the removal of diclofenac was greater than that of salicylic acid and LDH synthesized with Zn and Mg showed higher adsorption capacities. 1-Butanol conversion was also used as means of basicity and acidity characterization and the results compared to the adsorption performance.

As Zn LDH had the best adsorption performance, it was chosen to synthesize a new series of LDH, in this case with Zn always as Me^{2+} and a combination, in different proportions, of Al^{3+}/Ti^{3+} as Me^{3+} (chapter IV). Two different series were synthesized; one with commercial aluminum and the other with aluminum extracted from saline slags and their structural characterization was performed and compared. The adsorption capacities of these LDH were also tested for diclofenac and salicylic acid in both batch and fixed-bed adsorption. The results showed that the adsorption capacity of the samples was better when less titanium was incorporated as Me^{3+}.

Finally, the adsorption capacities of different commercial adsorbents were also tested for comparison purposes (chapter VII). Carbon nanotubes were tested for the removal of caffeine and salicylic acid. On the other hand activated carbon and the MOF basolite A100 were tested for the removal of DL-1,2-Isopropylideneglycerol (used in the production of biodiesel as additive of glycerol); diclofenac and caffeine removal were also tested in batch adsorption.

For the use of LDH as photocatalysts, experiments with TiO_2 on its own were performed in advance. To prevent the TiO_2 from electron-hole recombination, anatase was synthesized and modified with different content (0.5-5wt.%) of Fe and Ag (chapter V). Two different synthesis techniques were used (sol-gel and wet impregnation) to either dope (within the crystalline lattice) or impregnate the anatase with the metals. The different catalysts, together with UV light, were tested for the removal of salicylic acid of the aqueous media. Results showed that the catalyst most active in the degradation of the pollutant were those having the highest Fe content (5wt.%).

These results were used for the tests performed with LDH as photocatalysts. In this study the series with $Zn^{2+}/(Ti+Al)^{3+}$ LDH synthesized in chapter IV and tested as adsorbents, were tested as photocatalysts for the removal of salicylic acid and diclofenac (chapter VI). This LDH series performance was compared with the same series impregnated with 5wt.% of iron to prevent the electron-hole recombination of titanium obtaining better results. In addition, another series $Zn^{2+}/(Fe+Al)^{3+}$ materials with and without 5 wt.% impregnated titanium (Ti^{4+}) are tested as catalysts for comparison. Overall, the results showed that the ZnAlTi series were more effective catalysts than ZnAlFe for photodegradation of the emerging contaminants diclofenac and salicylic acid.

I.8. PUBLICATIONS GENERATED FROM THIS INVESTIGATION

Santamaría, L., Vicente, M.A., Korili, S.A., Gil, A. Progress in the removal of pharmaceutical compounds from aqueous solution using layered double hydroxides as adsorbents: a review. J. Environ. Chem. Eng. (in press).

Santamaría, L., Gil, A., Vicente, M.A., Korili, S.A., 2020. Chapter 5 - Hydrotalcite-like compounds and related materials as catalysts for the photodegradation of pharmaceutical compounds: Synthesis and catalytic performances, in: Singh, P.,

Borthakur, A., Mishra, P.K., Tiwary, D.B. (Eds.). Elsevier, pp. 79–90. https://doi.org/10.1016/B978-0-12-818598-8.00005-5

Santamaría, L., Devred, F., Gaigneaux, E.M., Vicente, M.A., Korili, S.A., Gil, A., 2020. Effect of the surface properties of Me^{2+}/Al layered double hydroxides synthesized from aluminum saline slag wastes on the adsorption removal of drugs. Microporous Mesoporous Mater. 110560. https://doi.org/10.1016/j.micromeso.2020.110560

Santamaría, L, López-Aizpún, M., García-Padial, M., Vicente, M.A., Korili, S.A., Gil, A., 2020. Zn-Ti-Al layered double hydroxides synthesized from aluminum saline slag wastes as efficient drug adsorbents. Appl. Clay Sci. 187, 105486. https://doi.org/10.1016/j.clay.2020.105486

Santamaría, L, Vicente, M.A., Korili, S.A., Gil, A., 2020. Effect of the preparation method and metal content on the synthesis of metal modified titanium oxide used for the removal of salicylic acid under UV light. Environ. Technol. 41, 2073–2084. https://doi.org/10.1080/09593330.2018.1555285

Santamaría, L, Vicente, M.A., Korili, S.A., Gil, A., 2020. Saline slag waste as an aluminum source for the synthesis of Zn–Al–Fe–Ti layered double-hydroxides as catalysts for the photodegradation of emerging contaminants. J. Alloys Compd. 156007. https://doi.org/10.1016/j.jallcom.2020.156007

Gil, A., Santamaría, L., Korili, S.A., 2018. Removal of Caffeine and Diclofenac from Aqueous Solution by Adsorption on Multiwalled Carbon Nanotubes. Colloid Interface Sci. Commun. 22, 25–28. https://doi.org/10.1016/j.colcom.2017.11.007

I.9. REFERENCES

Acero, J.L., Javier Benitez, F., Real, F.J., Teva, F., 2012. Coupling of adsorption, coagulation, and ultrafiltration processes for the removal of emerging contaminants in a secondary effluent. Chem. Eng. J. 210, 1–8. https://doi.org/10.1016/j.cej.2012.08.043

Ahmed, M.B., Zhou, J.L., Ngo, H.H., Guo, W., Thomaidis, N.S., Xu, J., 2017. Progress in the biological and chemical treatment technologies for emerging contaminant removal from wastewater: A critical review. J. Hazard. Mater. 323, 274–298.

https://doi.org/10.1016/j.jhazmat.2016.04.045

Antrekowitsch, H., Hanko, G., Ebner, P., 2002. Recycling of different types of magnesium scrap. TMS Annu. Meet. 43–48.

aus der Beek, T., Weber, F.A., Bergmann, A., Hickmann, S., Ebert, I., Hein, A., Küster, A., 2016. Pharmaceuticals in the environment-Global occurrences and perspectives. Environ. Toxicol. Chem. 35, 823–835. https://doi.org/10.1002/etc.3339

Beck, T.R., 2013. A new energy-efficient and environmentally friendly process to produce aluminum. Jom 65, 267–271. https://doi.org/10.1007/s11837-012-0517-8

Benito, P., Guinea, I., Labajos, F.M., Rives, V., 2008. Microwave-assisted reconstruction of Ni,Al hydrotalcite-like compounds. J. Solid State Chem. 181, 987–996. https://doi.org/10.1016/j.jssc.2008.02.003

Besha, A.T., Gebreyohannes, A.Y., Tufa, R.A., Bekele, D.N., Curcio, E., Giorno, L., 2017. Removal of emerging micropollutants by activated sludge process and membrane bioreactors and the effects of micropollutants on membrane fouling: A review. J. Environ. Chem. Eng. 5, 2395–2414. https://doi.org/10.1016/j.jece.2017.04.027

Bethi, B., Sonawane, S.H., Bhanvase, B.A., Gumfekar, S.P., 2016. Nanomaterials-based advanced oxidation processes for wastewater treatment: A review. Chem. Eng. Process. Process Intensif. 109, 178–189. https://doi.org/10.1016/j.cep.2016.08.016

Bolong, N., Ismail, A.F., Salim, M.R., Matsuura, T., 2009. A review of the effects of emerging contaminants in wastewater and options for their removal. Desalination 239, 229–246. https://doi.org/10.1016/j.desal.2008.03.020

Bouaziz, Z., Soussan, L., Janot, J.M., Jaber, M., Ben Haj Amara, A., Balme, S., 2018. Dual role of layered double hydroxide nanocomposites on antibacterial activity and degradation of tetracycline and oxytetracyline. Chemosphere 206, 175–183. https://doi.org/10.1016/j.chemosphere.2018.05.003

Boukhalfa, N., Boutahala, M., Djebri, N., 2017. Synthesis and characterization of ZnAl-layered double hydroxide and organo-K10 montmorillonite for the removal of diclofenac from aqueous solution. Adsorpt. Sci. Technol. 35, 20–36.

https://doi.org/10.1177/0263617416666548

Bureau of International Recycling (BIR) [WWW Document], 2020. URL https://www.bir.org/

Chen, C., Wang, P., Lim, T.T., Liu, L., Liu, S., Xu, R., 2013. A facile synthesis of monodispersed hierarchical layered double hydroxide on silica spheres for efficient removal of pharmaceuticals from water. J. Mater. Chem. A 1, 3877–3880. https://doi.org/10.1039/c3ta10197e

Chen, M., Wu, P., Huang, Z., Liu, J., Li, Y., Zhu, N., Dang, Z., Bi, Y., 2019. Environmental application of MgMn-layered double oxide for simultaneous efficient removal of tetracycline and Cd pollution: Performance and mechanism. J. Environ. Manage. 246, 164–173. https://doi.org/10.1016/j.jenvman.2019.06.002

de Souza dos Santos, G.E., Ide, A.H., Duarte, J.L.S., McKay, G., Silva, A.O.S., Meili, L., 2020. Adsorption of anti-inflammatory drug diclofenac by MgAl/layered double hydroxide supported on Syagrus coronata biochar. Powder Technol. 364, 229–240. https://doi.org/10.1016/j.powtec.2020.01.083

Deegan, A.M., Shaik, B., Nolan, K., Urell, K., Oelgemöller, M., Tobin, J., Morrissey, A., 2011. Treatment options for wastewater effluents from pharmaceutical companies. Int. J. Environ. Sci. Technol. 8, 649–666. https://doi.org/10.1007/BF03326250

del Mar Orta, M., Martín, J., Medina-Carrasco, S., Santos, J.L., Aparicio, I., Alonso, E., 2019. Adsorption of propranolol onto montmorillonite: Kinetic, isotherm and pH studies. Appl. Clay Sci. 173, 107–114. https://doi.org/10.1016/j.clay.2019.03.015

Deng, Fang; Zhao, Xiang; Pei, Xule; Luo, Xubiao; Li, Wentao; Au, C., 2016. Sol-Hydrothermal Synthesis of Inorganic-Framework Molecularly Imprinted TiO_2 Nanoparticle and Its Enhanced Photocatalytic Activity For Degradation of Target Pollutant. Sci. Adv. Mater. 8. https://doi.org/10.1166/sam.2016.2695

Di, G., Zhu, Z., Zhang, H., Zhu, J., Lu, H., Zhang, W., Qiu, Y., Zhu, L., Küppers, S., 2017. Simultaneous removal of several pharmaceuticals and arsenic on Zn-Fe mixed metal oxides: Combination of photocatalysis and adsorption. Chem. Eng. J. 328, 141–151. https://doi.org/10.1016/j.cej.2017.06.112

Dias, A.C., Fontes, M.P.F., 2020. Arsenic (V) removal from water using hydrotalcites as adsorbents: A critical review. Appl. Clay Sci. 191, 105615. https://doi.org/10.1016/j.clay.2020.105615

dos Santos Lins, P.V., Henrique, D.C., Ide, A.H., de Paiva e Silva Zanta, C.L., Meili, L., 2019. Evaluation of caffeine adsorption by MgAl-LDH/biochar composite. Environ. Sci. Pollut. Res. 26, 31804–31811. https://doi.org/10.1007/s11356-019-06288-3

dos Santos, R.M.M., Gonçalves, R.G.L., Constantino, V.R.L., da Costa, L.M., da Silva, L.H.M., Tronto, J., Pinto, F.G., 2013. Removal of Acid Green 68:1 from aqueous solutions by calcined and uncalcined layered double hydroxides. Appl. Clay Sci. 80–81, 189–195. https://doi.org/10.1016/j.clay.2013.04.006

Elhalil, A., Elmoubarki, R., Farnane, M., Machrouhi, A., Mahjoubi, F.Z., Sadiq, M., Qourzal, S., Abdennouri, M., Barka, N., 2019. Novel Ag-ZnO-$La_2O_2CO_3$ photocatalysts derived from the Layered Double Hydroxide structure with excellent photocatalytic performance for the degradation of pharmaceutical compounds. J. Sci. Adv. Mater. Devices 4, 34–46. https://doi.org/10.1016/j.jsamd.2019.01.002

Elhalil, A., Elmoubarki, R., Machrouhi, A., Sadiq, M., Abdennouri, M., Qourzal, S., Barka, N., 2017. Photocatalytic degradation of caffeine by ZnO-$ZnAl_2O_4$ nanoparticles derived from LDH structure. J. Environ. Chem. Eng. 5, 3719–3726. https://doi.org/10.1016/j.jece.2017.07.037

Elhalil, A., Farnane, M., Machrouhi, A., Mahjoubi, F.Z., Elmoubarki, R., Tounsadi, H., Abdennouri, M., Barka, N., 2018. Effects of molar ratio and calcination temperature on the adsorption performance of Zn/Al layered double hydroxide nanoparticles in the removal of pharmaceutical pollutants. J. Sci. Adv. Mater. Devices 3, 188–195. https://doi.org/10.1016/j.jsamd.2018.03.005

Eniola, J.O., Kumar, R., Mohamed, O.A., Al-Rashdi, A.A., Barakat, M.A., 2020. Synthesis and characterization of $CuFe_2O_4$/NiMgAl-LDH composite for the efficient removal of oxytetracycline antibiotic. J. Saudi Chem. Soc. 24, 139–150. https://doi.org/10.1016/j.jscs.2019.11.001

European Commission, 2018a. Commission notice on technical guidance on the

classification of waste. Off. J. Eur. Union. URL https://eur-lex.europa.eu/legal-content/EN/TXT/?uri=uriserv:OJ.C_.2018.124.01.0001.01.ENG&toc=OJ:C:2018:124:TOC

European Commission, 2018b. COMMISSION IMPLEMENTING DECISION (EU) 2018/840 of 5 June 2018. Off. J. Eur. Union 141, 9–12.

European Union, 2000. DIRECTIVE 2000/60/EC OF THE EUROPEAN PARLIAMENT AND OF THE COUNCIL of 23 October 2000 establishing a framework for Community action in the field of water policy [WWW Document]. Off. J. Eur. Union. URL https://eur-lex.europa.eu/legal-content/EN/ALL/?uri=CELEX:32000L0060

Executive Agency for Health and Consumers, 2013. Study on the environmental risks of medicinal products.

Garrido-Ramírez, E.G., Theng, B.K.G., Mora, M.L., 2010. Clays and oxide minerals as catalysts and nanocatalysts in Fenton-like reactions - A review. Appl. Clay Sci. 47, 182–192. https://doi.org/10.1016/j.clay.2009.11.044

Geissen, V., Mol, H., Klumpp, E., Umlauf, G., Nadal, M., van der Ploeg, M., van de Zee, S.E.A.T.M., Ritsema, C.J., 2015. Emerging pollutants in the environment: A challenge for water resource management. Int. Soil Water Conserv. Res. 3, 57–65. https://doi.org/10.1016/j.iswcr.2015.03.002

Gil, A., 2005. Management of the Salt Cake from Secondary Aluminum Fusion Processes. Ind. Eng. Chem. Res. 44, 8852–8857. https://doi.org/10.1021/ie050835o

Gil, A., Korili, S.A., 2016. Management and valorization of aluminum saline slags: Current status and future trends. Chem. Eng. J. 289, 74–84. https://doi.org/10.1016/j.cej.2015.12.069

Gogoi, A., Mazumder, P., Tyagi, V.K., Tushara Chaminda, G.G., An, A.K., Kumar, M., 2018. Occurrence and fate of emerging contaminants in water environment: A review. Groundw. Sustain. Dev. 6, 169–180. https://doi.org/10.1016/j.gsd.2017.12.009

Goh, K.H., Lim, T.T., Dong, Z., 2008. Application of layered double hydroxides for removal of oxyanions: A review. Water Res. 42, 1343–1368.

https://doi.org/10.1016/j.watres.2007.10.043

Grassi, M., Kaykioglu, G., Belgiorno, V., Lofrano, G., 2012. Emerging compounds removal from wastewater. Natural and Solar based treatments. https://doi.org/10.1007/978-94-007-2409-9

Haque, E., Jun, J.W., Jhung, S.H., 2011. Adsorptive removal of methyl orange and methylene blue from aqueous solution with a metal-organic framework material, iron terephthalate (MOF-235). J. Hazard. Mater. 185, 507–511. https://doi.org/10.1016/j.jhazmat.2010.09.035

Hasan, Z., Jeon, J., Jhung, S.H., 2012. Adsorptive removal of naproxen and clofibric acid from water using metal-organic frameworks. J. Hazard. Mater. 209–210, 151–157. https://doi.org/10.1016/j.jhazmat.2012.01.005

He, B. shu, Wang, J., Liu, J., Hu, X. min, 2017. Eco-pharmacovigilance of non-steroidal anti-inflammatory drugs: Necessity and opportunities. Chemosphere 181, 178–189. https://doi.org/10.1016/j.chemosphere.2017.04.084

Herney-Ramirez, J., Vicente, M.A., Madeira, L.M., 2010. Heterogeneous photo-Fenton oxidation with pillared clay-based catalysts for wastewater treatment: A review. Appl. Catal. B Environ. 98, 10–26. https://doi.org/10.1016/j.apcatb.2010.05.004

Hossein Beyki, M., Mohammadirad, M., Shemirani, F., Saboury, A.A., 2017. Magnetic cellulose ionomer/layered double hydroxide: An efficient anion exchange platform with enhanced diclofenac adsorption property. Carbohydr. Polym. 157, 438–446. https://doi.org/10.1016/j.carbpol.2016.10.017

Jácome-Acatitla, G., Tzompantzi, F., López-González, R., García-Mendoza, C., Alvaro, J.M., Gómez, R., 2014. Photodegradation of sodium naproxen and oxytetracycline hydrochloride in aqueous medium using as photocatalysts Mg-Al calcined hydrotalcites. J. Photochem. Photobiol. A Chem. 277, 82–89. https://doi.org/10.1016/j.jphotochem.2013.12.014

Johnson, A.C., Sumpter, J.P., 2001. Removal of endocrine-disrupting chemicals in activated sludge treatment works. Environ. Sci. Technol. 35, 4697–4703. https://doi.org/10.1021/es010171j

Khan, A.H., Khan, N.A., Ahmed, S., Dhingra, A., Singh, C.P., Khan, S.U.,

Mohammadi, A.A., Changani, F., Yousefi, M., Alam, S., Vambol, S., Vambol, V., Khursheed, A., Ali, I., 2020. Application of advanced oxidation processes followed by different treatment technologies for hospital wastewater treatment. J. Clean. Prod. 269. https://doi.org/10.1016/j.jclepro.2020.122411

Khan, N.A., Ahmed, S., Farooqi, I.H., Ali, I., Vambol, V., Changani, F., Yousefi, M., Vambol, S., Khan, S.U., Khan, A.H., 2020a. Occurrence, sources and conventional treatment techniques for various antibiotics present in hospital wastewaters: A critical review.Trends Anal. Chem. 129. https://doi.org/10.1016/j.trac.2020.115921

Khan, N.A., Khan, S.U., Ahmed, S., Farooqi, I.H., Yousefi, M., Mohammadi, A.A., Changani, F., 2020b. Recent trends in disposal and treatment technologies of emerging-pollutants- A critical review. Trends Anal. Chem. 122. https://doi.org/10.1016/j.trac.2019.115744

Khenniche, L., Aissani, F., 2010. Preparation and characterization of carbons from coffee residue: Adsorption of salicylic acid on the prepared carbons. J. Chem. Eng. Data 55, 728–734. https://doi.org/10.1021/je900426a

Lazaratou, C. V., Vayenas, D. V., Papoulis, D., 2020. The role of clays, clay minerals and clay-based materials for nitrate removal from water systems: A review. Appl. Clay Sci. 185, 105377. https://doi.org/10.1016/j.clay.2019.105377

Li, J., Zhang, N., Ng, D.H.L., 2015. Synthesis of a 3D hierarchical structure of γ-AlO(OH)/Mg-Al-LDH/C and its performance in organic dyes and antibiotics adsorption. J. Mater. Chem. A 3, 21106–21115. https://doi.org/10.1039/c5ta04497a

Li, Y., Bi, H.Y., Jin, Y.S., 2017. Facile preparation of rhamnolipid-layered double hydroxide nanocomposite for simultaneous adsorption of p-cresol and copper ions from water. Chem. Eng. J. 308, 78–88. https://doi.org/10.1016/j.cej.2016.09.030

Li, Z., Gómez-Avilés, A., Sellaoui, L., Bedia, J., Bonilla-Petriciolet, A., Belver, C., 2019. Adsorption of ibuprofen on organo-sepiolite and on zeolite/sepiolite heterostructure: Synthesis, characterization and statistical physics modeling. Chem. Eng. J. 371, 868–875. https://doi.org/10.1016/j.cej.2019.04.138

Liu, H.M., Zhao, X.J., Zhu, Y.Q., Yan, H., 2020. DFT study on MgAl-layered double hydroxides with different interlayer anions: Structure, anion exchange, host-guest interaction and basic sites. Phys. Chem. Chem. Phys. 22, 2521–2529.

https://doi.org/10.1039/c9cp05529k

Loos, R., Marinov, D., Sanseverino, I., Napierska, D., Lettieri, T., 2018. Review of the 1st Watch List under the Water Framework Directive and recommendations for the 2nd Watch List, Joint Research Center. https://doi.org/10.2760/614367

Lu, H., Zhu, Z., Zhang, H., Qiu, Y., 2016. In Situ Oxidation and Efficient Simultaneous Adsorption of Arsenite and Arsenate by Mg-Fe-LDH with Persulfate Intercalation. Water. Air. Soil Pollut. 227. https://doi.org/10.1007/s11270-016-2828-9

Machado, K.C., Grassi, M.T., Vidal, C., Pescara, I.C., Jardim, W.F., Fernandes, A.N., Sodré, F.F., Almeida, F. V., Santana, J.S., Canela, M.C., Nunes, C.R.O., Bichinho, K.M., Severo, F.J.R., 2016. A preliminary nationwide survey of the presence of emerging contaminants in drinking and source waters in Brazil. Sci. Total Environ. 572, 138–146. https://doi.org/10.1016/j.scitotenv.2016.07.210

Mandaric, L., Celic, M., Marcé, R., Petrovic, M., 2016. Introduction on emerging contaminants in rivers and their environmental risk, Handbook of Environmental Chemistry. https://doi.org/10.1007/698_2015_5012

Marti, E., Variatza, E., Balcazar, J.L., 2014. The role of aquatic ecosystems as reservoirs of antibiotic resistance. Trends Microbiol. 22, 36–41. https://doi.org/10.1016/j.tim.2013.11.001

Martín, J., Camacho-Muñoz, D., Santos, J.L., Aparicio, I., Alonso, E., 2012. Occurrence of pharmaceutical compounds in wastewater and sludge from wastewater treatment plants: Removal and ecotoxicological impact of wastewater discharges and sludge disposal. J. Hazard. Mater. 239–240, 40–47. https://doi.org/10.1016/j.jhazmat.2012.04.068

Meshram, A., Singh, K.K., 2018. Recovery of valuable products from hazardous aluminum dross: A review. Resour. Conserv. Recycl. 130, 95–108. https://doi.org/10.1016/j.resconrec.2017.11.026

Metson, J., 2011. 2 - Production of alumina, Woodhead Publishing Series in Metals and Surface Engineering. Woodhead Publishing, pp. 23–48. https://doi.org/10.1533/9780857090256.1.23

Michael, I., Frontistis, Z., Fatta-Kassinos, D., 2013. Chapter 11 - Removal of

Pharmaceuticals from Environmentally Relevant Matrices by Advanced Oxidation Processes (AOPs), in: Petrovic, M., Barcelo, D., Pérez, S.B.T.-C.A.C. (Eds.), Analysis, Removal, Effects and Risk of Pharmaceuticals in the Water Cycle. Elsevier, pp. 345–407. https://doi.org/10.1016/B978-0-444-62657-8.00011-2

Miklos, D.B., Remy, C., Jekel, M., Linden, K.G., Drewes, J.E., Hübner, U., 2018. Evaluation of advanced oxidation processes for water and wastewater treatment – A critical review. Water Res. 139, 118–131. https://doi.org/10.1016/j.watres.2018.03.042

Mishra, G., Dash, B., Pandey, S., 2018. Layered double hydroxides: A brief review from fundamentals to application as evolving biomaterials. Appl. Clay Sci. 153, 172–186. https://doi.org/10.1016/j.clay.2017.12.021

Mohapatra, L., Parida, K., 2016. A review on the recent progress, challenges and perspective of layered double hydroxides as promising photocatalysts. J. Mater. Chem. A 4, 10744–10766. https://doi.org/10.1039/c6ta01668e

Mompelat, S., Le Bot, B., Thomas, O., 2009. Occurrence and fate of pharmaceutical products and by-products, from resource to drinking water. Environ. Int. 35, 803–814. https://doi.org/10.1016/j.envint.2008.10.008

Mourid, E.H., Lakraimi, M., Benaziz, L., Elkhattabi, E.H., Legrouri, A., 2019. Wastewater treatment test by removal of the sulfamethoxazole antibiotic by a calcined layered double hydroxide. Appl. Clay Sci. 168, 87–95. https://doi.org/10.1016/j.clay.2018.11.005

Nalawade, P., Aware, B., Kadam, V.J., Hirlekar, R.S., 2009. Layered double hydroxides: A review. J. Sci. Ind. Res. (India). 68, 267–272.

Noguera-Oviedo, K., Aga, D.S., 2016. Lessons learned from more than two decades of research on emerging contaminants in the environment. J. Hazard. Mater. 316, 242–251. https://doi.org/10.1016/j.jhazmat.2016.04.058

NORMAN [WWW Document], 2019. URL http://www.norman-network.net/

Panplado, K., Subsadsana, M., Srijaranai, S., Sansuk, S., 2019. Rapid removal and efficient recovery of tetracycline antibiotics in aqueous solution using layered double hydroxide components in an in situ-adsorption process. Crystals 9.

https://doi.org/10.3390/cryst9070342

Papoulis, D., Komarneni, S., Panagiotaras, D., Nikolopoulou, A., Li, H., Yin, S., Tsugio, S., Katsuki, H., 2013. Palygorskite-TiO_2 nanocomposites: Part 1. Synthesis and characterization. Appl. Clay Sci. 83–84, 191–197. https://doi.org/10.1016/j.clay.2013.09.003

Park, H., Vecitis, C.D., Hoffmann, M.R., 2009. Electrochemical Water Splitting Coupled with Organic Compound Oxidation: The Role of Active Chlorine Species. J. Phys. Chem. C 113, 7935–7945. https://doi.org/10.1021/jp810331w

Patel, M., Kumar, R., Kishor, K., Mlsna, T., Pittman, C.U., Mohan, D., 2019. Pharmaceuticals of emerging concern in aquatic systems: Chemistry, occurrence, effects, and removal methods. Chem. Rev. 119, 3510–3673. https://doi.org/10.1021/acs.chemrev.8b00299

Praneeth, N.V.S., Paria, S., 2017. Clay-semiconductor nanocomposites for photocatalytic applications, in: Clay Minerals: Properties, Occurrence and Uses. pp. 143–184.

Protection, E., Agency, 2002. European Waste Catalogue and Hazardous Waste List.

Qadir, M., Wichelns, D., Raschid-Sally, L., McCornick, P.G., Drechsel, P., Bahri, A., Minhas, P.S., 2010. The challenges of wastewater irrigation in developing countries. Agric. Water Manag. 97, 561–568. https://doi.org/10.1016/j.agwat.2008.11.004

Qin, F.-X., Jia, S.-Y., Liu, Y., Li, H.-Y., Wu, S.-H., 2015. Adsorptive removal of bisphenol A from aqueous solution using metal-organic frameworks. Desalin. Water Treat. 54, 93–102. https://doi.org/10.1080/19443994.2014.883331

Quiñones, D.H., Álvarez, P.M., Rey, A., Contreras, S., Beltrán, F.J., 2015. Application of solar photocatalytic ozonation for the degradation of emerging contaminants in water in a pilot plant. Chem. Eng. J. 260, 399–410. https://doi.org/10.1016/j.cej.2014.08.067

Riva, F., Castiglioni, S., Fattore, E., Manenti, A., Davoli, E., Zuccato, E., 2018. Monitoring emerging contaminants in the drinking water of Milan and assessment of the human risk. Int. J. Hyg. Environ. Health 221, 451–457.

https://doi.org/10.1016/j.ijheh.2018.01.008

Rives, V., 2002. Characterisation of layered double hydroxides and their decomposition products. Mater. Chem. Phys. 75, 19–25. https://doi.org/10.1016/S0254-0584(02)00024-X

Rives, V. (Ed.). 2001. Layered double hydroxides: Present and future. Nova Science Publishers.

Rives, V., del Arco, M., Martín, C., 2014. Intercalation of drugs in layered double hydroxides and their controlled release: A review. Appl. Clay Sci. 88–89, 239–269. https://doi.org/10.1016/j.clay.2013.12.002

Rives, V., Del Arco, M., Martín, C., 2013. Layered double hydroxides as drug carriers and for controlled release of non-steroidal antiinflammatory drugs (NSAIDs): A review. J. Control. Release 169, 28–39. https://doi.org/10.1016/j.jconrel.2013.03.034

Rives, V., Ulibarri, M.A., 1999. Layered double hydroxides (LDH) intercalated with metal coordination compounds and oxometalates. Coord. Chem. Rev. 181, 61–120. https://doi.org/10.1016/S0010-8545(98)00216-1

Rodriguez-Mozaz, S., Ricart, M., Köck-Schulmeyer, M., Guasch, H., Bonnineau, C., Proia, L., de Alda, M.L., Sabater, S., Barceló, D., 2015. Pharmaceuticals and pesticides in reclaimed water: Efficiency assessment of a microfiltration-reverse osmosis (MF-RO) pilot plant. J. Hazard. Mater. 282, 165–173. https://doi.org/10.1016/j.jhazmat.2014.09.015

Rosenfeld, P.E., Feng, L.G.H., 2011. Emerging Contaminants. Risks Hazard. Wastes 215–222. https://doi.org/10.1016/b978-1-4377-7842-7.00016-7

Rosset, M., Sfreddo, L.W., Hidalgo, G.E.N., Perez-Lopez, O.W., Féris, L.A., 2019. Adsorbents derived from hydrotalcites for the removal of diclofenac in wastewater. Appl. Clay Sci. 175, 150–158. https://doi.org/10.1016/j.clay.2019.04.014

Rosset, M., Sfreddo, L.W., Perez-Lopez, O.W., Féris, L.A., 2020. Effect of concentration in the equilibrium and kinetics of adsorption of acetylsalicylic acid on ZnAl layered double hydroxide. J. Environ. Chem. Eng. 8, 103991. https://doi.org/10.1016/j.jece.2020.103991

Sato, T. et al., 1988. Synthesis of hydrotalcitye-like compounds and their physico-chemical properties. React. Solids. 219–228. https://doi.org/10.1016/0168-7336(88)80089-5

Sepehr, M.N., Al-Musawi, T.J., Ghahramani, E., Kazemian, H., Zarrabi, M., 2017. Adsorption performance of magnesium/aluminum layered double hydroxide nanoparticles for metronidazole from aqueous solution. Arab. J. Chem. 10, 611–623. https://doi.org/10.1016/j.arabjc.2016.07.003

Sevigné-Itoiz, E., Gasol, C.M., Rieradevall, J., Gabarrell, X., 2014. Environmental consequences of recycling aluminum old scrap in a global market. Resour. Conserv. Recycl. 89, 94–103. https://doi.org/10.1016/j.resconrec.2014.05.002

Simonin, J.P., 2016. On the comparison of pseudo-first order and pseudo-second order rate laws in the modeling of adsorption kinetics. Chem. Eng. J. 300, 254–263. https://doi.org/10.1016/j.cej.2016.04.079

Stuart, M., Lapworth, D., Crane, E., Hart, A., 2012. Review of risk from potential emerging contaminants in UK groundwater. Sci. Total Environ. 416, 1–21. https://doi.org/10.1016/j.scitotenv.2011.11.072

Suarez, S., Lema, J.M., Omil, F., 2009. Pre-treatment of hospital wastewater by coagulation-flocculation and flotation. Bioresour. Technol. 100, 2138–2146. https://doi.org/10.1016/j.biortech.2008.11.015

Sui, M., Zhou, Y., Sheng, L., Duan, B., 2012. Adsorption of norfloxacin in aqueous solution by Mg-Al layered double hydroxides with variable metal composition and interlayer anions. Chem. Eng. J. 210, 451–460. https://doi.org/10.1016/j.cej.2012.09.026

Tadkaew, N., Hai, F.I., McDonald, J.A., Khan, S.J., Nghiem, L.D., 2011. Removal of trace organics by MBR treatment: The role of molecular properties. Water Res. 45, 2439–2451. https://doi.org/10.1016/j.watres.2011.01.023

Teh, C.Y., Budiman, P.M., Shak, K.P.Y., Wu, T.Y., 2016. Recent Advancement of Coagulation-Flocculation and Its Application in Wastewater Treatment. Ind. Eng. Chem. Res. 55, 4363–4389. https://doi.org/10.1021/acs.iecr.5b04703

The European Parlament and the Council of the European Union, 2013. Directives of 12

August 2013 amending Directives 2000/60/EC and 2008/105/EC as regards priority substances in the field of water policy. Off. J. Eur. Union 2013, 1–17. http://eur-lex.europa.eu/legal-content/EN/TXT/?uri=celex:32013L0039

Tsakiridis, P.E., 2012. Aluminium salt slag characterization and utilization - A review. J. Hazard. Mater. 217–218, 1–10. https://doi.org/10.1016/j.jhazmat.2012.03.052

Ungureanu, C.A., Das, S., Jawahir, I.S., 2004. Therapeutics of the future. Pharm. J. 273, 136.

Van Boeckel, T.P., Gandra, S., Ashok, A., Caudron, Q., Grenfell, B.T., Levin, S.A., Laxminarayan, R., 2014. Global antibiotic consumption 2000 to 2010: An analysis of national pharmaceutical sales data. Lancet Infect. Dis. 14, 742–750. https://doi.org/10.1016/S1473-3099(14)70780-7

Verlicchi, P., Al Aukidy, M., Zambello, E., 2012. Occurrence of pharmaceutical compounds in urban wastewater: Removal, mass load and environmental risk after a secondary treatment-A review. Sci. Total Environ. 429, 123–155. https://doi.org/10.1016/j.scitotenv.2012.04.028

Vogelpohl, A., Kim, S.M., 2004. Advanced oxidation processes (AOPS) in wastewater treatment. J. Ind. Eng. Chem.

Wang, J., Bai, Z., 2017. Fe-based catalysts for heterogeneous catalytic ozonation of emerging contaminants in water and wastewater. Chem. Eng. J. 312, 79–98. https://doi.org/10.1016/j.cej.2016.11.118

Wang, J.L., Xu, L.J., 2012. Advanced oxidation processes for wastewater treatment: Formation of hydroxyl radical and application. Crit. Rev. Environ. Sci. Technol. 42, 251–325. https://doi.org/10.1080/10643389.2010.507698

Wang, X., Zhou, W., Wang, C., Chen, Z., 2018. Cotton fiber-supported layered double hydroxides for the highly efficient adsorption of anionic organic pollutants in water. New J. Chem. 42, 9463–9471. https://doi.org/10.1039/c8nj00678d

Wilkinson, J., Hooda, P.S., Barker, J., Barton, S., Swinden, J., 2017. Occurrence, fate and transformation of emerging contaminants in water: An overarching review of the field. Environ. Pollut. 231, 954–970. https://doi.org/10.1016/j.envpol.2017.08.032

Williams, M.E., Hestekin, J.A., Smothers, C.N., Bhattacharyya, D., 1999. Separation of organic pollutants by reverse osmosis and nanofiltration membranes: Mathematical models and experimental verification. Ind. Eng. Chem. Res. 38, 3683–3695. https://doi.org/10.1021/ie9901401

Wu, H., Gao, H., Yang, Q., Zhang, H., Wang, D., Zhang, W., Yang, X., 2018. Removal of Typical Organic Contaminants with a Recyclable Calcined Chitosan-Supported Layered Double Hydroxide Adsorbent: Kinetics and Equilibrium Isotherms. J. Chem. Eng. Data 63, 159–168. https://doi.org/10.1021/acs.jced.7b00752

Xiong, T., Yuan, X., Wang, H., Wu, Z., Jiang, L., Leng, L., Xi, K., Cao, X., Zeng, G., 2019a. Highly efficient removal of diclofenac sodium from medical wastewater by Mg/Al layered double hydroxide-poly(m-phenylenediamine) composite. Chem. Eng. J. 366, 83–91. https://doi.org/10.1016/j.cej.2019.02.069

Xiong, T., Yuan, X., Wang, H., Wu, Z., Jiang, L., Leng, L., Xi, K., Cao, X., Zeng, G., 2019b. Highly efficient removal of diclofenac sodium from medical wastewater by Mg/Al layered double hydroxide-poly(m-phenylenediamine) composite. Chem. Eng. J. 366, 83–91. https://doi.org/10.1016/j.cej.2019.02.069

Xu, Z., Fan, J., Zheng, S., Ma, F., Yin, D., 2009. On the Adsorption of Tetracycline by Calcined Magnesium-Aluminum Hydrotalcites. J. Environ. Qual. 38, 1302–1310. https://doi.org/10.2134/jeq2008.0246

Xu, Z.P., Stevenson, G.S., Lu, C.Q., Lu, G.Q., Bartlett, P.F., Gray, P.P., 2006. Stable suspension of layered double hydroxide nanoparticles in aqueous solution. J. Am. Chem. Soc. 128, 36–37. https://doi.org/10.1021/ja056652a

Yang, C., Wang, L., Yu, Y., Wu, P., Wang, F., Liu, S., Luo, X., 2020. Highly efficient removal of amoxicillin from water by Mg-Al layered double hydroxide/cellulose nanocomposite beads synthesized through in-situ coprecipitation method. Int. J. Biol. Macromol. 149, 93–100. https://doi.org/10.1016/j.ijbiomac.2020.01.096

Yang, Q., Wang, S., Chen, F., Luo, K., Sun, J., Gong, C., Yao, F., Wang, X., Wu, J., Li, X., Wang, D., Zeng, G., 2017. Enhanced visible-light-driven photocatalytic removal of refractory pollutants by Zn/Fe mixed metal oxide derived from layered double hydroxide. Catal. Commun. 99, 15–19. https://doi.org/10.1016/j.catcom.2017.05.010

Yang, Y., Owino, A.A., Gao, Y., Yan, X., Xu, C., Wang, J., 2016. Occurrence, composition and risk assessment of antibiotics in soils from Kenya, Africa. Ecotoxicology 25, 1194–1201. https://doi.org/10.1007/s10646-016-1673-3

Yoldi, M., Fuentes-Ordoñez, E.G., Korili, S.A., Gil, A., 2019. Efficient recovery of aluminum from saline slag wastes. Miner. Eng. 140, 105884. https://doi.org/10.1016/j.mineng.2019.105884

Younes, H.A., Khaled, R., Mahmoud, H.M., Nassar, H.F., Abdelrahman, M.M., Abo El-Ela, F.I., Taha, M., 2019. Computational and experimental studies on the efficient removal of diclofenac from water using ZnFe-layered double hydroxide as an environmentally benign absorbent. J. Taiwan Inst. Chem. Eng. 102, 297–311. https://doi.org/10.1016/j.jtice.2019.06.018

Zhang, Q., Yan, Z., Ouyang, J., Zhang, Y., Yang, H., Chen, D., 2018. Chemically modified kaolinite nanolayers for the removal of organic pollutants. Appl. Clay Sci. 157, 283–290. https://doi.org/10.1016/j.clay.2018.03.009

Zhao, Y., Zhang, S., Li, B., Yan, H., He, S., Tian, L., Shi, W., Ma, J., Wei, M., Evans, D.G., Duan, X., 2011. A Family of Visible-Light Responsive Photocatalysts Obtained by Dispersing CrO_6 Octahedra into a Hydrotalcite Matrix. Chem. – A Eur. J. 17, 13175–13181. https://doi.org/10.1002/chem.201101874

Zhou, W., Zhang, W., Chen, Z., 2017. Universal biomimetic preparation and immobilization of layered double hydroxide films and adsorption behavior. Appl. Surf. Sci. 392, 153–161. https://doi.org/10.1016/j.apsusc.2016.08.173

Zhu, J., Zhu, Z., Zhang, H., Lu, H., Qiu, Y., Zhu, L., Küppers, S., 2016. Enhanced photocatalytic activity of Ce-doped Zn-Al multi-metal oxide composites derived from layered double hydroxide precursors. J. Colloid Interface Sci. 481, 144–157. https://doi.org/10.1016/j.jcis.2016.07.051

Zhu, J., Zhu, Z., Zhang, H., Lu, H., Zhang, W., Qiu, Y., Zhu, L., Küppers, S., 2018. Calcined layered double hydroxides/reduced graphene oxide composites with improved photocatalytic degradation of paracetamol and efficient oxidation-adsorption of As(III). Appl. Catal. B Environ. 225, 550–562. https://doi.org/10.1016/j.apcatb.2017.12.003

Chapter II

Experimental methodology: materials and experimental techniques description

II.1. GASES AND REACTIVES USED

In the following tables (II.1, II.2) the chemical reagents used for the adsorbents/catalysts synthesis as well as the liquid/gas reagents employed for their characterization are detailed.

Table II.1. Chemical reagents used for the synthesis and comparison of the performance of the adsorbents/catalysts.

Reagent	Manufacturer (degree of purity)	CAS	Application
Titanium(IV) isopropoxide $Ti\{OCH(CH_3)_2\}_4$	Sigma-Aldrich (>97 %)	546-68-9	Catalyst synthesis
Isopropyl alcohol $CH_3CHOHCH_3$	Sigma-Aldrich (99 %)	67-63-0	
Hydrochloric acid HCl	Acros (37 %)	7647-01-0	
Iron(III) nitrate nonahydrate $Fe(NO_3)_3 \cdot 9H_2O$	Riedel-de Haën (96 %)	10421-48-4	Catalyst dopants
Silver nitrate $AgNO_3$	Panreac (99.8 %)	7761-88-8	
Titanium(IV) oxide, anatase TiO_2	Sigma-Aldrich (99 %)	1317-70-0	Catalytic activity comparison
Iron(III) oxide Fe_2O_3	Aldrich (99.99 %)	1317-61-9	Reference standards of TPR patterns
Silver(I) oxide Ag_2O	Sigma-Aldrich (99 %)	20667-12-3	
Sodium hydroxide NaOH	Panreac (98 %)	1310-73-2	Aluminum extraction

Reagent	Manufacturer (degree of purity)	CAS	Application
Zinc nitrate hexahydrate $Zn(NO_3)_2 \cdot 6H_2O$	Sigma-Aldrich (98 %)	10196-18-6	LDH synthesis
Sodium carbonate Na_2CO_3	Sigma-Aldrich (99.99 %)	497-19-8	
Titanium(III) chloride $TiCl_3$	Sigma-Aldrich (12 %)	7705-07-9	
Aluminum nitrate nonahydrate $Al(NO_3)_3 \cdot 9\ H_2O$	Merck (95 %)	7784-27-2	
Cobalt(II) nitrate hexahydrate $Co(NO_3)_2 \cdot 6H_2O$	Panreac (98 %)	10026-22-9	
Magnesium nitrate hexahydrate $Mg(NO_3)_2 \cdot 6H_2O$	Sigma-Aldrich (99.99 %)	13446-18-9	
Nickel(II) nitrate hexahydrate $Ni(NO_3)_2 \cdot 6H_2O$	Panreac (98 %)	13478-00-7	
Nitric acid HNO_3	Sigma-Aldrich (70 %)	7697-37-2	
Carbon nanotube, multi-walled	Sigma-Aldrich (90 %)	308068-56-6	Adsorbent
Activated carbon Hydrodarco 3000	Cabot Corporation	7440-44-0	
Metal Organic Framework Basolite A100 $C_8H_5AlO_5$	Sigma-Aldrich	654061-20-8	
Caffeine $C_8H_{10}N_4O_2$	Sigma-Aldrich	58-08-2	Adsorbate
Salicylic acid $2\text{-}(HO)C_6H_4COOH$	Sigma-Aldrich (>99 %)	69-72-7	
Diclofenac sodium salt $C_{14}H_{10}Cl_2NNaO_2$	Sigma-Aldrich	15307-79-6	

Table II.2. Reagents used for characterization purposes.

Reagent	Manufacturer (degree of purity)	CAS	Application
Helium (He)	Praxair (99.999 %)	7440-59-7	Pretreatment gas in catalyst acidity characterization
Nitrogen gas (N_2)	Praxair (99.999 %)	7727-37-9	Analysis gas in surface characterization/ pretreatment gas in TPR
Ammonia (NH_3)	Air Liquide (99.995 %)	7664-41-7	Analysis gas in catalyst acidity characterization
Argon (Ar)	Praxair (99.998 %)	7440-37-1	Carrier gas in ammonia TPD
Argon Hydrogen mix	Praxair (5 %)		Reducer gas in TPR
Liquid Nitrogen (N_2)	Praxair (99.999 %)	7727-37-9	TPR cold trap/temperature regulator in N_2 adsorption
Isopropyl alcohol $CH_3CHOHCH_3$	Sigma-Aldrich (99 %)	67-63-0	TPR cold trap
1-Butanol	Roth (99.95 %)	71-36-3	LDH acid and basic sites characterization

II.2. ADSORBENTS/CATALYSTS PREPARATION

Al from aluminum saline slags was extracted to synthesize LDH (chapters III, IV and VI) using the following procedure: 5 g of saline slag were added to 100 cm^3 of an aqueous reagent solution (NaOH 2 mol/dm^3) in a reflux system, stirred at 500 rpm and heated to 373 K for 60 min.

Four different hydrotalcites (LDH), with a molar ratio Me^{2+}:Al^{3+} of 3:1, were synthesized in chapter III using cobalt, magnesium, nickel and zinc as Me^{2+} utilizing the co-precipitation method. As an example, $Zn(NO_3)_2 \cdot 6H_2O$ (0.15 mol/dm^3) and Al (0.05 mol/dm^3) were added dropwise to Na_2CO_3 (0.015 mol/dm^3) to a final volume of 400

cm^3. NaOH was used during the process to adjust the pH to 10. The mixture was stirred at 500 rpm and 333 K for 60 min and aged for 24 h. The slurries obtained were centrifuged at 8000 rpm for 5 min and washed. This process was repeated several times until the washing water achieved a pH of 7. The samples were then dried at 353 K for 16 h, manually grounded with a mortar and calcined at 673 K for 4 h. In chapter IV the LDH were synthesized on a Zn^{2+}:(Al, Ti)$^{3+}$ 3:1 molar ratio, with aluminum and titanium proportions being modified in the series. This series was calcined at 673 K for 4 h, impregnated with 5 wt.% iron (chapter VI) and calcined again. Also in chapter VI, another LDH series containing $Zn_6(AlFe)_2$ at various Al/Fe proportions and with a Zn^{2+}/Me^{3+} molar ratio of 3:1 was prepared, and then impregnated with 5 wt.% titanium(IV) isopropoxide.

TiO_2 (chapter V) was either doped, within the crystalline lattice of the particle, or impregnated with the metals. Doped TiO_2 was synthetized using a procedure reported previously (Gil et al., 2017): A first solution (A) was prepared incorporating 1 cm^3 of HCl (1.5 mol/dm^3) and the appropriate amount of the doping agent, $AgNO_3$ or $Fe(NO_3)_3 \cdot 9H_2O$, for a final mass percentage of the dopant metal in the solid of 0.5 and 5 wt. %, into 20 cm^3 of isopropyl alcohol. Other solution (B) was made incorporating 5 cm^3 of titanium(IV) isopropoxide into 20 cm^3 of isopropyl alcohol. Solution A was dropwise added to B while constantly stirring for 30 min. The final suspension was heated at 333 K for 16 h in order to remove the solvent, obtaining a dry white powder which was calcined for 4 h at 673 K to remove both the water adsorbed during the process and the precursors utilized to integrate the doping elements. The same method was used for preparing titanium dioxide without the addition of modifiers, used as a blank reference. Impregnated titanium dioxide was synthetized using the bare TiO_2 catalyst in solution B instead of titanium(IV) isopropoxide.

II.3. CHARACTERIZATION TECHNIQUES: FUNDAMENTALS AND APPLICATIONS

II.3.1. ELEMENTAL ANALYSIS USING ICP-OES

Inductively coupled plasma optical emission spectrometry (ICP-OES) is one of the most useful techniques for the detection of chemical elements in a variety of matrices.

This emission spectroscopy technique is based on the measurement of the electromagnetic radiation emitted by the atoms and ions. Inductively coupled plasma excites the elements and its electrons go to a higher energy level. When relaxed, these electrons go back to their original ground state and emit energy (photons) at a wavelength characteristic of their respective elements (Nölte, 2020).

ICP-OES analyses were performed by the *Unidad Científico Técnica de Apoyo a la Investigación (UCTAI)* of the Universidad Pública de Navarra on a Vista-MPX (VARIAN) with a radial configuration (the plasma is viewed from the side). The technique was used to determine the content (percentage by weight) of aluminum, titanium and zinc withdrawn from the saline slags by basic extraction. It was also used to determine the content of iron and silver leached into the solution after the photocatalytic experiments performed in chapter V.

II.3.2. POWDER X-RAY DIFFRACTION (PXRD)

Techniques based on X-ray diffraction are most used for the characterization of minerals (Moore and Reynolds Jr, 1989). They are identified because of the deviation that X-rays suffer when they interact with the irradiated material. This technique gives us information about the crystalline phases present in a sample as well as about the bulk properties of the sample. The X-ray diffraction pattern can also measure the distance between single planes of atoms in a crystal and also provides a measurement of the layer's height (Cullity, 1956). Due to the difference between cell parameters, symmetry and space groups that crystalline materials have, characteristic diffraction patterns that work as a fingerprint to the material are produced. To understand what conditions are required for diffraction, Bragg's law (Eq. II. 1) provides a simplistic model that also is used to calculate the d-spacing (Figure II.1). For parallel planes of atoms (with a space d_{hkl} in between) constructive interference can only occur when this law is satisfied:

$$n\lambda = 2d_{hkl} \sin\theta \qquad \text{Eq. II.1}$$

where d is the interlayer distance between two consecutive layers, n is the diffraction order, θ is Bragg's angle (formed both by the incident X-ray beam and the diffracted by the planes) and λ is the wavelength of the X-rays (1.5418 Å for the copper anode).

Additionally, the plane normal (hkl) must be parallel to the diffraction vector s (bisects the angle between the incident and the diffracted beam). The crystallite size can also be calculated from the PXRD data. It is measured with the Scherrer formulae (Patterson, 1939):

$$\tau = \frac{K\lambda}{\beta_\tau cos\theta} \qquad \text{Eq. II.2}$$

where K is the shape factor = 0.9; β_τ is the width of the peak at half of the maximum intensity (FWHM) after subtraction of instrumental broadening and θ is the diffraction angle.

The measurements were carried out using a Siemens D-5000 X-ray diffractometer, with Ni-filtered Cu Kα radiation (λ = 0.1548 nm). The working conditions used were 30 mA, 40 kV and a scanning rate of 0.2-0.5° (2θ)/min. The 2θ range used TiO_2 powder (anatase) was from 10 to 100° and scherrer equation was used to compare the crystallite size of the samples (chapter V). With LDH the 2θ range used was from 5 to 80° and Bragg's equation was applied to measure both the interlayer distance and the average distance between metallic cations of the samples (chapters III, IV and VI). The identification of the crystalline phases was carried out with the *International Centre for Diffraction Data* (ICDD) database, and the program DIFRAC.EVA to interpret and process the data.

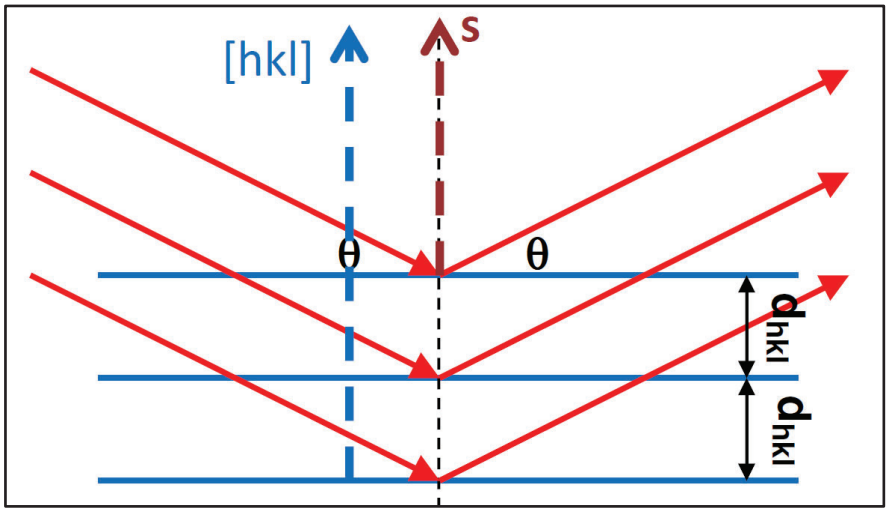

Figure II.1. Different paths followed by the X-rays.

II.3.3. THERMAL ANALYSIS (TG/DTG)

Thermogravimetric analysis measures the mass change of a sample over time as the temperature changes. This technique can be performed under different atmospheres such as air (our case), nitrogen or hydrogen. It is used to detect changes in a solid phase due to oxidation, decomposition or dehydration processes among others (Haines, 1995). In our LDH samples the most important mass changes were due first to loss of water and then to a decarbonation together with a dehydroxilation (Frost et al., 2005). Phase changes occur at temperatures characteristic to the substance and, thus, they provide us with qualitative and quantitative information of the samples. TG and DTG analysis were used to compare the LDH synthetized with commercial aluminum and aluminum extracted from saline slags (chapter IV) to compare the mass losses to those expected theoretically (chapter III) and, in general, to analyze their difference in relation with their resistance to temperature changes when variations in the composition were introduced. TG and DTG analysis were performed by the by the *Unidad Científico Técnica de Apoyo a la Investigación (UCTAI)* of the Universidad Pública de Navarra on a Hi-Res TGA2950 apparatus (TA-Instruments) using a 10 K/min heating rate from room temperature up to 1173 K under air atmosphere (60 cm^3/min).

II.3.4. SCANNING ELECTRON MICROSCOPY (SEM)

This technique is useful to study the surface composition and topography of a sample. A focused beam of electrons scans the surface of the sample and various signals are produced as the atoms of the sample interact with the electrons of the beam and produce secondary or retrodispersed electrons. Changes in the topology and composition of the sample are translated into different electron intensities. These emissions are gathered by detectors that generate electrical currents whose mission is to modulate the intensity of the electron beam that hits the screen of a cathode ray tube. An image is generated by a simultaneous combination of the sample incident beam and the screen incident beam (Stokes, 2008). Nowadays SEM can achieve a resolution passed 1 nanometer.

An EDX (Energy-dispersive X-ray spectroscopy) detector can be attached to the scanning electron microscope which is used to convert X-ray energy into electric potential difference. This signal is sent to a pulse processor for measuring and then to an

analyzer. This technique is based on the principle that each element has a unique atomic structure that creates an unique set of peaks on its electromagnetic emission spectrum (Goldstein J.I. et al, 2003). These techniques together are useful to examine the homogeneity and the morphology of the samples. In the LDH samples an JEOL, JSM-6400 instrument operating at 20 kV was mainly used to see if the laminar structure, characteristic of LDH, was present in the samples.

II.3.5. TEXTURAL ANALISIS: N_2 ADSORPTION-DESORPTION

Gas physisorption is a process that occurs in the surface of a solid (adsorbent) when gas molecules (adsorbate) are adsorbed to the solid by Van der Waals forces. It is an exothermic process whose heat of adsorption is usually between 20 and 40 kJ/mol. The N_2 adsorption-desorption at 77 K and atmospheric pressure is a standard method for the study of porous materials as it gives us information about the specific surface, shape, size, volume and pore size distribution. N_2 is usually chosen as adsorbate due to its non-specific interaction with the adsorbent, small size and affordable price (Gil Bravo, 2019).

In this work, the textural properties of the samples (0.2-0.4 g) were analyzed by nitrogen adsorption-desorption at 77 K using a Micromeritics ASAP 2020 Plus or Micromeritics ASAP 2010 adsorption analyzer. All samples were degassed beforehand at 423 K for 24 h under a pressure lower than 0.1 Pa. The specific surface area of the materials was estimated by the Brunauer-Emmer-Teller (BET) method applied to a relative pressure range of 0.05–0.20. The external surface area (S_{ext}) and the micropore volumes ($V_{\mu p}$) were also estimated using the t-plot method.

II.3.5.1. Adsorption isotherms

When working at a constant temperature, the relation between the pressure and the quantity of gas adsorbed shapes the adsorption isotherm. This isotherm gives us information about the porosity of the material, porous size, distribution and configuration. The pores are classified according to their size (Sing, 1985):

- Macropores: > 50 nm
- Mesopores: between 2 nm – 50 nm
- Micropores: < 2 nm

The IUPAC (International Union of Pure and Applied Chemistry) recommendations for physisorption isotherm types were updated by *Thommes et al.* (2015) and the updated classification is shown in Figure II.2.

- Type I isotherms are given by microporous solids like some activated carbons were type *a* materials have narrower micropores (< 1nm) and type *b* have a broader range of pore distribution.
- Type II isotherms are given by either nonporous or macroporous adsorbents. Point B can correspond to the completion of the monolayer when the knee is sharp. The thickness of the multilayer increases without limit when $p/p°=1$. This type of isotherms is typical of LDH (chapters III, IV and VI) and was also found in carbon nanotubes (chapter VII).
- Type III, also attributed to nonporous or macroporous adsorbents, where there is no detectable monolayer formation and the amount of N_2 adsorbed has a limit when $p/p°=1$.

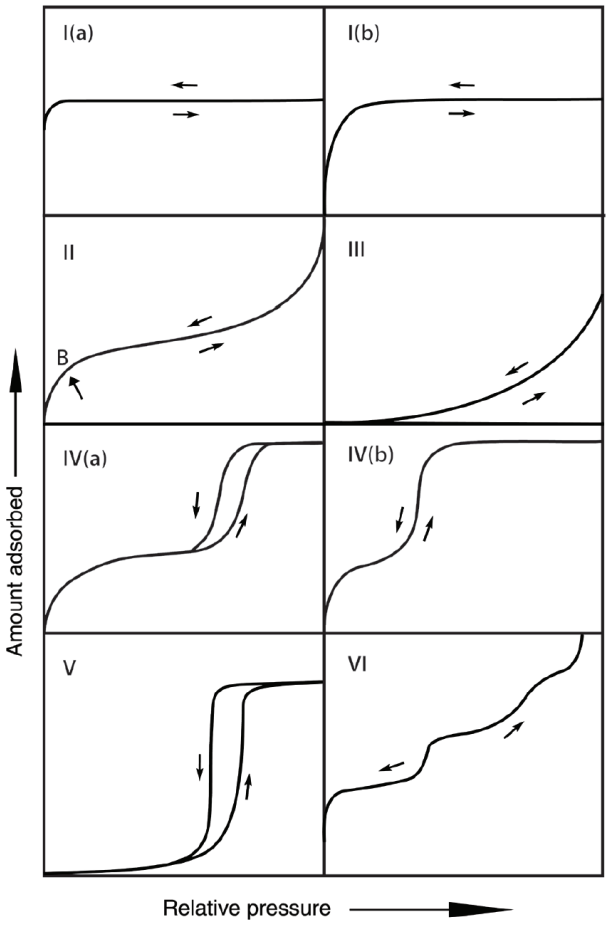

Figure II.2. Classification of physisorption isotherms.

- Type IV isotherms are given by mesoporous adsorbents where the initial monolayer-multilayer adsorption is followed by pore condensation and can have a hysteresis loop. This type of isotherm has a plateau in the end and was attributed in this work to TiO_2 particles (chapter V).
- Type V is usually attributed to weak adsorbent-adsorbate interactions. It starts similar to type III and is followed by pore filling.
- Type VI represents nonporous adsorbents with a very uniform surface, not usually found in N_2 as adsorbent but can appear with Ar or Kr.

II.3.5.2. Specific surface

Specific surface is one of the most useful characterization properties although is not easy to obtain a number that represents the real value. It can be estimated from the monolayer capacity and several models can be used for its estimation. The model used in this work is the Langmuir, Emmett and Teller or BET model (Brunauer et al., 1938) that has to be applied in relative pressures not smaller than 0.05 (so the energy centers are occupied) or greater than 0.35 (as from there the linearity is lost due to the multilayer adsorption). This range has to be verified in each system.

II.3.5.3. Micropores volume

The micropores volume (Vμp) was calculated with the t-plot method. The quantity of adsorbed gas is represented against the standard width of the multilayer of a nonporous material used as a reference. Figure II.3 shows a t-plot isotherm.

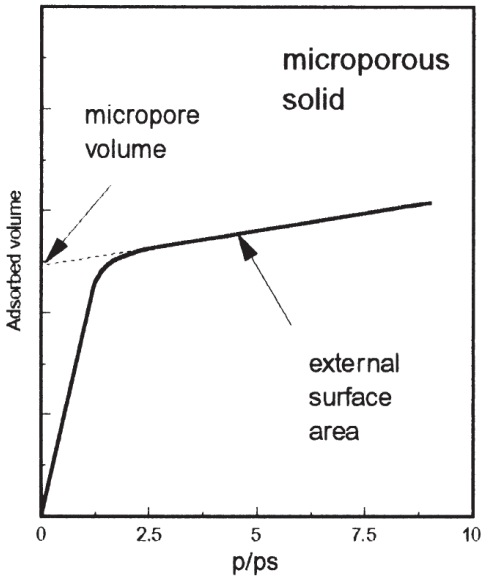

Figure II.3. Representation of a t-plot isotherm.

The volume of micropores is obtained from the intersection of the linear region with the ordinate axis and the external surface area (not due to micropores) is the slope of the straight line.

II.3.5.4. Pores size distribution

BJH method (Barrett, Joyner, and Halenda) is a procedure for calculating pore size distributions from experimental isotherms using the Kelvin model of pore filling. It calculates mesopore distribution from nitrogen adsorption. It was used to determine the pore diameter in chapter V (TiO_2 with a type IV isotherm). This method is applied to the desorption isotherm and assumes the presence of cylindrical pores opened at both ends (Gil Bravo, 2019).

II.3.6. TEMPERATURE PROGRAMMED REDUCTION (TPR)

This technique examines the surface chemistry of metal oxide catalysts while they are subjected to changing thermal conditions. TPR experiments were performed in a Micromeritics TPR/TPD 2900 instrument, and about 20 mg of the samples were used in each measurement. The samples were placed in a fixed bed reactor where they were pretreated with N_2 (Air Liquide, 99.999%) at 473 K for 2 h, under a 30 cm^3/min flow and a heating rate of 10 K/min. TPR tests were carried out using a flow of 5% H_2 in Ar (30 cm^3/min), and the sample was heated up to 1073 K from room temperature at a rate of 10 K/min. A cold trap (isopropyl alcohol/liquid nitrogen) was used to retain water and other compounds that might have been formed during metal reduction and precursor decomposition. A thermal conductivity detector (TCD) can determine where the peak reductions are located with the analysis of the chemical difference in atmospheric concentration, in other words, the H_2 uptake during the process. The reduction peaks are plotted against temperature giving us information about the catalyst chemical state and dispersion state (Malet and Caballero, 1988). These experiments were of great aid in order to determine the 1-butanol conversion results of some samples (chapter IV).

II.3.7. CATALYST ACIDITY EVALUATION BY NH_3 CHEMISORPTION

This analytical technique is useful to characterize the acid centers of a catalyst and, thus, predict its selectivity and activity. NH_3, as a Lewis base, is used as a probe

molecule to test the catalyst's surface acidic properties. In this work it was utilized to compare the different performance of the catalysts in the TiO_2 series (chapter V). Ammonia is molecularly adsorbed into the TiO_2 surface revealing its Lewis acidity. The heat of adsorption for NH_3 is larger than for CO_2 (frequently used to test the basic surface properties of a catalyst (Minot et al., 1995)). In the case of TiO_2, if free sites are available on its surface, ammonia is firmly adsorbed (a base on a Lewis acid site). If TiO_2 sites are surrounded with hydroxyl groups, this adsorption can be less strong (the basic character of NH_3 is used to form an N-OH bond in this case) (Markovits et al., 1996).

In this work the adsorption of NH_3 was quantified using a dynamic pulse method on a Micromeritics TPR/TPD 2900 instrument. All samples were pre-treated at a heating rate of 10 K/min, under a He (Praxair, 99.999%) flow of 30 cm^3/min, up to 673 K for 3 h and then cooled to 343 K in the same stream. After the pretreatment, known quantities of ammonia (Air Liquide, >99.995%) were injected as pulses (0.5 cm^3) at 343 K to a sample (20 mg) placed in a fixed bed until all the active centers have reacted. This is determined by a detector that measures the amount of ammonia that elutes the system after each injection. When all the active centers have been saturated the area of consecutive eluted pulses will be constant.

II.3.8. XPS

X-ray photoelectron spectroscopy (XPS) is a very useful technique to study the surface (up to 10 nm) of our adsorbents/catalysts. The elemental composition (%), chemical state and, with these, the empirical formula of our samples were determined. A beam of X-rays is used to irradiate the sample which gives electrons from the present elements enough energy to escape from the material. They are then captured by an electron energy analyzer. These electrons will have a binding energy (eV) which is related to its element and configuration within the atoms (Watts, J.F. and Wolstenholme, 2003). An XPS spectrum is a plot of the number of electrons detected (ordinate axis) versus their binding energy (abscissa). The binding energy of Carbon 1s, located in our analysis at 248.8 eV is usually used as a reference for the rest.

The interpretation of the results can be complicated due to the presence of Auger electrons. These are caused when an inner-shell electron is ejected from the atom due to

the high energy of the incident photon. An electron from a higher energy can replace it and, thus, energy is released. Usually this energy is in the form of an emitted photon, however sometimes a second electron is ejected, an Auger electron. For a better interpretation of the result, when required spectra were decomposed with the CasaXPS program (Casa Software Ltd., UK) with a Gaussian/Lorentzian product function after subtraction of a nonlinear baseline. Handbook of XPS (Moulder and Chastain, 1992) was also used for that purpose. Surface concentrations (% atomic) were calculated using peak areas normalized on the basis of acquisition parameters and sensitivity factors provided by the manufacturer. XPS analyses were carried out on a SSX 100/206 spectrometer for Surface Science Instruments (USA) equipped with a monochromatized and microfocused Al X-ray source (powered with 20 mA and 10 kV). The pressure within the analysis chamber was about 10^{-6} Pa as high vacuum conditions are required in the analysis. The zone analyzed was about 1.4 mm^2, and the pass energy was set at 150 eV for the general spectra and at 30 eV for the elementary spectra. To stabilize the charge an electron gun set at 8 eV and a nickel grid placed 3 mm above the surface of the samples were used.

II.3.9. POINT OF ZERO CHARGE

The point of zero charge (pH_{pzc}) is defined as the pH at which the net charge of a total adsorbent's surface is equal to cero. As the pH_{pzc} corresponds to a charge equilibrium situation in the material, pH values greater than the pH_{pzc} generate a negative charged surface whereas pH values lower than the pH_{pzc} generate a positive one. This way with the pH_{pzc} the most appropriate pH value can be determined in order to achieve the efficient elimination of an emerging contaminant of anionic or cationic nature (Rivera-Utrilla et al., 2003).

The pH_{pzc} was determined by the salt addition method (Bakatula et al., 2018). A 0.01 mol/dm^3 NaCl solution was used as background electrolyte. An equal quantity of background solution (50 cm^3) was apportioned into various flasks kept in series with increasing pH values from 2 to 12. 0.15 g of adsorbent was added to all these flasks and the change in pH of each solution was recorded after shaking the samples for 48 h. This change in pH was plotted against the initial pH values on the graph, and the PZC was identified as the pH when $\Delta pH = 0$.

II.4. ADSORPTION EXPERIMENTS

II.4.1. BATCH ADSORPTION

Kinetic experiments were performed at room temperature by placing the drug solution (adsorbate) in a beaker, adding the LDH (adsorbent) and shaking it with a stirring plate. Throughout the duration of the experiments the solution was sampled at various time intervals until equilibrium was achieved, up to 8 h. The quantity of organic compound adsorbed by the hydrotalcites was calculated from the difference between the initial and remaining concentrations. The sampled dispersions were filtered (0.45 μmol, Durapore) and the pollutant concentration remaining in the solution was determined by a Jasco V-730 UV–Vis spectrometer at the maximum absorption wavelength: 276, 297 and 273.5 nm for diclofenac, salicylic acid and caffeine, respectively. In the kinetic tests, to study the effect of the drug concentration, 50 mg of adsorbent were added to 250 cm^3 of solutions with drugs in varying concentrations of 25, 50 and 75 μmol/dm^3. The effect of the adsorbent dose was examined by changing the amount of the adsorbent (25, 50 and 100 mg) in solutions with an initial drug concentration of 75 μmol/ dm^3.

The adsorption capacity of the hydrotalcites in equilibrium was tested by modifying the initial drug concentration. 5 mg of adsorbent were added to glass tubes containing 10 cm^3 of the contaminant solution at initial concentrations between 0 and 1000 μmol/dm^3. The tubes were placed in a rotating shaker (orbit, J.P. Selecta), shaken for 8 h and the concentration of the pollutant remaining in the solution was separated from the solid by filtration and the remaining concentration was determined by UV–visible spectrophotometry as in the case of the adsorption kinetic experiments.

The adsorbate concentrations are given in μmol/dm^3 for an easier comparison of the different drugs.

II.4.2. FIXED-BED ADSORPTION EXPERIMENTS

The breakthrough curves of diclofenac and salicylic acid were performed on a column of 2 cm in diameter and 12 cm long packed with silicon carbide (0.5 mm) and 25 mg of hydrotalcites, in order to complete the volume and avoid dead volume. A solution containing 20 μmol/dm^3 of the organic molecule was fed at a flow of 0.2 cm^3/min using a peristaltic pump (Ecoline VC-380) in down-flow mode. The effluent

from each column was collected at various time intervals up to 120 min and the amount of remaining pollutants was quantified by means of ultraviolet-visible absorption spectrophotometry, as previously described for the batch experiments. The results were adjusted to the Thomas model which allows for a simple interpretation of the behavior inside the column.

II.5. CATALYTIC TESTS

The photocatalytic behavior of the materials under ultraviolet (UV) light was evaluated by measuring the concentration of diclofenac and salicylic acid in an aqueous solution (ultrapure water obtained from Milli-Q equipment, Millipore). The catalytic tests were carried out using a MPDS-Basis system from UV-Consulting Peschl (Spain) (Figure II.4), with a PhotoLAB Batch-L reactor of 1.0 dm^3 and a medium-pressure Hg lamp TQ 150Z1 (power 150 W). The spectrum of the lamp is continuous, with the mean peaks at 366 nm (radiation flux, Φ 6.4 W) and 313 nm (Φ 4.3 W). The lamp was enclosed in a water cooling jacket (PolyScience Digital Temperature) to maintain a constant temperature (298 K) and then placed in the middle of the reactor. The solution was magnetically stirred (700 rpm) and the whole process was carried out in a photon cabinet.

Figure II.4. Photocatalytic apparatus.

The adsorbate solution (0.7 dm^3), with a concentration between 5 and 15 mg/dm^3, was mixed in the reactor with the catalyst, with a concentration between 100 and 1000 $mg_{catalyst}/dm^3$, under the UV lamp. The suspension was then sampled every 15 min, filtered to remove the catalyst and then analyzed on a UV-vis spectrometer to evaluate the concentration of the organic molecule.

The absorbance was determined at the wavelength corresponding to the maximum absorbance of a solution of the organic molecule, and the concentration was estimated by application of Beer's law from a calibration curve of organic contaminant concentration vs. absorbance. Blind tests in the absence of a catalyst (photolysis test) were also carried out.

II.6. 1-BUTANOL CONVERSION PROCEDURE

1-Butanol conversion was used as a means of acidity and basicity characterization in chapter III. The metal oxides different reaction pathways in the dehydration/dehydrogenation of alcohols are employed as a model reaction that correlates with the strength and the concentration of the catalysts acid and basic sites (Gil et al., 2005). 1-Butanol was used as reagent in this experiment.

The dehydration and dehydrogenation reactions were carried out in a two-reactor system, one used as a blank with only glass balls inside (500 to 800 μm) and the other with 180 mg of catalyst mixed with glass balls up to a bed height of 2 cm and extra 0.5 cm of balls to homogenize the gas input. Before the reaction, catalysts were sieved, and the particle size fraction of 100-200 μm was used. The reactor was placed in a vertical furnace with temperature control. The real reaction temperature was measured by a thermocouple situated near the catalyst, in the middle part of the reactor. Sample pretreatment was made at 473 K for 2 h under a nitrogen flow (30 cm^3/min). After the pretreatment the reactor was heated to 373 K and nitrogen was saturated with 1-butanol vapor (Roth, ≥ 99.95%). The 1- butanol temperature was 337.75 K to obtain a 10% of butanol in the flow. To prevent the condensation of 1-butanol or reaction products, all lines from the saturator to the chromatograph were heated at 373 K. A first series of 6 chromatograms was performed over the blank reactor and then changed to the sample reactor to perform 6 chromatograms every 50 K from 373 K to 723 K. Unconverted 1-butanol and the dehydration and dehydrogenation products were analyzed by a Thermo

Scientific Trace 1300 gas chromatograph, equipped with a FID detector. A 30m*0.32 mm, 0.25µm (Stabilwax) capillary column was used for the separation of the various compounds. In addition, a Hayesep column (N 60-80, 0.25m*1/16" SS) with a TCD detector was used to quantify the nitrogen. The estimation of the initial contents of both nitrogen and butanol were made from the intensities measured in the blank chromatograms and, in the next steps, the other components signals were normalized to that of nitrogen.

II.7. REFERENCES

Bakatula, E.N., Richard, D., Neculita, C.M., Zagury, G.J., 2018. Determination of point of zero charge of natural organic materials. Environ. Sci. Pollut. Res. 25, 7823–7833. https://doi.org/10.1007/s11356-017-1115-7

Brunauer, S., Emmett, P.H., Teller, E., 1938. Adsorption of Gases in Multimolecular Layers. J. Am. Chem. Soc. 60, 309–319. https://doi.org/10.1021/ja01269a023

Cullity, B.D., 1956. Elements of X-ray Diffraction. Addison-Wesley Publishing.

Frost, R.L., Martens, W.N., Erickson, K.L., 2005. Thermal decomposition of the hydrotalcite: Thermogravimetric analysis and hot stage Raman spectroscopic study. J. Therm. Anal. Calorim. 82, 603–608. https://doi.org/10.1007/s10973-005-0940-y

Gil, A., García, A.M., Fernández, M., Vicente, M.A., González-Rodríguez, B., Rives, V., Korili, S.A., 2017. Effect of dopants on the structure of titanium oxide used as a photocatalyst for the removal of emergent contaminants. J. Ind. Eng. Chem. 53, 183–191. https://doi.org/10.1016/j.jiec.2017.04.024

Gil, A., Vicente, M.A., Korili, S.A., 2005. Effect of the Si/Al ratio on the structure and surface properties of silica-alumina-pillared clays. J. Catal. 229, 119–126. https://doi.org/10.1016/j.jcat.2004.10.013

Gil Bravo, A., 2019. Análisis textural de sólidos porosos mediante adsorción física de gases. Universidad Pública de Navarra.

Goldstein J.I. et al, 2003. Special Topics in Electron Beam X-Ray Microanalysis., in: Scanning Electron Microscopy and X-Ray Microanalysis. Springer US. https://doi.org/10.1007/978-1-4615-0215-9_10

Haines, P.J., 1995. Thermogravimetry BT - Thermal Methods of Analysis: Principles, Applications and Problems, in: Haines, P.J. (Ed.), Springer Netherlands, Dordrecht, pp. 22–62. https://doi.org/10.1007/978-94-011-1324-3_2

Malet, P., Caballero, A., 1988. The selection of experimental conditions in temperature-programmed reduction experiments. J. Chem. Soc. Faraday Trans. 1 Phys. Chem. Condens. Phases 84, 2369–2375.

Markovits, A., Ahdjoudj, J., Minot, C., 1996. A theoretical analysis of NH_3 adsorption on TiO_2. Surf. Sci. 365, 649–661. https://doi.org/10.1016/0039-6028(96)00753-4

Minot, C., Fahmi, A., Ahdjoudj, J., 1995. Periodic Hartree-Fock Calculations of the Adsorption of Small Molecules on TiO_2, in: The Synergy Between Dynamics and Reactivity at Clusters and Surfaces. p. 275. https://doi.org/10.1007/978-94-011-0133-2

Moore, D.M., Reynolds Jr, R.C., 1989. X-ray Diffraction and the Identification and Analysis of Clay Minerals. Oxford University Press (OUP).

Moulder, J.F., Chastain, J., 1992. Handbook of X-ray Photoelectron Spectroscopy: A Reference Book of Standard Spectra for Identification and Interpretation of XPS Data. Physical Electronics Division, Perkin-Elmer Corporation.

Nölte, J., 2020. ICP Emission Spectrometry: A Practical Guide. Wiley-VCH Verlag GmbH.

Patterson, A.L., 1939. The Scherrer formula for X-ray particle size determination. Phys. Rev. 56, 978.

Rivera-Utrilla, J., Bautista-Toledo, I., Ferro-García, M.A., Moreno-Castilla, C., 2003. Bioadsorption of Pb(II), Cd(II), and Cr(VI) on activated carbon from aqueous solutions. Carbon. 41, 323–330. https://doi.org/10.1016/S0008-6223(02)00293-2

Sing, K.S.W., 1985. Reporting physisorption data for gas/solid systems with special reference to the determination of surface area and porosity (Recommendations 1984). Pure Appl. Chem. 57, 603–619. https://doi.org/10.1351/pac198557040603

Stokes, D., 2008. Principles and practice of variable pressure/environmental scanning electron microscopy (VP-ESEM). John Wiley & Sons.

Thommes, M., Kaneko, K., Neimark, A. V., Olivier, J.P., Rodriguez-Reinoso, F., Rouquerol, J., Sing, K.S.W., 2015. Physisorption of gases, with special reference to the evaluation of surface area and pore size distribution (IUPAC Technical Report). Pure Appl. Chem. 87, 1051–1069. https://doi.org/10.1515/pac-2014-1117

Watts, J.F. and Wolstenholme, J., 2003. Electron Spectroscopy: Some Basic Concepts, in: An Introduction to Surface Analysis by XPS and AES, Wiley Online Books. pp. 1–15. https://doi.org/doi:10.1002/0470867930.ch1

Chapter III

Effect of the surface properties of Me^{2+}/Al Layered double hydroxides synthesized from aluminum saline slag wastes on the adsorption removal of drugs

ABSTRACT

This work presents the synthesis of Me^{2+} (Co, Mg, Ni and Zn)/Al layered double hydroxides (LDH) with a 3:1 molar ratio by the co-precipitation method. Structural characterization and comparison of the series has been achieved using powder X-ray diffraction (PXRD), scanning electron microscopy (SEM), nitrogen physisorption at 77 K, thermogravimetry measurements (TGA), temperature-programmed reduction (TPR), X-ray photoelectron spectroscopy (XPS), ammonia temperature-programmed desorption (NH_3-TPD) and point of zero charge (pHpzc). Batch experiments were performed to analyze the adsorption capacity of the different LDH on diclofenac and salicylic acid, as example of emergent pollutants. The pH, mass of adsorbent, contact time and concentration of pollutant were the parameters used to compare the adsorption performance of the synthesized materials. Samples showed different behavior and the equilibrium was reached at different times, Mg_6Al_2 and Zn_6Al_2 showed longer equilibrium times but had higher adsorption capacity. Various adsorption and isotherm equation models were employed to study both the kinetic and equilibrium results and, in general, the removal of diclofenac was greater than that of salicylic acid. 1-Butanol conversion was also used as a means of acidity and basicity characterization and the results were compared with the adsorption performance of the samples in order to explain the results found. A relationship between the amount of pollutants adsorbed and the butenes formed in the dehydrogenation reaction of 1-butanol was found.

III.1. INTRODUCTION

Even though priority pollutants are still the main focus in wastewater treatment, an increasing attention is being given to unregulated emerging contaminants. This type of compounds (which range from pharmaceuticals, hormones and steroids to flame retardants, gasoline and industrial additives) have undesired effects on the environment and need to be monitored in the near future (Petrie et al., 2015). Several techniques can be applied and membrane processes (Yangali-Quintanilla et al., 2011), adsorption (Gil et al., 2018) and photocatalysis (Santamaría et al., 2020b) have been proven to be amongst the most effective (Rodriguez-Narvaez et al., 2017). All of them having pros and cons, adsorption is one of the most studied due to its rapid pace and low energy consumption. Even if different adsorbents such as active carbons (Gil et al., 2018), zeolites (Kyzas and Kostoglou, 2014) or metal organic frameworks (Kyzas and Kostoglou, 2014) have been studied in the past, a new trend

towards greener adsorbents (Kyzas and Kostoglou, 2014; Rodriguez-Narvaez et al., 2017) or, like in this study, integrating hazardous waste remediation, seems to be congruent.

The secondary aluminum smelting process generates various types of wastes of which the largest, in % by mass, are saline slags. Catalogued as hazardous wastes in European Waste List (Commission Decision 2014/955/EU of 18 December 2014), they are generated because salts are added to prevent oxidation, enhance the thermal efficiency of the process and scatter the oxides present in the smelting furnace (Gil et al., 2014). Saline slags have a significant economic value. Alas its recovering process is not cost-effective and the wastes are currently stored in controlled landfills (Gil, 2005) once its metal fraction has been separated. However, aluminum saline slags, as a mixture of oxides, can be used for direct applications such as road paving or inert filling for construction or even recovered as a high-value product and used to synthesize salts or alumina (Gil and Korili, 2016). In this study, aluminum extracted from saline slags was used to synthesize layered double hydroxides.

Layered double hydroxides (LDH), also known as anionic clays, are compounds with a structure based on that of brucite [$Mg(OH)_2$] with the substitution of some Me^{2+} for Me^{3+} which creates a positive charge that is balanced by the presence of anions in the interlayer. The possibility of varying the identity and the relative proportions of the Me^{2+}, Me^{3+} and the anions in the interlayer shapes the LDH group, which follows the general formula $[Me^{2+}_{1-x}Me^{3+}_x(OH)_2]^{x+}[A^{n-}]_{x/n}\cdot yH_2O$. LDH is naturally formed and has a Mg/Al ratio of 3 (x=0.25) although ratios between 2 and 4 ($0.2 < x < 0.33$) are found in synthetic samples. Several studies have been completed to define the limits of which metal ions can form LDH such as ionic radii (Khan and O'Hare, 2002), solubility products (Kloprogge et al., 2002) or thermodynamic factors (Allada et al., 2005). The most commonly used Me^{2+} cations are Co, Cr, Cu, Mg, Mn, Ni and Zn; Al and Fe are usually the Me^{3+} and the most frequent anion is CO_3^{2-}. LDH can be calcined to extract the water and anions of the interlayer and form mixed metal oxides (MMO). These MMO have multiple applications primarily as adsorbents (Ni et al., 2007) and catalysts (Zhao et al., 2009). MMO can have the ability to recover their previous LDH structure when in contact with water of whom hydroxides serve as compensating ions, in the so called *memory effect* which can be used to trap different anions in the interlayer space.

Nonsteroidal anti-inflammatory drugs (NSAIDs) are emerging contaminants and over-the-counter pharmaceutical compounds used to reduce pain, decrease fever and inflammation. Their high consumption rates together with the inability of waste-water

treatment plants to efficiently remove some of them have pointed them out as excellent chemical markers of wastewater contamination (Ebele et al., 2017). Salicylic acid effects on the environment have been studied with different results (Cleuvers, 2004; Hayat et al., 2010; Pino et al., 2015; Nunes, 2019) and although in general it has good removal percentages, it is usually present in surface waters (Čelić et al., 2019). Diclofenac, with a more acute ecotoxicity and lower removal rates in wastewater treatments, has been incorporated into the European Commission's watch-list of substances for monitoring in the field of water policy 2015/495 (Directive 2008/105/EC of the European Parliament and of the Council, 2015).

In this work LDH with various Me^{2+} (Co, Mg, Ni and Zn) and aluminum extracted from saline slags as Me^{3+} (with a 3:1 Me^{2+}:Me^{3+} molar ratio) were synthesized by a modified co-precipitation method. These synthesized and calcined LDH were then studied as adsorbents of diclofenac and salicylic acid, as representative compounds of emergent pollutants. Special attention was given to the characterization of acid and basic sites of the calcined LDH to tentatively explain the adsorbance performance of rehydrated LDH.

III.2. EXPERIMENTAL PROCEDURE

III.2.1. MATERIALS

The materials used for the synthesis of hydrotalcites were: $Co(NO_3)_2 \cdot 6H_2O$ (Panreac, ≥ 98%), $Mg(NO_3)_2 \cdot 6H_2O$ (Sigma-Aldrich, ≥ 99.99%), $Ni(NO_3)_2 \cdot 6H_2O$ (Panreac, ≥ 98%), $Zn(NO_3)_2 \cdot 6H_2O$ (Sigma-Aldrich, ≥ 98%), Na_2CO_3 (Sigma-Aldrich, ≥ 99.99%), HNO_3 was used for pH adjustment and NaOH (Panreac) for both pH adjustment and aluminum extraction. 1-butanol (Roth, ≥ 99.95%), ammonia (Air Liquide, 99.995 %), helium (Praxair, 99.999%) and nitrogen (Praxair, 99.999%) were also used.

The following adsorbates were used without any modification: salicylic acid, (2-hydroxybenzoic acid, 2-$(HO)C_6H_4COOH$, ≥ 99.99%, Sigma-Aldrich) and diclofenac sodium salt (2-[(2,6-dichlorophenyl)amino]benzeneacetic acid sodium salt, $C_{14}H_{10}Cl_2NNaO_2$, Sigma-Aldrich).

III.2.2. HYDROTALCITE-LIKE COMPOUNDS SYNTHESIS

The aluminum used was extracted from saline slags using the procedure previously reported (Santamaría et al., 2020a). The aluminum concentration in the solution was determined by ICP-OES and found to be 6.15 (±) 0.14 g/dm^3.

Layered double hydroxides were synthesized by a modified co-precipitation method with a molar ratio Me^{2+}:Al^{3+} of 3:1. Four samples were synthesized using cobalt, magnesium, nickel and zinc as Me^{2+}. As an example, solutions 0.0266 mol/dm^3 of $Zn(NO_3)_2 \cdot 6H_2O$ and 0.080 mol/dm^3 of aluminum were added dropwise to a 0.015 mol/dm^3 solution of Na_2CO_3; the final volume was 400 cm^3. Both NaOH and HNO_3 were used to adjust the pH to 10. The mixture was stirred at 333 K and 500 rpm for 1 h and then aged for 24 h. The slurries obtained in the washing water were then centrifuged (8000 rpm) and washed several times until a pH of 7 was obtained. The samples were then dried for 16 h at 353 K, manually grounded with a mortar and calcined for 4 h at 673 K (LDH with Mg was calcined at 823 K). Samples were named as Co_6Al_2, Mg_6Al_2, Ni_6Al_2 and Zn_6Al_2, respectively.

III.2.3. CHARACTERIZATION TECHNIQUES

Powder X-ray diffraction (PXRD) patterns were measured at room temperature with a Siemens D-5000 X-ray diffractometer using a Ni-filtered Cu Kα radiation (λ=0.15418 nm) in a 2θ range from 5 to 70° and a scanning rate of 0.2° (2θ)/min. The X-ray source was working with 40 kV of voltage and a current of 30 mA.

The morphology of the samples was analyzed by scanning electron microscopy (SEM) on a Phenomenom World, XL operating at 15 kV.

N_2 physisorption was performed at 77 K with a Micromeritics ASAP 2020 Plus adsorption analyzer. The samples (0.4 g) were degassed under vaccum before measurement at 423 K for 24 h. The specific surface area (S_{BET}) was evaluated by the BET method in the range between 0.05-0.20 of relative pressure. The external surface area (S_{ext}) and the micropore volumes ($V\mu p$) were also estimated using the *t-plot* method.

The thermogravimetric measurements (TGA) were carried out in a Hi-Res TGA2950 apparatus (TA-Instruments). The samples were heated up from room temperature to 1173 K with a 10 K/min heating rate under a dry air atmosphere (60 cm^3/min).

Temperature-programmed reduction (TPR) studies were performed on a Micromeritics TPR/TPD 2900 instrument under a 30 cm^3/min flow of 5% H_2 (H_2/Ar, Praxair) carrier gas. A cold trap was used to retain compounds formed during the precursor decomposition, thus avoiding possible interferences with the measured signal.

X-ray photoelectron spectroscopy (XPS) analyses were carried out on a SSX 100/206 spectrometer for Surface Science Instruments (USA) equipped with a monochromatized and

microfocused Al X-ray source (powered with 20 mA and 10 kV). The pressure within the analysis chamber was about 10^{-6} Pa. The zone analyzed was about 1.4 mm^2, and the pass energy was set at 150 eV for the general spectra and at 30 eV for the elementary spectra. An electron gun set at 8 eV and a nickel grid placed 3 mm above the surface of the samples were used to stabilize the charge. The surface adventitious carbon peak, C 1s at 284.8 eV, was used as a reference for all the binding energies. When required, spectra were decomposed with the CasaXPS program (Casa Software Ltd., UK) with a Gaussian/Lorentzian product function after subtraction of a nonlinear baseline.

NH_3 adsorption and subsequent temperature-programmed desorption (NH_3-TPD) were carried out in a Hiden CATLAB-PCS combined microreactor and mass spectrometer (MS) system equipped with a quadrupole. Three steps were followed to perform the experiments: (1) stabilization of a flow of pure Ar (30 cm^3/min) at 323 K for 25 min in order to check the sensitivity factor of Ar and therewith to determine that of NH_3 during the later TPD (through the previously calibrated Ar/NH_3 sensitivity factors ratio) and subsequent heating to 673 K (still under 30 cm^3/min of pure Ar); (2) adsorption of NH_3 at 423 K for 1.5 h from a 95:5 Ar/NH_3 flow (25 cm^3/min) mixed with a flow of pure Ar (5 cm^3/min); (3) flush at 423 K under pure Ar (30 cm^3/min) for 2.5 h in order to eliminate physisorbed NH_3 and subsequent TPD from 423 to 923 K (10 K/min, still under 30 cm^3/min of pure Ar) in order to desorb chemisorbed NH_3. The amount of NH_3 desorbed allows the number of acid sites to be calculated, the desorption temperature reflects the strength of these sites.

The point of zero charge was determined with the salt addition method. A 0.01 mol/dm^3 NaCl solution was used as background electrolyte. A background solution (50 dm^3) was apportioned into various flasks kept in series with increasing pH values from 2 to 12. 0.15 g of adsorbent was added to all these flasks and the change in pH of each solution was recorded after shaking the samples for 48 h. This change in pH was plotted against the initial pH values on the graph, and the PZC was identified as the pH when ΔpH=0.

III.2.4. 1-BUTANOL CONVERSION PROCEDURE

The dehydration and dehydrogenation reactions were carried out in a two-reactor system, one used as a blank with only glass balls inside (500 to 800 μm) and the other with 180 mg of catalyst mixed with glass balls up to a bed height of 2 cm and extra 0.5 cm of balls to homogenize the gas input. Before the reaction, catalysts were sieved, and the particle size fraction of 100-200 μm was used. The reactor was placed in a vertical furnace with

temperature control. The real reaction temperature was measured by a thermocouple situated near the catalyst, in the middle part of the reactor. Sample pretreatment was made at 473 K for 2 h under a nitrogen flow (30 cm^3/min). After the pretreatment the reactor was heated to 373 K and nitrogen was saturated with 1-butanol vapor (Roth, ≥ 99.95%). The 1-butanol temperature was 337.75 K to obtain a 10% of butanol in the flow. To prevent the condensation of 1-butanol or reaction products, all lines from the saturator to the chromatograph were heated at 373 K. A first series of 6 chromatograms was performed over the blank reactor and then changed to the sample reactor to perform 6 chromatograms every 50 K from 373 K to 723 K. Unconverted 1-butanol and the dehydration and dehydrogenation products were analyzed by a Thermo Scientific Trace 1300 gas chromatograph, equipped with a FID detector. A 30m*0.32 mm, 0.25µm (Stabilwax) capillary column was used for the separation of the various compounds. In addition, a Hayesep column (N 60-80, 0.25m*1/16" SS) with a TCD detector was used to quantify the nitrogen. The estimation of the initial contents of both nitrogen and butanol were made from the intensities measured in the blank chromatograms and, in the next steps, the other components signals were normalized to that of nitrogen. The conversion (%) was defined as the ratio of the amount of converted butanol to the amount of butanol detected by the blank reactor. The selectivity for each product (%) was defined as:

$$Selectivity\ (\%) = \frac{quantity\ of\ product * correction\ factor}{(butanol\ initial\ quantity * conversion\ \%)} \qquad \text{Eq. III.1}$$

The correction factor was calculated from calibration and taking into account the number of carbons of the product.

III.2.5. ADSORPTION PROCEDURE

The adsorption isotherms of diclofenac and salicylic acid were determined under batch adsorption experiments. The selection of the initial pH was made by adjusting the drug solutions (50 µmol/dm^3) to a range of several pHs from 2 to 12 by adding HNO_3 or NaOH. 10 mg of the adsorbent were added to the beaker and shaken for 2 h at 298 K. The drug concentration in the filtered solutions (0.45 µmol, Durapore) was determined by a Jasco V-

730 UV–Vis spectrometer. Maximum adsorption wavelengths used were 276 nm for diclofenac and 297 nm for salicylic acid.

The kinetic tests were performed to study both the effect of the adsorbent dose and drug concentration. The adsorbent dose was examined by using various amounts of adsorbent (15, 30 and 60 mg) in a 150 cm^3 solution with a drug concentration of 75 μmol/dm^3. Samples were shaken in a stirring plate throughout the duration of the experiments. The effect of the drug concentration was studied by adding 30 mg of the adsorbent to solutions with several drug concentrations (25, 50 and 75 μmol/dm^3). Samples of the solution were taken at various time intervals until equilibrium was attained, or up to 7 h. The amount of drug adsorbed by the hydrotalcites was estimated by subtracting the initial and remaining concentrations, using the following equation:

$$q_{t,e} = \frac{V \cdot (C_0 - C_{t,e})}{m} \qquad \text{Eq. III.2}$$

where C_0 (μmol/dm^3) is the initial concentration and C_t is the concentration at a time t of the organic compound in solution, V (cm^3) was the volume of the solution and m (g) was the adsorbent mass. The sorption mechanism, i.e. transport of adsorbates inside the adsorbent particles was studied considering two kinetic modeling approaches: pseudo-first- (Eq. III.3) and pseudo-second-order rate (Eq. III.4) equations were applied using OriginPro program (version 2018) to test the experimental data.

$$\frac{dq}{dt} = k_1(q_e - q_t) \qquad \text{Eq. III.3}$$

$$\frac{dq}{dt} = k_2(q_e - q_t)^2 \qquad \text{Eq. III.4}$$

where q_e is the amount of adsorbed solute at equilibrium and q_t at a time t (μmol/g), k_1 is the reaction rate constant of pseudo-first-order and k_2 of pseudo-second-order.

Equilibrium studies were performed to study the hydrotalcites adsorption capacity for the two drugs as a function of the contaminant concentration. Glass tubes with 10 cm^3 of the drug solutions at various concentrations (between 20 and 1000 μmol/dm^3) were combined with 5 mg of adsorbent and shaken for 7 h. As in kinetic studies, drug concentrations of the filtered samples were estimated with UV–visible spectrophotometry and using Eq. (VI.1) (C_e, in μmol/dm^3, was the drug concentration at equilibrium).

The equilibrium experimental data obtained were used to better define the interactive behavior between solutes and adsorbents. Several models can be considered for that purpose. In our study we used Langmuir (Eq. III.5) and Freundlich (Eq. III.6) two-parameter isotherms and Toth (Eq. III.7) three-parameter isotherm. Langmuir isotherm assumes homogeneous and monolayer adsorption, with each molecule possessing constant enthalpy. Freundlich isotherm studies processes that happen in heterogeneous surfaces and defines the exponential distribution of the surface active sites. The Toth isotherm is an empirical modification of both the Langmuir and Freundlich equations which tries to reduce the difference between experimental data and predicted value of equilibrium data. This model is most useful in describing heterogeneous adsorption systems under both low and high end boundaries of adsorbate concentration (Ayawei et al., 2017).

$$q_e = \frac{k_L \cdot q_L \cdot C_e}{1 + k_L \cdot C_e} \qquad \text{Eq. III.5}$$

$$q_e = k_F \cdot C_e^{1/m_F} \qquad \text{Eq. III.6}$$

$$q_e = \frac{k_T \cdot q_T \cdot C_e}{[1 + (k_T \cdot C_e)^{m_T}]^{1/m_T}} \qquad \text{Eq. III.7}$$

where q_e (μmol of adsorbate/g of adsorbent) is the amount adsorbed, C_e (μmol/g) is the monolayer capacity, k_L is related to the adsorption capacity, k_F is the equilibrium constant, $1/m_F$ is the adsorption intensity (also indicates the heterogeneity of the adsorbate sites), k_T is the Toth isotherm constant and m_T characterizes the heterogeneity of the system (Ayawei et al., 2017).

In addition, the adsorption process in porous adsorbents was also examined with a fractional approach to the equilibrium, used to estimate the effective diffusion coefficient *F(t)* (Gil et al., 2018):

$$F(t) = \frac{C_0 - C_t}{C_0 - C_e} = \sqrt{1 - exp\left(-\frac{\pi^2 D t}{r^2}\right)} \qquad \text{Eq. III.8}$$

where *D* (m^2/s) is the intraparticle-diffusion coefficient and *r* (m) is the particle size radius assuming a perfect sphere.

III.3. RESULTS AND DISCUSSION

III.3.1. CHARACTERIZATION OF THE ADSORBENTS

The crystallographic phases present on the fresh LDH and on the calcined samples were analyzed by powder X-ray diffraction. The PXRD diffraction patterns obtained for the LDH structures dried at 353 K are shown in Figure III.1a. The results showed that single-phase materials were synthesized with the general formula $Me_6Al_2CO_3(OH)_{16} \cdot 4H_2O$ and the $3R_1$ polytype. The 2θ peaks located at 11.6 and 23.3º correspond to the diffractions of (003) and (006) basal planes of the LDH. Cell parameters were calculated using Bragg's equation with results represented in Table III.1. *a* parameter was calculated as $a = 2d_{(110)}$ and represents the average distance between cations. The different metal ionic sizes of Me^{2+} in the host layer are responsible for the differences in the metal-metal distance as can be seen in Figure III.2. The *c*-parameter corresponds to three times the basal spacing and is related to the thickness of the interlayer distance and was calculated as $c = 3/2\ (d_{003} + 2d_{006})$. *c* values are also quite similar, as CO_3^{2-} was the interlayer anion in all cases with small changes having the opposite tendency to *a* values. Small differences between the samples could be related to changes in interstitial water content or anion orientation/ordering (Naseem et al., 2019). The crystallite size is related to the sharpness of the peaks and was calculated by the Scherrer equation from the (003) reflection. Zn_6Al_2 LDH pattern is best defined than the other three samples and has at least the double of crystallite size. The thickness of the crystallite follows the same trend as the ionic radius and the opposite one to

the *c* parameter. Various authors have suggested that the number of layers of the LDH platelet in the order Zn > Co > Mg > Ni could be responsible for the crystallite thickness (Hernández et al., 2017; Naseem et al., 2019). A higher crystallinity for Zn_6Al_2 hydrotalcites seems to be a general trend (Johnson and Glasser, 2003; Manivannan and Pandurangan, 2009; Mahjoubi et al., 2016; Naseem et al., 2019). Overall, (00*l*) reflections seem to have narrower and more symmetric peaks in comparison with (01*l*) ones. An overlap of the planes (009) and (012) can be seen in Co_6Al_2, Ni_6Al_2 and especially in Mg_6Al_2 samples.

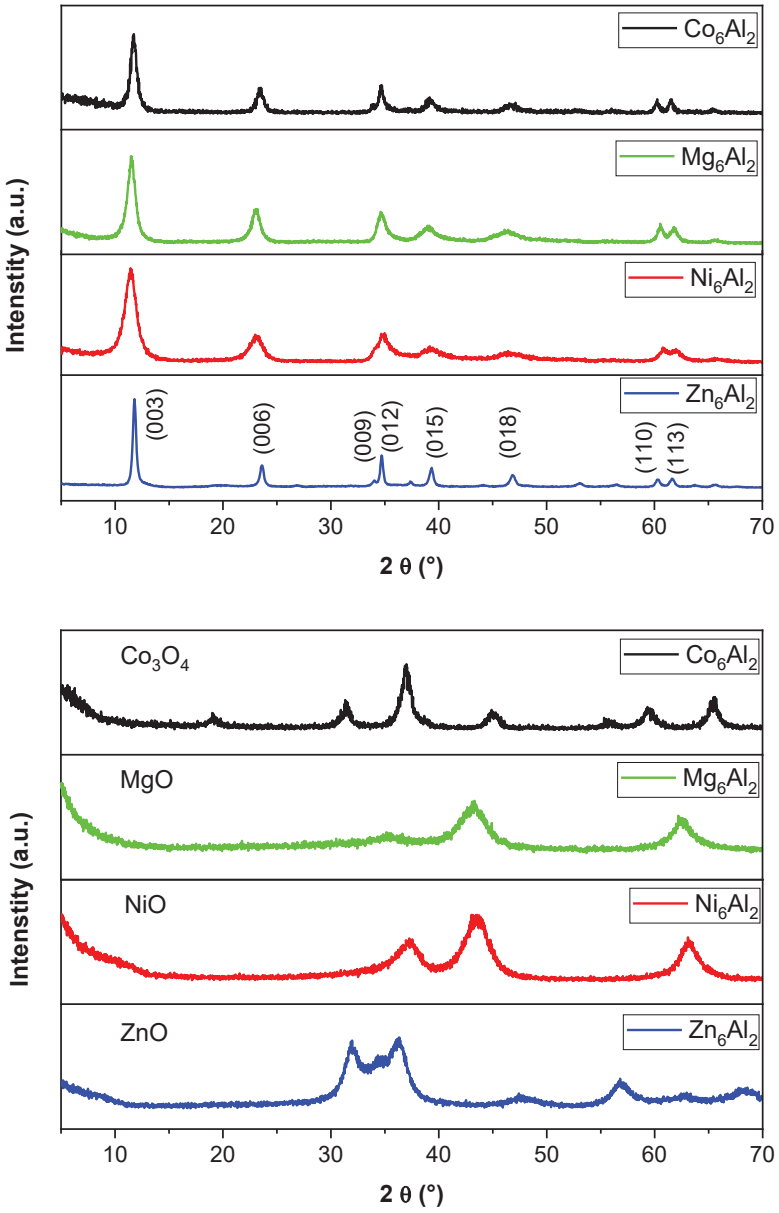

Figure III.1. Powder X-ray diffraction patterns of non-calcined (a) and calcined samples (b).

The broadening of the (01*l*) reflections has been associated with stacking faults, in particular to the presence of $3R_2$ motifs introduced into our $3R_1$ polytype, rather than due to particle-size effects (Thomas et al., 2004). These stacking disorders are differentiated from turbostratic disorder which manifests in the line shape of the (*hk*0) reflections. Turbostratic disorder appears when successive layers are randomly orientated along the c-crystallographic axis, resulting in a loss of registry (Prasanna et al., 2007). In our case Ni_6Al_2 sample, having a less defined (110) peak, could be the only sample affected. Samples were calcined for 4 h at 673 K (except for Mg_6Al_2 which was calcined at 823 K) causing the destruction of their layered structure and the formation of mixed oxides (see Figure III.1b).

In the case of the Mg_6Al_2 sample the periclase crystal structure of magnesium oxide was formed and peaks appeared at 35°, 43° and 62° 2θ corresponding to the (111), (200) and 220) planes, respectively. In the Zn_6Al_2 sample zincite was formed with peaks appearing at 32°, 36° and 57° 2θ corresponding to the (100), (101) and (110) planes. Ni_6Al_2 sample transformed into nickel oxide with peaks at 37° (111), 43° (200) and 63° (220). Co_6Al_2 could have formed a Co_3O_4 structure with main peaks at 37°, 59° and 65° corresponding to (311), (333) and (440) respectively or a $CoAl_2O_4$ structure as their diffractogram peaks are at the same positions. XPS analysis will confirm the presence of Co_3O_4 spinel. The reconstruction of the LDH structure in the presence of water depends on multiple factors such as the temperature of calcination, the formation of spinels and the properties of the divalent metal ions present in the matrix.

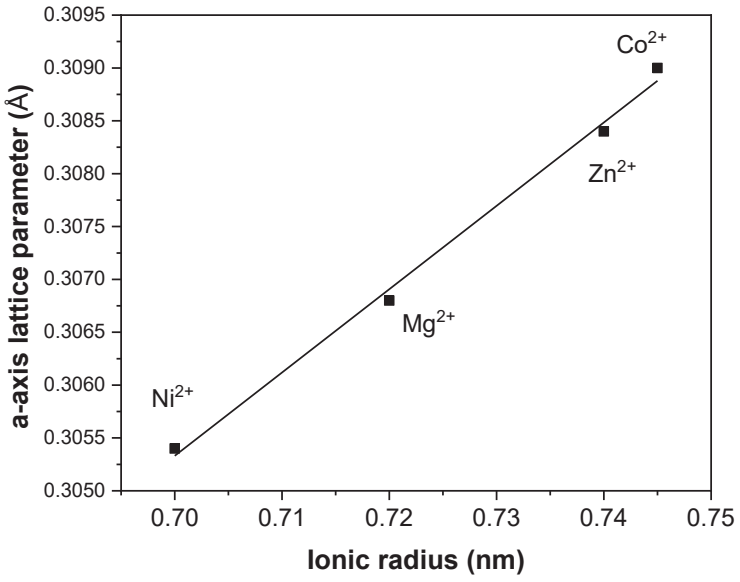

Figure III.2. Linear relationship between the dopant ionic radius and a-axis cell parameters.

Table III.1. Diffraction positions, crystallite size, *c* and *a* parameters of the non-calcined LDH samples.

Sample	$d_{(003)}$ (nm)	$d_{(006)}$ (nm)	*c* (nm)	$d_{(110)}$ (nm)	*a* (nm)	Crystallite size (nm)
Co_6Al_2	0.759	0.380	2.282	0.155	0.309	12.9
Mg_6Al_2	0.765	0.386	2.307	0.153	0.307	9.5
Ni_6Al_2	0.775	0.387	2.323	0.153	0.305	6.7
Zn_6Al_2	0.752	0.378	2.263	0.154	0.308	30.3

In our samples, Zn_6Al_2 and Mg_6Al_2 will recover its LDH structure in the presence of water whereas the memory effect does not appear for Ni_6Al_2 or Co_6Al_2. The former would need to be heated up to 523 K and 4 MPa for 12 h (Sato et al., 1988) and, in the latter, because of the formation of the highly stable Co_3O_4 spinel even at low temperatures (Benito et al., 2008).

SEM analysis of the calcined samples was performed and the micrographs obtained are shown in Figure III.3. Higher resolution of Figure III.3c and especially Figure III.3a allows to distinguish the platelet-like structures, characteristic of hydrotalcite-like compounds, still present after calcination.

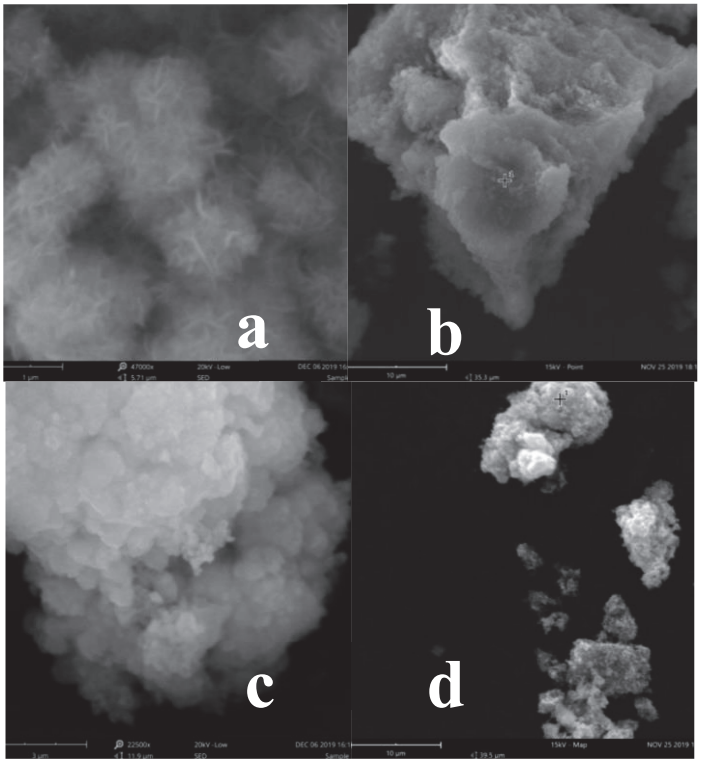

Figure III.3. SEM micrographs of the cobalt (a), magnesium (b), nickel (c) and zinc (d) samples.

EDX analysis shows a relatively small quantity of silicon (around 0.5%) present in all samples, which was also confirmed by XPS measurements, see below. Silicon comes from the aluminium extraction, as SiO_2 is usually present in the saline slags composition (Gil et al., 2014).

The adsorption-desorption isotherms of the samples both uncalcined (423 K) and calcined (673 or 823 K) are shown in Figure III.4. They all have a type II adsorption isotherm, related to the presence of nonporous or macroporous adsorbents, and a H3 hysteresis loop (IUPAC classification). This loop is caused by the typical non-rigid aggregates of plate-like particles with slit-shaped pores and does not exhibit a limiting adsorption at high relative pressures which implies a poor reliability in both the pore distribution and total pore volume (Thommes, 2010). The main textural properties of the samples dried at 423 K and calcined at 673 K (or 823 K) were summarized in Table III.2. As it is frequent with LDH, in all samples the BET surface is greater when the samples are calcined: in the case of Zn_6Al_2 sample the difference is minimal (from 79 to 83 m^2/g) but in the other three samples it is close to double: from 113 to 200 m^2/g in Ni_6Al_2, from 141 to 220 in Co_6Al_2 and from 115 to 245 in Mg_6Al_2.

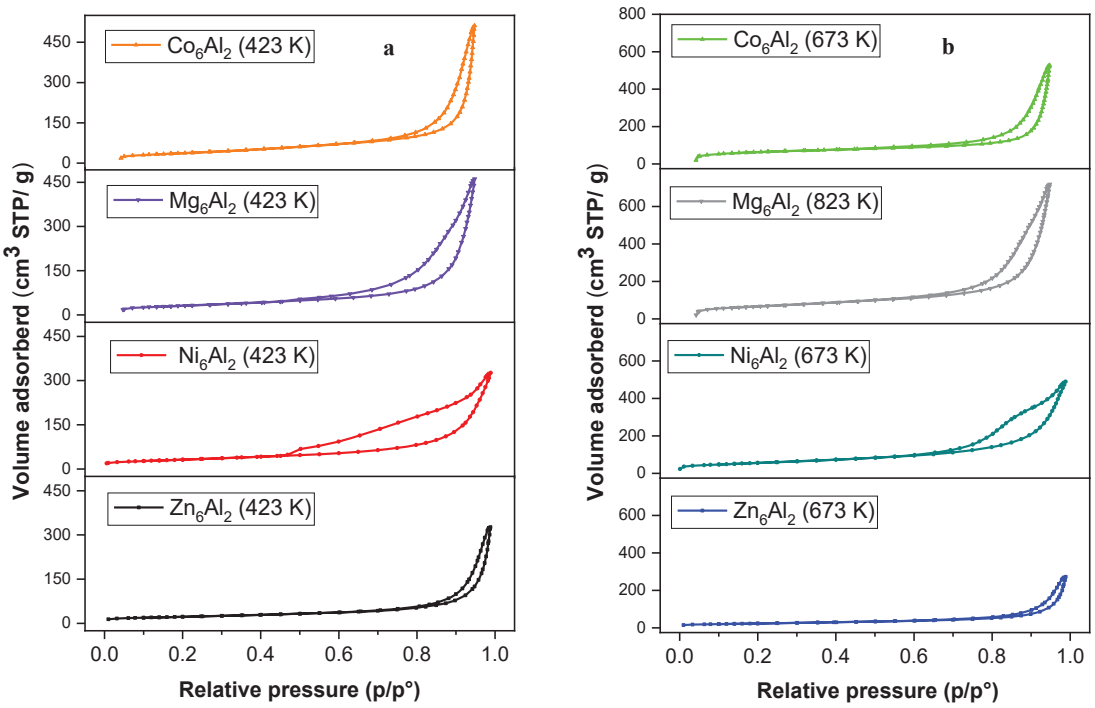

Figure III.4. Nitrogen adsorption-desorption isotherms of non-calcined (a) and calcined (b) series of LDH samples

This is due to the inaccesibility of nitrogen to the interlayer surface of the LDH due to both the relatively high charge density of the layers and the presence of CO_3^{2-} anions in the interlayer gallery (Hernández et al., 2017). The fact that zinc-containing samples have by far the smallest BET surface area could be related to its high crystallinity as its crystallite size twice bigger than those of all the other samples.

Table III.2. Textural properties of the non-calcined and calcined LDH samples.

Sample		S_{BET} (m^2/g)	S_{ext} (m^2/g)	$V_{\mu p}$ (cm^3/g)
Co_6Al_2	uncalcined	141	137	0.0006
	calcined	220	169	0.0273
Mg_6Al_2	uncalcined	115	103	0.0053
	calcined	245	218	0.0127
Ni_6Al_2	uncalcined	113	103	0.0042
	calcined	200	189	0.0042
Zn_6Al_2	uncalcined	79	71	0.0037
	calcined	83	73	0.0046

The thermal analysis behavior of the four LDH were examinated with thermogravimetric analysis and differential thermal analysis. The results are represented in Figure III.5 and the different mass loss steps are calculated and summarized in Table III.3.

The LDH decomposed in five stages and with a total mass loss of between 30 and 45%. The first step, that goes up to 400 K, is related to the loss of adsorbed water and gases. The second, up to 500 K, corresponds to the loss of interlayer water. In the case of Ni_6Al_2 there is not a clear separation between the two steps. The third step is the biggest one in all the samples and is due to the loss of both CO_2 (decarbonation) and –OH groups (dehydroxylation). In Ni_6Al_2 and Zn_6Al_2 two peaks can be observed. This step is located at different temperatures, Mg_6Al_2 is much more resistant to temperature changes than Co_6Al_2, whose structure colapses relatively early. That is the reason why Mg_6Al_2 calcination temperature was chosen to be 823 K, to eliminate the carbonates in the interlayer. Steps 4 and 5 were small and correspond to the formation of the mixed metal oxide and the beginning of a sintering process which collapses the pores.

Table III.3. Mass losses (%) in the steps indicated from the thermogravimetric analyses of the LDH samples.

Step → / Sample ↓	1	2	3	4	5	TOTAL
Co_6Al_2	300-400 K	400-465 K	465-538 K	538-823 K	823-1173 K	
	3.95	10.00	12.35	3.4	1.0	30.7
Mg_6Al_2	300-400 K	400-500 K	500-750 K	750-950 K	950-1173 K	
	6.8	11.28	23.21	3.29	1.12	45.7
Ni_6Al_2	300-500 K		500-650 K	650-850 K	850-1173 K	
	14.69		16.94	3.34	0.86	35.83
Zn_6Al_2	300-373 K	373-460 K	460-600 K	600-900 K	900-1173 K	
	1.72	10.45	12.87	3.82	2.08	30.94

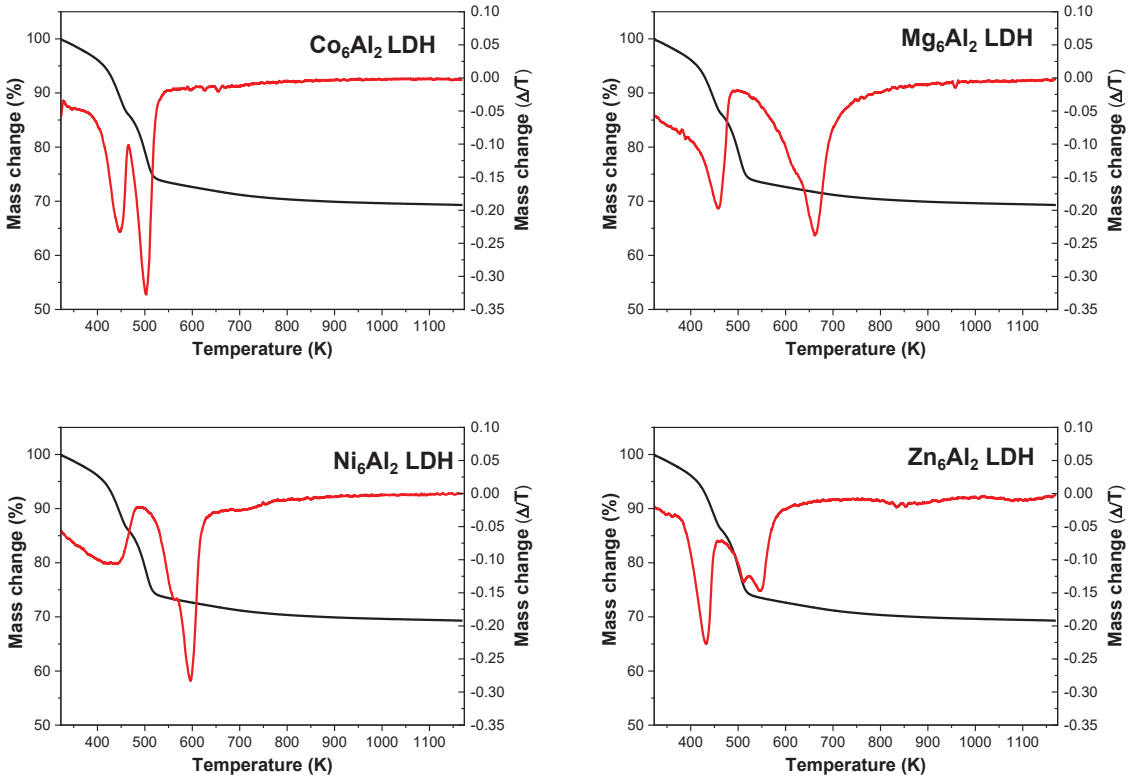

Figure III.5. TG and DTG curves of the LDH prepared with extracted aluminum. Total mass losses: Co_6Al_2 = 30.7 %, Mg_6Al_2 = 45.7 %, Ni_6Al_2 = 35.83 % and Zn_6Al_2 = 30.94 %.

The following equation (Naseem et al., 2019) was used to calculate the theoretical decomposition products of the samples, considering that CO_3^{2-} exits the system as CO_2.

$$\{Me_{(1-x)}Al_x(OH)_2\}\cdot\left\{CO_{3\frac{x}{2}}\cdot nH_2O\right\}\xrightarrow{\Delta}(1-x)MeO\cdot xAl_2O_3+yH_2O+xCO_2 \qquad \text{Eq.III.9}$$

The observed mass losses compared to those expected theoretically were included in Table III.4. The different percentages of mass losses are mainly due to the atomic mass of the divalent metals. Large deviations were not found and Zn_6Al_2 had the best correlation between theoretical and empirical results which could be related to its higher crystallinity. In the case of Co_6Al_2 sample, if cobalt is present only as Co_3O_4, the theoretical residue is larger than the measured residue, in accordance with the rest of the samples. This difference could be due to the water adsorbed outside the structure.

Table III.4. Comparison of theoretical remaining mass and measured remaining mass of the LDH samples.

LDH	Theoretical oxides structure	Theoretical remaining mass (%)	Measured remaining mass (%)	Variance from theoretical value
$Co_6Al_2CO_3(OH)_{16}\cdot 4H_2O$	$2Co_3O_4+Al_2O_3$	71.89	69.30	-2.59
$Mg_6Al_2CO_3(OH)_{16}\cdot 4H_2O$	$6MgO+Al_2O_3$	56.92	54.30	-2.62
$Ni_6Al_2CO_3(OH)_{16}\cdot 4H_2O$	$6NiO+Al_2O_3$	67.89	64.17	-3.72
$Zn_6Al_2CO_3(OH)_{16}\cdot 4H_2O$	$6ZnO+Al_2O_3$	69.40	69.06	-0.34

X-ray photoelectron spectroscopy (XPS) was used for better understanding the surface characteristics of our calcined samples. The surface spectrum of the samples confirmed the EDX results, as a small percentage of Si is present in the samples. The relative proportion of the metals on the surface are shown in Table III.5. The % of aluminum on the surface is a bit higher than the nominal ratio used 3:1. However this increase in Al concentration in the surface was to be expected as lighter metals tend to migrate to the surface with the increase of the temperature (Li et al., 2009). Spectra corresponding to Co 2p and Ni 2p were

presented in Figure III.6. The calcination process of Co_6Al_2 oxidizes cobalt to form Co_3O_4 (Figure III.6a) as PXRD diffraction pattern suggested.

Table III.5. Surface concentration (% atomic) and metals proportions of the calcined compounds on the surface of the LDH samples.

Sample	Me^{2+}	Al	O	C	Metals' proportions
Co_6Al_2	25.6	11	60.2	9.8	$Co_6Al_{3.5}$
Mg_6Al_2	26.2	8.3	51.9	13.5	$Mg_6Al_{1.9}$
Ni_6Al_2	21.4	10.7	53.1	14.8	Ni_6Al_3
Zn_6Al_2	20.4	8.8	49.5	21.2	$Zn_6Al_{2.6}$

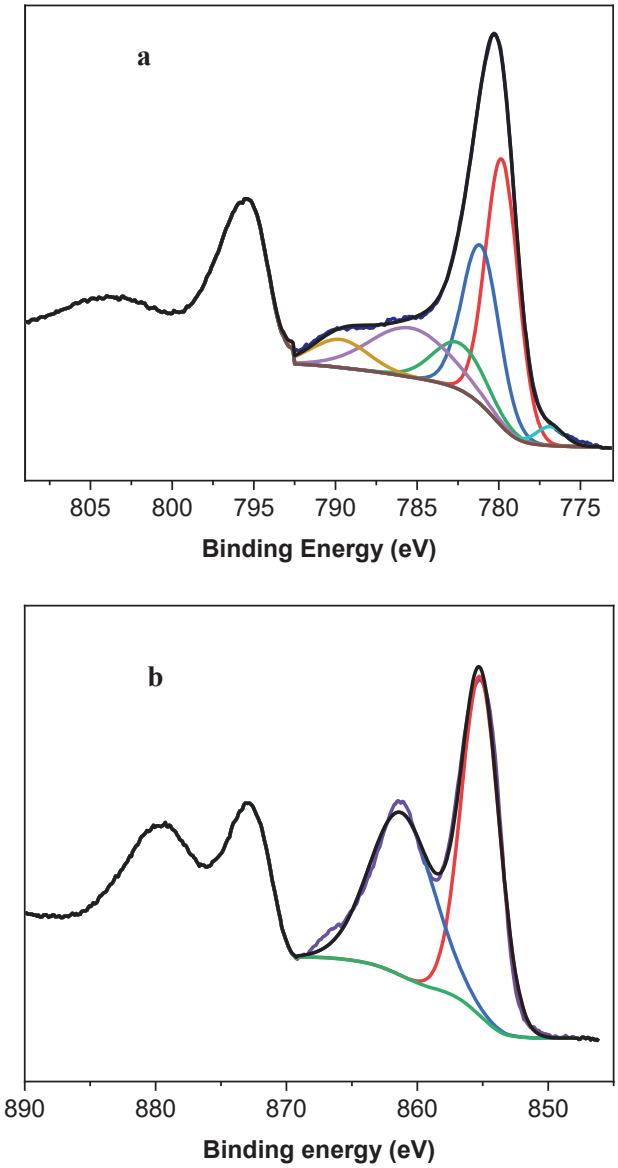

Figure III.6. XPS spectra for Co 2p (a) and Ni 2p (b).

Temperature-programmed reduction by hydrogen (H_2-TPR) was conducted to study the reducibility of the mixed oxides after calcination. Neither Zn_6Al_2 nor Mg_6Al_2 give significant peaks as can be seen in Figure III.7. Ni_6Al_2 sample exhibits one peak that goes from 600 to 1000 K with a maximum situated at 800 K which corresponds to the reduction of NiO to Ni. Co_6Al_2 profile shows two reduction steps: from 400 to 670 K, Co_3O_4 reduces to CoO and at 950 K changes from CoO to Co. This susceptibility to be reduced can have effects on its result in the butanol conversion, which will be later discused.

III.3.2. ACID AND BASIC SITES CHARACTERIZATION

Metal oxides have been widely used for the dehydration/dehydrogenation of alcohols. Their different reaction pathways are employed as a model reaction that correlates with the strength and the concentration of the catalysts acid and basic sites (Gil et al., 2005). 1-Butanol was used as reagent in this experiment. In general, acid sites tend to give predominantly dehydration products whereas basic sites dehydrogenate 1-butanol (Basi et al., 2001; Florea et al., 2011; Iriondo et al., 2012). As seen in Scheme III.1, 1-butanol can be intramolecularly dehydrated into butene in the presence of acid sites. In a mainly acid catalyst, 1-butene will be rapidly isomerized and cis/trans-2-butene will be the main reaction products. An intermolecular dehydration can also occur with the formation of dibutylether. This mechanism should requires the cooperation of both acid and basic sites to take place (Delsarte and Grange, 2004; Florea et al., 2011).

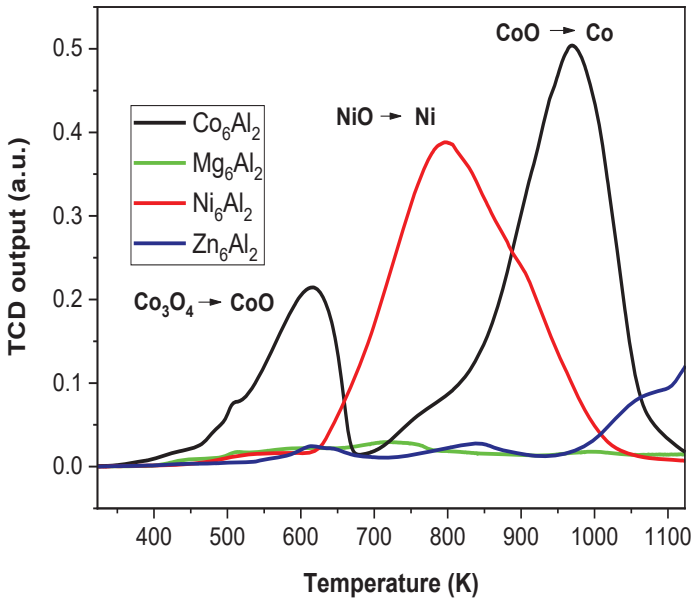

Figure III.7. H_2-TPR profile of Co_6Al_2, Mg_6Al_2, Ni_6Al_2 and Zn_6Al_2 calcined samples.

It can also occur in mainly acid catalysts (Schnee et al., 2017), however at temperatures above 550 K 1-butene is the main product (Delsarte and Grange, 2004). In the same way, strong basic sites will prevent 1-butanol from being dehydrated and a dehydrogenation process will appear instead (Delsarte and Grange, 2004) (see Scheme III.2). 1-Butanol is transformed then into butyraldehyde and both can react together to produce condensation products such as butyl-butyrate. The active sites of mixed oxides obtained by the thermal decomposition of LDH are expected to vary upon modification of the Me^{2+} in the structure. The nature of their active sites has been studied before (Pavel et al., 2012): as a guiding principle our samples will have weak Brønsted basic sites related with surface HO− groups; Lewis sites of medium-strength which are due to acid-basic pairs (both to M^{2+}–O^{2-} and Al^{3+}–O^{2-}); and strong Lewis basic sites which are associated with the presence of low coordinated O^{2-}.

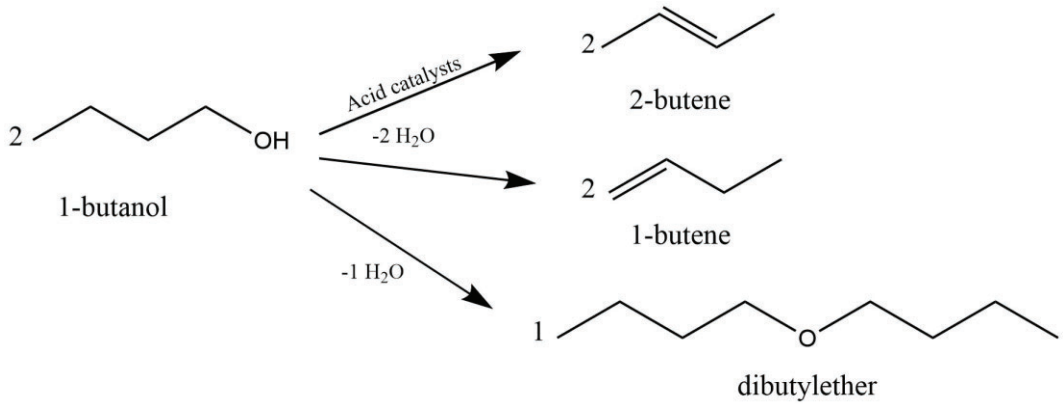

Scheme III.1. 1-Butanol dehydration pathways.

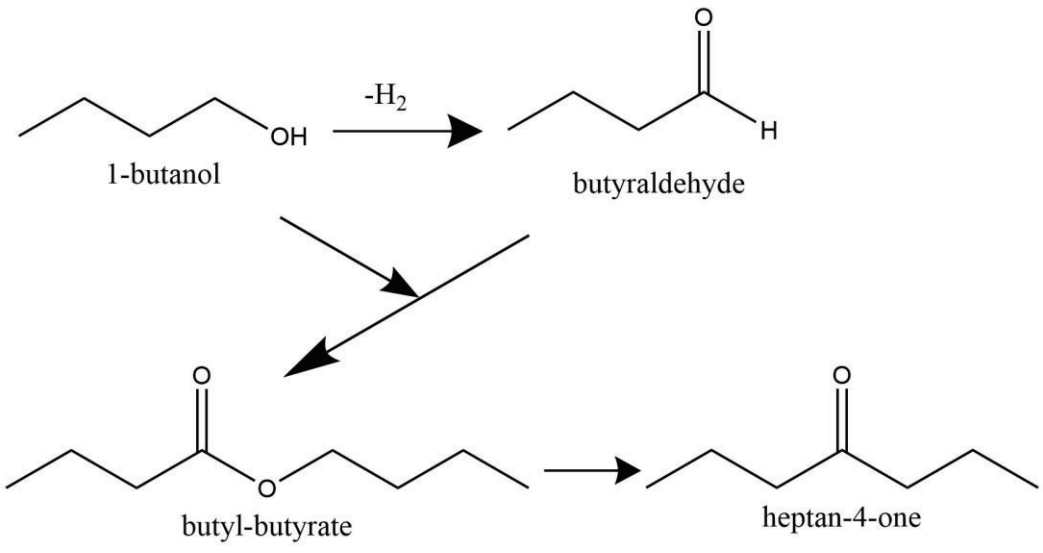

Scheme III.2. 1-Butanol dehydrogenation pathways.

When trying to study the active sites' nature of our samples we have to deal with the fact that, in water adsorption experiments, we work mainly with meixnerite-like LDH (which are difficult to characterize because of their high degree of hydration) and, in the 1-butanol conversion, mixed oxides have been formed by LDH calcination. While some authors have found a precise correlation (Prinetto et al., 2000) between the basicity of the mixed oxides (Lewis-type) and that of meixnerite-like samples (Brønsted-type), others have reported a different behavior between Lewis and Brønsted sites (Baertsch et al., 2002). The 1-butanol conversion with increasing temperatures is shown in Figure III.8a and Table III.6.

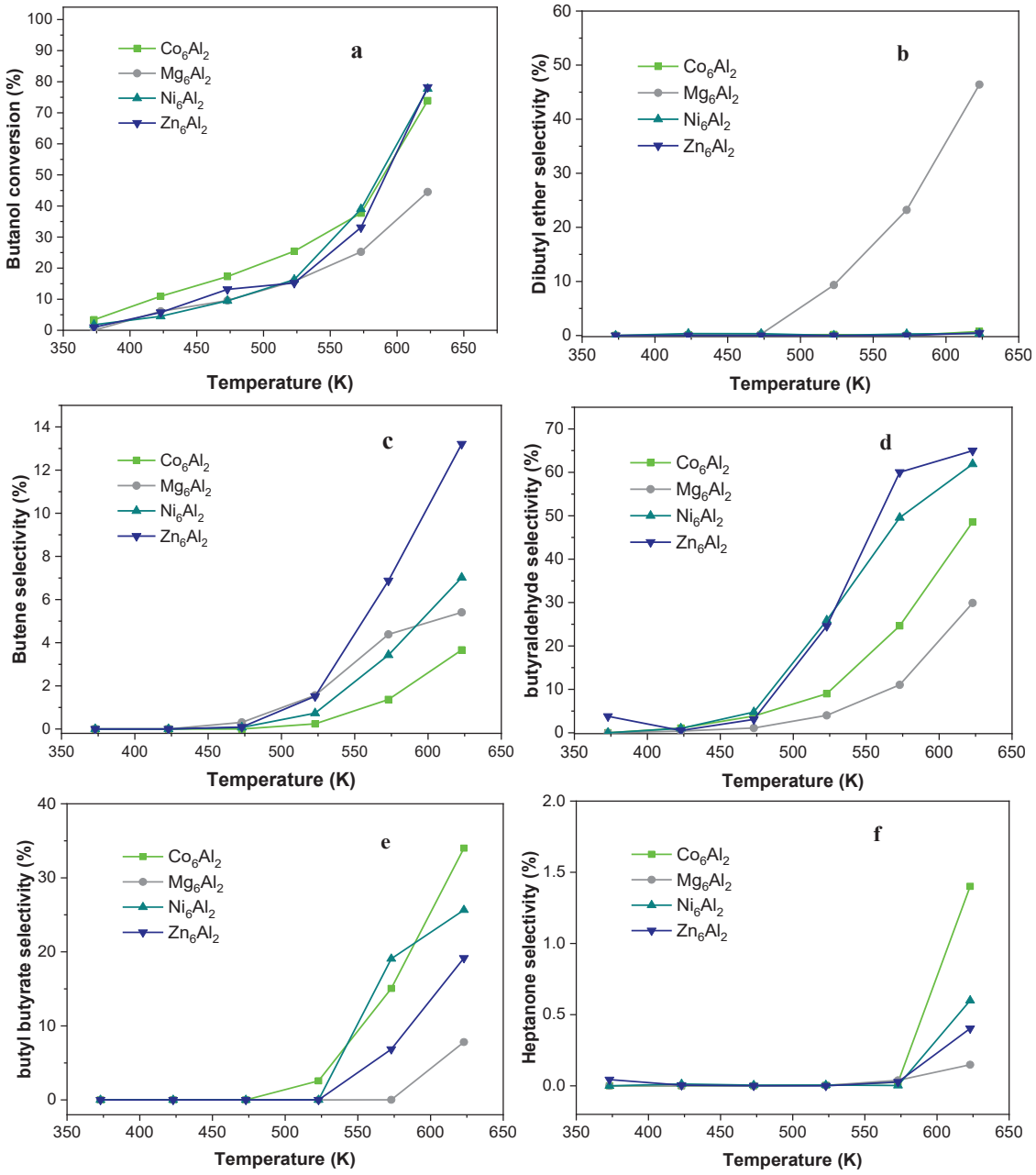

Figure III.8. 1-Butanol conversion and selectivity of Co_6Al_2, Mg_6Al_2, Ni_6Al_2 and Zn_6Al_2 calcined samples.

Co_6Al_2, Ni_6Al_2 and Zn_6Al_2 have a similar behavior and reach 1-butanol conversion of around 85% at 623K. However, Mg_6Al_2 only manages to convert 38%. The results of the dehydration of 1-butanol (both to dibutyl ether and butene) show that it is the only sample that forms dibutyl ether (38 %, Figure III.8b) and butene is formed by all the catalysts in various degrees (Figure III.8c). NH_3-TPD experiments were performed on both Mg_6Al_2 and Zn_6Al_2 for a better understanding of the results (see Figure III.9). Both samples have medium strength acid sites assigned to Me^{2+} and Al^{3+} (peak at 550 K) and Mg_6Al_2 also has weak acid sites (peak at 475 K). These extra Brønsted acid sites together with the medium strength basic sites can favor the formation of dibutyl ether (Berteau, P., Ruwet, M., Delmon, B., 1985; León et al., 2011) since the two samples present a very similar density of acid centers (5 10^{-4} mmol/m^2). *Cosimo et al.* (2003) found that ether formation is favored in the most hydroxylated samples (first peak in NH_3-TPD). In addition, although MgO samples have few acid sites, the increasing presence of Al in the samples can be linearly related to their growth of acid sites number (Díez et al., 2003). The dehydrogenation process favored by basic sites starts to the formation of butyraldehyde, samples selectivity towards it is shown in Figure III.8d. Ni_6Al_2 and Zn_6Al_2 have a similar selectivity percentage and Co_6Al_2 has a smaller one. This can be related with the catalysts susceptibility to be reduced. As seen in Figure III.6, in the range of temperatures considered (up to 623 K) Co_3O_4 is reduced to CoO in the presence of hydrogen and it should be expected that the most easily reducible catalysts would show highest selectivity towards higher degree of oxidation (butyl butyrate and heptanone), as seen in Figures III.8e and III.8f (Basi et al., 2001).

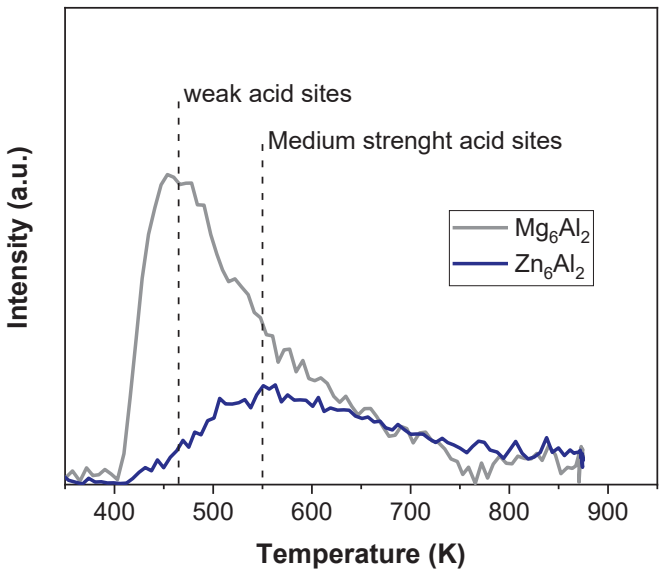

Figure III.9. NH_3 TPD patterns for Mg_6Al_2 and Zn_6Al_2 calcined samples.

The results found show that the LDH samples are characterized by the presence of basic surface sites. In the case of Mg_6Al_2, the sample also presents acid sites since the formation of dibutylether requires the cooperation of acid and basic surface sites at this temperature.

Table III.6. 1-Butanol conversion percentages on the samples.

Sample	Conversion due mainly to acid sites (%)			Conversion due mainly to basic sites (%)			
	Butene	Dibutyl ether	Total	butyraldehide	Butyl butyrate	Heptanone	Total
Co_6Al_2	3.7	0.7	4.4	48.6	34.0	1.4	84
Mg_6Al_2	5.4	46.4	51.8	29.9	7.8	0.1	37.8
Ni_6Al_2	7.0	0.4	7.4	61.9	25.7	0.6	86.1
Zn_6Al_2	13.2	0.5	13.7	65.0	19.2	0.4	84.6

III.3.3. ADSORPTION EXPERIMENTS

III.3.3.1. Effect of pH on adsorbate adsorption

Much care has to be taken when choosing the correct pH in adsorbance tests. Diclofenac sodium is a salt of a weak acidic drug (pK_a = 4.2). At a pH of less than 3, it is mainly present in the free acid form which is less soluble than the salt and gives low signal in the UV-vis. As the pH increases both the ionized and unionized forms are present and the UV-vis signal grows and at a pH higher than 6 only the ionized form exists and the UV-vis signal is stable (Chadha et al., 2003). Salicylic acid (pK_a = 2.8) is in the protonated form, HOC_6H_4COOH, at a pH smaller than the pK_a and in the deprotonated form $HOC_6H_4COO^-$ at a pH bigger than 4.5. This deprotonation produces a small shift in the λ_{max} of the UV-vis spectrum (Guo et al., 2012).

The point of zero charge of the calcined hydrotalcites was 7.3 for Co_6Al_2, 7.6 for Ni_6Al_2, 8.3 for Zn_6Al_2 and 9.9 for Mg_6Al_2 as shown in Figure III.10. This rise in pH is due to the proton consumption that takes place when hydroxides are formed in the meixnerite structure. The differences between the samples can be related to the inability of Co_6Al_2 and

Ni_6Al_2 to recover the LDH structure or/and the samples Me^{2+} average partial charge of oxygen which is also observed in the different decarbonation temperatures (see Table III.3, step 3) as the carbonates will be more attracted to more strongly charged oxygen (Valente et al., 2000). When the pH is higher than the point of zero charge the overall surface charge of the adsorbents will be negative which causes an electrostatic repulsion between the adsorbate anions, decreasing the adsorption capacity. In addition, at a pH higher than 10.5, aluminum hydroxide dissolves and magnesium hydroxide precipitates (Tamura et al., 2006). Taking all this into account together with adsorption experiments performed at different pH (results not shown), a pH of 6 was chosen to perform all the adsorption tests.

III.3.3.2. Batch adsorption results

The results of the adsorption experiments for the four samples considering several adsorbent doses (100, 200 and 400 mg/dm^3) and adsorbate concentrations (25, 50 and 75 µmol/dm^3) are represented in Figure III.11 (diclofenac) and Figure III.12 (salicylic acid). The adsorbent dose effect is represented in the first columns of the figures. As usual, an increase of adsorbent concentration implies a decline in the adsorption capacity. The change in drug concentration is represented in the second column; the increase of adsorbate concentration meant an increase of the adsorption capacity of the samples.

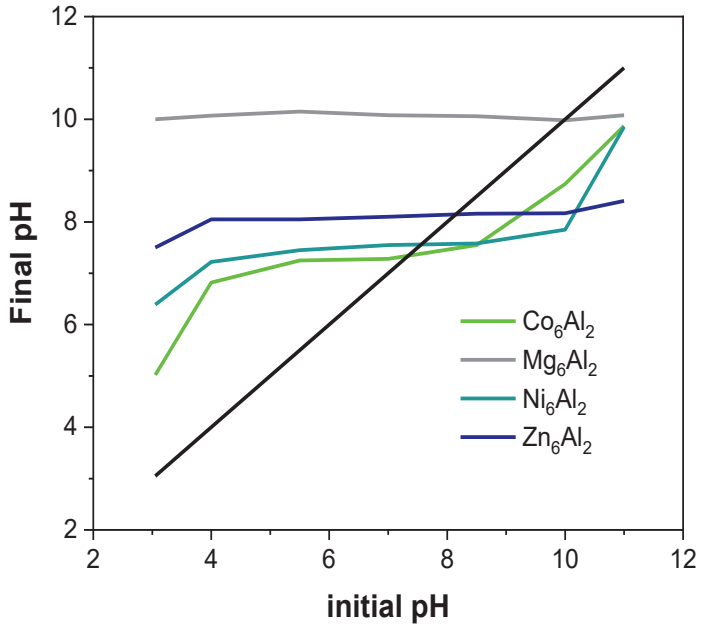

Fig. III.10. Point of zero charge of the LDH samples.

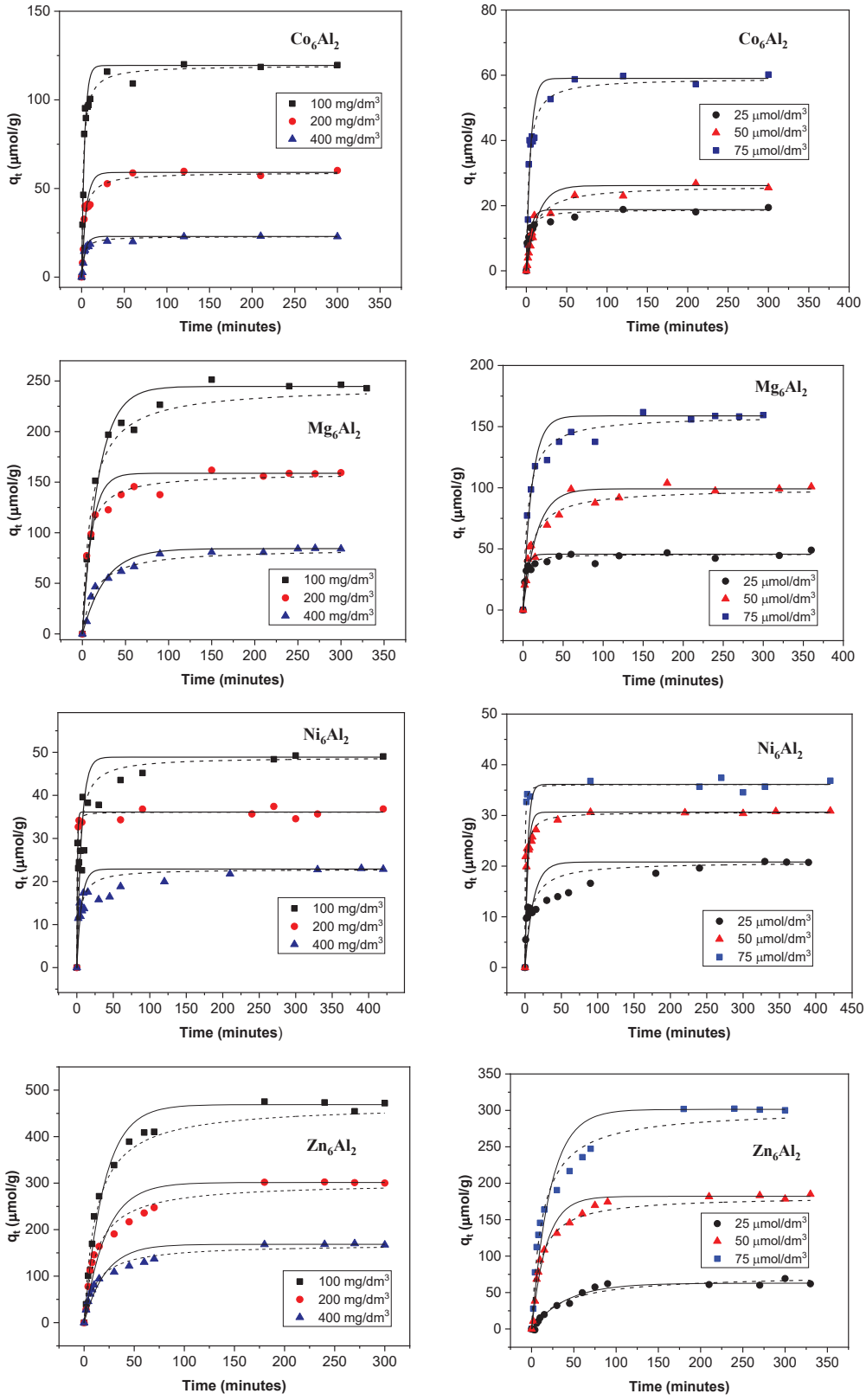

Figure III.11. Kinetic data for diclofenac adsorbed on Co_6Al_2 (first range), Ni_6Al_2 (second range), Mg_6Al_2 (third range) and Zn_6Al_2 (fourth range) with different amounts of adsorbent (first column) and different drug concentrations (second column). Adjustments to pseudo-first (solid line) and second order (dotted line) models are also shown.

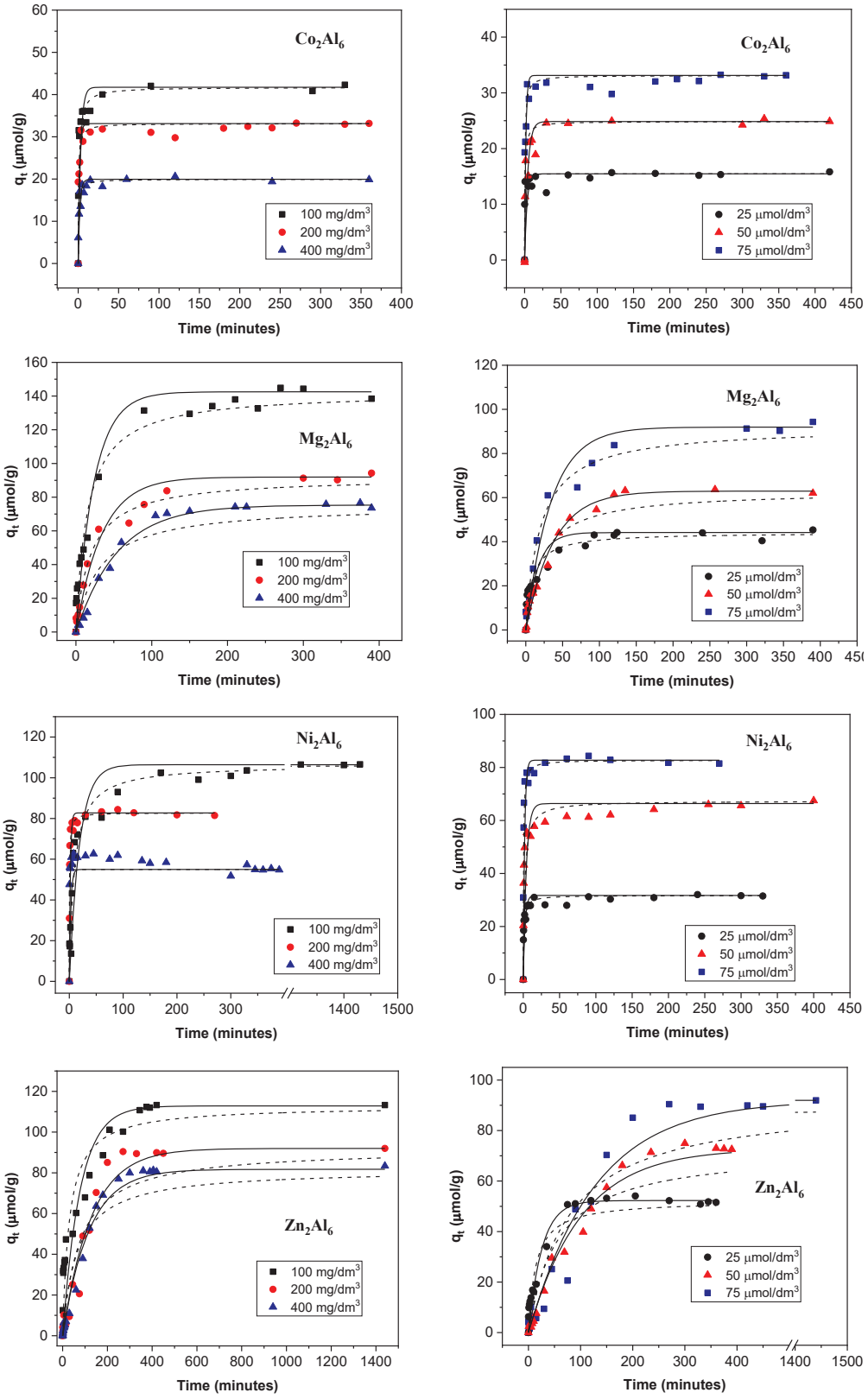

Figure III.12. Kinetic data of salicylic acid adsorbed on Co_6Al_2 (first range), Ni_6Al_2 (second range), Mg_6Al_2 (third range) and Zn_6Al_2 (fourth range) with different amounts of adsorbent (first column) and different drug concentrations (second column). Adjustments to pseudo-first (solid line) and second order (dotted line) models are also shown.

At a 200 mg/dm^3 adsorbent concentration and 75 µmol/dm^3 of adsorbate, the adsorption capacity of Zn_6Al_2 was the greatest, 301 µmol/g, followed by Mg_6Al_2 (159 µmol/g), Co_6Al_2 (59 µmol/g) and Ni_6Al_2 (36 µmol/g). These results are compared in Table III.7 with those obtained in various studies using activated carbon from agro-industrial wastes. Activated carbon is usually taken as a reference because it has more stable properties than other adsorbents (Kyzas et al., 2015).

Table III.7. Diclofenac adsorption capacities, comparison of several activated carbons obtained from different agro-industrial wastes.

Sample/precursor + activator	Adsorption conditions	C_0 (mg/dm^3)	Adsorption capacity (mg/g)	Ref.
AC from olive waste + H_3PO_4	1.5 g/dm^3, 298 K, pH 4.1	14.80	56.2	(Baccar et al., 2012)
AC from olive stones + H_2SO_4	5 g/dm^3, 296 K, pH 4.2	25-150	11.01	(Larous and Meniai, 2016)
AC from peach stones + H_3PO_4	2.4 g/dm^3, 298 K	30-530	200	(Torrellas et al., 2015)
AC from cyclamen tubes + $ZnCl_2$	5 g/dm^3, 298 K, pH 4	0-100	22.22	(Jodeh et al., 2016)
AC from pine chip + NaOH	1.6 g/dm^3, 298 K, pH 7	5.923	372	(Jung et al., 2015)
Commercial AC + H_2SO_4	25-100 mg/L, 298 K, pH 4.2-10	25-100	83-487	(Bhadra et al., 2016)
AC from cocoa pod husks	0.25-1.25 g/dm^3, 298 K, pH 3-11	10-30	5.53	(De Luna et al., 2017)
Co_6Al_2 LDH, Al from saline slags	0.1-0.4 mg/dm^3, 298 K, pH 6	8-24	6-38	This work
Mg_6Al_2 LDH, Al from saline slags	0.1-0.4 mg/dm^3, 298 K, pH 6	8-24	16-78	This work
Ni_6Al_2 LDH, Al from saline slags	0.1-0.4 mg/dm^3, 298 K, pH 6	8-24	7-16	This work
Zn_6Al_2 LDH, Al from saline slags	0.1-0.4 mg/dm^3, 298 K, pH 6	8-24	20-150	This work

In the case of salicylic acid, in the same conditions, Mg_6Al_2 and Zn_6Al_2 show an equal 92 µmol/g adsorption capacity, Ni_6Al_2 is not far at 83 µmol/g and Co_6Al_2 adsorbs the least at 33 µmol/g. Although both salicylic acid and diclofenac are supposed to form a hydrogen bond between their COO^- group and the hydroxyl groups of the LDH, salicylic acid tends to form an intramolecular hydrogen bond with and adjacent hydroxyl group which causes a weaker affinity towards the adsorbent. The results between the samples can be explained with the memory effect rather than the textural properties of solids. Zn_6Al_2 exhibits a much higher adsorption capacity than other materials despite its limited textural properties. Co_6Al_2 and Ni_6Al_2 are not capable of recovering its previous hydrotalcite configuration which means that the interlayer adsorption is not produced causing a decline in their adsorption capacity. Two types of kinetic modelling approaches have been proposed by several authors to describe the transport of adsorbates inside adsorbent surface and particles. One of these types of models considers simple relationships between the adsorption performance and operating conditions, showing how the mean adsorbent loading (q_t) changes with adsorption time (t). The second approach is the use of phenomenological models to describe the physics of the adsorption processes. The kinetic behavior of the samples was studied with pseudo-first and pseudo-second order linear reactions, simple models proposed from the first category of models, summarized in Figures III.11 and III.12 and k_1 and k_2 values in Tables III.8 and III.9. The goodness-of-fit of the samples was tested with chi square (χ^2) and the coefficient of determination (R). The results reveal that the adsorption procedure can be best described as a pseudo-second-order linear reaction. The k_2 values (see Table III.9) are bigger for Co_6Al_2 and Ni_6Al_2 samples. The adsorption rate is bigger in those two samples and the equilibrium is also achieved faster (less than 100 minutes) than in Mg_6Al_2 and Zn_6Al_2 samples. This could be due to: a) the time taken by both LDH to recover their structure when put in contact with water and/or b) the time taken by the drugs to enter the interlayer in those two samples. An analysis of the k_2 values also shows that it decreases as the initial organic molecule concentration increases from 25 to 75 µM and as the adsorbent mass decreases from 400 to 100 mg/dm^3. These results could be related to the number of active sites available for adsorption. The effective diffusion coefficient calculations are presented in Table III.10. There is no clear tendency in the samples as adsorbent mass and adsorbate concentration are increased. However, sample comparison makes clear that D/r^2 is significantly bigger in Co_6Al_2 and Ni_6Al_2 than the other two samples, as expected from the adsorption kinetics.

Table III.8. Pseudo-first-order adjustment of the experimental results.

Sample		Diclofenac					Salicylic acid				
		100 mg/dm^3 75 µM	200 mg/dm^3 75 µM	400 mg/dm^3 75 µM	200 mg/dm^3 25 µM	200 mg/dm^3 50 µM	100 mg/dm^3 75 µM	200 mg/dm^3 75 µM	400 mg/dm^3 75 µM	200 mg/dm^3 25 µM	200 mg/dm^3 50 µM
Co_6Al_2	k_1 (1/min)	0.289	0.187	0.233	0.198	0.0722	0.325	0.590	0.467	0.30	0.23
	χ^2	784.	321	42	79	66	78	33	16	61	44
	R	0.98	0.97	0.97	0.88	0.97	0.91	0.90	0.96	0.94	0.93
Mg_6Al_2	k_1 (1/min)	0.0536	0.0920	0.0380	0.236	0.0584	0.0411	0.0292	0.0182	0.0620	0.0267
	χ^2	2179	2016	374	308	1336	1820	589	137	551	168
	R	0.98	0.96	0.98	0.92	0.96	0.98	0.98	0.99	0.91	0.99
Ni_6Al_2	k_1 (1/min)	0.155	1.122	0.266	0.087	0.262	0.052	0.51	0.37	0.302	0.23
	χ^2	1057	15	159	87	41	948	61	846	52	44
	R	0.77	0.99	0.98	0.78	0.97	0.97	0.98	0.95	0.93	0.93
Zn_6Al_2	k_1 (1/min)	0.0501	0.0455	0.0471	0.0245	0.0571	0.0128	0.0079	0.0085	0.0390	0.0099
	χ^2	8263	12346	4055	230	2011	4859	938	329	268	218
	R	0.99	0.96	0.95	0.99	0.98	0.91	0.98	0.99	0.98	0.99

Table III.9. Pseudo-second-order adjustment of the experimental results.

Sample		Diclofenac					Salicylic acid				
		100 mg/dm^3 75 µM	200 mg/dm^3 75 µM	400 mg/dm^3 75 µM	200 mg/dm^3 25 µM	200 mg/dm^3 50 µM	100 mg/dm^3 75 µM	200 mg/dm^3 75 µM	400 mg/dm^3 75 µM	200 mg/dm^3 25 µM	200 mg/dm^3 50 µM
Co_6Al_2	k_2 (g/mg·min)	0.0044	0.0051	0.017	0.0188	0.0039	0.021	0.054	0.073	0.73	0.062
	χ^2	693	200	35	35	29	35	24	10	22	107
	R	0.98	0.98	0.97	0.95	0.99	0.97	0.96	0.97	0.95	0.95
Mg_6Al_2	k_2 (g/mg·min)	0.00040	0.0011	0.00084	0.010	0.0010	0.00046	0.00056	0.00043	0.0026	0.00077
	χ^2	1808	395	230	122	747	1226	274	967	290	334
	R	0.99	0.99	0.99	0.97	0.98	0.99	0.99	0.97	0.95	0.98
Ni_6Al_2	k_2 (g/mg·min)	0.0061	0.1277	0.117	0.0062	0.022	0.0010	0.026	1.19	0.73	0.062
	χ^2	621	8	7	88	13	255	27	413	22	131
	R	0.87	0.99	0.99	0.99	0.95	0.97	0.99	0.95	0.97	0.97
Zn_6Al_2	k_2 (g/mg·min)	0.00018	0.00027	0.00049	0.65	0.00052	0.00029	0.00014	0.00019	0.0014	0.00025
	χ^2	6882	2752	770	372	982	3073	2444	1646	478	1179
	R	0.99	0.99	0.99	0.99	0.99	0.94	0.96	0.97	0.97	0.97

Table III.10. Effective diffusion coefficients of the adsorption of diclofenac and salicylic acid by the LDH samples.

Sample		Diclofenac					Salicylic acid				
		100 mg/dm^3 75 μM	200 mg/dm^3 75 μM	400 mg/dm^3 75 μM	200 mg/dm^3 25 μM	200 mg/dm^3 50 μM	100 mg/dm^3 75 μM	200 mg/dm^3 75 μM	400 mg/dm^3 75 μM	200 mg/dm^3 25 μM	200 mg/dm^3 50 μM
Co_6Al_2	D/r^2(1/s)	$2.45\ 10^{-4}$	$1.31\ 10^{-4}$	$1.50\ 10^{-4}$	$4.3\ 10^{-6}$	$4.24\ 10^{-5}$	$6.75\ 10^{-4}$	$3.18\ 10^{-4}$	$5.70\ 10^{-4}$	$2.29\ 10^{-4}$	$2.40\ 10^{-4}$
	χ^2	0.062	0.086	0.025	0.12	0.068	0.16	0.34	0.076	0.17	0.17
	R	0.97	0.97	0.98	0.94	0.98	0.91	0.91	0.96	0.93	0.93
Mg_6Al_2	D/r^2 (1/s)	$4.76\ 10^{-5}$	$5.82\ 10^{-5}$	$3.08\ 10^{-5}$	$1.71\ 10^{-4}$	$3.90\ 10^{-5}$	$2.47\ 10^{-5}$	$3.37\ 10^{-5}$	$1.42\ 10^{-5}$	$4.12\ 10^{-5}$	$2.09\ 10^{-5}$
	χ^2	0.026	0.040	0.031	0.069	0.045	0.025	0.037	0.20	0.080	0.067
	R	0.99	0.98	0.996	0.96	0.98	0.996	0.99	0.97	0.98	0.99
Ni_6Al_2	D/r^2 (1/s)	$8.02\ 10^{-5}$	$7.93\ 10^{-4}$	$8.86\ 10^{-5}$	$4.20\ 10^{-5}$	$2.27\ 10^{-4}$	$5.14\ 10^{-5}$	$1.85\ 10^{-4}$	$9.79\ 10^{-4}$	$5.56\ 10^{-4}$	$7.10\ 10^{-4}$
	χ^2	0.29	0.035	0.27	0.41	0.21	0.14	0.024	0.13	0.17	0.13
	R	0.93	0.97	0.86	0.80	0.96	0.97	0.98	0.94	0.93	0.93
Zn_6Al_2	D/r^2 (1/s)	$3.61\ 10^{-5}$	$3.09\ 10^{-5}$	$3.20\ 10^{-5}$	$1.59\ 10^{-5}$	$3.64\ 10^{-5}$	$1.71\ 10^{-5}$	$6.32\ 10^{-6}$	$7.26\ 10^{-6}$	$3.15\ 10^{-5}$	$8.29\ 10^{-6}$
	χ^2	0.042	0.028	0.19	0.23	0.045	0.12	0.32	0.28	0.080	0.22
	R	0.99	0.99	0.99	0.95	0.99	0.97	0.95	0.97	0.97	0.96

Constants calculated from the isotherm equations are displayed in Table III.11. All models show a good representation of the experimental results (see Figure III.13), although the Toth equation shows a better accordance between the theoretical and experimental results than Langmuir and Freundlich equations. Toth model has already been proven to give a good correlation of adsorption experiments with activated carbons and organic molecules (Essandoh et al., 2015).

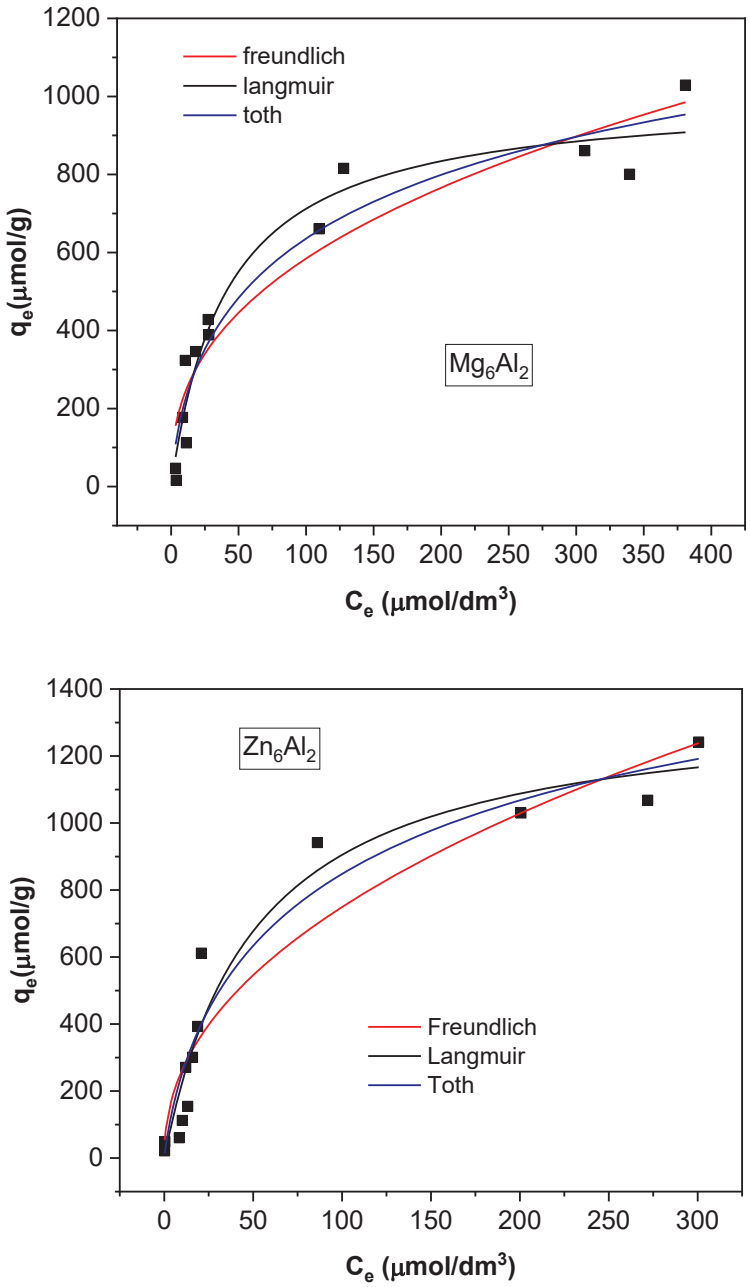

Figure III.13. Experimental results (scatter) and isotherm adjustment to Langmuir, Freundlich and Toth models for diclofenac adsorption on the LDH samples.

Table III.11. Freundlich, Langmuir and Toth parameters for the adsorption of diclofenac by the LDH. Equilibrium time = 24 h, T= 298 K, pH 6.

	Mg_6Al_2	Zn_6Al_2
Freundlich		
q_F	97	91
m_F	2.5	2.2
χ^2	1047	1756
R	0.95	0.95
Langmuir		
q_L **(mg/g)**	1006	1363
k_L **(cm^3/mg)**	0.024	0.020
χ^2	545	167
R	0.98	0.97
Toth		
q_t **(mg/g)**	1980	2013
K_t	0.043	0.025
m_T **(cm^3/mg)**	0.39	0.54
χ^2	19790	8070
R	0.995	0.999

There may be a relationship between the acid/basic properties of the LDH samples and the adsorption capacity of the contaminants. In this case, it is possible to observe a relationship between the amount of adsorbed pollutants (per external area) and the acidic properties of the adsorbents, see Figure III.14. The figure represents the maximum amount adsorbed of the two pollutants and per external area of adsorbent (see Table III.2) in order to avoid the limitation of the diffusion of pollutants inside of the structure of the LDH samples. As acidic properties, the selectivity to butenes observed in the dehydration reaction of 1-butanol has been considered. In the case of the basic properties, a similar relationship could be obtained, but the samples with the presence of Co and Ni show a greater performance in dehydrogenation, related to the properties of these metals, as already mentioned above from the TPR analysis performed.

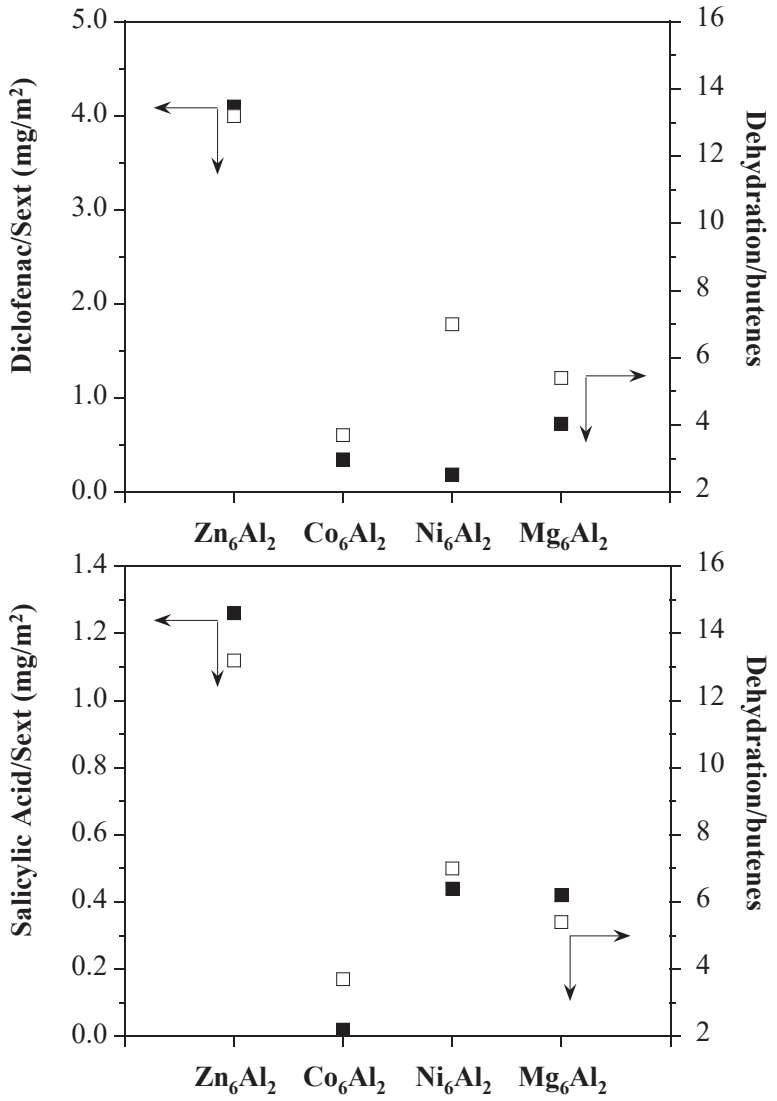

Figure III.14. Evolution of the amount of pollutants adsorbed/Sext to the butenes formation in the dehydrogenation reaction of 1-butanol. (■) pollutants, (□) dehydration.

III.4. CONCLUSIONS

A series of LDH with various Me^{2+} and a ratio of 3:1 was synthesized using Al^{3+} extracted from saline slags as aluminum source. All the samples have a LDH structure with differences between samples mainly due to Me^{2+} cations. Adsorption experiments of diclofenac and salicylic acid as examples of emerging contaminants were performed. Zn_6Al_2 and Mg_6Al_2 present the best adsorption capacity mainly due to their ability to recover their LDH structure when rehydrated. The adsorption capacities of the adsorbents correspond quite well to their acidic properties. Not so much in the case of the basic properties because the dehydrogenating capacity of the LDH samples is also affected by the redox properties of metals, Ni and Co.

III.5. REFERENCES

Allada, R. kumar, Navrotsky, A., Boerio-Goates, J., 2005. Thermochemistry of hydrotalcite-like phases in the MgO-Al_2O_3-CO_2-H_2O system: A determination of enthalpy, entropy, and free energy. Am. Mineral. 90, 329–335. https://doi.org/10.2138/am.2005.1737

Ayawei, N., Ebelegi, A.N., Wankasi, D., 2017. Modelling and Interpretation of Adsorption Isotherms. J. Chem. 2017. https://doi.org/10.1155/2017/3039817

Baccar, R., Sarrà, M., Bouzid, J., Feki, M., Blánquez, P., 2012. Removal of pharmaceutical compounds by activated carbon prepared from agricultural by-product. Chem. Eng. J. 211–212, 310–317. https://doi.org/10.1016/j.cej.2012.09.099

Baertsch, C.D., Komala, K.T., Chua, Y.H., Iglesia, E., 2002. Genesis of Brønsted acid sites during dehydration of 2-butanol on tungsten oxide catalysts. J. Catal. 205, 44–57. https://doi.org/10.1006/jcat.2001.3426

Basi, A., Klimkiewicz, R., Domka, F., 2001. Ru / Fe_2O_3 catalysts in n -butanol conversion. Appl. Catal. A Gen. 207, 287–294.

Benito, P., Guinea, I., Labajos, F.M., Rives, V., 2008. Microwave-assisted reconstruction of Ni,Al hydrotalcite-like compounds. J. Solid State Chem. 181, 987–996. https://doi.org/10.1016/j.jssc.2008.02.003

Berteau, P., Ruwet, M., Delmon, B., 1985. Reaction pathways in 1-butanol dehydration on y-alumina. Bull. SOC. Chim. Belg. 94, 473–480.

Bhadra, B.N., Seo, P.W., Jhung, S.H., 2016. Adsorption of diclofenac sodium from water using oxidized activated carbon. Chem. Eng. J. 301, 27–34. https://doi.org/10.1016/j.cej.2016.04.143

Čelić, M., Gros, M., Farré, M., Barceló, D., Petrović, M., 2019. Pharmaceuticals as chemical markers of wastewater contamination in the vulnerable area of the Ebro Delta (Spain). Sci. Total Environ. 652, 952–963. https://doi.org/10.1016/j.scitotenv.2018.10.290

Chadha, R., Kashid, N., Jain, D.V.S., 2003. Microcalorimetric studies to determine the enthalpy of solution of diclofenac sodium, paracetamol and their binary mixtures at 310.15 K. J. Pharm. Biomed. Anal. 30, 1515–1522. https://doi.org/10.1016/S0731-7085(02)00542-3

Cleuvers, M., 2004. Mixture toxicity of the anti-inflammatory drugs diclofenac, ibuprofen,

naproxen, and acetylsalicylic acid. Ecotoxicol. Environ. Saf. 59, 309–315. https://doi.org/10.1016/S0147-6513(03)00141-6

Commission Decision 2014/955/EU of 18 December 2014, About the Recovery Processes,Waste Treatments and European Wastes List [WWW Document], n.d. URL https://eur-lex.europa.eu/legal-content/EN/TXT/?uri=CELEX:02000D0532-20150601

Commission Implementing Regulation (EU) 2015/495 of 20 March 2015 establishing a watch list of substances for Union-wide monitoring in the field of water policy pursuant to Directive 2008/105/EC of the European Parliament and of the Council, 2015. Officia, n.d.

De Luna, M.D.G., Murniati, Budianta, W., Rivera, K.K.P., Arazo, R.O., 2017. Removal of sodium diclofenac from aqueous solution by adsorbents derived from cocoa pod husks. J. Environ. Chem. Eng. 5, 1465–1474. https://doi.org/10.1016/j.jece.2017.02.018

Delsarte, S., Grange, P., 2004. Butan-1-ol and butan-2-ol dehydration on nitrided aluminophosphates : influence of nitridation on reaction pathways. Appl. Catal. A Gen. 259, 269–279. https://doi.org/10.1016/j.apcata.2003.09.030

Díez, V.K., Apesteguía, C.R., Di Cosimo, J.I., 2003. Effect of the chemical composition on the catalytic performance of Mg_yAlO_x catalysts for alcohol elimination reactions. J. Catal. 215, 220–233. https://doi.org/10.1016/S0021-9517(03)00010-1

Ebele, A.J., Abou-Elwafa Abdallah, M., Harrad, S., 2017. Pharmaceuticals and personal care products (PPCPs) in the freshwater aquatic environment. Emerg. Contam. 3, 1–16. https://doi.org/10.1016/j.emcon.2016.12.004

Essandoh, M., Kunwar, B., Pittman, C.U., Mohan, D., Mlsna, T., 2015. Sorptive removal of salicylic acid and ibuprofen from aqueous solutions using pine wood fast pyrolysis biochar. Chem. Eng. J. 265, 219–227. https://doi.org/10.1016/j.cej.2014.12.006

Florea, M., Delsarte, S., Keulen, V., Grange, P., 2011. 1-butanol dehydration and dehydrogenation over vanadium aluminium oxynitride catalysts. Rev. Roum. Chim. 56, 151–159.

Gil, A., 2005. Management of the Salt Cake from Secondary Aluminum Fusion Processes. Ind. Eng. Chem. Res. 44, 8852–8857. https://doi.org/10.1021/ie050835o

Gil, A., Albeniz, S., Korili, S.A., 2014. Valorization of the saline slags generated during

secondary aluminium melting processes as adsorbents for the removal of heavy metal ions from aqueous solutions. Chem. Eng. J. 251, 43–50. https://doi.org/10.1016/j.cej.2014.04.056

Gil, A., Korili, S.A., 2016. Management and valorization of aluminum saline slags: Current status and future trends. Chem. Eng. J. 289, 74–84. https://doi.org/10.1016/j.cej.2015.12.069

Gil, A., Taoufik, N., García, A.M., Korili, S.A., 2018. Comparative removal of emerging contaminants from aqueous solution by adsorption on an activated carbon. Environ. Technol. 0, 1–14. https://doi.org/10.1080/09593330.2018.1464066

Gil, A., Vicente, M.A., Korili, S.A., 2005. Effect of the Si/Al ratio on the structure and surface properties of silica-alumina-pillared clays. J. Catal. 229, 119–126. https://doi.org/10.1016/j.jcat.2004.10.013

Guo, H.B., He, F., Gu, B., Liang, L., Smith, J.C., 2012. Time-dependent density functional theory assessment of UV absorption of benzoic acid derivatives. J. Phys. Chem. A 116, 11870–11879. https://doi.org/10.1021/jp3084293

Hayat, Q., Hayat, S., Irfan, M., Ahmad, A., 2010. Effect of exogenous salicylic acid under changing environment: A review. Environ. Exp. Bot. 68, 14–25. https://doi.org/10.1016/j.envexpbot.2009.08.005

Hernández, W.Y., Aliç, F., Verberckmoes, A., Van Der Voort, P., 2017. Tuning the acidic–basic properties by Zn-substitution in Mg–Al hydrotalcites as optimal catalysts for the aldol condensation reaction. J. Mater. Sci. 52, 628–642. https://doi.org/10.1007/s10853-016-0360-3

Iriondo, A., Requies, J., Gu, M.B., Arias, P.L., 2012. Biobutanol Dehydrogenation to Butyraldehyde over Cu , Ru and Ru – Cu Supported Catalysts . Noble Metal Addition and Different Support Effects 50–59. https://doi.org/10.1007/s10562-011-0725-9

Jodeh, S., Abdelwahab, F., Jaradat, N., Warad, I., Jodeh, W., 2016. Adsorption of diclofenac from aqueous solution using Cyclamen persicum tubers based activated carbon (CTAC). J. Assoc. Arab Univ. Basic Appl. Sci. 20, 32–38. https://doi.org/10.1016/j.jaubas.2014.11.002

Johnson, C.A., Glasser, F.P., 2003. Hydrotalcite-like minerals ($M_2Al(OH)_6(CO_3)_{0.5}XH_2O$, where M = Mg, Zn, Co, Ni) in the environment: Synthesis, characterization and

thermodynamic stability. Clays Clay Miner. 51, 1–8. https://doi.org/10.1346/CCMN.2003.510101

Jung, C., Chen, X., Cai, J., Lei, H., Yun, I., Kim, J., 2015. Boundary-preserving stereo matching with certain region detection and adaptive disparity adjustment. J. Vis. Commun. Image Represent. 33, 1–9. https://doi.org/10.1016/j.jvcir.2015.08.010

Khan, A.I., O'Hare, D., 2002. Intercalation chemistry of layered double hydroxides: recent developments and applications. J. Mater. Chem. 12, 3191–3198. https://doi.org/10.1039/B204076J

Kloprogge, J.T., Wharton, D., Hickey, L., Frost, R.L., 2002. Infrared and Raman study of interlayer anions CO_3^{2-}, NO_3^-, SO_4^{2-} and ClO^{4-} in Mg/Al-hydrotalcite. Am. Mineral. 87.

Kyzas, G.Z., Fu, J., Lazaridis, N.K., Bikiaris, D.N., Matis, K.A., 2015. New approaches on the removal of pharmaceuticals from wastewaters with adsorbent materials. J. Mol. Liq. 209, 87–93. https://doi.org/10.1016/j.molliq.2015.05.025

Kyzas, G.Z., Kostoglou, M., 2014. Green adsorbents for wastewaters: A critical review. Materials (Basel). 7, 333–364. https://doi.org/10.3390/ma7010333

Larous, S., Meniai, A.H., 2016. Adsorption of Diclofenac from aqueous solution using activated carbon prepared from olive stones. Int. J. Hydrogen Energy 41, 10380–10390. https://doi.org/10.1016/j.ijhydene.2016.01.096

León, M., Díaz, E., Ordóñez, S., 2011. Ethanol catalytic condensation over Mg-Al mixed oxides derived from hydrotalcites. Catal. Today 164, 436–442. https://doi.org/10.1016/j.cattod.2010.10.003

Li, Q., Meng, M., Tsubaki, N., Li, X., Li, Z., Xie, Y., Hu, T., Zhang, J., 2009. Performance of K-promoted hydrotalcite-derived CoMgAlO catalysts used for soot combustion, NOx storage and simultaneous soot-NOx removal. Appl. Catal. B Environ. 91, 406–415. https://doi.org/10.1016/j.apcatb.2009.06.007

Mahjoubi, F.Z., Khalidi, A., Abdennouri, M., Barka, N., 2016. M-Al-SO_4 layered double hydroxides (M=Zn, Mg or Ni): synthesis, characterization and textile dyes removal efficiency. Desalin. Water Treat. 57, 21564–21576. https://doi.org/10.1080/19443994.2015.1124055

Manivannan, R., Pandurangan, A., 2009. Formation of ethyl benzene and styrene by side chain methylation of toluene over calcined LDHs. Appl. Clay Sci. 44, 137–143. https://doi.org/10.1016/j.clay.2008.12.017

Naseem, S., Gevers, B., Boldt, R., Labuschagné, F.J.W.J., Leuteritz, A., 2019. Comparison of transition metal (Fe, Co, Ni, Cu, and Zn) containing tri-metal layered double hydroxides (LDHs) prepared by urea hydrolysis. RSC Adv. 9, 3030–3040. https://doi.org/10.1039/c8ra10165e

Ni, Z.-M., Xia, S.-J., Wang, L.-G., Xing, F.-F., Pan, G.-X., 2007. Treatment of methyl orange by calcined layered double hydroxides in aqueous solution: Adsorption property and kinetic studies. J. Colloid Interface Sci. 316, 284–291. https://doi.org/10.1016/j.jcis.2007.07.045

Nunes, B., 2019. Acute ecotoxicological effects of salicylic acid on the Polychaeta species Hediste diversicolor: evidences of low to moderate pro-oxidative effects. Environ. Sci. Pollut. Res. 26, 7873–7882. https://doi.org/10.1007/s11356-018-04085-y

Pavel, O.D., Tichit, D., Marcu, I.C., 2012. Acido-basic and catalytic properties of transition-metal containing Mg-Al hydrotalcites and their corresponding mixed oxides. Appl. Clay Sci. 61, 52–58. https://doi.org/10.1016/j.clay.2012.03.006

Petrie, B., Barden, R., Kasprzyk-Hordern, B., 2015. A review on emerging contaminants in wastewaters and the environment: Current knowledge, understudied areas and recommendations for future monitoring. Water Res. 72, 3–27. https://doi.org/10.1016/j.watres.2014.08.053

Pino, M.R., Val, J., Mainar, A.M., Zuriaga, E., Español, C., Langa, E., 2015. Acute toxicological effects on the earthworm Eisenia fetida of 18 common pharmaceuticals in artificial soil. Sci. Total Environ. 518–519, 225–237. https://doi.org/10.1016/j.scitotenv.2015.02.080

Prasanna, S. V., Kamath, P.V., Shivakumara, C., 2007. Synthesis and characterization of layered double hydroxides (LDHs) with intercalated chromate ions. Mater. Res. Bull. 42, 1028–1039. https://doi.org/10.1016/j.materresbull.2006.09.021

Prinetto, F., Ghiotti, G., Giuria, V.P., Durand, R., Tichit, D., 2000. Investigation of Acid - Base Properties of Catalysts Obtained from Layered Double Hydroxides. J. Phys. Chem. B 11117–11126. https://doi.org/10.1021/jp002715u

Rodriguez-Narvaez, O.M., Peralta-Hernandez, J.M., Goonetilleke, A., Bandala, E.R., 2017. Treatment technologies for emerging contaminants in water: A review. Chem. Eng. J. 323, 361–380. https://doi.org/10.1016/j.cej.2017.04.106

Santamaría, L., López-Aizpún, M., García-Padial, M., Vicente, M.A., Korili, S.A., Gil, A., 2020a. Zn-Ti-Al layered double hydroxides synthesized from aluminum saline slag wastes as efficient drug adsorbents. Appl. Clay Sci. 187, 105486. https://doi.org/10.1016/j.clay.2020.105486

Santamaría, L., Vicente, M.A., Korili, S.A., Gil, A., 2020b. Effect of the preparation method and metal content on the synthesis of metal modified titanium oxide used for the removal of salicylic acid under UV light. Environ. Technol. 41, 2073–2084. https://doi.org/10.1080/09593330.2018.1555285

Sato, T. et al., 1988. Synthesis of hydrotalcitye-like compounds and their physico-chemical properties. React. Solids, 5(2–3), 219–228. 5, 219–228. https://doi.org/10.1016/0168-7336(88)80089-5

Schnee, J., Fusaro, L., Aprile, C., Gaigneaux, E.M., 2017. Keggin $H_3PW_{12}O_{40}$ pore blockage by coke can be reversible in the gas phase methanol-to-DME reaction. Catal. Sci. Technol. 7, 6151–6160. https://doi.org/10.1039/C7CY01097D

Tamura, H., Chiba, J., Ito, M., Takeda, T., Kikkawa, S., Mawatari, Y., Tabata, M., 2006. Formation of hydrotalcite in aqueous solutions and intercalation of ATP by anion exchange. J. Colloid Interface Sci. 300, 648–654. https://doi.org/10.1016/j.jcis.2006.04.007

Thomas, G.S., Rajamathi, M., Kamath, P.V., 2004. DiffaX simulations of polytypism and disorder in hydrotalcite. Clays Clay Miner. 52, 693–699. https://doi.org/10.1346/CCMN.2004.0520603

Thommes, M., 2010. Physical adsorption characterization of nanoporous materials. Chemie-Ingenieur-Technik 82, 1059–1073. https://doi.org/10.1002/cite.201000064

Torrellas, S.Á., García Lovera, R., Escalona, N., Sepúlveda, C., Sotelo, J.L., García, J., 2015. Chemical-activated carbons from peach stones for the adsorption of emerging contaminants in aqueous solutions. Chem. Eng. J. 279, 788–798. https://doi.org/10.1016/j.cej.2015.05.104

Valente, J.S., Figueras, F., Gravelle, M., Kumbhar, P., Lopez, J., Besse, J.P., 2000. Basic

properties of the mixed oxides obtained by thermal decomposition of hydrotalcites containing different metallic compositions. J. Catal. 189, 370–381. https://doi.org/10.1006/jcat.1999.2706

Yangali-Quintanilla, V., Maeng, S.K., Fujioka, T., Kennedy, M., Li, Z., Amy, G., 2011. Nanofiltration vs. reverse osmosis for the removal of emerging organic contaminants in water reuse. Desalin. Water Treat. 34, 50–56. https://doi.org/10.5004/dwt.2011.2860

Zhao, Y., Wei, M., Lu, J., Wang, Z.L., Duan, X., 2009. Biotemplated Hierarchical Nanostructure of Layered Double Hydroxides with Improved Photocatalysis Performance. ACS Nano 3, 4009–4016. https://doi.org/10.1021/nn901055d

Chapter IV

Zn-Ti-Al layered double hydroxides synthesized from aluminum saline slag wastes as efficient drug adsorbents

ABSTRACT

This work reports the synthesis of Zinc-Titanium-Aluminum (ZnTiAl) layered double hydroxides (LDH) with various proportions of Al-Ti and a Zn/(Al-Ti) molar ratio of 3:1 by the co-precipitation method. Two series, made with commercial aluminum (Al) and aluminum extracted from saline slags (Al*), have been considered. Structural characterization and comparison of the two series has been made using powder X-ray diffraction (PXRD), Nitrogen physisorption at 77 K, Scanning electron microscopy (SEM), X-ray photoelectron spectroscopy (XPS) and Thermogravimetry measurements. The adsorption capacity of diclofenac and salicylic acid, as examples of emergent pollutants, by the different LDH on batch and fixed-bed column experiments has been analyzed. The effect of various parameters, such as the pH, the initial concentration of pollutant, the mass of adsorbent and the contact time, on the sorption behavior were studied and compared. The contact time to attain equilibrium for maximum adsorption was found to be between 100 – 400 min. The kinetic and equilibrium results were correlated to several adsorption and isotherm equation models. The synthesized materials were more effective in removing diclofenac than salicylic acid, being $Zn_6Al^*_2$ the hydrotalcite that showed the highest adsorption capacity. The results showed a new application of a material obtained from the valorization of an industrial waste such as aluminum saline slags.

IV.1. INTRODUCTION

Secondary aluminum refers to aluminum that is produced from recycled aluminum. The process of recycling aluminum has proven to be very cost-effective as it only uses between 5% and 20% of the energy needed for the production of primary aluminum and emits barely 5% of the greenhouse gas (Krammer, 2011; Tsakiridis, 2012); besides, the savings in raw materials should be taken into account. However, during the secondary aluminum smelting processes, aluminum saline slags are generated. These materials have been classified as hazardous wastes and as such must be deposited in secure deposits as their landfill disposal is forbidden in most European countries (European Waste Catalogue and Hazardous Waste List, 2002). Due to their heterogeneous composition, their applications are limited, with one of the most promising ones being the recovery of aluminum as a high-value-added product (Gil and Korili, 2016).

Non-steroidal anti-inflammatory drugs (NSAIDs) are water pollutants of increasing concern due to its proven presence in wastewater (Luo et al., 2014; Mompelat et al., 2009). Among them, diclofenac and salicylic acid are usually detected in water waste sediments, or even in drinking water samples (Carmona et al., 2014; Vulliet and Cren-Olivé, 2011). Several compounds have different removal efficiencies in wastewater treatment plants (Korma and Lambropoulou, 2014) and a low removal efficiency combined with a high ecotoxicity has resulted in diclofenac to be included in the European Commission's watch-list of substance for monitoring in the field of water policy 2015/495 (2015). Diclofenac in extremely low concentrations, lower than 1 $\mu g/dm^3$, has been proven to change the liver ultrastructure of rainbow trout, to impair osmoregularity ability of a green shore crab and to significantly increase lipid peroxidation of zebra mussel, among other harms (Eades and Waring, 2010; Feito et al., 2012; Haap et al., 2008; Nassef et al., 2010; Quinn et al., 2011; Triebskorn et al., 2007). Salicylic acid was also found to be ecotoxic, although in greater concentrations than diclofenac (Caminada et al., 2006; Ginebreda et al., 2010).

The best ways to remove these toxic and persistent organic compounds from water has been examined with various procedures such as Fenton processes (Bautista et al., 2008), membrane processes (Radjenovic et al., 2008), flocculation (Suarez et al., 2009), photocatalysis (Santamaría et al., 2020) or adsorption (Gil et al., 2019). Adsorption methods are among the most popular due to their low cost, their capacity to adsorb several types of pollutants and their simple and versatile use (Khenniche and Aissani, 2010).

Layered double hydroxides (LDH) are composed of positively charged brucite-like layers with negatively-charged balancing ions in the interlayer regions. They are also known as hydrotalcite-like compounds, because of the structural similarity to the natural occurring Hydrotalcite mineral, with formula $Mg_6Al_2CO_3(OH)_{16}\cdot 4H_2O$. LDH can be easily synthesized in laboratory where Mg^{2+} and Al^{3+} can be substituted for a large variety of Me^{2+} and Me^{3+} metallic cations. Although believed to be synthetic, recent discoveries have found a natural occurring Zn-Al-CO_3 mineral in Italy and Spain (Lozano et al., 2012). LDH are usually used as precursors for fabricating mixed metal oxides (MMO). By calcination at enough temperature, the structure collapses as CO_3^{2-} and H_2O disappear from the interlayer. If the calcination temperature is not excessively high, the resulting solids show, in the presence of water, a significant feature of LDH, the so-called "memory effect", and their original lamellar structure is recovered. In a Zn-Al LDH, zinc aluminum hydroxide hydrate is then formed, where the LDH is intercalated with OH^- as compensating ions in the interlayer (Kikhtyanin et

al., 2017). This new compound has been proven to have unique characteristics such as intercalation, topological transformation and self-assembly (Li et al., 2014) to be used both as adsorbent and catalyst (Goh et al., 2008; Mohapatra and Parida, 2016). The presence of metals in the LDH structure opens the opportunity of new applications and can control/modify the existents. Several investigators have focused their research work on modifying the structure of TiO_2 to make it most sensitive, such as doping with transition metals or other elements (Gil et al., 2017; Santamaría et al., 2020). The incorporation of Ti in the structure of LDH materials can improve the potential of these materials in applications to waste water treatments (Gao et al., 2011; Gomes Silva et al., 2009; Mendoza-Damián et al., 2013; Shao et al., 2011; Xia et al., 2013).

The use of LDH for the removal of pollutants by adsorption has been explored by several groups, mainly focusing their attention on the removal of anionic pollutants, from simple anions (chromate, phosphate, nitrate, arsenate, etc.) to organic contaminants containing at least one anionic group (carboxylate, sulphonate, phosphonate, etc.) such as surfactants, dyes, herbicides, and pesticides (Costantino et al., 2013; Ulibarri et al., 2001). Other strategy involving LDH for the decrease of the amount of contaminants in soils and waters consists on the preparation of controlled-release formulations, which supply fertilizers, plant nutrients, pesticides, and herbicides in agriculture in a more appropriate way (Costantino et al., 2013). This strategy has also been studied for the preparation of controlled-release formulations of medicines (Rives et al., 2014). However, the use of hydrotalcites as adsorbents for the control of emerging pollutants has been less explored. In the particular case of salycilic acid, Silion et al. (2009) have reported its intercalation in LDH solids, and also Haraketi et al. (2016), who studied its controlled release, while Gualandi et al. (2011) have reported its removal by electrocatalytic oxidation using a Pt electrode coated with a Co/Al hydrotalcite, while up to our knowledge, its adsorption by LDH materials from aqueous solutions has been only reported by Elhalil et al. (2018). In the case of diclofenac, its intercalation in LDH has been reported by Heraldy et al. (2016) and San Román et al. (2012), while Ambrogi et al. (2002) studied its controlled release, and Khatem et al. (2015) and Boukhafa et al. (2017) have studied its adsorption from aqueous solutions using these materials.

The main objective of this work was the use of aluminum solutions (Al*) obtained from alkaline extraction of saline slag wastes as aluminum source for the synthesis of ZnAlTi hydrotalcites by a co-precipitation method. Zinc, as the Me^{2+} metallic cation, and a combination of Al-Ti in several proportions, as the Me^{3+} metallic cation, were used. Although

the use of aluminum slags as a source for the preparation of hydrotalcite type solids has been recently explored (Gil and Korili, 2016; Gil et al., 2018), up to our best knowledge the preparation and use of ZnAlTi-LDH from this resource have not been reported elsewhere. Commercial aluminum solutions (Al) were also used for comparison purposes. The synthesized and calcined LDH were then considered as adsorbents for the removal of diclofenac and salicylic acid, as representative compounds of emergent pollutants. This method of preparation of materials and their use may confer an important applicability, not previously reported, to aluminum saline slags.

IV.2. EXPERIMENTAL PROCEDURE

IV.2.1. MATERIALS

The materials used for the synthesis of hydrotalcites were: $Zn(NO_3)_2 \cdot 6H_2O$ (≥98%, Sigma-Aldrich), Na_2CO_3 (≥99.99%, Sigma-Aldrich), $TiCl_3$ (≥12%, Sigma-Aldrich), NaOH (Panreac) for pH adjustment and aluminum extraction, and $Al(NO_3)_3 \cdot 9\ H_2O$ (≥95%, Merck). Salicylic acid, (2-hydroxybenzoic acid, 2-$(HO)C_6H_4COOH$, ≥99.99%, Sigma-Aldrich) and diclofenac sodium salt (2-[(2,6-dichlorophenyl)amino]benzeneacetic acid sodium salt, $C_{14}H_{10}Cl_2NNaO_2$, Sigma-Aldrich) were also used without any modification.

IV.2.2. HYDROTALCITE-LIKE COMPOUNDS SYNTHESIS

Al* was extracted from aluminum saline slags using the following procedure: 5 g of saline slag were added to 100 cm^3 of an aqueous reagent solution (NaOH 2 mol/dm^3) in a reflux system, stirred at 500 rpm and heated to 373 K for 60 min. The slurries were separated by filtration and the aluminum concentration in the solution was determined by ICP-OES and found to be 7.03 g/dm^3.

Hydrotalcites were synthesized on a Zn^{2+}:(Al, Ti)$^{3+}$ 3:1 molar ratio utilizing the co-precipitation method, with aluminum and titanium proportions being modified in the series. As an example, $Zn(NO_3)_2 \cdot 6H_2O$ (0.15 mol/dm^3), Al* (0.0375 mol/ dm^3) and Ti^{3+} (0.0125 mol/ dm^3) were added dropwise to Na_2CO_3 (0.015 mol/ dm^3) to a final volume of 400 cm^3. NaOH was used during the process to adjust the pH to 10. The mixture was stirred at 500 rpm and 333 K for 60 min and aged for 24 h. The slurries obtained were centrifuged at 8000 rpm for 5 min and washed. This process was repeated several times until the washing water achieved a pH of 7. The samples were then dried at 353 K for 16 h, manually grounded with a

mortar and calcined at 673 K for 4 h. The nomenclature used for the samples was $Zn_6Al_xTi_y$, with x+y= 2 to maintain the 3:1 ratio. The same series were synthesized using commercial and extracted aluminum.

IV.2.3. CHARACTERIZATION OF THE ADSORBENTS

The textural properties of the samples (0.4 g) were analyzed by nitrogen (Praxair, 99.999%) adsorption-desorption at 77 K (Micromeritics ASAP 2020 Plus adsorption analyzer). All samples were degassed beforehand at 423 K for 24 h under a pressure lower than 0.1 Pa. The specific surface area (SSA) of the materials was estimated by the Brunauer-Emmer-Teller (BET) method applied to a relative pressure range of 0.05 – 0.20. The external surface area (S_{ext}) and the micropore volumes ($V_{\mu p}$) were also estimated using the t-plot method.

The crystalline phase of the samples was identified by powder X-ray diffraction (PXRD) using a Siemens D-5000 X-ray diffractometer with Ni-filtered Cu Kα radiation (λ = 0.1548 nm) in a 2θ range from 5 to 80° and a scanning rate of 0.2° (2θ)/min.

Scanning electron microscopy (SEM) was used to analyze the morphology of the samples (JEOL, JSM-6400 instrument operating at 20 kV).

X-ray photoelectron spectroscopy (XPS) analyses were carried out on a SPECS Phoibos 150 1DDLD spectrometer equipped with an Al Kα source of 1486.7 eV. The surface adventitious carbon peak, C 1s at 284.8 eV, was used as a reference for all the binding energies. Acquisition parameters and sensibility factors provided by the manufacturer were used to normalize peak areas and calculate surface concentrations (% atomic).

Thermogravimetric measurements were performed on a Hi-Res TGA2950 apparatus (TA-Instruments) using a 10 K/min heating rate from room temperature up to 1173 K under an air atmosphere (60 cm^3/min).

The salt addition method was used to determine the point of zero charge (Bakatula et al., 2018). A 0.01 mol/dm^3 NaCl solution was used as background electrolyte. An equal quantity of background solution (50 cm^3) was apportioned into various flasks kept in series with increasing pH values from 2 to 12. 0.15 g of adsorbent was added to all these flasks and the change in pH of each solution was recorded after shaking the samples for 48 h. This change in pH was plotted against the initial pH values on the graph, and the PZC was identified as the pH when ΔpH = 0.

IV.2.4. ADSORPTION PROCEDURE

IV.2.4.1. Batch experiments

The adsorption of diclofenac and salicylic acid on the hydrotalcites was studied by determining the adsorption isotherms considering previous works of our research group (Gil et al., 2019). The effect of pH was considered up front. Drug solutions (25 μmol/dm^3) were adjusted to a pH range of 2–12 using either HCl or NaOH, placed in a beaker with 50 mg of adsorbent and shaken for 2 h in a stirring plate at room temperature. The dispersions were then filtered (0.45 μmol, Durapore) and the pollutant concentration remaining in the solution was determined by a Jasco V-730 UV-Vis spectrometer at the maximum absorption wavelength, 276 and 297 nm for diclofenac and salicylic acid, respectively.

In the kinetic tests, to study the effect of the drug concentration, 50 mg of adsorbent were added to 250 cm^3 of solutions with drugs in varying concentrations of 25, 50 and 75 μmol/dm^3. The effect of the adsorbent dose was examined by changing the amount of the adsorbent (25, 50 and 100 mg) in solutions with an initial drug concentration of 75 μmol/dm^3. Throughout the duration of the experiments, samples were shaken in a stirring plate and the solution was sampled at various time intervals until equilibrium was achieved, up to 8 h. The quantity of organic compound adsorbed by the hydrotalcites was calculated from the difference between the initial and remaining concentrations according to the following equation:

$$q_{t,e} = \frac{V \cdot (C_0 - C_{t,e})}{m} \qquad \text{Eq. IV.1}$$

where C_0 and C_t (μmol/dm^3) were the initial and final concentrations of organic compound in solution, respectively, V (cm^3) was the volume of the solution and m (g) was the adsorbent mass.

To describe the transport to adsorbates inside adsorbent particles, several kinetic modelling approaches can be considered; in this study pseudo-first- and pseudo-second-order rate equations were applied using OriginPro program (version 9.0) to test the experimental data.

$$\frac{dq}{dt} = k_1 (q_e - q_t)$$ Eq. IV.2

$$\frac{dq}{dt} = k_2 (q_e - q_t)^2$$ Eq. IV.3

where q_e and q_t (μmol/g) were the amounts of solute adsorbed at equilibrium and at a certain time, t, respectively, k_1, and k_2 were the reaction rate constants of pseudo-first and pseudo-second-order rate, respectively. Equations IV.2 and IV.3 are obtained considering mass balances to the liquid phase in the batch system and assuming the kinetic models inducted for the driving force. After integration, the well-known equations for pseudo-first and pseudo-second-order kinetic models are found.

The adsorption capacity of the hydrotalcites in equilibrium was tested by modifying the initial drug concentration. 5 mg of adsorbent were added to glass tubes containing 10 cm^3 of the contaminant solution at initial concentrations between 0 and 1000 μmol/dm^3. The tubes were shaken for 8 h and the concentration of the pollutant remaining in the solution was separated from the solid by filtration and the remaining concentration determined by UV–visible spectrophotometry as in the case of the adsorption kinetic experiments. The amount of organic compound adsorbed per unit mass of adsorbent at equilibrium was determined according to Eq. (IV.1), where C_e (μmol/dm^3) was the concentration of that compound at equilibrium.

The equilibrium experimental data obtained were used to better interpret the interactive behavior between solutes and adsorbents, considering three equilibrium adsorption isotherms: Freundlich, Langmuir and Toth.

$$q_e = k_F \cdot C_e^{1/m_F}$$ Eq. IV.4

$$q_e = \frac{k_L \cdot q_L \cdot C_e}{1 + k_L \cdot C_e}$$ Eq. IV.5

$$q_e = \frac{k_T \cdot q_T \cdot C_e}{[1 + (k_T \cdot C_e)^{m_T}]^{1/m_T}} \qquad \text{Eq. IV.6}$$

where q_e (µmol of adsorbate/g of adsorbent) was the amount adsorbed, C_e (µmol/g) was the monolayer capacity, k_i the equilibrium constant (k_F) or the binding affinity (k_L, k_T) and m_i characterized the mobility of the molecules adsorbed and the heterogeneity of the system.

The adsorption process in porous adsorbents was also examined with the estimation of the effective diffusion coefficient by applying a fractional approach to the equilibrium, *F(t)* (Khraisheh et al., 2002):

$$F(t) = \frac{C_0 - C_t}{C_0 - C_e} = \sqrt{1 - exp\left(-\frac{\pi^2 D t}{r^2}\right)} \qquad \text{Eq. IV.7}$$

where D (m^2/s) is the intraparticle-diffusion coefficient and r (m) is the particle size radius assuming a perfect sphere.

IV.2.4.2. Fixed-Bed adsorption experiments

The breakthrough curves of diclofenac and salicylic acid were performed on a column of 2 cm in diameter and 12 cm long packed with silicon carbide (0.5 mm) and 25 mg of hydrotalcites, in order to complete the volume and avoid dead volume. A solution containing 20 µmol/dm^3 of the organic molecules was fed at a flow of 0.2 cm^3/min using a peristaltic pump (Ecoline VC-380) in down-flow mode. The effluent from each column was collected at various time intervals up to 120 minutes and the amount of remaining pollutants was quantified by means of ultraviolet-visible absorption spectrophotometry, as previously described for the batch experiments. The results were adjusted to the Thomas model which allows for a simple interpretation of the behavior inside the column. This model takes into account only direct adsorption in the unused capacity of the adsorbent and ignores the intraparticle mass transfer resistance and the external resistance (i.e. the adsorbate adsorbed onto the solid surface directly) (Poulopoulos and Vassilis, 2006).The non-linearized Thomas equation (Thomas, 1944) can be expressed as follows:

$$\frac{C_t}{C_0} = \frac{1}{1 + \exp(\frac{k_{Th} q_{ads} m}{Q} - k_{Th} C_0 t)}$$ Eq. IV.8

where C_0 (μmol/dm^3) and C_t (μmol/dm^3) were the influent and effluent adsorbate concentration, respectively, at a time t, m was the mass of the adsorbent (g), Q was the volumetric flow rate (cm^3/min), k_{Th} (cm^3/min·μmol) was the Thomas rate constant and q_{ads} (μmol/g) was the equilibrium adsorbate uptake per g of the stabilized system.

IV.3. RESULTS AND DISCUSSION

IV.3.1. HYDROTALCITES CHARACTERIZATION

The powder X-ray diffraction patterns of the non-calcined and calcined samples can be seen in Figure IV.1. First, a study was conducted on how pH could affect the synthesis of the hydrotalcite. The relevance of the pH throughout the synthesis is shown in Fig. IV.1a, when keeping the pH stable at 10 during the process, a layered double hydroxide type structure was formed (marked as 1). A no crystalline structure or a mixture of hydrotalcite and zincite (ZnO, marked as 2) was found when the synthesis pH was lower (pH = 5) or higher (pH = 12) than 10. When calcined, the structure collapsed and zincite appeared at pH 10 and 12 (see Figure IV.1b).

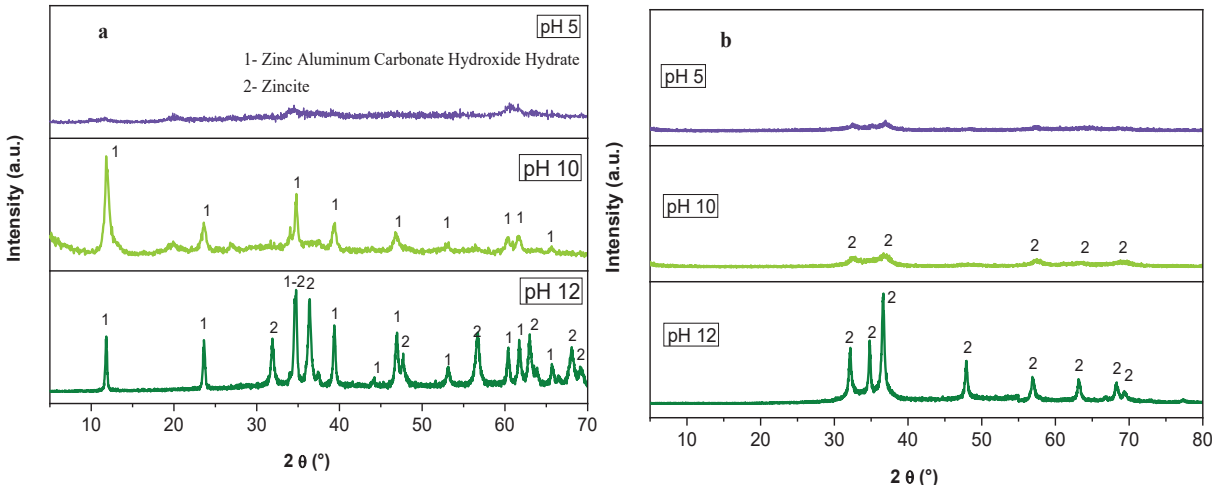

Figure IV.1. Powder X ray diffraction patterns of non-calcined (a) and calcined (b) samples synthesized at various pH values.

PXRD diffraction patterns of the non-calcined samples synthesized from commercial aluminum (Al) and extracted aluminum (Al*) were compared in Figures IV.2a and IV.3a. The crystallinity decreased with the increase of the titanium content and no diffraction reflections corresponding to titanium compounds were observed in the XRD patterns, suggesting that titanium was incorporated into the octahedral positions of the LDH or well dispersed into the LDH structure. The distinct basal (003) reflection, characteristic of hydrotalcite-like materials, was found at around 11.7°. The *c* parameter was calculated using the reflection (003) values, $c = 3d_{003}$, with *c* corresponding to three times the basal value (see Table IV.1). Several factors can affect the *c* parameter (Mendoza-Damián et al., 2013). The results found in this work can be related to the effect of the substitution of Al^{3+} by titanium, modifying the interaction between the brucite-like layer and the interlayer. *d* had a value of around 0.76 nm in the four

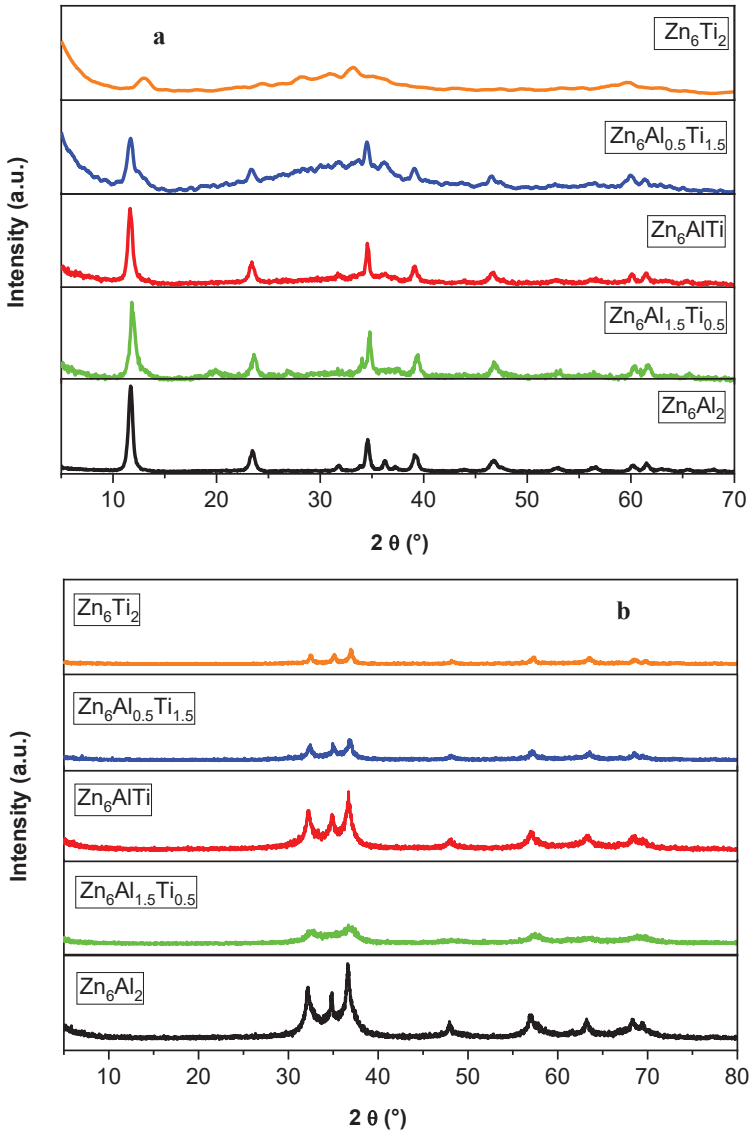

Figure IV.2. Powder X ray diffraction patterns of non-calcined (a) and calcined (b) samples synthesized with commercial aluminum.

first samples which accorded well to other experimental results for ZnAl-LDH with carbonated anions (Fraccarollo et al., 2010).In the case of Zn_6Ti_2, the small basal value suggested that the hydrotalcite structure was not properly formed. From the experimental results obtained, both series of hydrotalcites synthesized were similar between them, with more defined hydrotalcite patterns when there was more aluminum in the sample. After calcination at 673 K, the structure was destroyed and zincite was found in all the cases (see Figures IV.2b and 3b, for Al and Al* samples). No diffraction reflections corresponding to TiO_2 phases, anatase or rutile, were observed suggesting a high dispersion of the oxides or a low crystallinity. To test the memory effect, a study with the sample $Zn_6Al^*_2$ has been considered (see Figure IV.4).

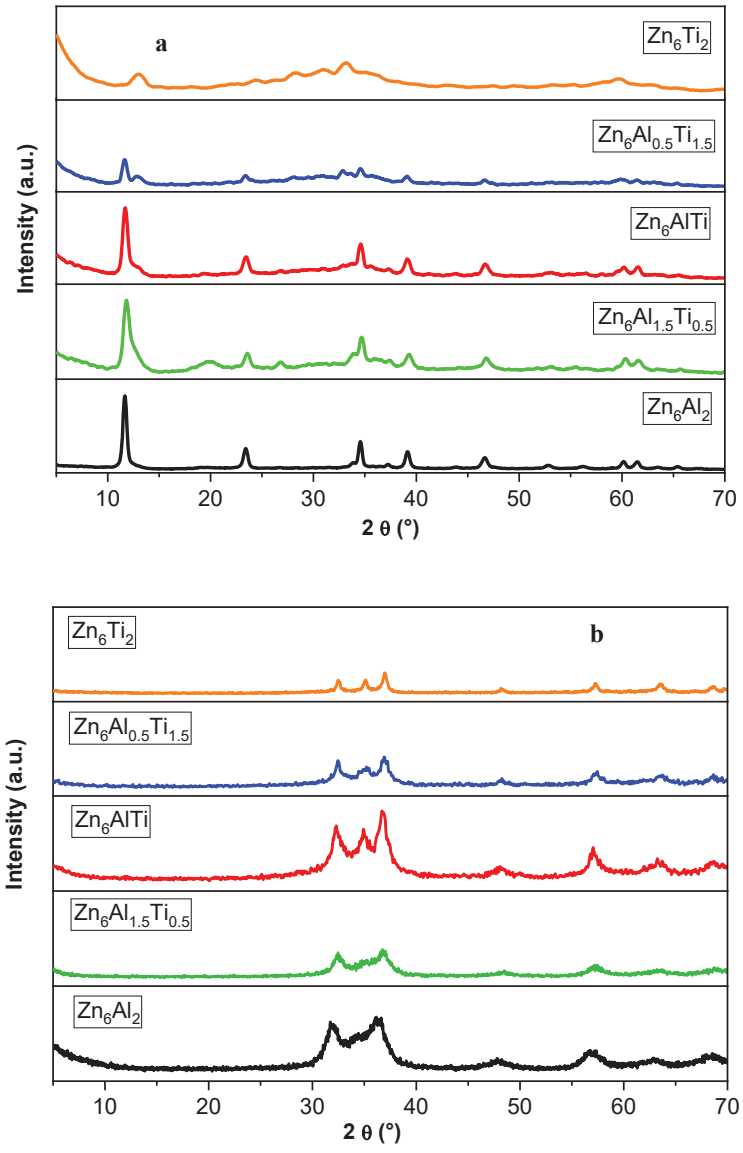

Figure IV.3. Powder X ray diffraction patterns of non-calcined (a) and calcined (b) samples synthesized with extracted aluminum.

The calcined sample $Zn_6Al^*_2$ was submerged in water for 2 h, dried at 353 K and the hydrotalcite structure (marked as 1) was recovered, but a part of zincite (marked as 2) also remained (see Fig. IV.4c). The elimination of the carbonates in the rehydration experiment lowered the basal value from 0.761 to 0.734 nm (see Table IV.1).

Table IV.1. Basal value and interlayer distance of Al* LDH series.

Sample	d(003) (nm)	*c* (nm)	Interlayer height(nm)
$Zn_6Al^*_2$	0.761	2.286	0.291
$Zn_6Al^*_{1.5}Ti_{0.5}$	0.752	2.255	0.281
Zn_6Al^*Ti	0.757	2.270	0.286
$Zn_6Al^*_{0.5}Ti_{1.5}$	0.761	2.282	0.290
Zn_6Ti_2	0.686	2.059	0.215
Rehydrated $Zn_6Al^*_2$	0.734	2.208	0.263
Rehydrated $Zn_6Al^*_2$ with diclofenac	1.097-0.746	3.291-2.238	0.626-0.275

Considering the thickness of the host layer to be 0.471 nm (Conterosito et al., 2013), that left the interlayer space, occupied by hydroxides in 0.263 nm as opposed to 0.291 nm when the interlayer contained carbonates. An aqueous solution of 25 μmol/dm^3 of diclofenac and 1 g/dm^3 of calcined $Zn_6Al^*_2$ were also combined for 2 h and the XRD pattern showed a new distinctive reflection appearing at 8.05º (2θ degrees) (see Fig. IV.4d), corresponding to an interlayer height of 0.626 nm.

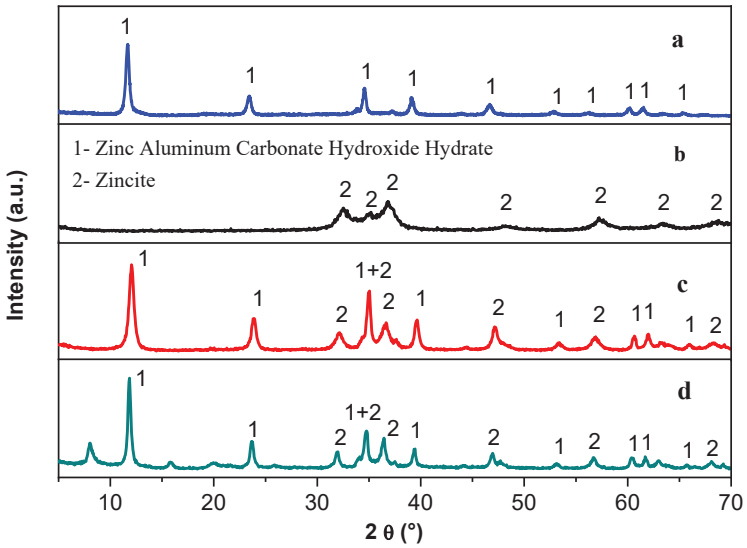

Figure IV.4. Memory effect of $Zn_6Al^*_2$ hydrotalcite. Non-calcined (a), calcined (b), rehydrated (c) and rehydrated with diclofenac (d).

The size of diclofenac was between 0.766 and 0.957 nm, thus the molecules were likely to be intercalated in an almost horizontal position between the layers (Brindley and Kao, 1984).

In order to further study the morphology of the samples, SEM analysis of the materials was performed (see Figure IV.5).

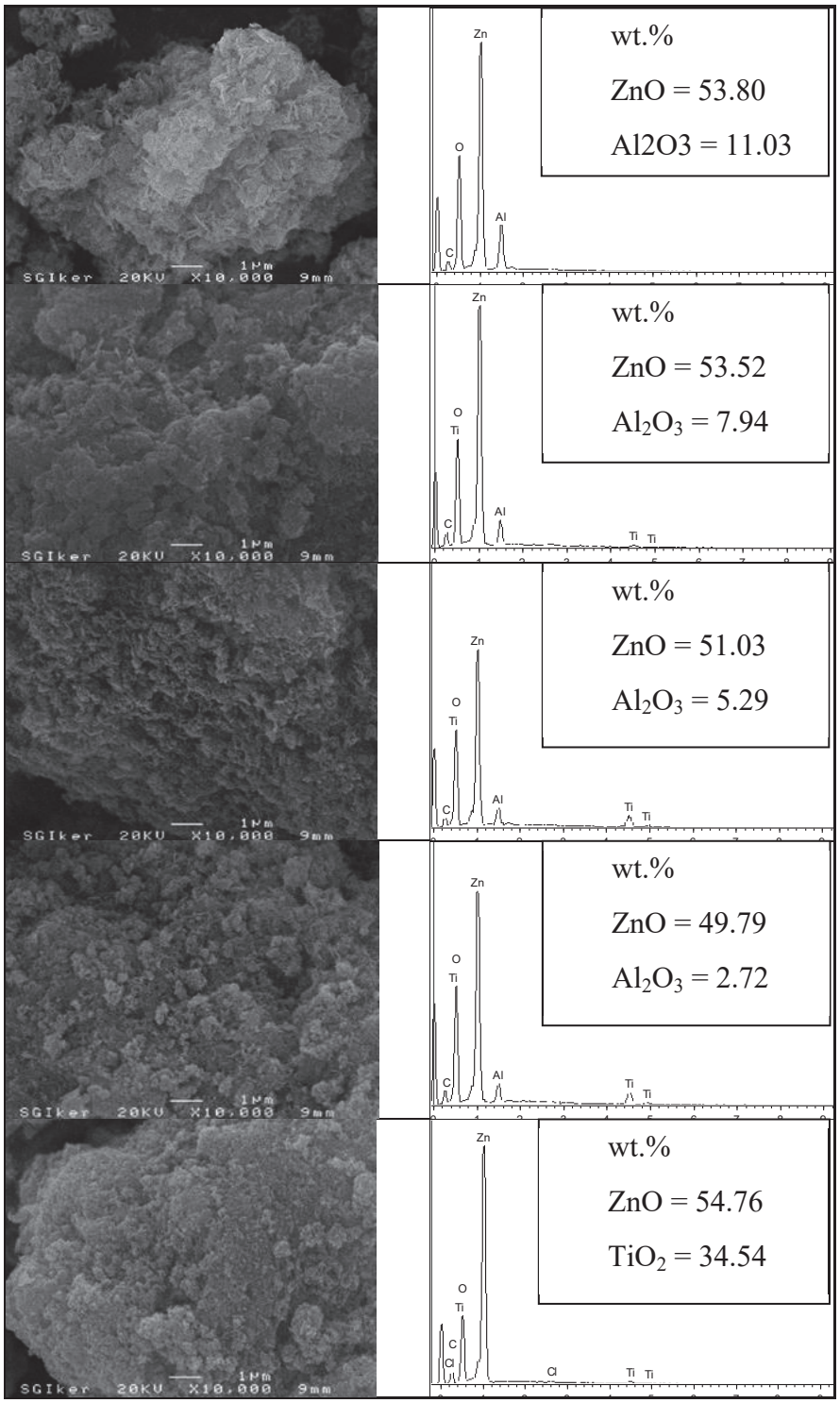

Figure IV.5. SEM micrographs and EDX analysis of $Zn_6Al^*_2$ (a), $Zn_6Al^*_{1.5}Ti_{0.5}$ (b), Zn_6AlTi (c), $Zn_6Al_{0.5}Ti_{1.5}$ (d) and Zn_6Ti_2 (e) samples.

The characteristic flat structure with sharp edges evidenced that the layered structure remained after calcination, as reported elsewhere (Castro et al., 2011; Xie et al., 2006). The release of water and CO_2 and their replacement by hydroxyl groups did not drastically affect the crystal structure of the LDH. The addition of Ti^{3+} caused morphological modifications of the samples. As the proportion of titanium increased, the layered flat structure gradually disappeared to form rounder particles which were the only ones remaining in the Zn_6Ti_2 sample. These results were in accord to the XRD patterns. EDX analyses were also performed to determine the composition of the samples. No impurities were observed, however chlorine was found because titanium source was $TiCl_3$.

The N_2 adsorption-desorption isotherms of dried and calcined samples are presented in Figure IV.6. According to the IUPAC classification, type II adsorption isotherms were observed in all the samples, related to the presence of nonporous or macroporous adsorbents. They all had a type H3 hysteresis loop, typical of non-rigid aggregates of plate-like particles (Thommes et al., 2015) with slit-shaped pores of non-uniform size and shape (Lowell et al., 2004).

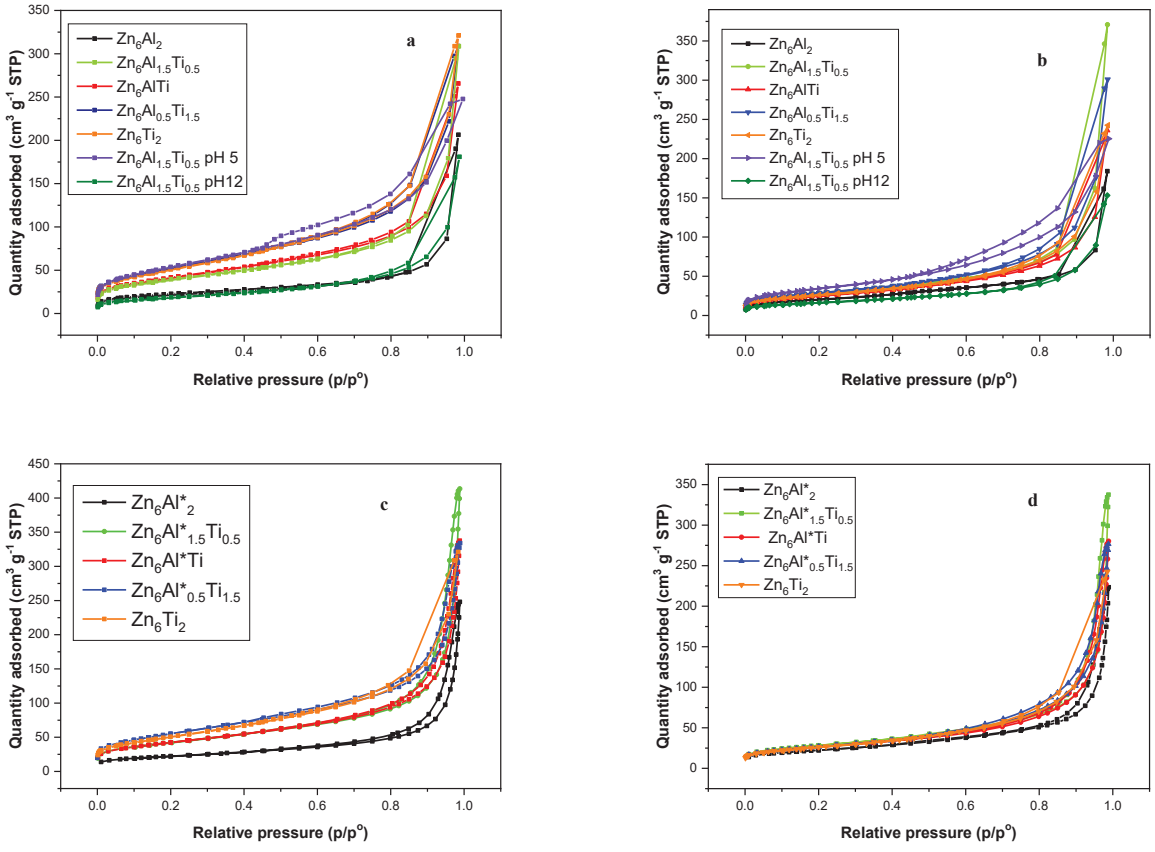

Figure IV.6. The nitrogen adsorption-desorption isotherms of non-calcined (a) and calcined (b) Al series and non-calcined (c) and calcined (d) Al* series of LDH.

For the Al series (see Table IV.2), the maximum value of SSA corresponded to the sample made at pH = 5, while the minimum value corresponded to the sample obtained at pH = 12. For the samples synthesized at pH = 10, the nitrogen monolayer volume increased with the addition of titanium: Zn_6Al_2 sample has a S_{BET} of 81 m^2/g, when titanium was incorporated the SSA went up to between 142 and 190 m^2/g. Similar results were found for the Al* series (see Table IV.3). The results of external SSAs and micropore volumes confirm the non-porous character of the samples. Since the N_2 diameter is larger than the interlayer space for carbonate containing layered double hydroxides, the SSA measured by this method corresponded to the surface area.

Table IV.2. Textural properties of the series synthesized with commercial aluminum.

Sample	S_{BET} (m^2/g)	S_{ext} (m^2/g)	$V_{\mu p}$ (cm^3/g)	S_{BET} (m^2/g)	S_{ext} (m^2/g)	$V_{\mu p}$ (cm^3/g)
	Non calcined			*Calcined*		
n_6Al_2 pH10	81	61	0.0079	73	73	0
Zn_6AlTi pH10	150	141	0.0025	91	89	0.0002
Zn_6 $Al_{0.5}Ti_{1.5}$ pH10	190	184	0.0008	104	104	0
Zn_6 Ti_2 pH10	184	184	0	95	95	0
$Zn_6Al_{1.5}Ti_{0.5}$ pH10	142	125	0.0061	103	95	0.0030
$Zn_6Al_{1.5}Ti_{0.5}$ pH5	196	196	0	126	126	0
$Zn_6Al_{1.5}Ti_{0.5}$ pH12	67	65	0.0006	59	58	0.0004

Table IV.3. Textural properties of the series synthesized with extracted aluminum.

Sample	S_{BET} (m^2/g)	S_{ext} (m^2/g)	$V_{\mu p}$ (cm^3/g)	S_{BET} (m^2/g)	S_{ext} (m^2/g)	$V_{\mu p}$ (cm^3/g)
	Non calcined			*Calcined*		
$Zn_6Al^*_2$ pH10	78	69	0.0045	79	69	0.0046
$Zn_6Al^*_{1.5}Ti_{0.5}$ pH10	152	145	0.0027	100	91	0.0041
Zn_6Al^*Ti pH10	152	148	0.0013	93	86	0.0029
$Zn_6Al^*_{0.5}Ti_{1.5}$ pH10	199	199	0	95	89	0.0023
Zn_6Ti_2 pH10	184	184	0	95	95	0

A well-defined hydrotalcite had better crystallinity and bigger particles, whereas poor crystalline samples were usually formed by smaller particles, where interactions between

particles were bigger, thus increasing the total surface (Albiston et al., 1996; Benito et al., 2006). Surface areas of LDH prepared with Al and Al* were in the same order, the maximum difference was found in $Zn_6Al_{1.5}Ti_{0.5}$: 142 m^2/g in the sample with Al and 152 m^2/g in the sample with Al*. When the samples were calcined, the SSA was decreased in all cases, except in Zn_6Al_2*sample. The samples synthesized at pH = 10 went from a range of 142-190 m^2/g to a range of 91-104 (Al) and from 152-199 m^2/g to 93-100 m^2/g (Al*). The SSA were more homogeneous after calcination. This surface decrease has been reported before (Hadnadjev-Kostic at el., 2013) as various types of LDH respond diversely to calcination (Cavani and Trifiro, 1991).

The thermogravimetric analysis of $Zn_6Al_2CO_3(OH)_{16} \cdot 4H_2O$ has been reported by several authors (Frost et al., 2005; Theiss et al., 2013), with similar results to the samples included in this work (see Figure IV.7). Five mass loss steps were observed and the results were summarized in Table IV.4.

Table IV.4. Mass losses (%) in the steps indicated from the thermogravimetric analyses of the LDH series.

Sample	1	2	3	4	5	TOTAL (%)
Zn_6Al_2	0-373 K	373-473 K	473-673 K	673-923 K	923-1123 K	
	2.2	12.0	13.1	2.9	1.1	31.52
$Zn_6Al_{1.5}Ti_{0.5}$	0-383 K	383-458 K	458-673 K	673-923 K	923-1123 K	
	5.1	6.0	15.1	2.0	0.6	28.87
Zn_6AlTi	0-403 K	403-673 K	448-673 K	673-923 K	923-1123 K	
	3.0	4.6	13.17	2.0	0.6	23.09
$Zn_6\ Al_{0.5}Ti_{1.5}$	0-373 K	373-448 K	448-673 K	673-923 K	923-1123 K	
	2.3	4.2	12.2	1.5	0.3	21.12
$Zn_6\ Ti_2$	0-473 K		473-698 K	698-923 K	923-1123 K	
	11.5		10.37	1.4	1.1	24.46

The first two mass losses, at less than 373 K and around 423 K, corresponded to the loss of water. Step 1 was associated with adsorbed water and step 2, always bigger than step 1, to the loss of interlayer water. The mass of water in Zn_6Al_2 was equal to 14.2%, with 12% in the form of interlayer water, which diminished in the series as the amount of titanium was increased. In the sample Zn_6Ti_2 water loss steps 1 and 2 were combined into one located around 373 K. This was due to the poor crystallinity of the sample, the hydrotalcite structure

was limited thus there was no interlayer water. The third step, located at around 523 K, was the most intense in all the cases with the exception of Zn_6Ti_2. This step corresponded to a combination of dehydroxylation and decarbonation which, in the case of the sample without titanium, can be proposed as:

$$Zn_6Al_2CO_3(OH)_{16} \rightarrow Zn_6Al_2O_8CO_3 \rightarrow 6ZnO \bullet Al_2O_3$$

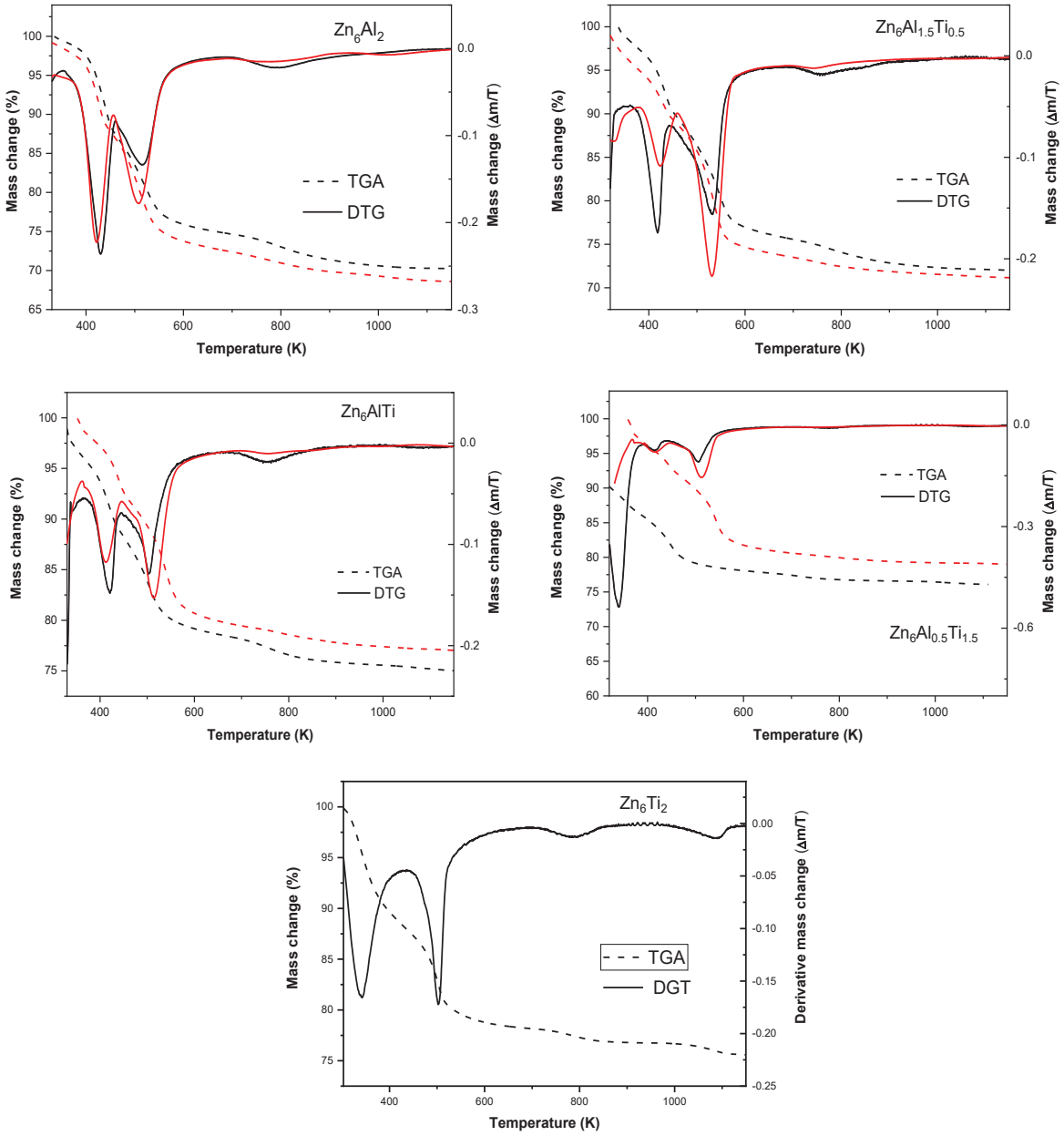

Figure IV.7. TG and DTG curves of the LDH prepared from commercial aluminum (black) and extracted aluminum (red).

Step 4 and 5 were quite small and usually interpreted as the further decomposition of the mixed metal oxide. Results in the series prepared with Al* *vs* the series with Al were close, with a bigger percentage of water loss in samples with commercial aluminum and, consequently, a smaller one in dehydroxylation/decarbonation. Impurities brought with aluminum, which slightly decreases the crystallinity of the samples, could be responsible for a smaller interlayer surface.

XPS analysis were conducted to study the chemical states on the surface of the five samples with Al* and to further analyze the structure variation when Ti^{3+} was introduced. The main differences in the XPS spectra of the samples (Figure IV.8) can be found in the peaks for Al* and Ti. The surface concentration (% atomic) and elemental formula of the samples (see Table IV.5) were close to predictions, with a slight increase in the amount of aluminum.

Table IV.5. Surface concentration (% atomic) and proposed elemental formula of the calcined compounds on the surface of the LDH.

	Zn	Al	O	Ti	Proposed formula
$Zn_6Al^*_2$	25.6	10.4	55.9	--	$Zn_6Al^*_{2.4}$
$Zn_6Al^*_{1.5}Ti_{0.5}$	25	8.6	56	1.5	$Zn_6Al^*_{2.1}Ti_{0.4}$
Zn_6Al^*Ti	25.8	5.2	56.5	4.4	$Zn_6Al^*_{1.2}Ti_{1.0}$
$Zn_6Al^*_{0.5}Ti_{1.5}$	26.8	3.1	55.1	5.9	$Zn_6Al^*_{0.7}Ti_{1.3}$
Zn_6Ti_2	26.5	--	56.1	9	$Zn_6Ti_{2.0}$

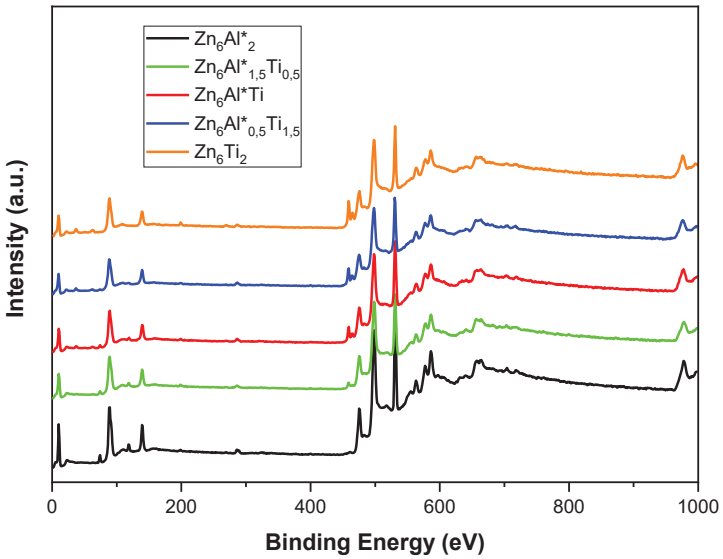

Figure IV.8. XPS spectra for the Al* calcined series.

High resolution spectra of Zn 2p, O 1s, Al 2p and Ti 2p were shown in Figure IV.9. Core level O 1s spectra were displayed in Figure. IV.9b. After the spectra deconvolution of Zn_6Al_2* three peaks were detected: O-metal at 531.14 eV bound to metal cations of the structure, hydroxide at 532.24 eV could appear due to a weak bonded surface oxygen and in the form of adsorbed water at 533.04 eV (Lu et al., 2012; Wang et al., 2015). As titanium was introduced in the structure, O 1s peaks shifted towards lower binding energies, this was due to two factors: the appearance of a Ti-O bond located at 530 eV (Moulder, 1992) moved towards the left the O-metal peak, and the decrease of adsorbed water in the interlayer made hydrotalcite structure less defined and reduced the peak located at the right. Zinc $2p_{3/2}$ (Figure IV.9a) peak was located in all cases near 1022 eV, and corresponded to ZnO (Xiong et al., 2019). There was no direct bond between zinc and titanium as no significant shift was found when titanium was introduced in the samples. Ti 2p (Figure IV.9d) spectra showed how the intensity of the peaks increased with titanium proportion. Deconvolution of Zn_6Ti_2 formed two peaks at $2p_{3/2}$ corresponding to Ti^{4+} (459.1 eV) and Ti^{3+} (457.2 eV) and another two peaks at $2p_{1/2}$ at 464.8 and 463.0 eV for Ti^{4+} and Ti^{3+}, respectively. The molar percentage was calculated to be 14.7% of Ti^{3+} with Ti^{4+} accounting for the rest.

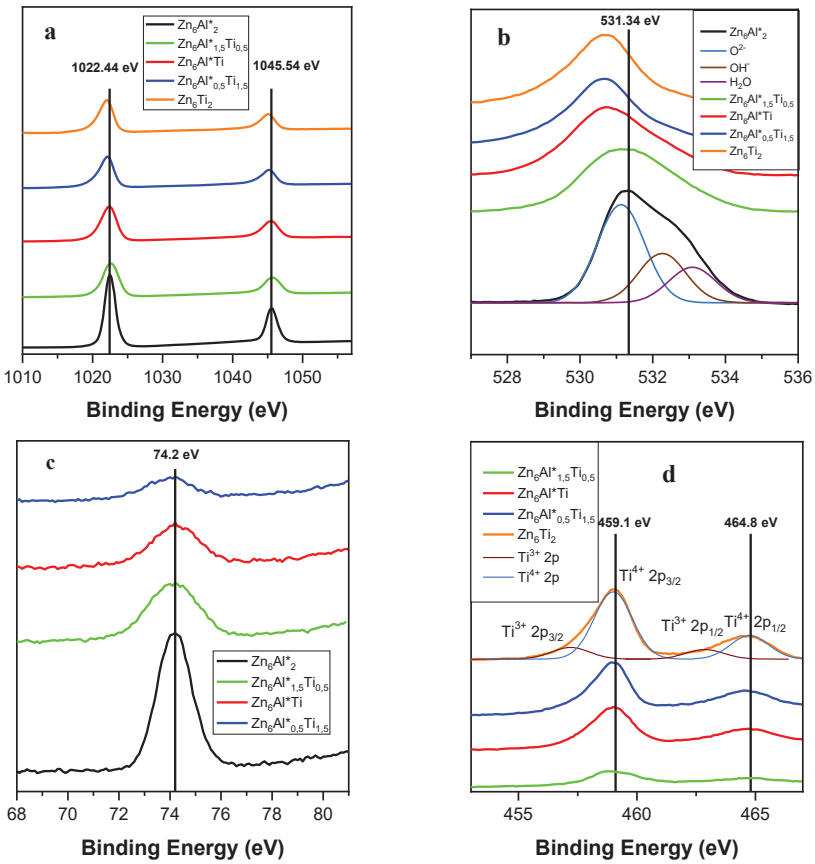

Figure IV.9. XPS spectra of Zn 2p (a), O 1s (b), Al 2p (c) and Ti 2p (d) of the calcined Al* series.

IV.3.2. ADSORPTION EXPERIMENTS

IV.3.2.1. Batch adsorption results

The adsorption process depended on several factors such as the pH of the solution, the adsorbent dose and the drug concentration. The pH effect was studied up front (Table IV.6). The best pH values for the adsorption of diclofenac and acid salicylic were 4.2 and 2.7, respectively, which were the pH of the aqueous solutions without any modification. For that reason, these pH values were chosen for the experiments. It was inferred from the Table that the more basic the pH was, the less amount of drugs was adsorbed.

Table IV.6. $Zn_6Al^*_2$ adsorption data at various pH values.

pH	q_t (diclofenac) (µmol/g)	pH	q_t (salicylic acid) (µmol/g)
		2	3
2	unstable	**2.7**	19
4.2	108	**4**	13
6	72	**6**	4
8	40	**8**	0.4
10	no adsorption	**10**	no adsorption

The kinetic adsorption data for diclofenac and salicylic acid, respectively, on four hydrotalcites considering several drug concentrations and adsorbent amounts are presented in Figures IV.10 and IV.11. Sample Zn_6Ti_2 was not capable of adsorbing any of the anti-inflammatory drugs. The effect of the adsorbent was studied (first columns of Figures IV.10 and IV.11), considering several quantities: 25, 50 and 100 mg of adsorbent in 0.25 dm^3 of water and 75 µmol/dm^3 of drug. The experiments on diclofenac showed the decrease of the adsorption capacity with the increase of adsorbent concentration. This might be due to the partial overlapping or aggregation of adsorption sites when the amount of adsorbent was raised, which produced a reduction in the available specific surface area (Gil et al., 2019). There was a great difference in the adsorption capacity between the samples. With a 100 mg/dm^3 concentration of adsorbent, its adsorption capacity ranged from 38 µmol/g in $Zn_6Al^*_{0.5}Ti_{1.5}$ to more than 409 µmol/g in $Zn_6Al^*_2$. In the case of salicylic acid, the adsorption capacity also changed, from 7 µmol/g ($Zn_6Al^*_{0.5}Ti_{1.5}$) to 80 µmol/g ($Zn_6Al^*_2$). The results when the initial drug dose was modified were shown in the second columns.

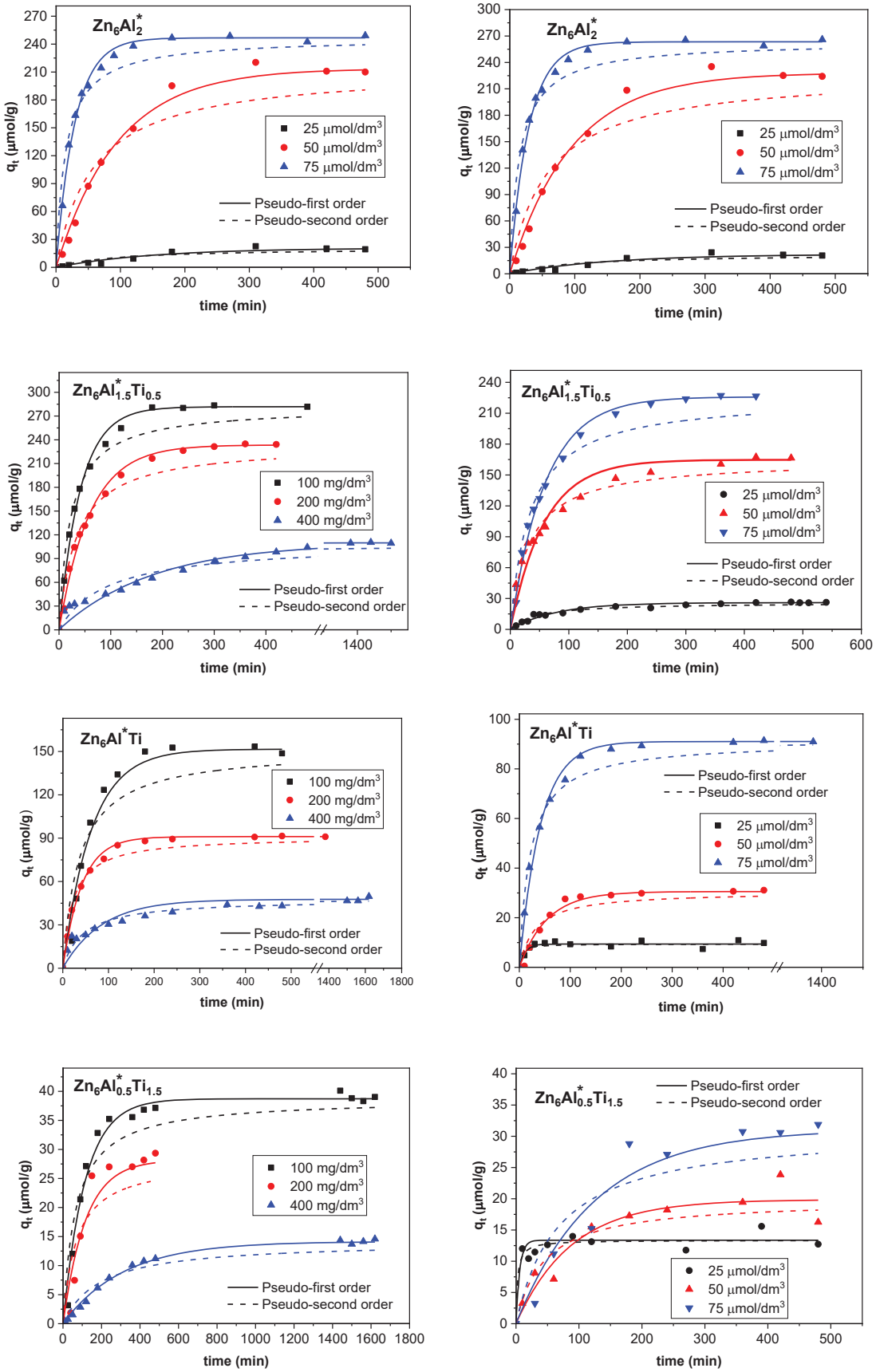

Figure IV.10. Kinetic data for diclofenac adsorbed on $Zn_6Al^*_2$ (first range), $Zn_6Al^*_{1.5}Ti_{0.5}$ (second range), Zn_6Al^*Ti (third range) and $Zn_6Al^*_{0.5}Ti_{1.5}$ (fourth range) with different amounts of adsorbent (first column) and different drug concentrations (second column). Adjustments to pseudo-first and second order models are also shown.

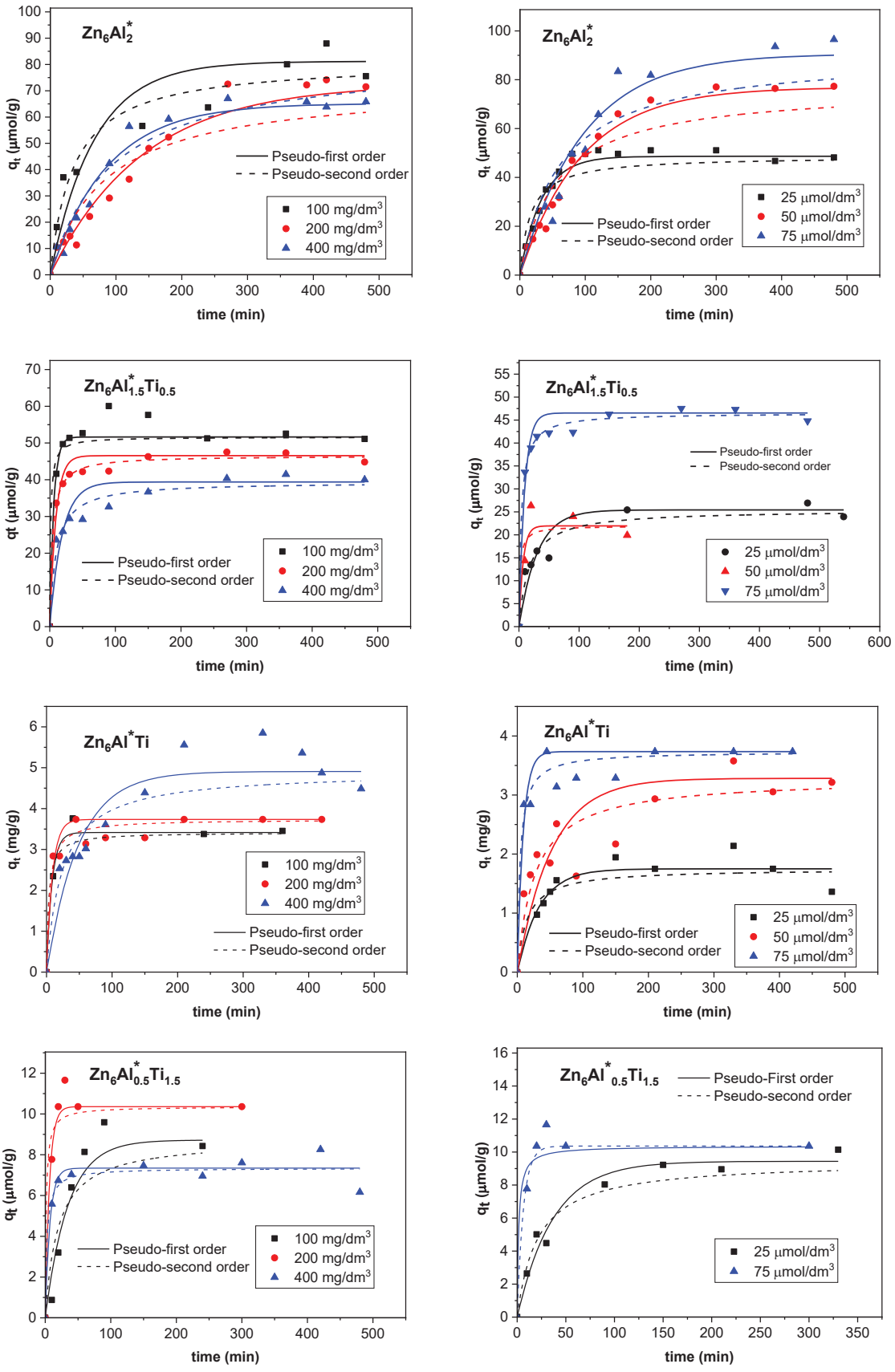

Figure IV.11. Kinetic data for salicylic acid adsorbed on $Zn_6Al^*_2$ (first range), $Zn_6Al^*_{1.5}Ti_{0.5}$ (second range), Zn_6Al^*Ti (third range) and $Zn_6Al^*_{0.5}Ti_{1.5}$ (fourth range) with different amounts of adsorbent (first column) and different drug concentrations (second column). Adjustments to pseudo-first and second order models are also shown.

The quantities of diclofenac and salicylic acid considered ranged from 25 to 75 μmol/dm^3 and the amount of adsorbent was 50 mg, i.e. 200 mg/dm^3, in all the experiments. In this case, an increase in the initial drug dose favored its adsorption. This was because each adsorbent had the capacity to adsorb a fixed amount of adsorbate species. Until this amount was reached, an increase in the adsorbate concentration meant an increase in the adsorption capacity of the adsorbate. Comparing the adsorbates, the diclofenac adsorption capacity of $Zn_6Al^*_2$ was the greatest (more than 250 μmol/g with a 75 μmol/dm^3 initial dose of adsorbate) and went down until 30 μmol/g for $Zn_6Al^*_{0.5}Ti_{1.5}$. For the salicylic acid, these amounts went from 87 to 10 μmol/g, respectively.

The capacity of the samples to adsorb diclofenac and salicylic acid can be explained by means of the point of zero charge values (7.5 – 7.7). A pH below the pH_{pzc} meant that the net charge of the adsorbent was positive and a pH above the pH_{pzc} the adsorbent was charged negatively. At the pH of the experiments (2.7 for salicylic acid and 4.2 for diclofenac) the adsorbents had a net positive charge in their surface. It has been proven that in both the salicylic acid and diclofenac adsorption a hydrogen bond between the COO^- and the hydroxyl groups occurred (Mosangi et al., 2016; Xiong et al., 2019), which can be responsible for overcoming the small electrostatic barrier. Considering the quantity of drug adsorbed, the amount of diclofenac adsorbed by the four studied hydrotalcites was higher than that for salicylic acid. Salicylic acid (see Table IV.7) had a benzene ring attached to a hydroxyl group and, adjacent to it, a –COOH group was present. Being the carboxylic group an electron withdrawing group, it pulled electrons toward itself and forced the adjacent hydroxyl group to give up its electron and to get as proton released. This intramolecular hydrogen bond made salicylic acid less prone to bond with the adsorbent.

The adsorption capacity of the LDH decreased as titanium was incorporated into the structure. This was to be expected as the addition of titanium worsened the LDH structure (see PXRD and SEM results, Figures IV.3 and IV.5) and less hydroxyl groups were found (see XPS results, Figure IV.9). The possible effect of the micropores can be considered negligible from the micropore volumes estimated for these samples.

Table IV.7. General characteristics of the pharmaceutical drugs adsorbed.

	Diclofenac sodium	**Salicylic acid**
Molecular structure	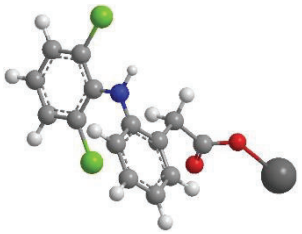	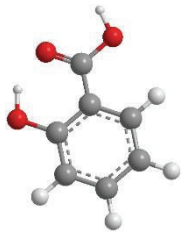
IUPAC name	Sodium; 2-(2-(2,6-Dichloranilino) phenyl)acetate	2-Hydroxybenzoic acid
Chemical formula	$C_{14}H_{10}Cl_2NNaO_2$	$C_7H_6O_3$
Molecular mass	318.13	138.12
pK_a	4.15	2.97; 13.6
λ_{max}	276	297

Pseudo-first- and pseudo-second-order rate equations were applied to the experimental data of Figures IV.10 and IV.11, and k_1 and k_2 values are shown in Tables IV.8 and IV.9. In order to test the best correlation of the experimental data, chi-square (χ^2) and the coefficient of determination (R) were used. It seemed that the inclusion of data close to, or at, equilibrium to determine the best kinetic formula have introduced a methodological bias that has promoted pseudo-second-order kinetics as the number one model (Simonin, 2016). For this reason, sample collection was stopped once the equilibrium was achieved. The results thus revealed that the adsorption of both drugs can be best described as a pseudo-first-order linear reaction. When comparing k_1 values results, they were in accord to the experimental data, that is, k_1 constant increased with the increase of the initial drug concentration and decreased as the adsorbent concentration increased from 100 mg/dm^3 to 400 mg/dm^3. The preference of any adsorbate to link to high energy sites, when available, resulted in faster reaction kinetics and, as these sites were occupied, lower energy ones will be taken which decelerated the process and could explain the evolution of the k_1 constants (Chu, 2002). The estimated effective diffusion coefficients (Table IV.10) indicated that the intraparticle diffusion had a low effect on the adsorption of diclofenac and salicylic acid by the ZnTiAl LDH. As a general effect, it was found that the diffusion coefficient decreased when the amount of adsorbent increased and tended to increase with the concentration of the pollutant used.

Table IV.8. Pseudo-first-order adjustment of the experimental results.

Sample		Diclofenac					Salicylic acid				
		100 mg/dm^3 75 μM	200 mg/ dm^3 75 μM	400 mg/dm^3 75 μM	200 mg/dm^3 25 μM	200 mg/dm^3 50 μM	100 mg/dm^3 75 μM	200 mg/ dm^3 75 μM	400 mg/dm^3 75 μM	200 mg/dm^3 25 μM	200 mg/dm^3 50 μM
Zn_6Al_2	k_1 (1/min)	0.033	0.034	0.012	0.0065	0.010	0.015	0.0071	0.012	0.030	0.011
	χ^2	371	42	184.74	4.9	74	166	5.8	3.3	1.8	3.1
	R	0.99	0.99	0.97	0.97	0.99	0.94	0.98	0.99	0.99	0.99
$Zn_6Al_{1.5}Ti_{0.5}$	k_1 (1/min)	0.024	0.017	0.0055	0.013	0.017	0.16	0.11	0.053	0.033	0.15
	χ^2	65	55	102	4.9	165	2.1	1.2	3.2	1.1	0.87
	R	0.99	0.99	0.97	0.98	0.97	0.98	0.98	0.94	0.94	0.95
Zn_6AlTi	k_1 (1/min)	0.016	0.024	0.012	0.088	0.019	0.12	0.11	0.021	0.030	0.019
	χ^2	83	7.2	39	1.2	3.6	0.14	1.1	3.5	0.36	3.6
	R	0.99	0.99	0.93	0.94	0.99	0.99	0.95	0.94	0.57	0.82
$Zn_6Al_{0.5}Ti_{1.5}$	k_1 (1/min)	0.0088	0.0085	0.0032	0.17	0.011	0.031	0.15	0.14	0.027	
	χ^2	50	94	2.5	2.0	4.5	0.10	0.044	0.049	0.055	
	R	0.99	0.96	0.99	0.94	0.96	0.97	0.99	0.97	0.98	

Table IV.9. Pseudo-second-order adjustment of the experimental results.

Sample		Diclofenac					Salicylic acid				
		100 mg/dm^3 75 µM	200 mg/ dm^3 75 µM	400 mg/dm^3 75 µM	200 mg/dm^3 25 µM	200 mg/dm^3 50 µM	100 mg/dm^3 75 µM	200 mg/ dm^3 75 µM	400 mg/dm^3 75 µM	200 mg/dm^3 25 µM	200 mg/dm^3 50 µM
Zn_6Al_2	k_2 (g/mg·min)	0.00050	0.00084	1.79	0.0016	0.00025	0.0025	0.0012	0.0022	0.0093	0.0017
	χ^2	1152	272	185	11.2	559	7.7	20.8	12.1	8.8	17.7
	R	0.97	0.98	0.97	0.94	0.96	0.97	0.94	0.95	0.94	0.95
$Zn_6Al_{1.5}Ti_{0.5}$	k_2 (g/mg·min)	0.00051	0.00041	0.00032	0.0028	0.00059	0.10	0.039	0.019	0.017	0.17
	χ^2	310	309	102	5.4	76	2.9	0.25	1.02	0.64	1.26
	R	0.98	0.98	0.97	0.98	0.99	0.97	0.99	0.98	0.97	0.92
Zn_6AlTi	k_2 (g/mg·min)	0.00057	0.0016	0.0015	0.079	0.0033	0.11	0.062	0.0086	0.040	0.011
	χ^2	362	25.4	11.3	1.85	14.1	2.10	0.54	4.31	0.54	1.95
	R	0.94	0.99	0.98	0.91	0.95	0.92	0.98	0.92	0.91	0.90
$Zn_6Al_{0.5}Ti_{1.5}$	k_2 (g/mg·min)	0.00039	0.00051	0.00036	0.099	0.0036	0.043	0.46	0.37	0.037	
	χ^2	205	228	24.2	1.36	6.6	0.27	0.10	0.050	0.08	
	R	0.97	0.90	0.97	0.96	0.94	0.92	0.97	0.97	0.98	

Table IV.10. Effective diffusion coefficients of the adsorption of diclofenac and salicylic acid by the LDH.

Sample		Diclofenac					Salicylic acid				
		100 mg/dm^3 75 µM	200 mg/ dm^3 75 µM	400 mg/dm^3 75 µM	200 mg/dm^3 25 µM	200 mg/dm^3 50 µM	100 mg/dm^3 75 µM	200 mg/dm^3 75 µM	400 mg/dm^3 75 µM	200 mg/dm^3 25 µM	200 mg/dm^3 50 µM
Zn_6Al_2	D/r^2(1/s)	$3.02\ 10^{-5}$	$3.03\ 10^{-5}$	$5.95\ 10^{-6}$	$4.3\ 10^{-6}$	$8.21\ 10^{-6}$	$9.11\ 10^{-6}$	$5.91\ 10^{-6}$	$1.12\ 10^{-5}$	$6.75\ 10^{-5}$	$9.43\ 10^{-6}$
	χ^2	0.050	0.024	0.025	0.57	0.13	0.064	0.20	0.28	0.028	0.15
	R	0.993	0.997	0.98	0.85	0.96	0.96	0.94	0.92	0.99	0.95
$Zn_6Al_{1.5}Ti_{0.5}$	D/r^2 (1/s)	$2.05\ 10^{-5}$	$1.33\ 10^{-5}$	$4.56\ 10^{-6}$	$8.85\ 10^{-6}$	$1.35\ 10^{-5}$	$2.84\ 10^{-4}$	$6.61\ 10^{-4}$	$3.1\ 10^{-5}$	$3.12\ 10^{-5}$	$1.77\ 10^{-4}$
	χ^2	0.021	0.042	0.034	0.062	$4.7\ 10^{-3}$	0.048	0.053	0.067	0.103	0.43
	R	0.997	0.993	0.99	0.98	0.998	0.98	0.98	0.98	0.96	0.84
Zn_6AlTi	D/r^2 (1/s)	$8.4\ 10^{-6}$	$2.02\ 10^{-6}$	$5.30\ 10^{-4}$	$9.50\ 10^{-4}$	$1.73\ 10^{-5}$	$1.38\ 10^{-4}$	$1.26\ 10^{-5}$	$2.52\ 10^{-5}$	$3.80\ 10^{-5}$	$1.46\ 10^{-5}$
	χ^2	0.055	0.021	0.036	$5.75\ 10^{-3}$	0.15	0.018	0.20	0.21	0.53	0.17
	R	0.92	0.997	0.98	0.93	0.97	0.99	0.94	0.94	0.84	0.91
$Zn_6Al_{0.5}Ti_{1.5}$	D/r^2 (1/s)	$6.51\ 10^{-6}$	$601\ 10^{-5}$	$2.31\ 10^{-6}$	$3.82\ 10^{-5}$	$9.91\ 10^{-6}$	$8.50\ 10^{-5}$		$8.50\ 10^{-4}$	$2.05\ 10^{-5}$	
	χ^2	0.146	0.41	0.13	0.45	0.14	0.52		0.13	0.024	
	R	0.97	0.90	0.97	0.86	0.94	0.89		0.94	0.99	

Once the equilibrium time was selected, the equilibrium adsorption isotherm of diclofenac on the $Zn_6Al^*_2$ hydrotalcite as adsorbent with a higher adsorption capacity was also plotted. Langmuir, Freundlich and Toth isotherm equations modeled the experimental data for diclofenac. The results are shown in Figure IV.12 and the goodness of fit of the models was evaluated with χ^2 and R (see Table IV.11). The adsorption isotherm can be related to a L-type behavior according to the classification proposed by Giles (1974). This behavior was related to a system in which the contaminant interacted strongly with the surface of the adsorbent. The three models fitted well with the experimental data although Toth represented the data with more accuracy.

Table IV.11. Freundlich, Langmuir and Toth parameters for the diclofenac adsorption process on $Zn_6Al^*_2$.

Freundlich		**Langmuir**		**Toth**	
q_F	58.8	q_L (μmol/g)	1172	q_T (μmol/g)	3036
m_F	3.01	k_L (cm^3/μmol)	0.015	k_T (cm^3/μmol)	0.114
χ^2	3623	χ^2	7490	m_T	0.27
R	0.98	**R**	0.96	χ^2	2392
				R	0.98

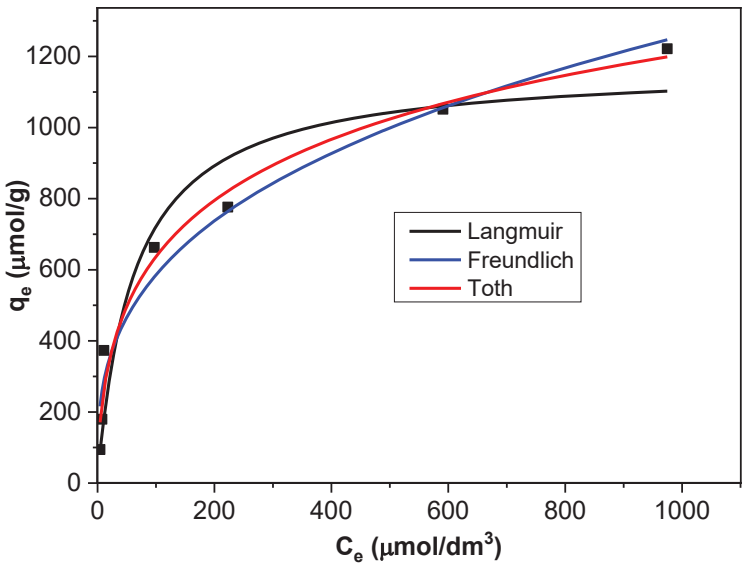

Figure IV.12. Experimental results (scatter) and isotherm adjustment to Langmuir, Freundlich and Toth models for diclofenac adsorption on $Zn_6Al^*_2$.

IV.3.2.2. Fixed-Bed adsorption results

Breakthrough behavior of the column adsorption process with diclofenac and salicylic acid on the $Zn_6Al^*_2$ hydrotalcite was also investigated. The breakthrough curves obtained for the drugs were included in Figure IV.13. Experimental results were adjusted considering the Thomas equation (see Table IV.12). R showed that the Thomas model had good adjustment to both drugs. The diclofenac molecule crosses the adsorbent bed at a faster rate than the salicylic acid molecule. There were a minor interaction with the adsorbent, which can be explained by the larger size of the diclofenac molecule compared to the size of the salicylic acid molecule (see Table IV.7). In the batch experiments the time to reach the equilibrium was high, between 100 and 400 min, so if the diclofenac molecule could diffuse into the adsorbent lattice, it had enough time to do so. In the case of these experiments, it was not possible so it is retained in a smaller proportion than salicylic acid.

Table IV.12. Thomas model parameters for the fixed-bed column adsorption of drugs on $Zn_6Al^*_2$ without pH modification.

	Diclofenac	**Salicylic acid**
k_{Th} (cm^3/min·μmol)	0.035	0.008
q_{ads} (μmol/g)	1157	4597
χ^2	1.03	0.094
R	0.96	0.98
m	0.0264	0.0264

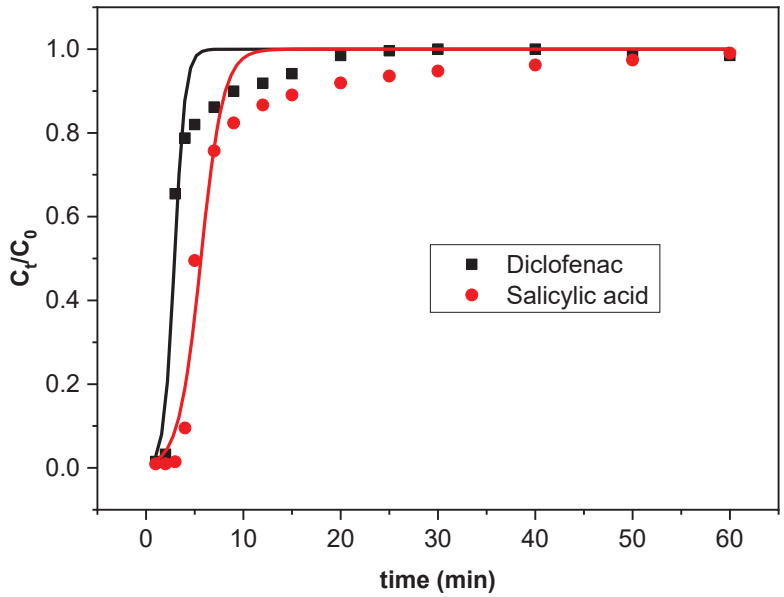

Figure IV.13. Comparison of the breakthrough curve for diclofenac and salicylic acid in a column with 25 mg of $Zn_6Al^*_2$ and their adjustment to the Thomas model (line).

IV.4. SUMMARY AND CONCLUSIONS

Herein, a new procedure for the recovery of aluminum present in saline slags generated during the secondary recycling processes of aluminum as an adsorbent of diclofenac and salicylic acid, as examples of emerging contaminants, has been reported. For this purpose, the aluminum extracted with aqueous NaOH solutions was used as an alternative source of aluminum for the synthesis of hydrotalcite-type ZnTiAl, with a molar ratio Zn/(Al + Ti) = 3 and several Al/Ti ratios, by a coprecipitation method at pH = 10. The uncalcined and without Ti samples evidenced the presence of the typical hydrotalcite structure with a high crystallinity from the XRD analyses. As the amount of Ti increased, the crystallinity of the samples decreased appreciably. After calcination at 673 K, the hydrotalcite structure was destroyed and zincite (ZnO) was found. The textural properties, namely the specific surface area, decreased with the calcination temperature, related to the presence of amorphous mixed oxides, while increased when incorporating Ti into the structure from 78 to 199 m^2/g. By calcination of the samples at 673 K, these properties decreased due to the presence of amorphous mixed oxides. The presence of Ti in the LDH structure was confirmed by XPS analysis. All these characterization results were also confirmed by the synthesis of ZnTiAl LDH from aluminum nitrate as a commercial source.

The kinetic study of the adsorption process showed that 100-400 min were necessary for the emerging pollutants/hydrotalcites systems to reach the equilibrium. The hydrotalcites synthesized retained more diclofenac than salicylic acid (409 and 80 μmol/g, respectively), and the adsorption capacity was greater when Ti content in the adsorbents was lower. Zn_6Al*_2 solid was very effective in retaining this type of organic pollutants.

IV.5. REFERENCES

Albiston, L., Franklin, K.R., Lee, E., Smeulders, J.B.A.F., 1996. Rheology and microstructure of aqueous layered double hydroxide dispersions. J. Mater. Chem. 6, 871–877. http://dx.doi.org/10.1039/JM9960600871

Ambrogi, V., Fardella, G., Grandolini, G., Perioli, L., Tiralti, M.C., 2001. Intercalation compounds of hydrotalcite-like anionic clays with anti-inflammatory agents. II: uptake of diclofenac for a controlled release formulation. AAPS PharmSciTech 3, article 26. https://doi.org/10.1208/pt030326

Bakatula, E.N., Richard, D., Neculita, C.M., Zagury, G.J., 2018. Determination of point of zero charge of natural organic materials. Environ. Sci. Pollut. Res. 25, 7823–7833. https://doi.org/10.1007/s11356-017-1115-7

Bautista, P., Mohedano, A.F., Casas, J.A., Zazo, J.A., Rodriguez, J.J., 2008. An overview of the application of Fenton oxidation to industrial wastewaters treatment. J. Chem. Technol. Biotechnol. 83, 1323–1338. https://doi.org/10.1002/jctb.1988

Benito, P., Labajos, F.M., Rocha, J., Rives, V., 2006. Influence of microwave radiation on the textural properties of layered double hydroxides. Micropor. Mesopor. Mater. 94, 148–158. https://doi.org/10.1016/j.micromeso.2006.03.038

Boukhalfa, N., Boutahala, M., Djebri, N., 2017. Synthesis and characterization of ZnAl-layered double hydroxide and organo-K10 montmorillonite for the removal of diclofenac from aqueous solution. Adsorpt. Sci. Technol. 35, 20–36. https://doi.org/10.1177/0263617416666548

Brindley, G.W., Kao, C.-C., 1984. Structural and IR relations among brucite-like divalent metal hydroxides. Phys. Chem. Miner.10, 187–191. https://doi.org/10.1007/BF00311476

Caminada, D., Escher, C., Fent, K., 2006. Cytotoxicity of pharmaceuticals found in aquatic systems: comparison of PLHC-1 and RTG-2 fish cell lines. Aquat. Toxicol. 79, 114–https://doi.org/10.1016/j.aquatox.2006.05.010

Carmona, E., Andreu, V., Picó, Y., 2014. Occurrence of acidic pharmaceuticals and personal care products in Turia river basin: from waste to drinking water.Sci. Total Environ. 484, 53–63. http://dx.doi.org/10.1016/j.scitotenv.2014.02.085

Castro, C.S., Cardoso, D., Nascente, P.A.P., Assaf, J.M., 2011. MgAlLi mixed oxides derived from hydrotalcite for catalytic transesterification. Catal. Lett. 141, 1316–1323. https://doi.org/10.1007/s10562-011-0650-y

Cavani, A.V.F., Trifiro, F., 1991. Hydrotalcite-type anionic clays: preparation, properties and applications. Catal. Today 11, 173–301. https://doi.org/10.1016/0920-5861(91)80068-K

Chu, K.H., 2002. Removal of copper from aqueous solution by chitosan in Prawn Shell: adsorption equilibrium and kinetics. J. Hazard. Mater. 90, 77–95. https://doi.org/10.1016/S0304-3894(01)00332-6

Commission Implementing Regulation (EU) 2015/495 of 20 March 2015 establishing a watch

list of substances for Union-wide monitoring in the field of water policy pursuant to Directive 2008/105/EC of the European Parliament and of the Council, Official Journal of the European Union, 24.3.2015, L78/40 - L78/42. http://data.europa.eu/eli/dec_impl/2015/495/oj

Conterosito, E., Croce, G., Palin, L., Pagano, C., Perioli, L., Viterbo, D., Boccaleri, E., Paul, G., Milanesio, M., 2013. Structural characterization and thermal and chemical stability of bioactive molecule-hydrotalcite (LDH) nanocomposites. Phys. Chem. Chem. Phys. 15, 13418–13433. https://doi.org/10.1039/c3cp51235e

Costantino, U., Leroux, F., Nocchetti, M., Mousty, C., 2013. LDH in physical, chemical, biochemical, and life sciences. In Bergaya, F., Lagaly, G. (Eds.) Handbook of Clay Science, Second Edition, Part B. Elsevier (Chapter 6). https://doi.org/10.1016/B978-0-08-098259-5.00026-3

Eades, C., Waring, C.P., 2010. The effects of diclofenac on the physiology of the green shore crab carcinus maenas. Mar. Environ. Res. 69, S46–S48. http://dx.doi.org/10.1016/j.marenvres.2009.11.001

Elhalil, A., Farnane, M., Machrouhi, A., Mahjoubi, F.Z., Elmoubarki, R., Tounsadi, H., Abdennouri, M., Barka, N., 2018. Effects of molar ratio and calcination temperature on the adsorption performance of Zn/Al layered double hydroxide nanoparticles in the removal of pharmaceutical pollutants. J. Sci. Adv. Mater. Devices 3, 188–195. https://doi.org/10.1016/j.jsamd.2018.03.005

European Waste Catalogue and Hazardous Waste List, Environmental Protection Agency, 2002. https://ec.europa.eu/environment/waste/framework/list.htm

Feito, R., Valcárcel, Y., Catalá, M., 2012. Biomarker assessment of toxicity with miniaturised bioassays: diclofenac as a case study. Ecotoxicology 21, 289–296. https://doi.org/10.1007/s10646-011-0790-2

Fraccarollo, A., Cossi, M., Marchese, L., 2010. DFT simulation of Mg/Al hydrotalcite with different intercalated anions: periodic structure and solvating effects on the iodide/triiodide redox couple. Chem. Phys. Lett. 494, 274–278. http://dx.doi.org/10.1016/j.cplett.2010.06.029

Frost, R.L., Martens, W.N., Erickson, K.L., 2005. Thermal decomposition of the hydrotalcite: thermogravimetric analysis and hot stage Raman spectroscopic study. J. Therm. Anal. Calorim. 82, 603–608. https://doi.org/10.1007/s10973-005-0940-y

Gao, Z., Du, B., Zhang, G., Gao, Y., Li, Z., Zhang, H., Duan, X., 2011. Adsorption on pentachlorophenol from aqueous solution on dodecylbenzenesulfonate modified nickel-tianium layered double hydroxide nanocomposites. Ind. Eng. Chem. Res. 50, 5334–5345. https://doi.org/10.1021/ie101766e

Gil, A., Korili, S.A., 2016. Management and valorization of aluminum saline slags: current status and future trends. Chem. Eng. J. 289, 74–84. http://dx.doi.org/10.1016/j.cej.2015.12.069

Gil, A., García, A.M., Fernández, M., Vicente, M.A., González–Rodríguez, B., Rives, V., Korili, S.A., 2017. Effect of dopants on the structure of titanium oxide used as a photocatalyst for the removal of emergent contaminants. J. Ind. Eng. Chem. 53, 183-191. http://dx.doi.org/10.1016/j.jiec.2017.04.024

Gil, A., Arrieta, E., Vicente, M.A., Korili, S.A., 2018. Synthesis and CO_2 adsorption properties of hydrotalcite-like compounds prepared from aluminum saline slag wastes. Chem. Eng. J. 334, 1341–1350. https://doi.org/10.1016/j.cej.2017.11.100

Gil, A., Taoufik, N., García, A.M., Korili, S.A., 2019. Comparative removal of emerging contaminants from aqueous solution by adsorption on an activated carbon. Environ. Technol. 40, 3017-3030. https://doi.org/10.1080/09593330.2018.1464066

Giles, C.H., Smith, D., Huitson, A., 1974. A general treatment and classification of the solute adsorption isotherm. I. Theoretical. J. Colloid Interf. Sci. 47, 755-765. https://doi.org/10.1016/0021-9797(74)90252-5

Ginebreda, A., Muñoz, I., de Alda, M.L., Brix, R., López-Doval, J., Barceló, D., 2010. Environmental risk assessment of pharmaceuticals in rivers: relationships between hazard indexes and aquatic macroinvertebrate diversity indexes in the Llobregat river (NE Spain). Environ. Int. 36, 153–162. http://dx.doi.org/10.1016/j.envint.2009.10.003

Goh, K.H., Lim, T.T., Dong, Z., 2008. Application of layered double hydroxides for removal of oxyanions: a review. Water Res. 42, 1343–1368. https://doi.org/10.1016/j.watres.2007.10.043

Gomes Silva, C., Bouizi, Y., Fornés, V., García, H., 2009. Layered double hydroxides as highly efficient photocatalysts for visible light oxygen generation from water. J. Am. Chem. Soc. 131, 13833–13839. https://doi.org/10.1021/ja905467v

Gualandi, I., Scavetta, E., Zappoli, S., Tonelli, D., 2011. Electrocatalytic oxidation of salicylic

acid by a cobalt hydrotalcite-like compound modified Pt electrode. Biosens. Bioelectron. 26, 3200–3206. http://dx.doi.org/10.1016/j.bios.2010.12.026

Haap, T., Triebskorn, R., Köhler, H.R., 2008. Acute effects of diclofenac and DMSO to Daphnia Magna: immobilisation and hsp70-Induction. Chemosphere 73, 353–359. https://doi.org/10.1016/j.chemosphere.2008.05.062

Hadnadjev-Kostic, M., Vulic, T., Ranogajec, J., Marinkovic-Neducin, R., Radosavljevic-Mihajlovic, A., 2013. Thermal and photocatalytic behavior of Ti/LDH nanocomposites. J. Therm. Anal. Calorim. 111, 1155–1162. https://doi.org/10.1007/s10973-012-2226-5

Haraketi, M., Hosni, K., Srasra, E., 2016. Intercalation of salicylic acid into ZnAl and MgAl layered double hydroxides for a controlled release formulation. Colloid J. 78, 533–541. https://doi.org/10.1134/S1061933X16040062

Heraldy, E., Suprihatin, R.W., Pranoto, 2016. Intercalation of diclofenac in modified Zn/Al hydrotalcite-like preparation. IOP Conf. Series Mater. Sci. Eng. 107, 012026. https://doi.org/10.1088/1757-899X/107/1/012026

Khatem, R., Real Ojeda, M., Bakhti, A., 2015. Use of synthetic clay for removal of diclofenac anti-inflammatory. Eurasian J. Soil Sci. 4, 126–136. https://doi.org/10.18393/ejss.29678

Khraisheh, M.A.M., Al-Degs, Y.S., Allen, S.J., Ahmad, M.N., 2002. Elucidation of controlling steps of reactive dye adsorption on activated carbon. Ind. Eng. Chem. Res. 41, 1651–1657. https://doi.org/10.1021/ie000942c

Khenniche, L., Aissani, F., 2010. Preparation and characterization of carbons from coffee residue: adsorption of salicylic acid on the prepared carbons. J. Chem. Eng. Data 55, 728–734. https://doi.org/10.1021/je900426a

Kikhtyanin, O., Tišler, Z., Velvarská, R., Kubička, D., 2017. Reconstructed Mg-Al hydrotalcites prepared by using different rehydration and drying time: physico-chemical properties and catalytic performance in aldol condensation. Appl. Catal. A Gen. 536, 85–96. https://doi.org/10.1016/j.apcata.2017.02.020

Kosma, C.I., Lambropoulou, D.A., Albanis, T.A., 2014. Investigation of PPCPs in wastewater treatment plants in Greece: occurrence, removal and environmental risk assessment. Sci. Total Environ. 466–467, 421–438. http://dx.doi.org/10.1016/j.scitotenv.2013.07.044

Krammer, C., 2011. Aluminum Handbook, Vol. 1: Fundamentals and Materials;Verlag: Beuth. https://books.google.es/books?id=YPSQpwAACAAJ

Li, C., Wei, M., Evans, D.G., Duan, X., 2014. Layered double hydroxide-based nanomaterials as highly efficient catalysts and adsorbents. Small 10, 4469–4486. https://doi.org/10.1002/smll.201401464

Lowell, S., Shields, J.E., Thomas, M.A., Thommes, M. (Eds.), 2004. Characterization of Porous Solids and Powders: Surface Area, Pore Size and Density, Kluwer Academic Publishers: New York. https://doi.org/10.1007/978-1-4020-2303-3

Lozano, R.P., Rossi, C., La Iglesia, Á., Matesanz, E., 2012. Zaccagnaite-3R, a new Zn-Al hydrotalcite polytype from El Soplao Cave (Cantabria, Spain). Am. Mineral. 97, 513–523. https://doi.org/10.2138/am.2012.3908

Lu, R., Xu, X., Chang, J., Zhu, Y., Xu, S., Zhang, F., 2012. Improvement of photocatalytic activity of TiO_2 nanoparticles on selectively reconstructed layered double hydroxide. Appl. Catal. B Environ. 111–112, 389–396. https://doi.org/10.1016/j.apcatb.2011.10.022

Luo, Y., Guo, W., Ngo, H.H., Nghiem, L.D., Hai, F.I., Zhang, J., Liang, S., Wang, X.C., 2014. A review on the occurrence of micropollutants in the aquatic environment and their fate and removal during wastewater treatment. Sci. Total Environ. 473–474, 619–641. http://dx.doi.org/10.1016/j.scitotenv.2013.12.065

Mendoza-Damián, G., Tzompantzi, F., Mantilla, A., Barrera, A., Lartundo-Rojas, L., 2013. Photocatalytic degradation of 2,4-dichlorophenol with MgAlTi mixed oxides catalysts obtained from layered double hydroxides. J. Hazard. Mater. 263, 67-72. https://doi.org/10.1016/j.jhazmat.2013.09.047

Mohapatra, L., Parida, K., 2016. A review on the recent progress, challenges and perspective of layered double hydroxides as promising photocatalysts. J. Mater. Chem. A 4, 10744–10766. http://dx.doi.org/10.1039/C6TA01668E

Mompelat, S., Le Bot, B., Thomas, O., 2009. Occurrence and fate of pharmaceutical products and by-products, from resource to drinking water. Environ. Int. 35, 803–814. http://dx.doi.org/10.1016/j.envint.2008.10.008

Mosangi, D., Moyo, L., Kesavan Pillai, S., Ray, S.S., 2016. Acetyl salicylic acid-ZnAl layered double hydroxide functional nanohybrid for skin care application. RSC Advances 6, 105862–105870. http://dx.doi.org/10.1039/C6RA22172F

Moulder, J.F., 1992. Handbook of X-Ray Photoelectron Spectroscopy: A Reference Book of

Standard Spectra for Identification and Interpretation of XPS Data. Chastain, J. (Ed.) Physical Electronics Division, Perkin-Elmer Corporation. https://books.google.es/books?id=A_XGQgAACAAJ

Nassef, M., Kim, S.G., Seki, M., Kang, I.J., Hano, T., Shimasaki, Y., Oshima, Y., 2010. In ovo nanoinjection of triclosan, diclofenac and carbamazepine affects embryonic development of medaka fish (Oryzias latipes). Chemosphere 79, 966–973. https://doi.org/10.1016/j.chemosphere.2010.02.002

Poulopoulos, S., Vassilis, I. (Eds), 2006. Adsorption, Ion Exchange and Catalysis - Design of Operations and Environmental Applications, 1st Edition, Elsevier. https://doi.org/10.1016/B978-044452783-7/50004-5

Quinn, B., Schmidt, W., O'Rourke, K., Hernan, R., 2011. Effects of the pharmaceuticals gemfibrozil and diclofenac on biomarker expression in the zebra mussel (Dreissena polymorpha) and their comparison with standardised toxicity tests. Chemosphere 84, 657–663. http://dx.doi.org/10.1016/j.chemosphere.2011.03.033

Radjenović, J., Petrović, M., Ventura, F., Barceló, D., 2008. Rejection of pharmaceuticals in nanofiltration and reverse osmosis membrane drinking water treatment. Water Res. 42, 3601–3610. https://doi.org/10.1016/j.watres.2008.05.020

Rives, V., Del Arco, M., Martin, C., 2014. Intercalation of drugs in layered double hydroxides and their controlled release: a review. Appl. Clay Sci. 88–89, 239–269. https://doi.org/10.1016/j.clay.2013.12.002

San Román, M.S., Holgado, M.J., Salinas, B., Rives, V., 2012. Characterisation of diclofenac, ketoprofen or chloramphenicol succinate encapsulated in layered double hydroxides with the hydrotalcite-type structure. Appl. Clay Sci. 55, 158–163. https://doi.org/10.1016/j.clay.2011.11.010

Santamaría, L., Vicente, M.A., Korili, S.A., Gil, A., 2020. Effect of the preparation method and metal content on the synthesis of metal modified titanium oxide used for the removal of salicylic acid under UV light. Environ. Technol. 41, 2073–2084. https://doi.org/10.1080/09593330.2018.1555285

Shao, M., Han, J., Wei, M., Evans, D.G., Duan, X., 2011. The synthesis of hierarchical Zn-Ti layered double hydroxide for efficient visible-light photocatalysis. Chem. Eng. J. 186, 519–524. https://doi.org/10.1016/j.cej.2011.01.016

Silion, M., Hritcu, D., Popa, M.I., 2009. Intercalation of salicylic acid into ZnAl layered double hydroxides by ion-exchange and coprecipitation method. J. Optoelectron. Adv. Mater. 11, 528–534. https://doi.org/10.1134/S1061933X16040062

Simonin, J.P., 2016. On the comparison of pseudo-first order and pseudo-second order rate laws in the modeling of adsorption kinetics. Chem. Eng. J. 300, 254–263. http://dx.doi.org/10.1016/j.cej.2016.04.079

Suarez, S., Lema, J.M., Omil, F., 2009. Pre-treatment of hospital wastewater by coagulation-flocculation and flotation. Bioresour. Technol. 100, 2138–2146. http://dx.doi.org/10.1016/j.biortech.2008.11.015

Theiss, F.L., Ayoko, G.A., Frost, R.L., 2013. Thermogravimetric analysis of selected layered double hydroxides. J. Therm. Anal. Calorim. 112, 649–657. https://doi.org/10.1007/s10973-012-2584-z

Thomas, H.C., 1944. Heterogeneous ion exchange in a flowing system. J. Am. Chem. Soc. 66, 1664–1666. https://doi.org/10.1021/ja01238a017

Thommes, M., Kaneko, K., Neimark, A.V., Olivier, J.P., Rodriguez-Reinoso, F., Rouquerol, J., Sing, K.S.W., 2015. Physisorption of gases, with special reference to the evaluation of surface area and pore size distribution (IUPAC technical report). Pure Appl. Chem. 87, 1051–1069. https://doi.org/10.1515/pac-2014-1117

Triebskorn, R., Casper, H., Scheil, V., Schwaiger, J., 2007. Ultrastructural effects of pharmaceuticals (carbamazepine, clofibric acid, metoprolol, diclofenac) in rainbow trout (*Oncorhynchus Mykiss*) and common carp (*Cyprinus Carpio*). Anal. Bioanal. Chem. 387, 1405–1416. https://doi.org/10.1007/s00216-006-1033-x

Tsakiridis, P.E., 2012. Aluminium salt slag characterization and utilization - A review. J. Hazard. Mater. 217–218, 1–10. http://dx.doi.org/10.1016/j.jhazmat.2012.03.052

Ulibarri, M.A., Hermosin, M.C., 2001. Layered double hydroxides in water decontamination. In Rives, V. (Ed.) Layered Double Hydroxides: Present and Future. Nova Science Publishers (Chapter 9). http://www.novapublishers.org/catalog/product_info.php?products_id=53842

Vulliet, E., Cren-Olivé, C., 2011. Screening of pharmaceuticals and hormones at the regional scale, in surface and groundwaters intended to human consumption. Environ. Pollut. 159, 2929–2934. http://dx.doi.org/10.1016/j.envpol.2011.04.033

Wang, M., Jiang, L., Kim, E.J., Hahn, S.H., 2015. Electronic structure and optical properties of $Zn(OH)_2$: LDA+U calculations and intense yellow luminescence. RSC Advances 5, 87496–87503. http://dx.doi.org/10.1039/C5RA17024A

Xia, S.-J., Liu, F.-X., Ni, Z.-M., Xue, J.-L., Qian, P.-P., 2013. Layered double hydroxides as efficient photocatalysts for visible-light degradation of Rhodamine B. J. Colloid Interface Sci. 405, 195–200. http://dx.doi.org/10.1016/j.jcis.2013.05.064

Xie, W., Peng, H., Chen, L., 2006. Calcined Mg-Al hydrotalcites as solid base catalysts for methanolysis of soybean oil. J. Mol. Catal. A Chem. 246, 24–32. https://doi.org/10.1016/j.molcata.2005.10.008

Xiong, T., Yuan, X., Wang, H., Wu, Z., Jiang, L., Leng, L., Xi, K., Cao, X., Zeng, G., 2019. Highly efficient removal of diclofenac sodium from medical wastewater by Mg/Al layered double hydroxide-poly(m-phenylenediamine) composite. Chem. Eng. J. 366, 83–91. https://doi.org/10.1016/j.cej.2019.02.069

Chapter V

Effect of the preparation method and metal content on the synthesis of metal modified titanium oxide used for the removal of salicylic acid under UV light

ABSTRACT

Titanium dioxide modified with Ag and Fe was synthesized using two preparation methods, characterized and applied to the photocatalytic degradation of salicylic acid in aqueous solution. The modified TiO_2 samples were prepared by the sol-gel and wet impregnation methods starting from titanium(IV) isopropoxide and using $AgNO_3$ and $Fe(NO_3)_3 \cdot 9H_2O$ as precursors of the modifiers, with their content varying between 0 and 5 wt.%. Catalysts characterization was based on powder X-ray diffraction (PXRD), nitrogen physisorption at 77 K, temperature programmed reduction (H_2-TPR), chemisorption of NH_3 at 343 K and X-ray photoelectron spectroscopy (XPS). The photocatalytic degradation of salicylic acid by modified TiO_2 was investigated under ultraviolet irradiation at 298 K considering various concentrations of the catalyst, between 100 and 1000 $mg_{catalyst}/dm^3$, and of the organic molecule, between 0 and 15 mg/dm^3. The catalysts most active in the degradation of salicylic acid were those having the highest Fe content.

V.1. INTRODUCTION

The worldwide increase in the production and consumption of drugs has generated awareness on the need for an effective operating procedure concerning the disposal and control of pharmaceutical waste. Several studies provide evidence for the presence of emerging contaminants and, particularly, non-steroidal anti-inflammatory drugs (NSAIDs) in the aquatic environment (Halling-Sorensen et al., 1998; Loos et al., 2010; Valcárcel et al., 2011). NSAIDs are released in the environment in a variety of ways: from landfill leachates, hospital waste and effluents from sewage treatment plants to drug production facilities (Ashton et al., 2004; Mompelat et al., 2009). These types of contaminants can be considered as anthropogenic markers for wastewater contamination. Salicylic acid, in particular, has characterized toxicological effects on fishes (Nunes et al., 2015) and mammals (Doi and Horie, 2010), that include abnormalities in the gills, fusion of the secondary lamellae and induction of oxidative stress. The growth of worldwide population and the fact that some drugs are used in non-prescription medication and thus are commonly available highlight the need for effective methods to remove them from wastewater. Several methods including ozonation (Huber et al., 2003), photocatalysis (Kanakaraju et al., 2014), UV-H_2O_2

methods (Vogna et al., 2004) and adsorption and Fenton processes (Pliego et al., 2015; Gil et al., 2019) have been used for this purpose. Photocatalysis is used due to its complete mineralization of the organic pollutants in addition to being used at ambient temperature and pressure. There is no an ideal photocatalyst even though there are several semiconductors to choose from among oxides and sulfides, such as ZnO (Saravanan et al., 2016), Fe_2O_3 (Jaramillo-Páez et al., 2017), CdS (Li et al., 2012), ZnS (Bai et al., 2017), BiOX (Yang et al., 2018) and TiO_2 (Barbosa et al., 2015). The last is the one generally chosen because of its ability to decompose organic pollutants, low cost, long durability, powerful oxidizing effect and inertness for living organisms (Hoffmann et al., 1995).

The photocatalytic properties of TiO_2 occur when it absorbs ultraviolet (UV, $\lambda <$ 400 nm) light of energy greater than the band gap and excites an electron from the valence to the conduction band creating positively charged holes in the valence band. The positive holes and conduction band electrons migrate to the surface of TiO_2, where they initiate oxidation and reduction reactions with adsorbed species. Hydroxyl radicals (•OH) are formed when the holes generated in the valence band diffuse to the surface of the titanium dioxide particle and react with molecules of water (Rincón and Pulgarin, 2006). Organic molecules close to the TiO_2 surface are then oxidized by the hydroxyl radicals and the generated holes (see Figure V.1) (Parsons, 2005; Nakata and Fujishima, 2012). TiO_2 can have several structures such as rutile, anatase and brookite and the best photocatalytic results are generally found with anatase, which may be due to its low particle size, larger specific surface area and pore structure, and the different band gap values (Nagy and Balogh, 2013). There are however two main drawbacks that limit TiO_2 performance, namely the low efficiency under visible radiation and an unwelcome recombination of electrons and holes (Silva et al., 2009). In order to overcome them, several methods that require the tailoring of the catalyst surface have been developed. These methods can include doping or co-doping of the catalyst with a noble metal (Mohite et al., 2015), transition metal (Chaudhari et al., 2018) or a non-metal (Choi et al., 2007). These species can act as electron traps, facilitating electron-hole separation and promoting the interfacial electron transfer process, which can enhance the efficiency of the catalysts (see Figure V.1). In addition, choosing an appropriate preparation method has a paramount importance as it is related to the surface properties of the catalysts. Various procedures, as sol-gel, co-precipitation, flame hydrolysis,

plasma assisted pyrolysis, mechanical alloying, metal organic chemical vapor deposition, hydrothermal methods and the wet impregnation technique, among others, have been reported to incorporate metals and to modify the properties of TiO_2. In the same way, titanium alkoxides, titanium(IV) chloride and elemental titanium are the selected precursors for the synthesis of TiO_2. In the sol-gel method, the precursor solution contains titanium and the doping ions allowing that these doping ions can incorporate into the TiO_2 lattice (Navio et al., 1999), while by doping TiO_2 with iron by impregnation technique, the formation of Fe_2TiO_5 or Fe_2O_3 on the surface of TiO_2 has been reported (Navío et al., 1998). With the first method, there must be an intimate

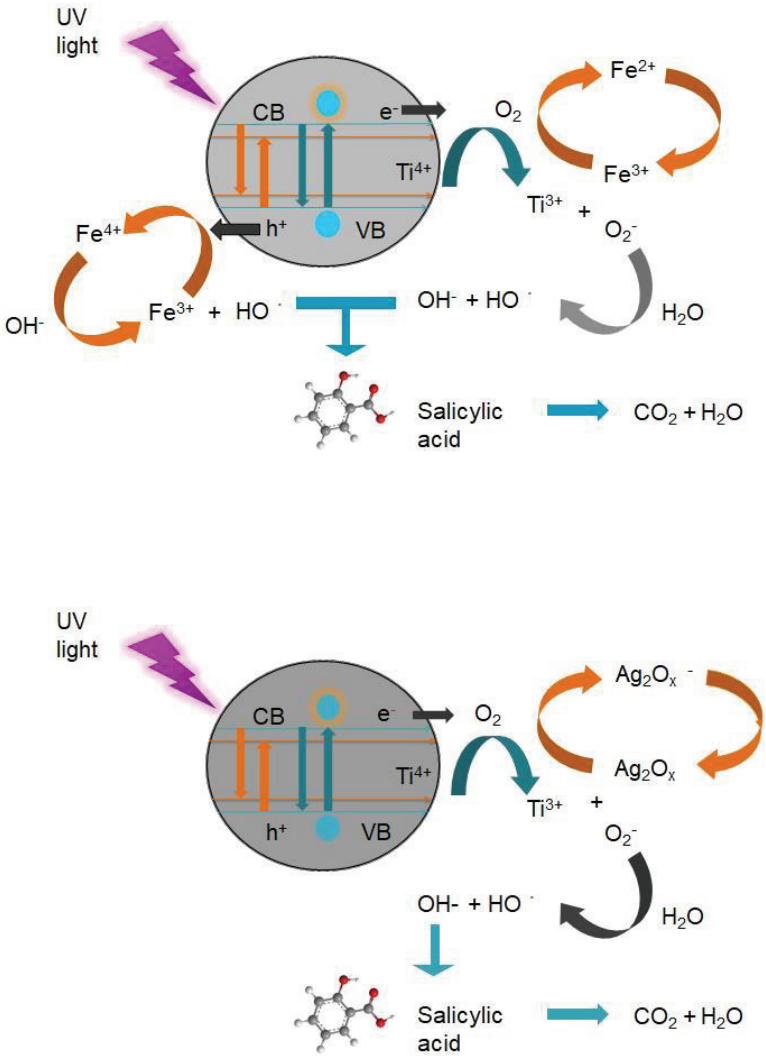

Figure V.1. Schematic diagram of the photocatalytic reaction mechanism taking place on the surface of modified TiO_2 catalysts.

contact between the dopant and the TiO_2, increasing the possibilities for the redox mechanism that allows the degradation of the organic molecule to take place. By impregnation, the formation of Fe_2TiO_5 and Fe_2O_3 may be disadvantageous in principle, since their photocatalytic activity is low and they occupy the effective surface sites for adsorption and photocatalysis. Regardless of the method used, the control of the amount of dopant and its distribution seem very important (Zhu et al., 2004; Ambrus et al., 2008), being key factors in the effect of doping. In the case of silver, the Ag particles on the TiO_2 surface can also act as electron traps enhancing the electron-hole separation.

Salicylic acid is frequently found in wastewater because it is the major metabolite of the acetyl-salicylic acid used on the production of analgesics like aspirin, and is also used in several cosmetic, dermatological, food and pharmaceutical formulations. For these reasons, it can be considered a potential chemical marker of domestic wastewater contamination. To our knowledge, studies on its degradation by photocatalytic processes are limited (Badawy et al., 2014; Yoo et al., 2015; Garza-Campos et al., 2016; Arfanis et al., 2017; Gil et al., 2017; Plavac et al., 2017). In this scenario, the objective of the work is to examine the effectiveness of a TiO_2 synthesized in our laboratories modified with a transition metal (Fe) and a noble metal (Ag) for the degradation of salicylic acid from aqueous solutions at a concentration up to 15 mg/dm^3.

V.2. EXPERIMENTAL

V.2.1. MATERIALS

Materials considered for the synthesis of doped titanium dioxide were: titanium(IV) isopropoxide (>97%, Sigma-Aldrich), isopropyl alcohol (>99%, Sigma-Aldrich), hydrochloric acid (HCl, 37%, Acros), iron(III) nitrate nonahydrate ($Fe(NO_3)_3 \cdot 9H_2O$, 96 %, Riedel-de Haën), silver nitrate ($AgNO_3$, 99.8 %, Panreac). As a reference material, a commercial form of titanium(IV) oxide, anatase (>99%, Sigma-Aldrich) was also used. Salicylic acid (SA, 2-hydroxybenzoic acid, >99%, Sigma-Aldrich) was used without any purification.

V.2.2. PREPARATION OF DOPED TiO_2

TiO_2 nanoparticles were either doped, within the crystalline lattice of the particle, or impregnated with the metals. Doped TiO_2 nanoparticles were synthetized using a procedure reported previously (Gil et al., 2017): A first solution (A) was prepared incorporating 1 cm^3 of HCl (1.5 mol/dm^3) and the appropriate amount of the doping agent, $AgNO_3$ or $Fe(NO_3)_3 \cdot 9H_2O$, for a final mass percentage of the dopant metal in the solid of 0.5 and 5 wt.%, into 20 cm^3 of isopropyl alcohol. Other solution (B) was made incorporating 5 cm^3 of titanium(IV) isopropoxide into 20 cm^3 of isopropyl alcohol. Solution A was dropwise added to B while constantly stirring for 30 min. The final suspension was heated at 333 K for 16 h in order to remove the solvent, obtaining a dry white powder which was calcined for 4 h at 673 K to remove both the water adsorbed during the process and the precursors utilized to integrate the doping elements. The same method was used for preparing titanium dioxide without the addition of modifiers, used as a blank reference. Impregnated titanium dioxide particles were synthetized using the bare TiO_2 catalyst in solution B instead of titanium(IV) isopropoxide.

Catalysts were labelled according to the metal used, its mass percentage and its location in the particle as follows; Ag0.5Ti (TiO_2 doped with 0.5 wt.% Ag), Fe5/Ti (TiO_2 impregnated with 5 wt.% Fe) or TiO_2 (bare TiO_2).

V.2.3. CHARACTERIZATION TECHNIQUES

In order to characterize the crystalline phases of the catalysts, their powder X-ray diffraction (PXRD) patterns were obtained using a Siemens D-5000 diffractometer. The diffraction patterns were recorded at room temperature using Ni-filtered Cu Kα radiation (λ = 0.1548 nm). The working conditions used were 30 mA, 40 kV and a scanning rate of 0.5° (2θ)/min from 10 to 100°.

The textural properties of the catalysts were measured by nitrogen (Air Liquide, 99.999%) adsorption at 77 K using a static volumetric apparatus, Micromeritics ASAP 2010 adsorption analyzer model. Prior to the adsorption measurements, 0.2 g of the samples were degassed *in situ* under vacuum with residual pressure less than 0.1 Pa, at 473 K for 24 h.

Temperature-programmed reduction (H_2-TPR) was performed in a Micromeritics TPR/TPD 2900 instrument, and about 20 mg of the samples were used in each measurement. The samples were first pretreated with N_2 (Air Liquide, 99.999%) at 473 K for 2 h, under a 30 cm^3/min flow and a heating rate of 10 K/min. TPR tests were carried out using a flow of 5% H_2 in Ar (30 cm^3/min), and the sample was heated up to 1073 K from room temperature at a rate of 10 K/min. A cold trap (isopropyl alcohol /liquid nitrogen) was used to retain water and other compounds that might have been formed during metal reduction and precursor decomposition. The H_2 uptake during the reduction was measured by a thermal conductivity detector (TCD).

Catalyst acidity was evaluated by adsorption of NH_3 (Air Liquide, >99.995%) using a dynamic pulse method on a Micromeritics TPR/TPD 2900 instrument with 20 mg of catalyst. All samples were pre-treated at a heating rate of 10 K/min, under a He (Praxair, 99.999%) flow of 30 cm^3/min, up to 673 K for 3 h and then cooled to 343 K in the same stream. Ammonia pulses (0.5 cm^3) were injected at 343 K until the area of consecutive eluted pulses was constant.

X-ray photoelectron spectroscopy (XPS) measurements were performed on a SPECS Phoibos 150 1D-DLD spectrometer equipped with an Al Kα (1486.7 eV) X-ray source. All the binding energies were referenced to the C 1s peak at 284.8 eV of the surface adventitious carbon. The spectra were fitted to the respective element signal using the CasaXPS software (Casa Software Ltd, UK). Surface concentrations (% atomic) were calculated using peak areas normalized on the basis of acquisition parameters and sensitivity factors provided by the manufacturer.

V.2.4. PHOTOCATALYTIC PERFORMANCE

The photocatalytic behavior of the nanoparticles under ultraviolet (UV) light was evaluated by measuring the concentration of salicylic acid in an aqueous solution (ultrapure water obtained from Milli-Q equipment, Millipore). The catalytic tests were carried out using a MPDS-Basis system from UV-Consulting Peschl (Spain), with a PhotoLAB Batch-L reactor of 1.0 dm^3 and a medium-pressure Hg lamp TQ 150Z1 (power 150 W). The spectrum of the lamp is continuous, with the mean peaks at 366 nm (radiation flux, Φ 6.4 W) and 313 nm (Φ 4.3 W). The lamp was enclosed in a water cooling jacket (PolyScience Digital Temperature) to maintain a constant temperature

(298 K) and then placed in the middle of the reactor. The solution was magnetically stirred (700 rpm) and the whole process was carried out in a photon cabinet. The pH value of the solution was adjusted between 6.5 and 7.5 by addition of NaOH (aq). The pH values of the salicylic solution were measured using a pH meter (cyberscan pH 2100, Eutech). The solution of salicylic acid (0.7 dm^3), with a concentration between 5 and 15 mg/dm^3, was mixed in the reactor with the catalyst, with a concentration between 100 and 1000 $mg_{catalyst}/dm^3$, under the UV lamp. The suspension was then sampled every 15 min, filtered (Durapore membrane filters, 0.45 μm) to remove the catalyst and then analyzed on a UV-vis spectrometer (Jasco V-730) to evaluate the concentration of the organic molecule. The absorbance was determined at the wavelength corresponding to the maximum absorbance of a solution of the organic molecule, and the concentration was estimated by application of Beer's law from a calibration curve of organic contaminant concentration vs. absorbance. Blind tests in the absence of a catalyst (photolysis test) were also carried out. The experiments were conducted in duplicate.

V.3. RESULTS AND DISCUSSION

V.3.1. CHARACTERIZATION OF TITANIUM OXIDE CATALYSTS

The powder X-ray diffraction patterns of samples dried at 333 K and calcined at 673 K are shown in Figure V.2. The effect of the calcination temperature on the crystallinity of pure TiO_2 was studied previously, concluding that peaks were well-defined at 673 K (Gil et al., 2017). All the diffraction peaks recorded correspond to the anatase phase of TiO_2 (JCPDS file 78-2486). In the modified samples, no bulk crystalline phase containing the dopant was detected. In the case of Fe, various authors suggest that highly dispersed Fe^{3+} ions can be, at least partially, incorporated to the titania lattice with homogeneously dispersed crystallites formed because the ion radii of Fe^{3+} (0.645 Å) and Ti^{4+} (0.605 Å) are close (Pecchi et al., 2003; Liu and He, 2010). When adding silver to TiO_2, usually no diffraction peaks from Ag phases are observed at silver concentrations similar to those now used, which might be due to the low amount, the amorphous state of Ag species or the low temperature of calcination (Guin et al., 2007; Zhang et al., 2008; Mogal et al., 2014). These results could also be confirmed considering that the ion radii of Ag^+ (1.26 Å) is considerably larger than that

of Ti^{4+} (Chen and Mao, 2007; Li et al., 2008). Thus, the Ag^{+} ion is not going to fit easily into the anatase crystal lattice (Rao et al., 2003). Finally, a low intensity diffraction peak is observed at 30.8º in the case of the XRD patterns of Fe5/Ti, Ag5Ti and Ag5/Ti that can correspond to the brookite phase of TiO_2 (JCPDS file 29-1360).

In order to determine the possible effect of doping on the unit cell parameters, the crystallite sizes of pure and modified titanium oxide samples were calculated from the most intense diffraction peak (101) of the anatase phase, placed at 25.55°, with the Scherrer equation:

$$\tau = \frac{K\lambda}{\beta_\tau cos\theta} \qquad \text{Eq. III.1}$$

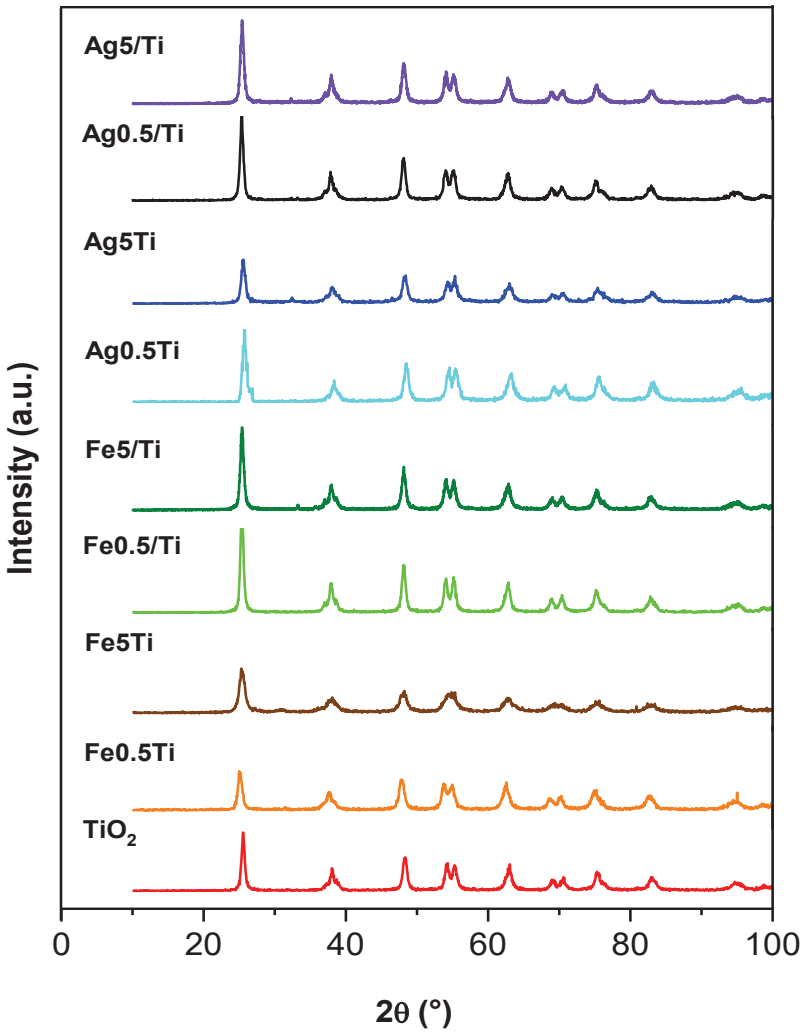

Figure V.2. PXRD patterns of TiO_2 and the doped solids treated at 673 K.

where K is the shape factor = 0.9; β_τ is the width of the peak at half of the maximum intensity (FWHM) after subtraction of instrumental broadening and θ is the diffraction angle. These values are referred to a value of 1 for the TiO_2 sample (see Figure V.3). Both dopants have a similar effect on the crystallite sizes, that of Fe being more significant. When TiO_2 was doped with iron, the crystallite size decrease was 30% (Fe0.5Ti) and even more than 50% (Fe5Ti); while when Ag was used, the size reduction was 15 and 30%, respectively (Ag0.5Ti, Ag5Ti). When Fe and Ag were impregnated, the size shift was much less noticeable, with results varying from 2% bigger (Fe0.5/Ti) to 13% smaller (Fe5/Ti). The cause of these results may be the preparation method itself. When the wet impregnation method is used, it is based on a well-formed TiO_2 support with a series of properties. In the case of the sol-gel method, the metals interact with the TiO_2 during its formation process, and they can modify the properties of the catalysts synthesized. These effects have been also reported by other authors (Adán et al., 2007).

The nitrogen adsorption-desorption isotherms of the samples are shown in Figure V.4. All the adsorption isotherms correspond to type IV in the IUPAC classification with H3 hysteresis loops (Thommes et al., 2015), characteristic of mesoporous adsorbents. The results relating to the textural properties of the samples are listed in Table V.1. The BET surface area (S_{BET}) was calculated from adsorption data in the relative pressure range 0.05-0.20, taking the cross-sectional area of the nitrogen molecule to be 0.162 nm^2.

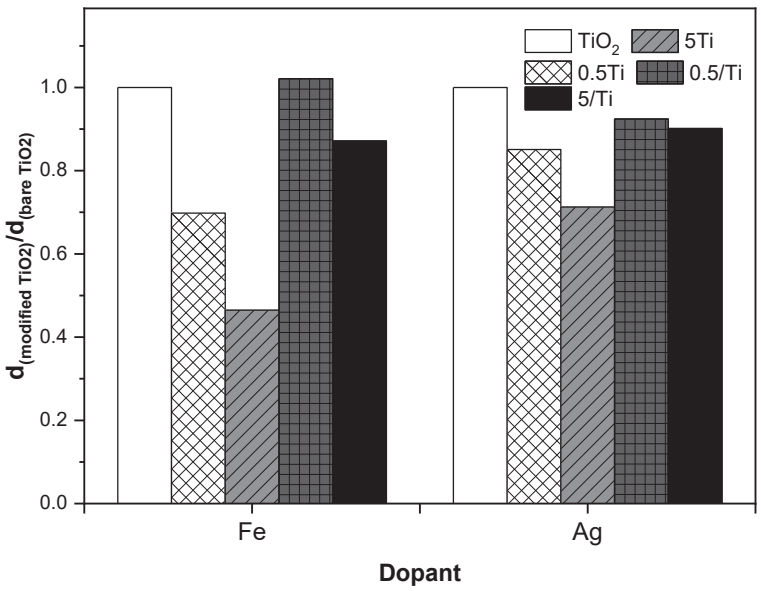

Figure V.3. Effect of iron and silver on the crystallite size of TiO_2 particles, referred to the size of the undoped titanium oxide.

The total pore volume (Vp_T) was determined from the amount of nitrogen adsorbed at a relative pressure of 0.98, assuming the density of the nitrogen condensed in the pores being equal to that of liquid nitrogen at 77 K (0.81 g/cm^3). Bare TiO_2 showed a S_{BET} of 78 m^2/g and a pore volume of 0.211 cm^3/g, the amount of adsorbed N_2 increased for Fe5Ti whereas the amount adsorbed by Ag5Ti was significantly smaller. The textural properties of the samples were related to their particle size, increasing with the decreasing of crystallite size (see Figure V.3). This result suggests that doping Fe interferes the sol-gel process, reducing the crystallinity of TiO_2 and increasing its porosity. There is an exception in the case of Ag5Ti, the S_{BET} was 30 m^2/g and the pore volume decreased to 0.087 cm^3/g which might indicate that the silver oxide particles existed inside the pores or blocked the entrances of pore channels, decorating the surface (Chowdhury et al., 2016; Jabłońska et al., 2017). The same trends have been

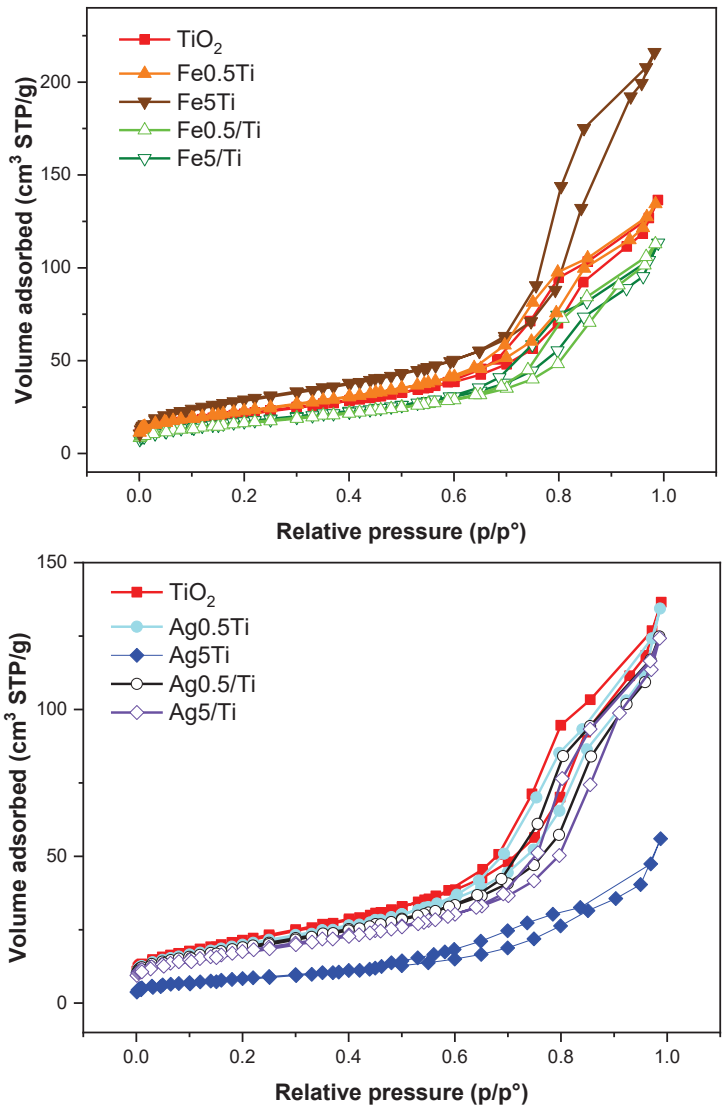

Figure V.4. Experimental adsorption-desorption isotherms of N_2 at 77 K.

found by (Li et al., 2008). As in the case of Fe, doping Ag can also interfere the sol-gel process, decreasing in this case the textural properties of TiO_2.

Table V.1. Specific surface areas, total pore volumes, pore diameter from nitrogen adsorption at 77 K and acidity properties of the samples.

Sample	S_{BET} (m^2/g)	Vp_T (cm^3/g)	dp_{BJH} (nm)	V_{NH3} (μmol/g)	V_{NH3} (μmol/m^2)
TiO_2	78	0.211	11.6	259	3.32
Fe0.5Ti	83	0.208	11.5	250	3.01
Fe5Ti	106	0.334	15.7	278	2.62
Fe0.5/Ti	60	0.175	11.9	171	2.85
Fe5/Ti	63	0.175	11.6	164	2.60
Ag0.5Ti	72	0.208	11.6	253	3.51
Ag5Ti	30	0.087	11.7	155	5.17
Ag0.5/Ti	68	0.193	11.7	217	3.19
Ag5/Ti	63	0.192	11.7	158	2.51

S_{BET}: specific surface area from the BET method; Vp_T: specific total pore volume; dp_{BJH}: pore diameter from the BJH method; V_{NH3}: chemisorbed NH_3 volume.

The surface composition and chemical state of the catalysts are investigated by X-ray photoelectron spectroscopy. The XPS spectra of the samples are included in Figure V.5.

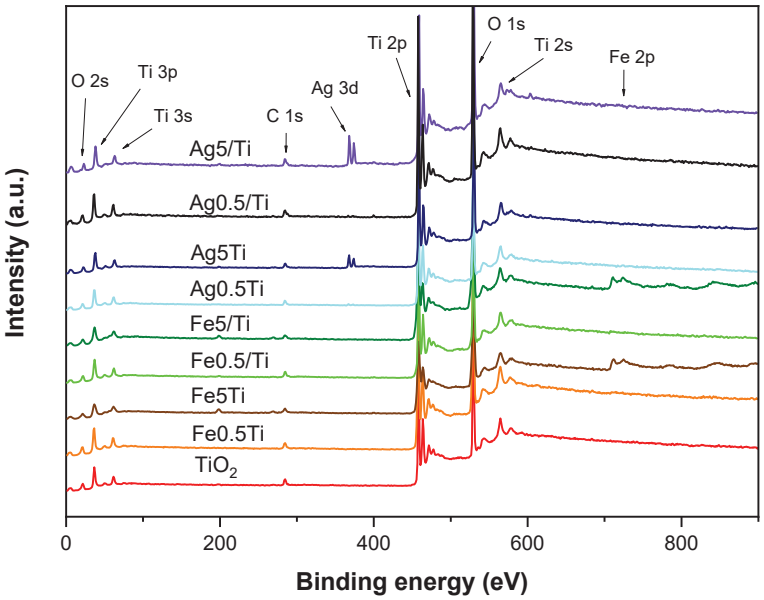

Figure V.5. Overall XPS spectra for the TiO_2 samples.

In the survey spectrum, the peak at 284.6 eV is associated to C 1s and was used as a reference to locate the other peaks. Peaks for Ti, O, Fe and Ag can also be observed. Both the surface concentration (% atomic) and the binding energies obtained from XPS analysis are included in Table V.2. In the case of iron, the percentage in the surface is in the same order to that used in the synthesis, while silver percentage is far from it.

Table V.2. Surface concentration (% atomic) and XPS signals (eV) obtained from XPS analysis of the catalysts.

Sample	C	O	Ti	X[a]	Formula[b]	O 1s	Ti 2p	
TiO_2	8.3	60.1	31.6		$TiO_{1.90}$	529.8	458.6	464.3
Fe0.5Ti	6.9	61.4	31.2	0.5	$TiO_{1.97}Fe_{0.02}$	529.4	458.2	463.9
Fe5Ti	8.0	62.0	25.6	4.4	TiO_2 $0.17FeO_{2.4}$	529.8	458.7	464.3
Fe0.5/Ti	8.5	59.9	31.3	0.2	$TiO_{1.91}Fe_{0.006}$	529.7	458.4	464.2
Fe5/Ti	6.2	62.7	27.0	4.1	$TiO_2 \cdot 0.15FeO_{2.1}$	529.3	457.9	463.4
Ag0.5Ti	7.2	60.8	31.9	0.1	$TiO_{1,91}Ag_{0.004}$	530.1	459.0	464.8
Ag5Ti	6.2	61.4	31.2	1.2	$TiO_{1.97}Ag_{0.04}$	530.3	458.9	464.7
Ag0.5/Ti	8.3	60.7	29.7	0.1	$TiO_{2.04}Ag_{0.003}$	529.8	458.6	464.3
Ag5/Ti	9.2	59.4	29.1	2.3	$TiO_{2.03}Ag_{0.08}$	529.8	458.7	464.4

[a] doping elements. [b] proposed elemental formula of the compounds on the surface of the solids.

The Ti $2p_{3/2}$ and Ti $2p_{1/2}$ spin-orbital splitting photoelectrons for pure TiO_2 are located at 458.6 and 464.3, respectively, with a quantified splitting of 5.7 eV (see Figure V.6a and Table V.2). These values match the characteristic spectrum of Ti^{4+} for anatase TiO_2 (Moulder and Chastain, 1992). These binding energies are not greatly affected by the presence of the doping agent in TiO_2 host lattices, indicating low concentrations of dopant ion. In the case of iron, the shift was always towards lower binding energies, which confirms the incorporation of iron into the titanium oxide lattice (Matsumoto et al., 2010). When silver was added, the Ti 2p binding energies of silver loaded catalysts are equal, in Ag0.5/Ti, or higher to that of bare-TiO_2. This shift may occur because of the transfer of conduction band electrons of TiO_2 to the surface of the silver oxide, which results in a decrease in the outer electron cloud density of Ti ions, leading to an

increase in binding energy values (Guin et al., 2007; Bahadur et al., 2011). Only one peak was recorded in the O 1s spectra (Figure V.6b). The main peak shifts on loading the dopants were in the same order to those observed in the positions of the Ti 2p peaks. It can be observed that signals of Ag0.5/Ti did not change with respect to those of TiO_2 which indicates that the TiO_2 lattice was not altered. If the atomic concentration ratio between O 1s to Ti 2p is taken into account, it is close to 2 in all samples, indicating that the surfaces are not hydrated or hydroxylated. The signals of Fe are weak, due to the low doping level (see Figure V.6c). The binding energies from 711.0 to 711.8 eV and from 725.4 to 726.0 eV should be assigned to $2p_{3/2}$ and $2p_{1/2}$ of Fe^{3+}. There is a positive shift with respect to those of Fe_2O_3 (710.7 eV for $2p_{3/2}$ and 724.3 eV for $2p_{1/2}$) indicating a more positively charged surface Fe^{3+} and a possible diffusion of Fe^{3+} into the anatase lattice, forming Fe-O-Ti bonds. As this changes the electron density of Ti^{4+} and O^{2-} and alters the charge distributions of the surface atoms, it can also improve the photocatalytic performance of the oxides (Abazović et al., 2009).

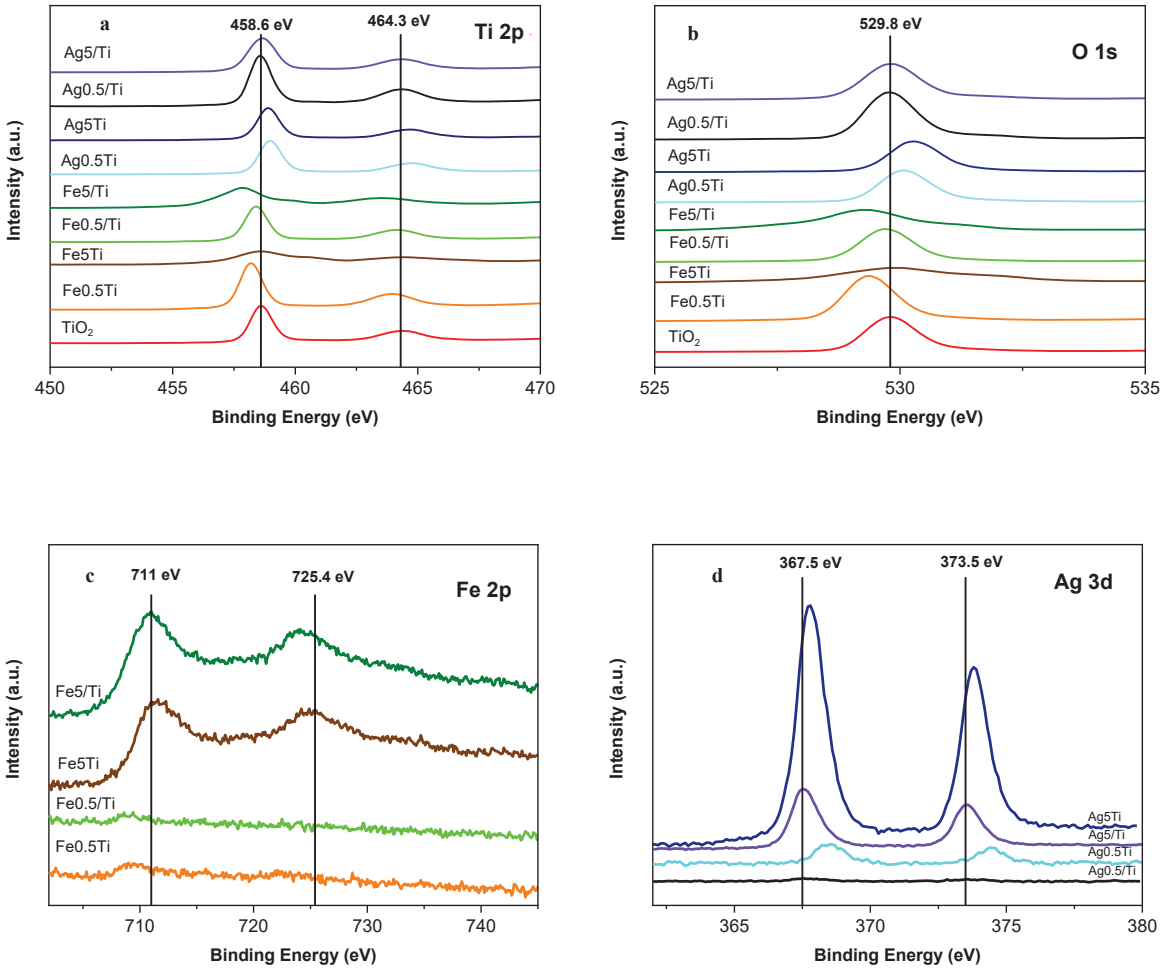

Figure V.6. XPS spectra of Ti 2p (a), O 1s (b), Fe 2p (c) and Ag 3d (d) of the samples.

The characteristic double peaks (see Figure V.6d) for Ag were observed at binding energies from 367.5 to 367.8 eV and from 373.5 to 373.8 eV for Ag $3d_{5/2}$ and Ag $3d_{3/2}$ respectively, with a separation of 6 eV. Due to the same binding energies of Ag^+ and Ag^0, it is difficult to know the oxidation state. Usually a Ag $3d_{5/2}$ value between 366 and 368 eV is assigned to Ag^+ and values from 368 upwards are attributed to Ag^0 (Kumar et al., 2015). It has been reported that due to the high redox potential, Ag^+ ions gradually reduced into Ag^0 by heat and TiO_2 photocatalytic reduction (Lai et al., 2008). These results are not possible to confirm from XRD because no silver species are detected.

The H_2-TPR profiles are shown in Figure V.7. The profiles obtained for unsupported Fe_2O_3 and Ag_2O have been also included as insets in the top of Figures V.7a and V.7b.

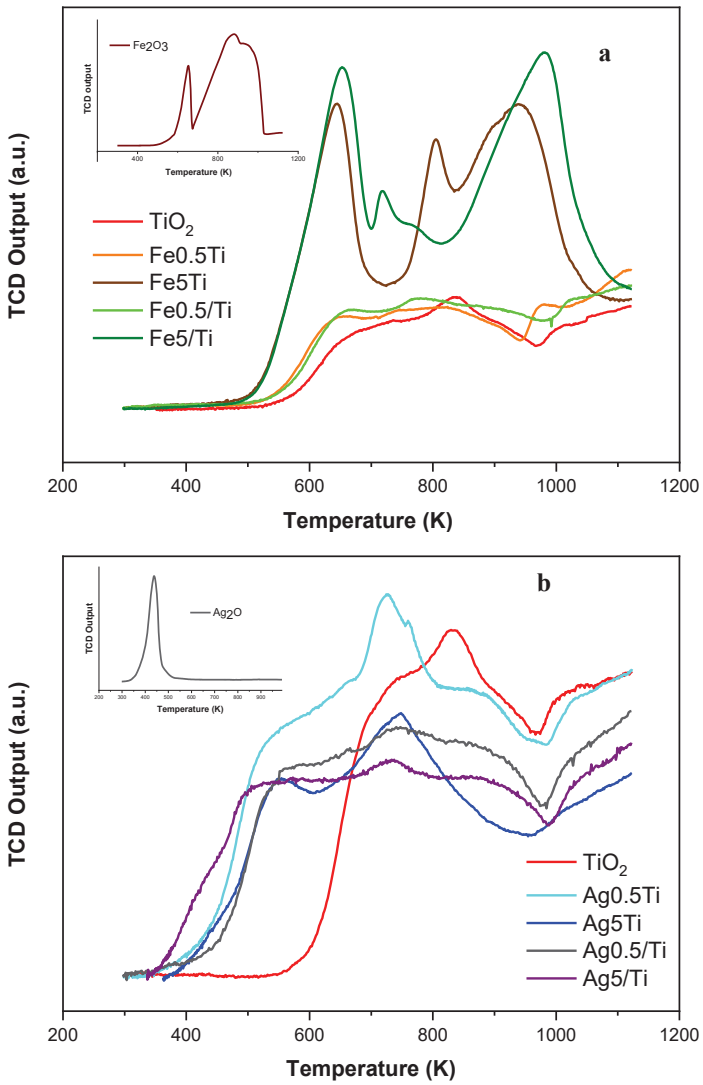

Figure V.7. H_2-TPR profile of (a) Fe-TiO_2 and (b) Ag-TiO_2 samples.

These results allow comparison of the profiles obtained when these oxides are supported on TiO_2. Usually TiO_2 is reluctant to reduce. In presence of hydrogen, the reduction temperature is reported at 1573 K (Dewan et al., 2009). However, a partial reduction of some Ti^{4+} to Ti^{3+} at lower temperatures and the dehydroxylation of TiO_2 on the surface is usually reported (Zhu et al., 2000; Inturi et al., 2014). In our sample, this occurs at 838 K. TPR results show that the interaction of TiO_2 with transition metals is different in each catalyst, with the reduction transition depending on the metal dispersion, particle size and the interaction between both parts. When iron was incorporated to the particles, there were no significant changes with the 0.5 wt.% concentration, but for the samples with 5 wt.% iron, both doped and impregnated, there was a significant increase in the hydrogen consumption. The peaks in both samples have been assigned to iron, as they were related with those of a Fe_2O_3 sample used as a reference (see Figure V.7a). An effect was observed close to 633 K which was assigned to the fraction of readily reducible $Fe^{3+} \rightarrow Fe^{2+}$ iron oxide particles. Another peak appearing at 953 K is assigned to the reduction of Fe^{2+} to metallic iron (Inturi et al., 2014).

The H_2-TPR profiles of the silver samples were presented in Figure V.7b. Its H_2 consumption was inferior to that of TiO_2 and the TPR profiles of the samples containing silver differentiate only in an earlier start of oxygen consumption, with a small reduction peak of Ag_2O at around 533 K (Prakash et al., 2015). It may be considered than, for the same metallic mass content, the number of mole of Ag is approximately the half of that of iron, and it may be in the form of Ag^+, exchanging only one electron, leading to low intense effects. The high dispersion of silver species and the interaction with TiO_2 justifies the high reduction temperature. The heterojunction interactions between Ag_2O and TiO_2 at 733 K is evidenced by the second peak of the H_2-TPR curve (Wang et al., 2017).

Ammonia chemisorption provides an estimation of both Brönsted and Lewis acidity. As amphoteric compounds, titanium oxides adsorb NH_3 when there are free available sites, thus revealing the Lewis acidity of the surface (Markovits et al., 1996). The total acidity data, expressed as μmol of chemisorbed NH_3 per gram of sample and per m^2 of surface, are given in Table V.1. The variation of acidity runs parallel to the change of surface area and the only sample where the amount of NH_3 adsorbed is greater than that of TiO_2 is Fe5Ti. When comparing the amount adsorbed by m^2 of

surface area, in the case of iron doped samples, the amount adsorbed decreases as more iron is added (from 3.3 to 2.6 μmol/m^2). However, the surface acidity increased for TiO_2 after Ag doping (from 3.3 to 5.2 μmol/m^2), indicating generation of additional acid sites on the Ag-TiO_2 framework. These results are in accord to those reported elsewhere (Adán et al., 2007; Jabłońska et al., 2017).

V.3.2. PHOTOCATALYTIC DEGRADATION OF SALICYLIC ACID

The decrease in contaminant concentration, for 15 $mg_{salicylic\ acid}/dm^3$ and 1000 $mg_{catalyst}/dm^3$, with irradiation time is shown in Figure V.8. $C_{0,t}$ represents the concentration of salicylic acid in the solution before illumination and at a time t after illumination has started. The catalysts with the highest concentration of iron are the most effective ones. In the case of the catalysts containing Ag, there is no improvement in the catalytic behavior, probably because the Ag contents used are outside the range of improvement of the activity. The results obtained indicate that the presence of Fe favors the action of TiO_2 in the degradation of salicylic acid, while the presence of Ag decreases the action of the catalyst. A behavior similar to that included in Figure V.8 has been obtained when using other catalyst weights and a lower concentration of salicylic acid, see Figure V.9. In this case, the degradation conversion of salicylic acid is represented according to the type of catalyst, the weight and the concentration of acid.

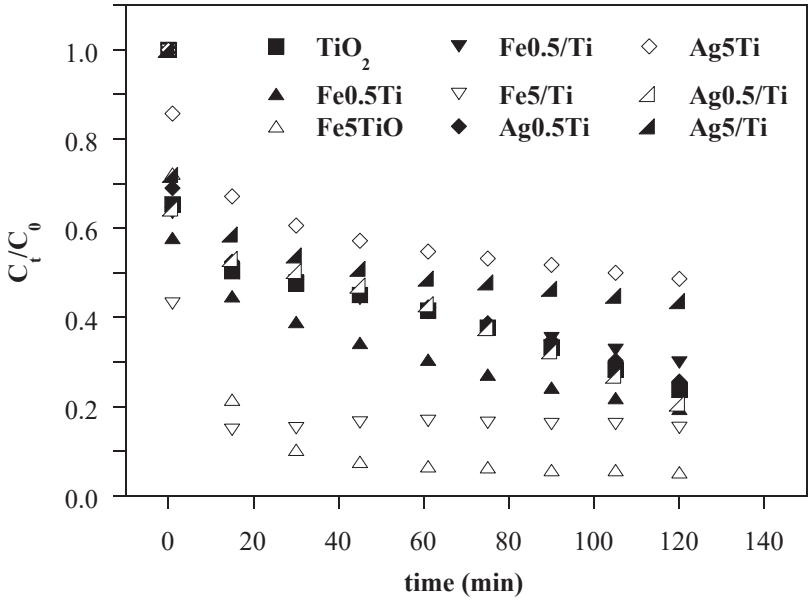

Figure V.8. Evolution with irradiation time of the concentration of salicylic acid, with respect to the initial concentration, using doped TiO_2 as catalyst (15 $mg_{salicylic\ acid}/dm^3$ and 1000 $mg_{catalyst}/dm^3$).

The results show that as the catalyst weight increases, for the same concentration of salicylic acid, the conversion also increases. The conversion of degradation is greater for the concentration of 5 $mg_{salicylic\ acid}/dm^3$, compared to the concentration of 15 $mg_{salicylic\ acid}/dm^3$. The preparation method and the content do not show a clear trend. A control test was also carried out under the same conditions of the photocatalytic test, with 15 $mg_{salicylic\ acid}/dm^3$ and under UV-radiation, but without using the catalyst. The degradation of the organic molecule was low, almost negligible, only 1.2% of the molecule was degraded after 2 h of UV radiation and could thus be ignored in comparison. This result confirms that the salicylic acid degradation is due to the presence of TiO_2. Various authors found that the incorporation of Fe in an adequate content increases the catalytic behavior of undoped TiO_2 for the liquid phase photocatalytic decolorization of active yellow XRG dye (Zhu et al., 2004, 2006) and the degradation of formic acid (Araña et al., 2003), methyl orange (Zhang et al., 2006), acetaldehyde (Oh et al., 2003), malachite green (Vijayan et al., 2009; Narayana et al., 2011), and 2,4,6-trichlorophenol, among other organic molecules. When Fe-doped TiO_2 catalysts are irradiated by light, in our case Fe0.5Ti and Fe5Ti, a 3d electron may be excited from Fe^{3+} to the TiO_2 conduction band leaving behind Fe^{4+} in the energy level of Fe^{3+}/Fe^{4+}. Fe^{4+} can oxidize OH^- in the salicylic acid solution to form hydroxyl radical •OH.

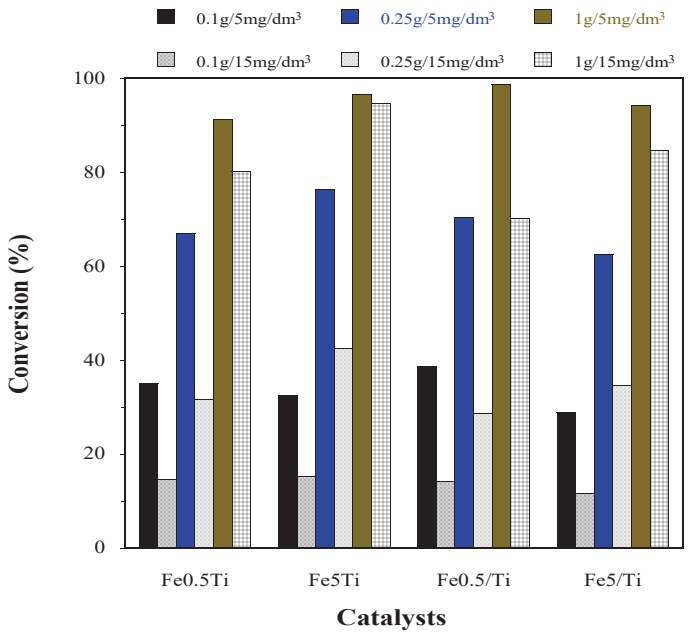

Figure V.9. Comparison of the degradation conversion of salicylic acid with the type of Fe catalyst, at a time of 120 min, using three weights (0.1, 0.25 and 1.0 $g_{catalyst}$) and two concentrations (5 and 15 $mg_{salicylic\ acid}/dm^3$).

In this case, the photogenerated electrons can reduce dissolved oxygen molecules to produce O_2^- radical anions, which are the responsible for the degradation of salicylic acid. When Fe_2O_3 nanoparticles were deposited on the surface of TiO_2, in our case Fe0.5/Ti and Fe5/Ti, Fe_2O_3 can be easily activated and yield charge carriers under light irradiation. The photogenerated electrons migrated from the conduction band of Fe_2O_3 to the conduction band of TiO_2 under the action of built-in electric field and the concentration gradient of electrons, while photogenerated holes were accumulated in the valence band of Fe_2O_3. The electrons on the conduction band of TiO_2 can be further transferred to dissolved oxygen molecules to form O_2^-, while the accumulated holes on the valence band of Fe_2O_3 can be consumed by participating in the reaction with OH^- in the salicylic acid solution to produce •OH (Peng et al., 2010). A detrimental catalytic performance is also reported in some cases, related to the blocking of the core level semiconductor surface by the presence of high Fe contents (Ranjit and Viswanathan, 1997; Zhu et al., 2004; Vijayan et al., 2009). Therefore, Fe doped or impregnated is responsible for the catalytic performance of Fe-Ti catalysts. In the case of Ag, various authors have reported that an optimum amount of doping silver is also necessary for the effective degradation reactions (Sung-Suh et al., 2004; Coleman et al., 2005; Xin et al., 2005; Guin et al., 2007; Seery et al., 2007; Cao et al., 2008; Zielińska et al., 2010). The catalytic performance is attributed to finely dispersed silver oxide species, which acts as an electron trap/electron-hole separation center, creating a low-energy band gap. At high silver content, the silver particles can act as recombination centers, decreasing the photocatalytic activity of TiO_2. In this situation, (Gunawan et al., 2009) also indicate that the amount of doping silver may decrease in the surface of TiO_2 and block the surface reaction sites, decreasing the photocatalytic performance.

The acid/base characteristics of the catalysts can intervene in the catalytic behavior, directly or through the structural changes induced by the incorporated metals. Thus, the catalysts prepared by wet impregnation decrease the acid centers of TiO_2, while in the sol-gel process the metals increase them. The results included in Table V.1 and Figure V.8 seem to indicate that they increase the removal capacity of salicylic acid, but this aspect should be confirmed with other metallic contents, as well as with other organic molecules.(Adán et al., 2007) also conclude in this sense, indicating that other structural properties of the catalysts seem to have a minor effect on the photocatalytic behavior of these systems.

To evaluate the possible leaching of Ag and Fe, samples of the water after the experiment were taken and analyzed with a radial ICP, determining the concentration of the dopants. Silver was not found and the highest concentration of iron was 4.84 mg/dm^3 (in the 1000 mg_{Fe5Ti}/dm^3 and 5 $mg_{salicylic\ acid}/dm^3$ experiment). A new experiment was carried out, using 4.84 mg/dm^3 of iron (in the form of Fe_2O_3) as catalyst, instead of anatase. A little more than 10% of the 5 mg/dm^3 of salicylic acid was degraded, result that does not justify that the catalytic behavior found for FeTi can be related to Fe dissolved in water.

The differences between the characteristics summarized in Table V.1 do not have a significant effect on the photocatalytic behavior of the solids included in this study, since the catalysts with lower performance among those modified with Fe (Fe0.5Ti and Fe0.5/Ti) show surface areas of the same order (83 and 60 m^2/g) than the synthesized TiO_2 (78 m^2/g). This observation can verify that the higher activity of the modified Fe-Ti compared to TiO_2 is not a result of the differences found in the textural properties, but rather is a consequence of the active phase structure.

Experiments were also performed in order to compare our TiO_2 catalyst with a commercial one (Titanium(IV) oxide, anatase >99%, Sigma-Aldrich). The results are shown in Figure V.10.

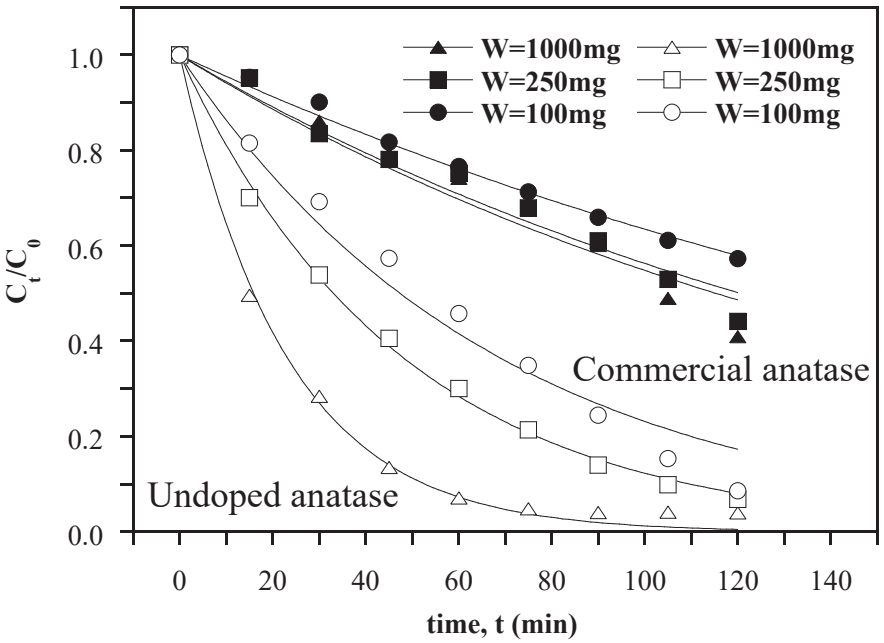

Figure V.10. Comparison of the evolution with irradiation time of the concentration of salicylic acid, with respect to the initial concentration, using undoped TiO_2 and a commercial TiO_2 anatase as catalysts (5 $mg_{salicylic\ acid}/dm^3$).

With a 5 $mg_{salicylic\ acid}/dm^3$ concentration of salicylic acid, TiO_2 degraded more than 90% at all the concentrations whereas commercial anatase degraded between 40 and 60%. These results show that the catalysts prepared in this work are much more active than the commercial catalyst. Although in the two catalysts studied TiO_2 has an anatase-like structure, there are other factors to be taken into account that affect the catalytic behavior: method of preparation, particle size, textural and acid-base properties. To study these factors would be important in order to explain the different catalytic behavior found. For a quantitative comparison between the catalysts, the kinetic constants were determined assuming a first-order rate equation. The undoped TiO_2 catalyst shows the highest kinetic constant values, between 0.015 and 0.044 cm^{-1} as the weight catalyst increase, in comparison to the commercial TiO_2, between 0.0045 and 0.0060 cm^{-1} as the weight catalyst increase, thus indicating the highest performance.

V.4. SUMMARY AND CONCLUSIONS

TiO_2 doped and impregnated with iron and silver at various mass contents were prepared from Ti(IV) isopropoxide and calcined at 673 K. The results of PXRD show the crystalline structure of anatase, with no signals from dopants due to its low content or high dispersion on titanium dioxide. The textural analyses of the catalysts allowed to observe an increase of these properties when the sol-gel method was used. The surface and the volume of pores decrease when using the technique of wet impregnation. The presence of Fe_2O_3 was confirmed by H_2-TPR analyses, in the case of catalysts with high Fe content. In the case of the catalysts with Ag, its high dispersion seems to be confirmed. The degradation tests of salicylic acid indicate that doping the catalyst with iron can improve its effectiveness, while the largest performance was observed for the catalysts containing 5 wt.% Fe.

V.5. REFERENCES

Abazović, N.D., Mirenghi, L., Janković, I.A., Bibić, N., Šojić, D. V., Abramović, B.F., Čomor, M.I., 2009. Synthesis and characterization of rutile TiO_2 nanopowders doped with iron ions. Nanoscale Res. Lett. 4, 518–525. https://doi.org/10.1007/s11671-009-9274-1

Adán, C., Bahamonde, A., Fernández-García, M., Martínez-Arias, A., 2007. Structure

and activity of nanosized iron-doped anatase TiO_2 catalysts for phenol photocatalytic degradation. Appl. Catal. B Environ. 72, 11–17. https://doi.org/10.1016/j.apcatb.2006.09.018

Ambrus, Z., Balázs, N., Alapi, T., Wittmann, G., Sipos, P., Dombi, A., Mogyorósi, K., 2008. Synthesis, structure and photocatalytic properties of Fe(III)-doped TiO_2 prepared from $TiCl_3$. Appl. Catal. B Environ. 81, 27–37. https://doi.org/10.1016/j.apcatb.2007.11.041

Araña, J., González Díaz, O., Doña Rodríguez, J.M., Herrera Melián, J.A., Garriga i Cabo, C., Pérez Peña, J., Carmen Hidalgo, M., Navío-Santos, J.A., 2003. Role of Fe^{3+}/Fe^{2+} as TiO_2 dopant ions in photocatalytic degradation of carboxylic acids. J. Mol. Catal. A Chem. 197, 157–171. https://doi.org/10.1016/S1381-1169(02)00591-5

Arfanis, M.K., Adamou, P., Moustakas, N.G., Triantis, T.M., Kontos, A.G., Falaras, P., 2017. Photocatalytic degradation of salicylic acid and caffeine emerging contaminants using titania nanotubes. Chem. Eng. J. 310, 525–536. https://doi.org/10.1016/j.cej.2016.06.098

Ashton, D., Hilton, M., Thomas, K. V., 2004. Investigating the environmental transport of human pharmaceuticals to streams in the United Kingdom. Sci. Total Environ. 333, 167–184. https://doi.org/10.1016/j.scitotenv.2004.04.062

Badawy, M.I., Souaya, E.M.R., Gad-Allah, T.A., Abdel-Wahed, M.S., Ulbricht, M., 2014. Fabrication of Ag/TiO_2 photocatalyst for the treatment of simulated hospital wastewater under sunlight. Environ. Prog. Sustain. Energy 33, 886–894. https://doi.org/10.1002/ep.11869

Bahadur, N., Jain, K., Pasricha, R., Govind, Chand, S., 2011. Selective gas sensing response from different loading of Ag in sol-gel mesoporous titania powders. Sensors Actuators, B Chem. 159, 112–120. https://doi.org/10.1016/j.snb.2011.06.058

Bai, J., Li, Y., Jin, P., Wang, J., Liu, L., 2017. Facile preparation 3D ZnS nanospheres-reduced graphene oxide composites for enhanced photodegradation of norfloxacin. J. Alloys Compd. 729, 809–815. https://doi.org/10.1016/j.jallcom.2017.07.057

Barbosa, L.V., Marçal, L., Nassar, E.J., Calefi, P.S., Vicente, M.A., Trujillano, R., Rives, V., Gil, A., Korili, S.A., Ciuffi, K.J., De Faria, E.H., 2015. Kaolinite-titanium oxide nanocomposites prepared via sol-gel as heterogeneous photocatalysts for dyes degradation. Catal. Today 246, 133–142. https://doi.org/10.1016/j.cattod.2014.09.019

Cao, Y., Tan, H., Shi, T., Tang, T., Li, J., 2008. Preparation of Ag-doped TiO_2 nanoparticles for photocatalytic degradation of acetamiprid in water. J. Chem. Technol. Biotechnol. 83, 546–552. https://doi.org/10.1002/jctb.1831

Chaudhari, S.M., Gawal, P.M., Sane, P.K., Sontakke, S.M., Nemade, P.R., 2018. Solar light-assisted photocatalytic degradation of methylene blue with Mo/TiO_2: a comparison with Cr- and Ni-doped TiO_2. Res. Chem. Intermed. 44, 3115–3134. https://doi.org/10.1007/s11164-018-3296-1

Chen, X., Mao, S.S., 2007. Titanium dioxide nanomaterials: Synthesis, properties, modifications and applications. Chem. Rev. 107, 2891–2959. https://doi.org/10.1021/cr0500535

Choi, H., Antoniou, M.G., Pelaez, M., De La Cruz, A.A., Shoemaker, J.A., Dionysiou, D.D., 2007. Mesoporous nitrogen-doped TiO_2 for the photocatalytic destruction of the cyanobacterial toxin microcystin-LR under visible light irradiation. Environ. Sci. Technol. 41, 7530–7535. https://doi.org/10.1021/es0709122

Chowdhury, I.H., Ghosh, S., Naskar, M.K., 2016. Aqueous-based synthesis of mesoporous TiO_2 and Ag-TiO_2 nanopowders for efficient photodegradation of methylene blue. Ceram. Int. 42, 2488–2496. https://doi.org/10.1016/j.ceramint.2015.10.049

Coleman, H.M., Chiang, K., Amal, R., 2005. Effects of Ag and Pt on photocatalytic degradation of endocrine disrupting chemicals in water. Chem. Eng. J. 113, 65–72. https://doi.org/10.1016/j.cej.2005.07.014

Dewan, M.A.R., Zhang, G., Ostrovski, O., 2009. Carbothermal reduction of titania in different gas atmospheres. Metall. Mater. Trans. B 40, 62–69. https://doi.org/10.1007/s11663-008-9205-z

Doi, H., Horie, T., 2010. Salicylic acid-induced hepatotoxicity triggered by oxidative stress. Chem. Biol. Interact. 183, 363–368.

https://doi.org/10.1016/j.cbi.2009.11.024

Garza-Campos, B., Brillas, E., Hernández-Ramírez, A., El-Ghenymy, A., Guzmán-Mar, J.L., Ruiz-Ruiz, E.J., 2016. Salicylic acid degradation by advanced oxidation processes. Coupling of solar photoelectro-Fenton and solar heterogeneous photocatalysis. J. Hazard. Mater. 319, 34–42. https://doi.org/10.1016/j.jhazmat.2016.02.050

Gil, A., García, A.M., Fernández, M., Vicente, M.A., González-Rodríguez, B., Rives, V., Korili, S.A., 2017. Effect of dopants on the structure of titanium oxide used as a photocatalyst for the removal of emergent contaminants. J. Ind. Eng. Chem. 53, 183–191. https://doi.org/10.1016/j.jiec.2017.04.024

Gil, A., Taoufik, N., García, A.M., Korili, S.A., 2019. Comparative removal of emerging contaminants from aqueous solution by adsorption on an activated carbon. Environ. Technol. 40, 3017–3030. https://doi.org/10.1080/09593330.2018.1464066

Guin, D., Manorama, S. V., Latha, J.N.L., Singh, S., 2007. Photoreduction of silver on bare and colloidal TiO_2 nanoparticles/nanotubes: Synthesis, characterization, and tested for antibacterial outcome. J. Phys. Chem. C 111, 13393–13397. https://doi.org/10.1021/jp072646k

Gunawan, C., Teoh, W.Y., Marquis, C.P., Lifia, J., Amal, R., 2009. Reversible Antimicrobial Photoswitching in Nanosilver. Small 5, 341–344. https://doi.org/10.1002/smll.200801202

Halling-Sorensen, B., Halling-Sorensen, B., Nielsen, S.N., Nielsen, S.N., Lanzky, P.F., Lanzky, P.F., Ingerslev, F., Ingerslev, F., Holten Lutzhoft, H.C., Holten Lutzhoft, H.C., S.E., J., S.E., J., 1998. Occurence, fate and effects of pharmaceuticals substance in the environment - A review. Chemosphere 36, 357–393. http://dx.doi.org/10.1016/S0045-6535(97)00354-8

Hoffmann, M.R., Martin, S.T., Choi, W., Bahnemann, D.W., 1995. Environmental Applications of Semiconductor Photocatalysis. Chem. Rev. 95, 69–96. https://doi.org/10.1021/cr00033a004

Huber, M.M., Canonica, S., Park, G.Y., Von Gunten, U., 2003. Oxidation of

pharmaceuticals during ozonation and advanced oxidation processes. Environ. Sci. Technol. 37, 1016–1024. https://doi.org/10.1021/es025896h

Inturi, S.N.R., Boningari, T., Suidan, M., Smirniotis, P.G., 2014. Visible-light-induced photodegradation of gas phase acetonitrile using aerosol-made transition metal (V, Cr, Fe, Co, Mn, Mo, Ni, Cu, Y, Ce, and Zr) doped TiO_2. Appl. Catal. B Environ. 144, 333–342. https://doi.org/10.1016/j.apcatb.2013.07.032

Jabłońska, M., Ciptonugroho, W., Góra-Marek, K., Al-Shaal, M.G., Palkovits, R., 2017. Preparation, characterization and catalytic performance of Ag-modified mesoporous TiO_2 in low-temperature selective ammonia oxidation into nitrogen and water vapour. Microporous Mesoporous Mater. 245, 31–44. https://doi.org/10.1016/j.micromeso.2017.02.070

Jaramillo-Páez, C., Navío, J.A., Hidalgo, M.C., Bouziani, A., Azzouzi, M. El, 2017. Mixed α-Fe_2O_3/Bi_2WO_6 oxides for photoassisted hetero-Fenton degradation of Methyl Orange and Phenol. J. Photochem. Photobiol. A Chem. 332, 521–533. https://doi.org/10.1016/j.jphotochem.2016.09.031

Kanakaraju, D., Glass, B.D., Oelgemöller, M., 2014. Titanium dioxide photocatalysis for pharmaceutical wastewater treatment. Environ. Chem. Lett. 12, 27–47. https://doi.org/10.1007/s10311-013-0428-0

Kumar, R., Rashid, J., Barakat, M.A., 2015. Zero valent Ag deposited TiO_2 for the efficient photocatalysis of methylene blue under UV-C light irradiation. Colloids Interface Sci. Commun. 5, 1–4. https://doi.org/10.1016/j.colcom.2015.05.001

Lai, Y., Chen, Y., Zhuang, H., Lin, C., 2008. A facile method for synthesis of Ag/TiO_2 nanostructures. Mater. Lett. 62, 3688–3690. https://doi.org/10.1016/j.matlet.2008.04.055

Li, H., Gui, X., Ji, C., Li, P., Li, Z., Zhang, L., Shi, E., Zhu, K., Wei, J., Wang, K., Zhu, H., Wu, D., Cao, A., 2012. Photocatalytic, recyclable CdS nanoparticle-carbon nanotube hybrid sponges. Nano Res. 5, 265–271. https://doi.org/10.1007/s12274-012-0206-5

Li, X.S., Fryxell, G.E., Wang, C., Engelhard, M.H., 2008. The synthesis of Ag-doped mesoporous TiO_2. Microporous Mesoporous Mater. 111, 639–642. https://doi.org/10.1016/j.micromeso.2007.07.042

Liu, F., He, H., 2010. Structure−Activity Relationship of Iron Titanate Catalysts in the Selective Catalytic Reduction of NO_x with NH_3. J. Phys. Chem. C 114, 16929–16936. https://doi.org/10.1021/jp912163k

Loos, R., Locoro, G., Contini, S., 2010. Occurrence of polar organic contaminants in the dissolved water phase of the Danube River and its major tributaries using SPE-LC-MS2 analysis. Water Res. 44, 2325–2335. https://doi.org/10.1016/j.watres.2009.12.035

Markovits, A., Ahdjoudj, J., Minot, C., 1996. A theoretical analysis of NH_3 adsorption on TiO_2. Surf. Sci. 365, 649–661. https://doi.org/10.1016/0039-6028(96)00753-4

Matsumoto, Y., Katayama, M., Abe, T., Ohsawa, T., Ohkubo, I., Kumigashira, H., Oshima, M., Koinuma, H., 2010. Chemical trend of Fermi-level shift in transition metal-doped TiO_2 films. J. Ceram. Soc. Japan 2, 993–996. https://doi.org/10.2109/jcersj2.118.993

Mogal, S.I., Gandhi, V.G., Mishra, M., Tripathi, S., Shripathi, T., Joshi, P.A., Shah, D.O., 2014. Single-Step Synthesis of Silver-Doped Titanium Dioxide: Influence of Silver on Structural, Textural, and Photocatalytic Properties. Ind. Eng. Chem. Res. 53, 5749–5758. https://doi.org/10.1021/ie404230q

Mohite, V.S., Mahadik, M.A., Kumbhar, S.S., Hunge, Y.M., Kim, J.H., Moholkar, A. V., Rajpure, K.Y., Bhosale, C.H., 2015. Photoelectrocatalytic degradation of benzoic acid using Au doped TiO_2 thin films. J. Photochem. Photobiol. B Biol. 142, 204–211. https://doi.org/10.1016/j.jphotobiol.2014.12.004

Mompelat, S., Le Bot, B., Thomas, O., 2009. Occurrence and fate of pharmaceutical products and by-products, from resource to drinking water. Environ. Int. 35, 803–814. https://doi.org/10.1016/j.envint.2008.10.008

Moulder, J.F., Chastain, J., 1992. Handbook of X-ray Photoelectron Spectroscopy: A Reference Book of Standard Spectra for Identification and Interpretation of XPS Data. Physical Electronics Division, Perkin-Elmer Corporation.

Nagy, I., Balogh, A., 2013. New Developments in Metal Oxides Research, Chemistry research and applications. Nova Science Publishers, Incorporated.

Nakata, K., Fujishima, A., 2012. TiO_2 photocatalysis: Design and applications. J.

Photochem. Photobiol. C Photochem. Rev. 13, 169–189. https://doi.org/10.1016/j.jphotochemrev.2012.06.001

Narayana, R.L., Matheswaran, M., Aziz, A.A., Saravanan, P., 2011. Photocatalytic decolourization of basic green dye by pure and Fe, Co doped TiO_2 under daylight illumination. Desalination 269, 249–253. https://doi.org/10.1016/j.desal.2010.11.007

Navio, J. a, Colón, G., As, M., Real, C., Litter, M.I., Navío, J.A., Colón, G., Macías, M., Real, C., Litter, M.I., 1999. Iron-doped titania semiconductor powders prepared by a sol-gel method. Part I: Synthesis and characterization. Appl. Catal. A Gen. 177, 111–120. https://doi.org/10.1016/S0926-860X(98)00255-5

Navío, J.A., Colón, G., Trillas, M., Peral, J., Domènech, X., Testa, J.J., Padrón, J., Rodríguez, D., Litter, M.I., 1998. Heterogeneous photocatalytic reactions of nitrite oxidation and Cr(VI) reduction on iron-doped titania prepared by the wet impregnation method. Appl. Catal. B Environ. 16, 187–196. https://doi.org/10.1016/S0926-3373(97)00073-8

Nunes, B., Campos, J.C., Gomes, R., Braga, M.R., Ramos, A.S., Antunes, S.C., Correia, A.T., 2015. Ecotoxicological effects of salicylic acid in the freshwater fish Salmo trutta fario: Antioxidant mechanisms and histological alterations. Environ. Sci. Pollut. Res. 22, 667–678. https://doi.org/10.1007/s11356-014-3337-2

Oh, S.-M., Kim, S.-S., Lee, J.E., Ishigaki, T., Park, D.-W., 2003. Effect of additives on photocatalytic activity of titanium dioxide powders synthesized by thermal plasma. Thin Solid Films 435, 252–258. https://doi.org/10.1016/S0040-6090(03)00388-2

Parsons, S., 2005. Advanced Oxidation Processes for Water and Wastewater Treatment. https://doi.org/10.2166/9781780403076

Pecchi, G., Reyes, P., López, T., Gómez, R., Moreno, A., Fierro, J.L.G., Martínez-Arias, A., 2003. Catalytic Combustion of Methane on Fe-TiO_2 Catalysts Prepared by Sol-Gel Method. J. Sol-Gel Sci. Technol. 27, 205–214. https://doi.org/10.1023/A:1023758819596

Peng, L., Xie, T., Lu, Y., Fan, H., Wang, D., 2010. Synthesis, photoelectric properties and photocatalytic activity of the Fe_2O_3/TiO_2 heterogeneous photocatalysts. Phys. Chem. Chem. Phys. 12, 8033–8041. https://doi.org/10.1039/c002460k

Plavac, B., Grčić, I., Brnardić, I., Grozdanić, V., Papić, S., 2017. Kinetic study of salicylic acid photocatalytic degradation using sol–gel anatase thin film with enhanced long-term activity. React. Kinet. Mech. Catal. 120, 385–401. https://doi.org/10.1007/s11144-016-1090-x

Pliego, G., Zazo, J.A., Garcia-Muñoz, P., Munoz, M., Casas, J.A., Rodriguez, J.J., 2015. Trends in the Intensification of the Fenton Process for Wastewater Treatment: An Overview. Crit. Rev. Environ. Sci. Technol. 45, 2611–2692. https://doi.org/10.1080/10643389.2015.1025646

Prakash, M.G., Mahalakshmy, R., Krishnamurthy, K.R., Viswanathan, B., 2015. Studies on Ni-M (M=Cu, Ag, Au) bimetallic catalysts for selective hydrogenation of cinnamaldehyde. Catal. Today 263, 105–111. https://doi.org/10.1016/j.cattod.2015.09.053

Ranjit, K.T., Viswanathan, B., 1997. Synthesis, characterization and photocatalytic properties of iron-doped TiO_2 catalysts. J. Photochem. Photobiol. A Chem. 108, 79–84. https://doi.org/10.1016/S1010-6030(97)00005-1

Rao, K.V.S., Lavédrine, B., Boule, P., 2003. Influence of metallic species on TiO_2 for the photocatalytic degradation of dyes and dye intermediates. J. Photochem. Photobiol. A Chem. 154, 189–193. https://doi.org/10.1016/S1010-6030(02)00299-X

Rincón, A.-G., Pulgarin, C., 2006. Comparative evaluation of Fe^{3+} and TiO_2 photoassisted processes in solar photocatalytic disinfection of water. Appl. Catal. B Environ. 63, 222–231. https://doi.org/10.1016/j.apcatb.2005.10.009

Saravanan, R., Sacari, E., Gracia, F., Khan, M.M., Mosquera, E., Gupta, V.K., 2016. Conducting PANI stimulated ZnO system for visible light photocatalytic degradation of coloured dyes. J. Mol. Liq. 221, 1029–1033. https://doi.org/10.1016/j.molliq.2016.06.074

Seery, M.K., George, R., Floris, P., Pillai, S.C., 2007. Silver doped titanium dioxide nanomaterials for enhanced visible light photocatalysis. J. Photochem. Photobiol. A Chem. 189, 258–263. https://doi.org/10.1016/j.jphotochem.2007.02.010

Silva, A.M.T., Silva, C.G., Dražić, G., Faria, J.L., 2009. Ce-doped TiO_2 for

photocatalytic degradation of chlorophenol. Catal. Today 144, 13–18. https://doi.org/10.1016/j.cattod.2009.02.022

Sung-Suh, H.M., Choi, J.R., Hah, H.J., Koo, S.M., Bae, Y.C., 2004. Comparison of Ag deposition effects on the photocatalytic activity of nanoparticulate TiO_2 under visible and UV light irradiation. J. Photochem. Photobiol. A Chem. 163, 37–44. https://doi.org/10.1016/S1010-6030(03)00428-3

Thommes, M., Kaneko, K., Neimark, A. V., Olivier, J.P., Rodriguez-Reinoso, F., Rouquerol, J., Sing, K.S.W., 2015. Physisorption of gases, with special reference to the evaluation of surface area and pore size distribution (IUPAC Technical Report). Pure Appl. Chem. 87, 1051–1069. https://doi.org/10.1515/pac-2014-1117

Valcárcel, Y., Alonso, S.G., Rodríguez-Gil, J.L., Maroto, R.R., Gil, A., Catalá, M., 2011. Analysis of the presence of cardiovascular and analgesic/anti-inflammatory/antipyretic pharmaceuticals in river- and drinking-water of the Madrid Region in Spain. Chemosphere 82, 1062–1071. https://doi.org/10.1016/j.chemosphere.2010.10.041

Vijayan, P., Mahendiran, C., Suresh, C., Shanthi, K., 2009. Photocatalytic activity of iron doped nanocrystalline titania for the oxidative degradation of 2,4,6-trichlorophenol. Catal. Today 141, 220–224. https://doi.org/10.1016/j.cattod.2008.04.016

Vogna, D., Marotta, R., Napolitano, A., Andreozzi, R., D'Ischia, M., 2004. Advanced oxidation of the pharmaceutical drug diclofenac with UV/H_2O_2 and ozone. Water Res. 38, 414–422. https://doi.org/10.1016/j.watres.2003.09.028

Wang, C., Cai, X., Chen, Y., Cheng, Z., Luo, X., Mo, S., Jia, L., Lin, P., Yang, Z., 2017. Improved hydrogen production from glycerol photoreforming over sol-gel derived TiO_2 coupled with metal oxides. Chem. Eng. J. 317, 522–532. https://doi.org/10.1016/j.cej.2017.02.033

Xin, B., Jing, L., Ren, Z., Wang, B., Fu, H., 2005. Effects of simultaneously doped and deposited Ag on the photocatalytic activity and surface states of TiO_2. J. Phys. Chem. B 109, 2805–2809. https://doi.org/10.1021/jp0469618

Yang, Y., Zhang, C., Lai, C., Zeng, G., Huang, D., Cheng, M., Wang, J., Chen, F., Zhou, C., Xiong, W., 2018. BiOX (X = Cl, Br, I) photocatalytic nanomaterials:

Applications for fuels and environmental management. Adv. Colloid Interface Sci. 254, 76–93. https://doi.org/10.1016/j.cis.2018.03.004

Yoo, S.M., Rawal, S.B., Lee, J.E., Kim, J., Ryu, H.-Y., Park, D.-W., Lee, W.I., 2015. Size-dependence of plasmonic Au nanoparticles in photocatalytic behavior of Au/TiO_2 and Au@SiO_2/TiO_2. Appl. Catal. A Gen. 499, 47–54. https://doi.org/10.1016/j.apcata.2015.04.003

Zhang, H., Wang, G., Chen, D., Lv, X., Li, J., 2008. Tuning Photoelectrochemical Performances of Ag - TiO_2 Nanocomposites via Reduction / Oxidation of Ag Ti-C. Chem. Mater. 6543–6549. https://doi.org/10.1021/cm801796q

Zhang, X., Zhou, M., Lei, L., 2006. Co-deposition of photocatalytic Fe doped TiO_2 coatings by MOCVD. Catal. Commun. 7, 427–431. https://doi.org/10.1016/j.catcom.2005.12.023

Zhu, J., Chen, F., Zhang, J., Chen, H., Anpo, M., 2006. Fe^{3+}-TiO_2 photocatalysts prepared by combining sol-gel method with hydrothermal treatment and their characterization. J. Photochem. Photobiol. A Chem. 180, 196–204. https://doi.org/10.1016/j.jphotochem.2005.10.017

Zhu, J., Zheng, W., He, B., Zhang, J., Anpo, M., 2004. Characterization of Fe–TiO_2 photocatalysts synthesized by hydrothermal method and their photocatalytic reactivity for photodegradation of XRG dye diluted in water. J. Mol. Catal. A Chem. 216, 35–43. https://doi.org/10.1016/j.molcata.2004.01.008

Zhu, Z.D., Hartmann, M., Maes, E.M., Czernuszewicz, R.S., Kevan, L., 2000. Physiochemical characterization of chromium oxides immobilized in mesoporous MeMCM-41 (Me = Al, Ti, and Zr) molecular sieves. J. Phys. Chem. B 104, 4690–4698. https://doi.org/10.1021/jp994335i

Zielińska, A., Kowalska, E., Sobczak, J.W., Łącka, I., Gazda, M., Ohtani, B., Hupka, J., Zaleska, A., 2010. Silver-doped TiO_2 prepared by microemulsion method: Surface properties, bio- and photoactivity. Sep. Purif. Technol. 72, 309–318. https://doi.org/10.1016/j.seppur.2010.03.002

Chapter VI

Saline slag waste as an aluminum source for the synthesis of Zn-Al-Fe-Ti layered double-hydroxides as catalysts for the photodegradation of emerging contaminants

ABSTRACT

In this work, aluminum extracted from saline slag waste is valorized to create a layered double-hydroxide series containing zinc and various proportions of aluminum/titanium. Materials were synthesized by the co-precipitation method with an Me^{2+}/Me^{3+} molar ratio of 3:1 and tested for the removal of diclofenac and salicylic acid from water under UV radiation. The incorporation of 5 wt.% iron by wet impregnation is evaluated. In addition, another series of zinc, aluminum/iron materials with and without 5 wt.% impregnated titanium are tested as catalysts for comparison. Structural characterization and comparison of the two series was performed by powder X-ray diffraction (PXRD), nitrogen adsorption at 77 K, scanning electron microscopy (SEM), X-ray photoelectron spectroscopy (XPS) and temperature-programmed reduction (TPR) measurements. The uncalcinated samples had a typical hydrotalcite structure with a high crystallinity; the presence of ZnO, $ZnFe_2O_4$ or Fe_3O_4 was found after calcination. The specific surface areas of the dried samples ranged from 78 to 199 m^2/g, being highest for $Zn_6Al_{0.5}Ti_{1.5}$. Overall, the results showed that the ZnAlTi series were more effective catalysts than ZnAlFe for photodegradation of the emerging contaminants diclofenac and salicylic acid, under UV light at 298 K, considering two concentrations of the organic molecules (5 and 50 $\mu mol/dm^3$).

VI.1. INTRODUCTION

Recent progress in analytical methods and scientific instrumentation (Pérez-Fernández et al., 2017; Miller et al., 2018) in the field of emerging contaminants show that a reliable approach to solving current water pollution problems should be an environmental priority. In this context, one of the family of materials that has received great attention lately as a possible alternative to TiO_2 is that of layered double hydroxides (LDH), which have proven to be effective in both adsorption (Goh et al., 2008; Santamaría et al., 2020a) and catalysis, more specifically (Goh et al., 2008; Valente et al., 2009; Li et al., 2014; Nayak and Parida, 2018; Nayak et al., 2018, 2019). LDH, which are also known as anionic clays, are synthetic minerals with a structure similar to that of brucite ($Mg(OH)_2$). Substitution of part of the Me^{2+} ions by Me^{3+} generates a positive charge in the layers, which is compensated by the inclusion of anions to give the general formula $[Me_{1-x}^{2+}Me_x^{3+}(OH)_2]^{x+}(A^{n-})_{x/n}\bullet mH_2O$, where A is the anion intercalated in between the layers (usually CO_3^{2-}). Their octahedral

framework confers LDH with several characteristics that are very useful for photocatalysis. For instance, Me^{2+} and Me^{3+} present in the structure of LDH are distributed in a uniform manner in the hydroxide layers, thus meaning that the high degree of dispersion of the transition metal octahedra enables electron transfer and avoids the recombination of electrons and holes. Similarly, the surface OH^- groups of the brucite layers react with valence band holes to yield hydroxyl radicals (•OH), which have a very high oxidation potential and are considered to be an important intermediate for photo-oxidation reactions (Mohapatra and Parida, 2016). Apart from the fundamental structure, several modifications have proven to be effective for photodegradation. Thus, metal ion doping can give LDH the properties of doped semiconductors (Mantilla et al., 2010), and the combination with TiO_2 may enhance performance as a result of the surface OH^- groups (Xia et al., 2013, 2014). LDH contain two or more different metal ions and the proportion between these metals can be controlled, as in doped semiconductors, where a higher valent cation acts as dopant. The presence of different transition metal ions enables LDH to exhibit a broad spectrum of photocatalysis properties. Thus, the combination of metals such as CoCr, CuCr, ZnCr, ZnFe, ZnTi, MgCr, MgFe and NiFe leads to a photoresponse in these materials. The interlayer space also plays an important role in improving the photocatalytic performance as this space facilitates the reaction between the photogenerated charge carriers and the reactant molecules. Finally, as photodegradation is a surface phenomenon, a previous adsorption process is advantageous to make the material more efficient (Li et al., 2014; Miranda et al., 2015). LDH can take up species by either surface adsorption or by the "memory effect", in other words reconstruction of the hydrotalcite structure when suspended in water, although this structure is lost after calcination. This uncommon layered structure, combined with their straightforward synthesis, low cost and compositional flexibility, has made LDH one of the most promising alternatives to TiO_2 as photocatalysts in advanced oxidation processes.

The environmental problems surrounding the disposal of industrial waste, such as the leaching of hazardous heavy metals (Lambolez et al., 1994) or the emission of particulate material (Power et al., 2011), suggest that the valorization of waste materials is the most appropriate method to overcome these problems (Shammas, 2010). Only a limited number of methods, including incineration, storage in landfills and security tanks, stabilization, amongst others, are available for the treatment of hazardous wastes. The best method, however, is valorization (either total or partial) of its components. If these possibilities are not applicable, the only option is storage in security tanks. In the present work, a further step forward is proposed as the aluminum present in the catalyst is obtained from a valorization

process developed by our group (Gil et al., 2018). Saline slags are generated during the secondary aluminum processing, i.e. the recycling of aluminum. Their average composition includes mainly metallic aluminum, several oxides and flux brines as principal components, with the content of non-metallic products varying depending on the nature of the material (Gil et al., 2014; Gil and Korili, 2016). As the difference in composition makes it difficult to propose a standard recovery method, waste is currently stored in controlled landfills. In this context, a few successful valorization strategies have been described previously. For example, *Cocheci et al*. (2018) extracted zinc from zinc ash generated during the hot-dip galvanizing process to form ZnAl-CO_3-LDH, and *Galindo et al*. (2014) synthesized MgAl-CO_3-LDH using aluminum extracted from the waste generated in the tertiary aluminum industry. Similarly, both *Murayama et al*. (2009), who synthesized MgAl-CO_3-LDH from aluminum dross, and *Kuwahara et al.* (2010), who used blast furnace slags generated in the iron making process to form CaAl-CO_3-LDH, tested their adsorption properties towards arsenic and phosphate, respectively, and *Das et al.* (2010) reported the synthesis of LDH containing Mg, Al and Ti from titanium-rich bauxite applied to the removal of fluoride and chromium(IV). All these studies rely upon acid leaching to perform the extractions. However, as LDH synthesis has to be carried out at a constant basic pH of between 9 and 10, a more cost-effective approach may involve basic extraction of the aluminum. To the best of our knowledge, the photodegradation ability of such *valorized* LDH has never been tested as no further uses, other than for adsorption, have been found.

Salicylic acid and diclofenac were chosen as emergent contaminants as they are the most widely consumed non-steroidal anti-inflammatory drugs (NSAIDs). The high toxicity of diclofenac, even at low concentrations, the low capacity of wastewater treatment plants to retain it (Ferrari et al., 2003) and the detection of both salicylic acid and diclofenac in drinking water are their main causes of concern in this regard (Vulliet et al., 2011; Carmona et al., 2014).

In this work, two series of Zn-Al-CO_3 LDH prepared using aluminum obtained from the basic extraction of saline slags have been tested for the photodegradation of diclofenac and salicylic acid. Several different proportions of Fe^{3+} and $Ti^{3+/4+}$ were used to dope (in the structure) or impregnate (on the surface) the LDH. One series consisted of Zn-AlFe-CO_3 LDH with various Al/Fe ratios as Me^{3+} and impregnated with 5 wt.% titanium (labelled as 5Ti/), and the other series comprised Zn-AlTi-CO_3 LDH with Al/Ti various ratios and impregnated with 5 wt.% iron (labelled as 5Fe/).

VI.2. EXPERIMENTAL PROCEDURE

VI.2.1. MATERIALS

The materials used to synthesize hydrotalcites were $Zn(NO_3)_2 \cdot 6H_2O$ (≥98%, Sigma-Aldrich), Na_2CO_3 (≥99.99%, Sigma-Aldrich), $TiCl_3$ (≥ 12%, Sigma-Aldrich), $Ti[OCH(CH_3)_2]_4$ (>97%, Sigma Aldrich), $Fe(NO_3)_3 \cdot 9H_2O$ (Riedel-deHaën, >96%), and NaOH (Panreac) for pH adjustment and aluminum extraction. Salicylic acid (2-hydroxybenzoic acid, 2-$(HO)C_6H_4COOH$, ≥ 99.99%, Sigma-Aldrich) and diclofenac sodium salt (2-[(2,6-dichlorophenyl)amino]benzeneacetic acid sodium salt, $C_{14}H_{10}Cl_2NNaO_2$, Sigma-Aldrich) were also used as received.

VI.2.2. SYNTHESIS OF HYDROTALCITE-LIKE COMPOUNDS

The material used in the present study was an aluminum saline slag previously treated with hot water in order to separate the soluble salts. The main characteristics of this slag waste were reported previously (Yoldi et al., 2019). This material was submitted to aluminum chemical extraction, which was carried out using 2 mol/dm^3 aqueous solutions of NaOH, for 2 h under reflux conditions, the extracted aluminum subsequently being used to synthesize the hydrotalcites (Gil et al., 2018). Layered double-hydroxides containing $Zn_6(AlFe)_2$ at various Al/Fe proportions and with a Zn^{2+}/Me^{3+} molar ratio of 3:1 were prepared at a constant pH of 10 using the co-precipitation method (Gil et al., 2018). For the synthesis, 200 cm^3 of a 0.75 mol/dm^3 solution of Zn^{2+} and 0.25 mol/dm^3 solution of (Al^{3+} + Fe^{3+}) were added dropwise to a stirred solution of Na_2CO_3 (0.2 mol/dm^3). The resulting solid materials were separated by filtration and washed with hot water to remove unreacted substances. The cakes obtained were dried at 333 K for 16 h, calcinated at 673 K for 4 h to remove the anions from the interlayer, and then impregnated with 5 wt.% titanium(IV) isopropoxide. Another series containing $Zn_6(AlTi)_2$ with various Al/Ti proportions and using $TiCl_3$ as titanium source was also synthesized following the same procedure and impregnated with 5 wt.% iron. Finally, all materials were calcinated at 673 K for 4 h.

VI.2.3. CHARACTERIZATION OF THE CATALYSTS

The texture of the samples (0.4 g), previously degassed at 423 K for 24 h at a pressure of less than 0.1 Pa, was analyzed by low temperature nitrogen (Praxair, 99.999%) adsorption

at 77 K using a Micromeritics ASAP 2020 Plus adsorption analyzer. The amount of nitrogen adsorbed at a relative pressure of 0.98 was used to estimate the total pore volume (V_p) and the surface area of the samples was calculated using the Brunauer-Emmer-Teller (BET) method. The crystalline phases present in the samples were identified by powder X-ray diffraction (PXRD) and patterns were obtained using a Siemens D-5000 X-ray diffractometer with Ni-filtered Cu Kα radiation (λ = 0.1548 nm). The working conditions were 30 mA, 40 kV in a 2θ range from 5 to 70° and a scanning rate of 2° (2θ)/min. Thermogravimetric measurements were performed using a Hi-Res TGA2950 apparatus (TA-Instruments), heating from room temperature up to 1173 K at a rate of 10 K/min under an air atmosphere (60 cm^3/min). Scanning electron microscopy (SEM) was used to analyze the morphology of the samples (Phenom Pro X, Paralab). X-ray photoelectron spectra (XPS) were recorded using a SPECS Phoibos 150 1DDLD spectrometer equipped with an Al Kα source (1486.7 eV). Temperature-programmed reduction (TPR) studies were carried out using a Micromeritics TPR/TPD 2900 instrument under a total flow of 30 cm^3/min of carrier gas (5% H_2 in Ar) and a heating rate of 10 K/min up to 1050 K. The samples (20 mg) were first pretreated with N_2 (Praxair, 99.999%) at a heating rate of 10 K/min up to 473 K for 120 min. Water and other compounds that might be formed during the metal reduction and precursor decomposition were retained by a cold trap (isopropyl alcohol/liquid nitrogen), thus avoiding possible interferences with the measured signal.

VI.2.4. DEGRADATION PROCEDURE

The photodegradation of salicylic acid and diclofenac under ultraviolet (UV) radiation was analyzed using the calcinated samples as catalysts. The process was carried out in a photon cabinet containing a 1dm^3 PhotoLAB Batch-L reactor (MPDS-Basis system from UV-Consulting Peschl) with a 150 W medium-pressure TQ 150Z1 Hg lamp (continuous spectrum, with mean peaks at 366 and 313 nm) enclosed in a cooling jacket to maintain a constant temperature of 298 K. A 700 cm^3 solution of diclofenac at a concentration of either 5 or 50 μmol/dm^3 was mixed in the reactor with the catalyst and stirred at 700 rpm and a concentration of 1.0 gcatalyst/dm^3 under UV radiation. Samples were taken every 15 minutes, filtered and the drug concentration measured using a UV-vis spectrometer (Jasco V-730) at its maximum adsorption wavelength (276 nm). The same procedure and concentrations were used for salicylic acid (λ_{max} 297 nm). Adsorption tests, without irradiation, were carried out for every experiment, and photolysis tests, in the absence of a catalyst, were also performed.

VI.3. RESULTS AND DISCUSSION

VI.3.1. CHARACTERIZATION OF HYDROTALCITES

The X-ray diffraction patterns of the non-calcinated samples from series ZnAlFe and ZnAlTi are shown in Figures VI.1a and VI.1b.

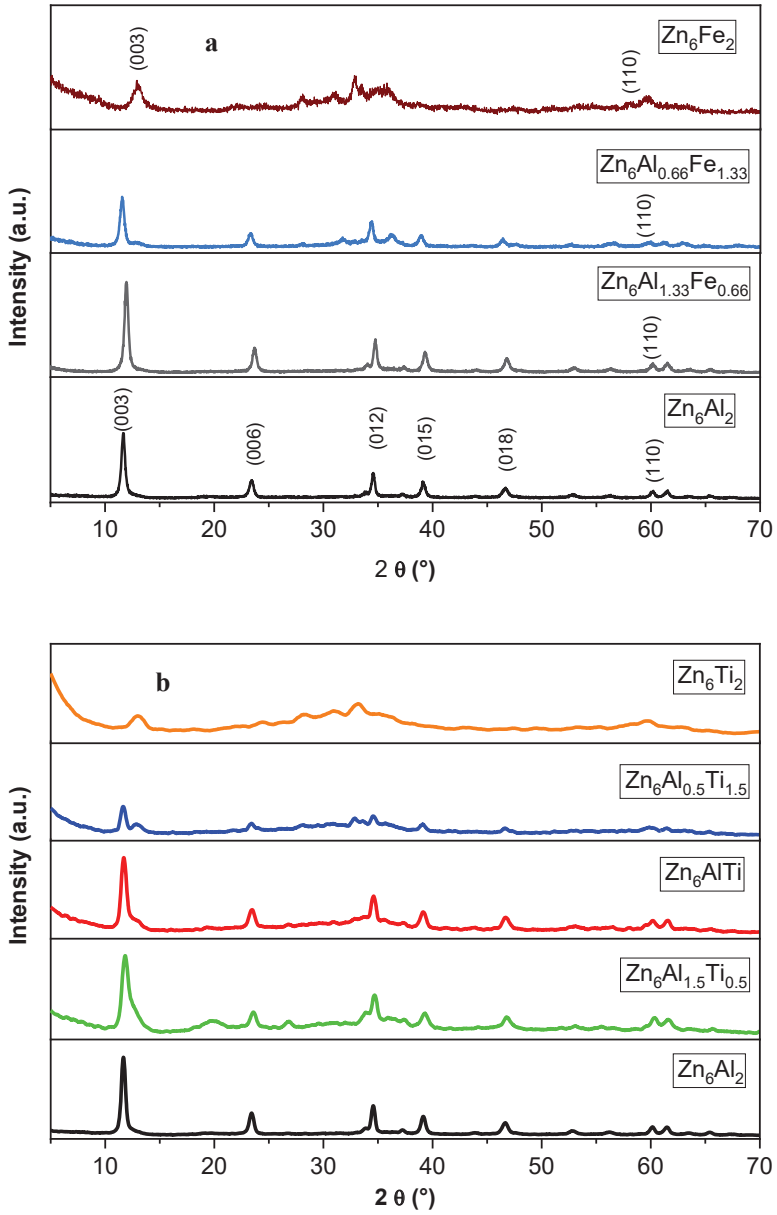

Figure VI.1. Powder X-ray diffraction patterns for non-calcinated samples (a: Zn-Al-Fe; b: Zn-Al-Ti)

These aluminum-containing samples clearly exhibit a double layered hydroxide type structure, which is less defined in Zn_6Fe_2 and Zn_6Ti_2. All samples have a well-defined peak at $2\theta \approx 12°$ that matches the (003) reflection and an interlayer distance characteristic of hydrotalcite-like materials, in accordance with the results reported by other authors (Parida et al., 2007; Carriazo et al., 2011; Shao et al., 2011; Xia et al., 2013, 2014). If a 3R symmetry is assumed (Cavani et al., 1991), the cell parameters can be calculated applying the Bragg equation (Cullity, 1978), using the values for the (003), (006) and (110) reflections to give $c = 3[1/2\ (d_{003} + 2d_{006})]$ and $a = 2d_{110}$. The values for c and a (see Table VI.1) show an opposite trend, with the average metal-metal distance increasing as the interlayer distance decreases. These results are in accordance with the radii of the cations incorporated into the LDH as, for example, the ionic radius of Fe^{3+} is larger than that of Al^{3+} (Shannon, 1976).

Table VI.1. Basal spacing, and c and a parameters for the non-calcinated ZnAlFe-LDH samples.

Sample	$d_{(003)}$	c (nm)	$d_{(110)}$	a (nm)
Zn_6Al_2	0.761	2.278	0.153	0.307
$Zn_6Al_{1.33}Fe_{0.66}$	0.739	2.233	0.154	0.307
$Zn_6Al_{0.66}Fe_{1.33}$	0.766	2.289	0.154	0.307
Zn_6Fe_2	0.688	2.063	0.158	0.316
$Zn_6Al_{1.5}Ti_{0.5}$	0.752	2.253	0.153	0.306
Zn_6AlTi	0.757	2.275	0.153	0.307
$Zn_6Al_{0.5}Ti_{1.5}$	0.761	2.281	0.153	0.307
Zn_6Ti_2	0.686	2.059	0.155	0.310

The LDH structure disappears after calcination of the samples at 673 K, leading to a zincite pattern (ZnO phase) as well as to the possible presence of the zinc aluminate spinel $ZnAl_2O_4$ (see Figures VI.2a and VI.2b). Cheng et al. (2010) found that the layered structure of ZnAl hydrotalcites was preserved after thermal treatment at 423 and 473 K, although the crystallinity was lowered given the broadening of the lines and decrease in their intensities. The LDH phase decreased and was replaced by ZnO and possibly $ZnAl_2O_4$ spinel phases as the calcination temperature increased. A similar loss of crystallinity and the appearance of

ZnO at 473 K were described previously by dos Reis et al. (2010). The preparation and characterization of various ZnAl hydrotalcites have also been reported by Carriazo el al. (2011). After calcination at 773 K, these authors found collapse of the layered structure and new diffraction lines related to several metal oxides, including ZnO and the $ZnAl_2O_4$ spinel. The crystallinity of these oxides increased at calcination temperatures higher than 773 K, as suggested by the higher intensity and sharpness of the diffraction lines. A similar behavior was also found by *Hadnadjev-Kostic et al.* (2017). As more iron is incorporated into the

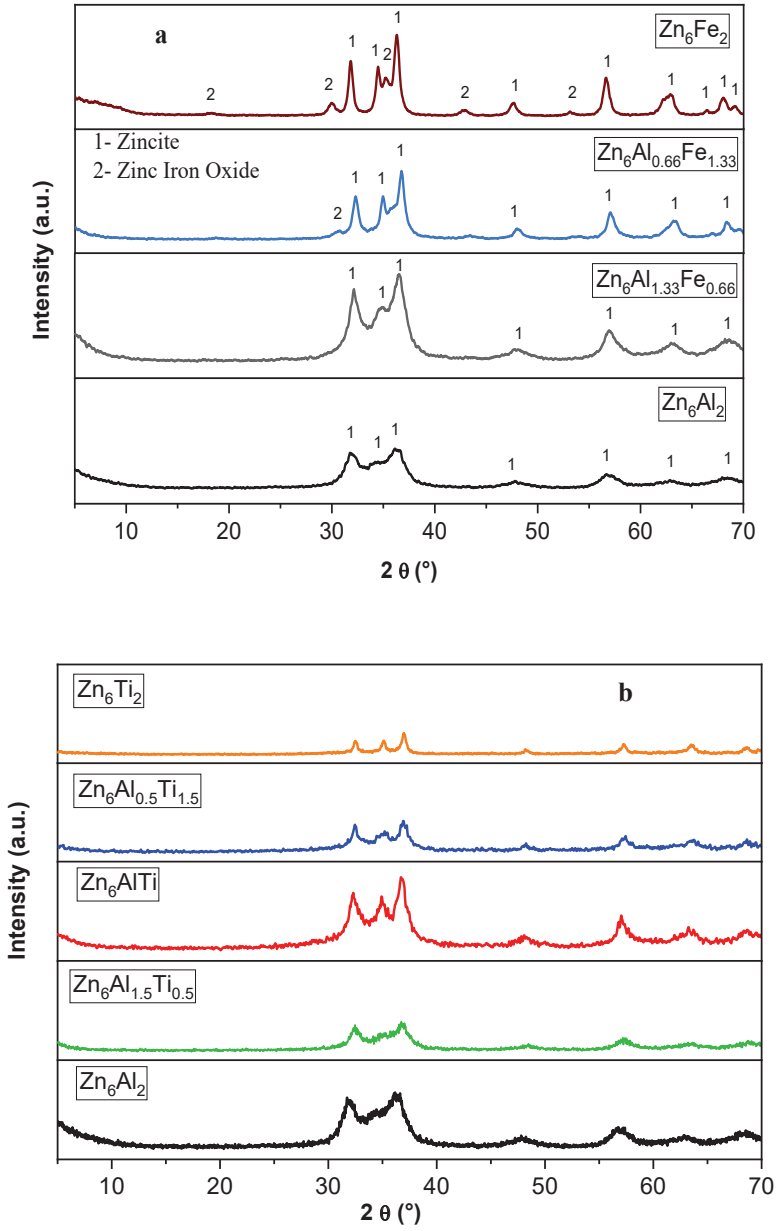

Figure VI.2. Powder X-ray diffraction pattern after treatment at 673 K (a: Zn-Al-Fe; b: Zn-Al-Ti).

samples, the peaks become more defined and zinc iron oxide ($ZnFe_2O_4$) appears in the diffractogram (Balasamy et al., 2011). In the case of the samples synthesized in the presence of titanium, no diffraction peaks corresponding to TiO_2, $ZnTiO_3$ or Zn_2TiO_4 phases were observed (Mohammadi and Fray, 2010; Lak et al., 2012; Saber and Zaki, 2014; Hosni et al., 2015; Hadnadjev-Kostic et al., 2017), thus suggesting a possible high dispersion of the oxides or a low crystallinity. These phases were found by Seftel et al. (2014) after thermal treatment at 873 K.

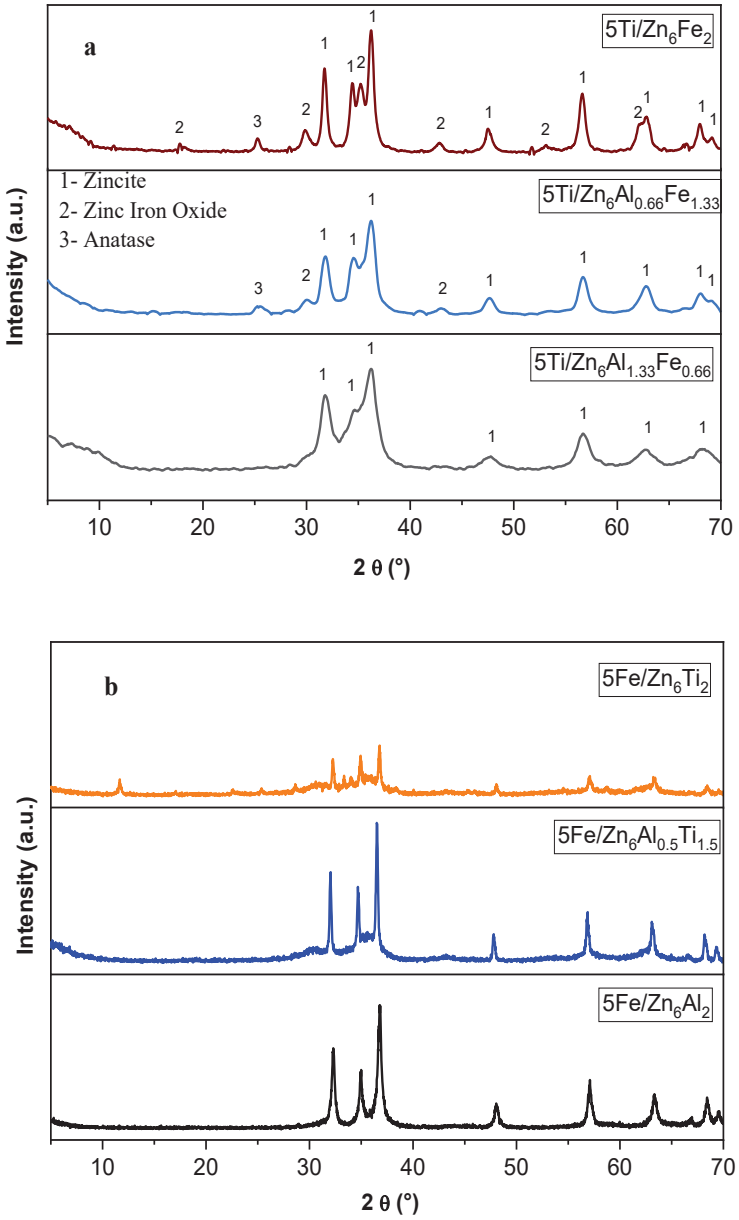

Figure VI.3. Powder X-ray diffraction patterns for (a) ZnAlFe-LDH series impregnated with 5 wt.% titanium, and (b) ZnAlTi-LDH series impregnated with 5 wt.% iron.

Impregnation of the samples with 5 wt.% titanium did not significantly change their structure, although low intensity anatase peaks were observed for $5Ti/Zn_6Al_{0.66}Fe_{1.33}$ and $5Ti/Zn_6Fe_2$ (Figure VI.3a). Similarly, impregnation of the ZnAlTi series with 5 wt.% iron (patterns shown in Figure VI.3b) also led to the zincite structure. The addition of iron cannot be observed in the patterns, although the peaks formed are sharper and better defined after impregnation.

Although the PXRD patterns display a structural change in the samples as a result of the calcination process, the SEM images of sample $Zn_6Al_{1.33}Fe_{0.66}$ after calcination clearly show differentiated rose petal-like shapes (Figure VI.4). The layered structure of the samples is still preserved, as reported previously (Chen et al., 2014; Fang et al., 2015).

Thermogravimetric analysis showed the presence of five mass-loss steps (see Figure VI.5). The first two mass losses, between 298 and 423 K, are related to the loss of water (adsorbed on the surface and located in the interlayer). The third step, centered at around 523 K, is related to dehydroxylation and decarbonation processes, whereas the following two steps, between 673 and 1123 K, have low intensity and may be related to further decomposition of the mixed oxides.

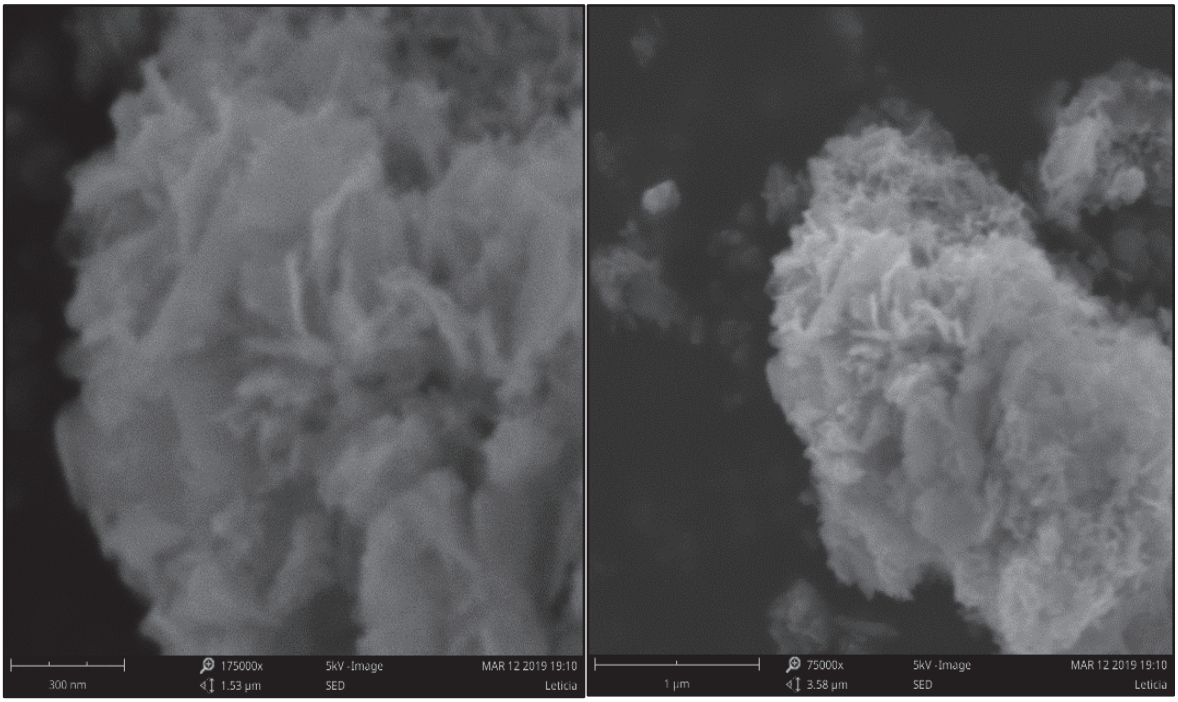

Figure VI.4. SEM micrographs of $Zn_6Al_{1.33}Fe_{0.66}$.

The adsorption-desorption isotherms for the non-calcinated, calcinated, Ti-impregnated ZnAlFe-LDH and Fe-impregnated ZnAlTi-LDH are presented in Figure VI.6. All N_2 adsorption isotherms are type II in the IUPAC classification, where N_2 adsorption does not reach a plateau at high relative pressures. In all cases, the desorption branch leads to an H3 hysteresis loop, which may indicate small, slit-shaped pores. The BET surface areas and total pore volumes are shown in Table VI.2. For uncalcinated Zn_6Me_2 samples, Zn_6Ti_2 had the largest BET specific surface area (184 m^2/g), while Zn_6Al_2 had the lowest (78 m^2/g). Calcination at 673 K caused a marked decrease in the BET surface area of some samples, with the initial value decreasing by between 29% ($Zn_6Al_{0.66}Fe_{1.33}$) and 57% (Zn_6Fe_2). The BET surface areas for $Zn_6Al_{1.33}Fe_{0.66}$ and Zn_6Al_2 were not modified by the calcination process. Impregnation of the samples with 5 wt.% titanium or iron did not cause major changes in the BET surface areas of the samples, with a small decrease in $5Ti/Zn_6Al_{1.33}Fe_{0.66}$, from 112 to 109 m^2/g, and small increases in the other two samples (Zn_6Fe_2 from 53 to 55 m^2/g and $Zn_6Al_{0.66}Fe_{1.33}$ from 72 to 84 m^2/g). In the case of the ZnAlTi-LDH series, all BET surface areas were similar, with $5Fe/Zn_6Ti_2$ having the smallest value (71 m^2/g).

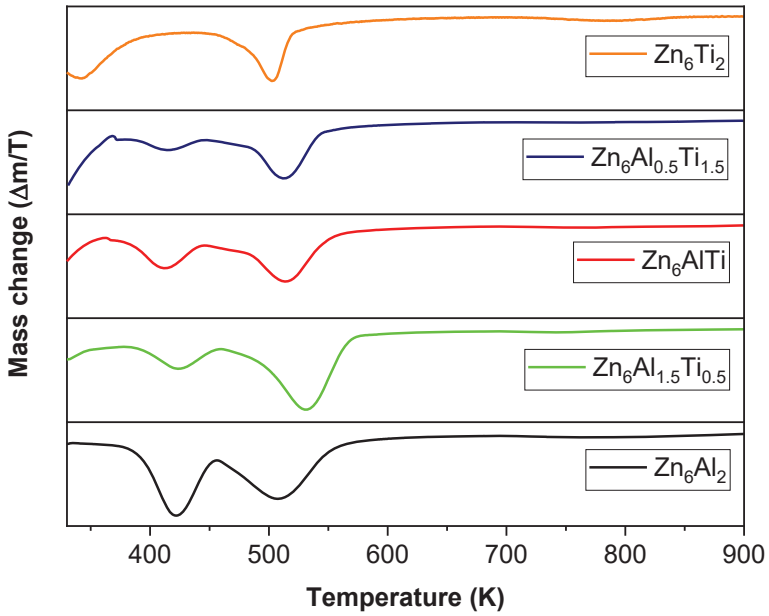

Figure VI.5. DTG curves for the ZnAlTi-LDH materials.

Table VI.2. BET specific surface areas and total pore volumes for the ZnAlFe and ZnAlTi-LDH samples.

		Sample	S_{BET} (m^2/g)	V_p (cm^3/g)
ZnAlFe–LDH series	Non-calcined samples	Zn_6Al_2	78	0.384
		$Zn_6Al_{1.33}Fe_{0.66}$	114	0.558
		$Zn_6Al_{0.66}Fe_{1.33}$	102	0.537
		Zn_6Fe_2	124	0.497
	Calcined samples	Zn_6Al_2	77	0.348
		$Zn_6Al_{1.33}Fe_{0.66}$	112	0.640
		$Zn_6Al_{0.66}Fe_{1.33}$	72	0.307
		Zn_6Fe_2	53	0.316
		$5Ti/Zn_6Al_2$	91	0.361
		$5Ti/Zn_6Al_{1.33}Fe_{0.66}$	109	0.494
		$5Ti/Zn_6Al_{0.66}Fe_{1.33}$	84	0.330
		$5Ti/Zn_6Fe_2$	55	0.291
ZnAlTi–LDH series	Non-calcined samples	Zn_6Al_2	78	0.384
		$Zn_6Al_{1.5}Ti_{0.5}$	152	0.640
		Zn_6AlTi	152	0.522
		$Zn_6Al_{0.5}Ti_{1.5}$	199	0.517
		Zn_6Ti_2	184	0.497
	Calcined samples	Zn_6Al_2	79	0.345
		$Zn_6Al_{1.5}Ti_{0.5}$	100	0.522
		Zn_6AlTi	93	0.433
		$Zn_6Al_{0.5}Ti_{1.5}$	95	0.428
		Zn_6Ti_2	95	0.375
		$5Fe/Zn_6Al_2$	79	0.509
		$5Fe/Zn_6Al_{1.5}Ti_{0.5}$	81	0.474
		$5Fe/Zn_6AlTi$	70	0.312
		$5Fe/Zn_6Al_{0.5}Fe_{1.5}$	78	0.234
		$5Fe/Zn_6Ti_2$	71	0.286

The H_2-TPR profiles obtained for the calcinated ZnAlTi-LDH series are shown in Figure VI.7a. Before iron impregnation, the Zn_6Al_2 sample did not give any strong signal, with only a small peak at around 850 K that could be related to the reduction of Zn^{2+} to Zn^0 as a result of the presence of amorphous ZnO and $ZnAl_2O_4$ (Benito et al., 2008). When iron is added, two distinctive peaks, which are assigned to different Fe^{3+} reduction steps, appear at 690 and 850 K. When pure iron oxide is considered, Fe_2O_3 is reduced to Fe_3O_4 at around 850 K and a second reduction peak, which combines the reduction of Fe_3O_4 to FeO and to Fe^0, appears at around 1000 K (Webb et al., 1997). In the case of $ZnFe_2O_4$, a direct reduction to Fe_3O_4 and then to FeO and Fe has been suggested, with the presence of three reduction peaks (Liang et al., 2009). $ZnFe_2O_4$ is more prone to be reduced as the presence of the semiconductor ZnO promotes the reduction of metal (Liang et al., 2009; Naknam et al., 2009), as also reported in the case of Ni-Zn-Al (Fuentes et al., 2011) and Fe-Zn-Al (Balasamy et al., 2011) hydrotalcites.

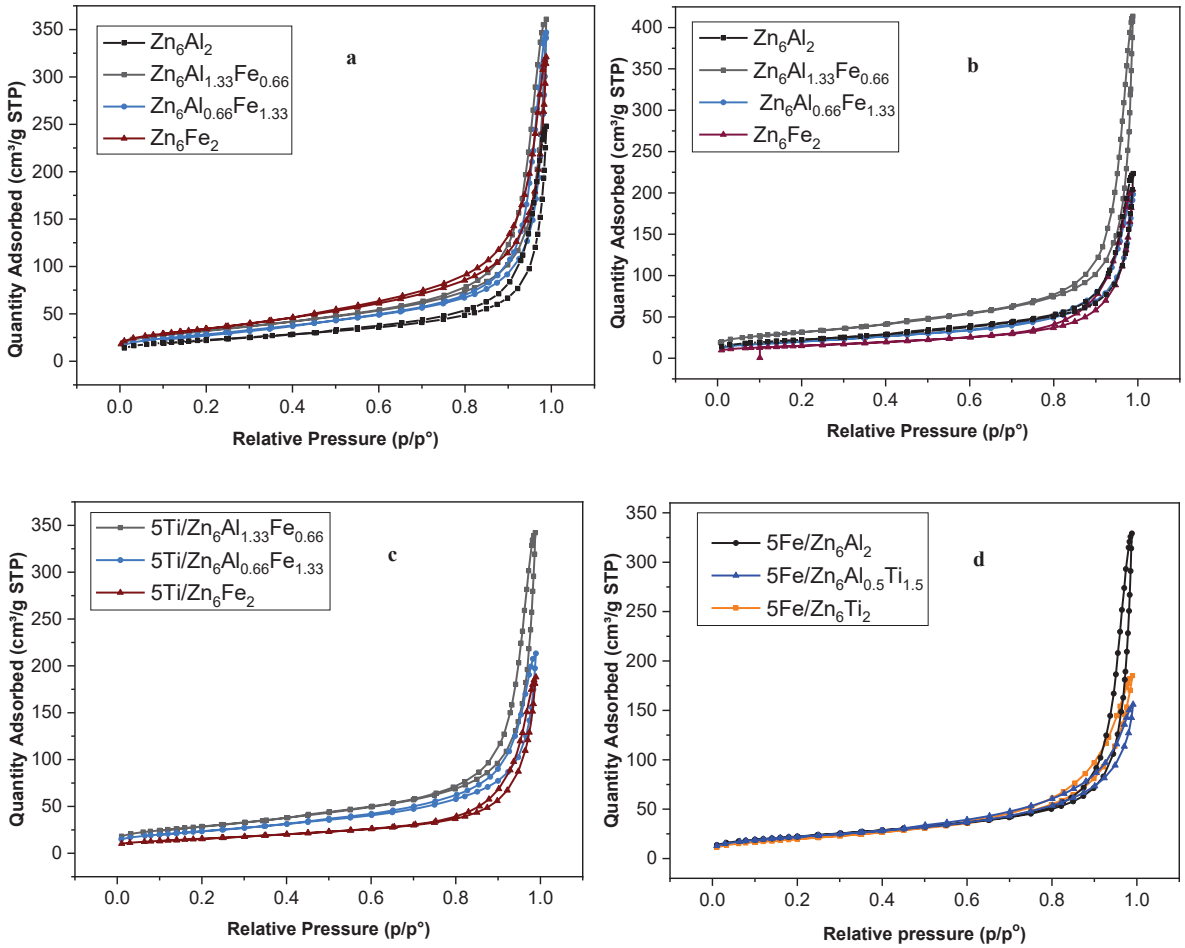

Figure VI.6. Nitrogen adsorption-desorption isotherms of non-calcined (a), calcined (b), ZnAlFe-LDH samples impregnated with 5 wt.% Titanium (c), and ZnAlTi-LDH series impregnated with 5 wt.% iron (d).

When iron is impregnated on $Zn_6Al_{0.5}Ti_{1.5}$ and Zn_6Ti_2, these peaks are not so easily observed and a wider peak seems to overlap several reduction stages, in other words reduction of Fe_3O_4 to FeO occurs at a lower temperature, probably due to the smaller particle size, lower cristallinity and, consequently, greater instability of the samples (Khan and Smirniotis, 2008).

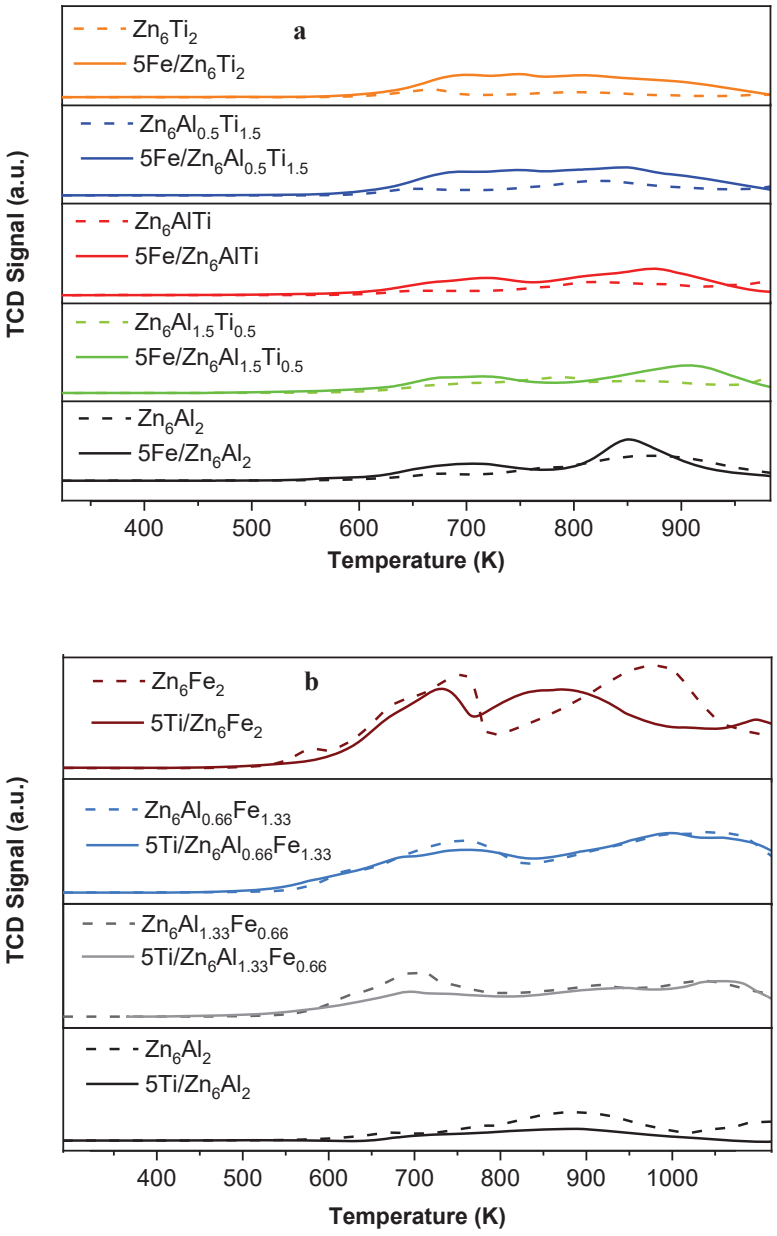

Figure VI.7. H_2-TPR profile of (a) ZnAlTi-LDH and (b) ZnAlFe-LDH.

The H_2-TPR profiles for the ZnAlFe-LDH series are shown in Figure VI.7b. H_2 consumption increases with iron content in the LDH, with the Zn_6Fe_2 signal having almost double the intensity of that for $Zn_6Al_{1.33}Fe_{0.66}$. The addition of titanium onto the surface causes minor changes in the $Zn_6Al_{1.33}Fe_{0.66}$ and $Zn_6Al_{0.66}Fe_{1.33}$ H_2 consumption profiles, with the $ZnFe_2O_4$ reduction peak being less-well resolved, possibly because H_2 has greater difficulty in accesing $ZnFe_2O_4$ once the titanium has been impregnated. In Zn_6Fe_2, however, the addition of titanium lowers the temperature of Fe_3O_4 reduction from 959 to 750 K, and that of $ZnFe_2O_4$ from 750 to 650 K. In the case of titanium oxide, a partial reduction of Ti^{4+} to Ti^{3+} could occur in the temperature range studied; this process has been reported to occur at 838 K (Santamaría et al., 2020b). As described above, other reduction processes also occur at this temperature, therefore it was not possible to differentiate which processes these signals correspond to.

X-ray photoelectron spectroscopy is a useful technique for investigating the surface composition and chemical states of the elements present on the solid samples. The O 1s core level spectra of the samples for the two series are shown in Figure VI.8 and VI.9. The surface concentration and proposed elemental formulae for the calcinated compounds present on the surface of the LDH can be found in Table VI.3.

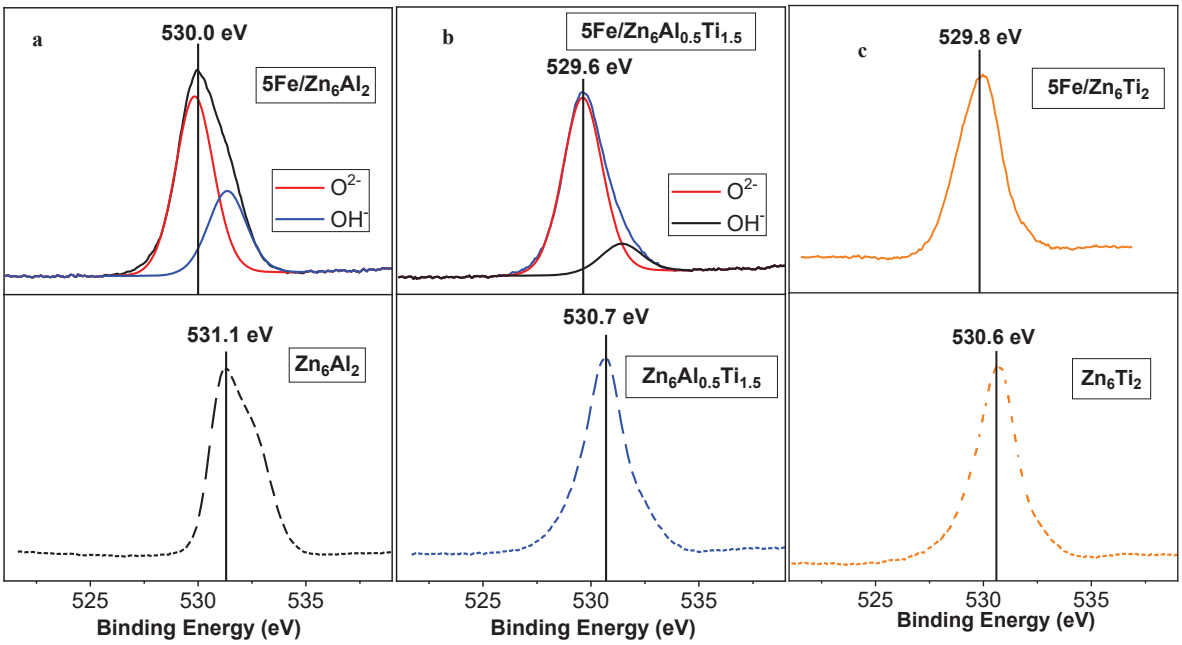

Figure VI.8. XPS O 1s spectra for the ZnAlTi-LDH series (a) Zn_6Al_2, (b) $Zn_6Al_{0.5}Ti_{1.5}$, (c) Zn_6Ti_2.

Table VI.3. Surface concentration (% atomic) and proposed elemental formula of the calcinated compounds on the surface of the LDH.

	Zn	Al	O	Ti	Fe	Proposed formula
Zn_6Al_2	25.6	10.4	55.9	--	--	$Zn_6Al_{2.4}$
$Zn_6Al_{1.5}Ti_{0.5}$	25	8.6	56	1.5	--	$Zn_6Al_{2.1}Ti_{0.4}$
Zn_6AlTi	25.8	5.2	56.5	4.4	--	$Zn_6Al_{1.2}Ti_{1.0}$
$Zn_6Al_{0.5}Ti_{1.5}$	26.8	3.1	55.1	5.9	--	$Zn_6Al_{0.7}Ti_{1.3}$
Zn_6Ti_2	26.5	--	56.1	9	--	$Zn_6Ti_{2.0}$
$5Fe/Zn_6Al_2$	16.6	12.1	53.4	--	5.0	$5Fe/Zn_6Al_{4.4}$
$5Fe/Zn_6Al_{0.5}Ti_{1.5}$	18.5	3.9	52.4	4.5	7.2	$7.2Fe/Zn_6Al_{1.3}Ti_{1.5}$
$5Fe/Zn_6Ti_2$	19.5	--	53.0	7.1	8.4	$8.4Fe/Zn_6Ti_{2.2}$
	Zn	**Al**	**O**	**Fe**	**Ti**	**Proposed formula**
$Zn_6Al_{1.33}Fe_{0.66}$	24.6	7.6	55.5	3.3	--	$Zn_6Al_{1.8}Fe_{0.8}$
$Zn_6Al_{0.66}Fe_{1.33}$	29.5	3.6	56	5.3	--	$Zn_6Al_{0.7}Fe_{1.1}$
Zn_6Fe_2	34.1	--	53.5	6.6	--	$Zn_6Fe_{1.2}$
$5Ti/Zn_6Al_{1.33}Fe_{0.66}$	21.0	7.0	54.2	2.7	3.3	$3.3Ti/Zn_6Al_2Fe_{0.77}$

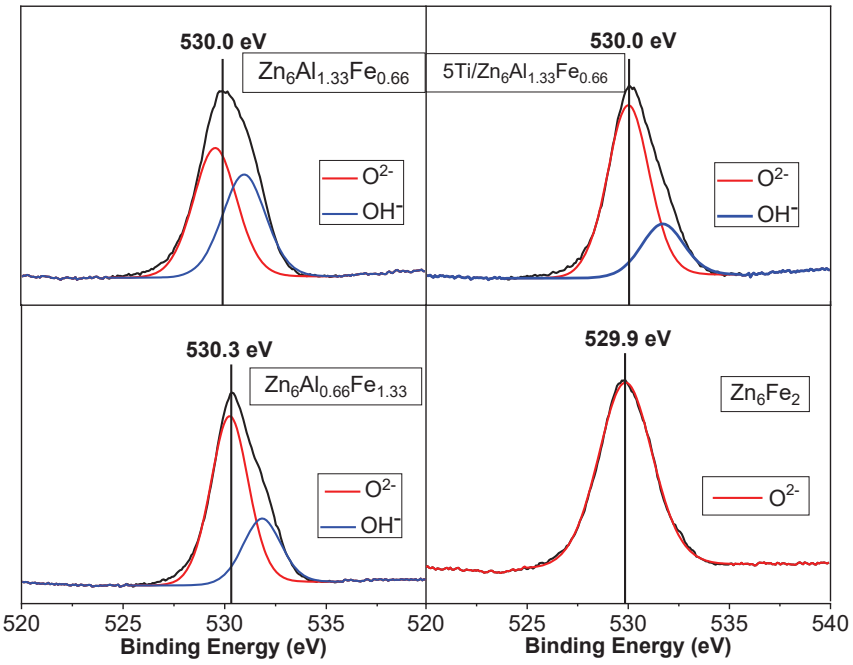

Figure VI.9. XPS O 1s spectra for the ZnAlFe-LDH series.

The signal can be split into two peaks in all aluminum-containing samples. The first peak (≈ 530 eV) was attributed to the lattice oxygen bound to metal cations of the structure (both Zn_6Fe_2 and Zn_6Ti_2 samples have this peak exclusively), whereas the second peak is found at higher binding energy (≈531.5 eV) and can be attributed mainly to hydroxyl groups, although a small percentage of this peak is associated with organic contamination and chemisorbed water (McCafferty and Wightman, 1998). The presence of these hydroxyl groups can benefit the photocatalytic process as they help to create hydroxyl radicals (•OH) (Santamaría et al., 2020b). In all cases, the addition of 5 wt.% of either Fe or Ti favors the increase of oxygen bound to metal cations as Ti is added as TiO_2 and Fe as Fe_3O_4 (Fe^{2+} represents 33% and Fe^{3+} 66% in the three samples).

VI.3.2. DEGRADATION AND ADSORPTION EXPERIMENTS

Photolysis experiments were performed with diclofenac and salicylic acid, resulting in degradation percentages of 6% and 0%, respectively. In the case of the adsorption experiments, the results obtained indicate that this process is important in some cases, thus meaning that each particular case should be discussed individually to explain the photodegradation results.

VI.3.2.1. ZnAlTi-LDH series with and without iron

The hydrotalcites with the composition ZnAlTi showed a higher ability to degrade diclofenac and salicylic acid than their ZnAlFe counterparts. The change in contaminant concentration in relation to the initial concentration when using 5 μM solutions of diclofenac and salicylic acid and 1g/dm^3 of catalyst is plotted in Figures VI.10a and 10c, respectively. Zn_6Al_2 is much more effective at removing both drugs than the other two samples (Zn_6Ti_2 and $Zn_6Al_{0.5}Ti_{1.5}$). In order to be able to discern the contribution of the catalytic process, the adsorption capacity of these materials was also investigated under the same experimental conditions. These results are included in Table VI.4. From the diclofenac results, it can be seen that the adsorption capacity decreases as the amount of Ti in the samples increases. In the most favorable case (Zn_6Al_2), and for a concentration of 5 μmol/dm^3, 93% is adsorbed and in the worst case, adsorption was null (Zn_6Ti_2). At a higher concentration (50 μmol/dm^3) the percentage adsorbed is lower. Under the conditions of photodegradation, no differences were observed with respect to the adsorption tests when the initial concentration was 5 μmol/dm^3, with the quantity of diclofenac eliminated increasing if the concentration of 50

μmol/dm^3 is considered. According to previous studies from our research group, these series of hydrotalcites adsorb less salicylic acid than diclofenac, and thus, in the case of salicylic acid, there is a clear difference between the amounts adsorbed and photodegraded, although no differences are observed between the two concentrations (5 and 50 μmol/dm^3). The difference between these materials is the Ti content and the degree of crystallinity/laminar structure. Upon increasing the Ti content and decreasing the degree of crystallinity/layered structure, the adsorption capacity of these materials is also decreased. In this case, a well-defined LDH structure favors the adsorption of these contaminants.

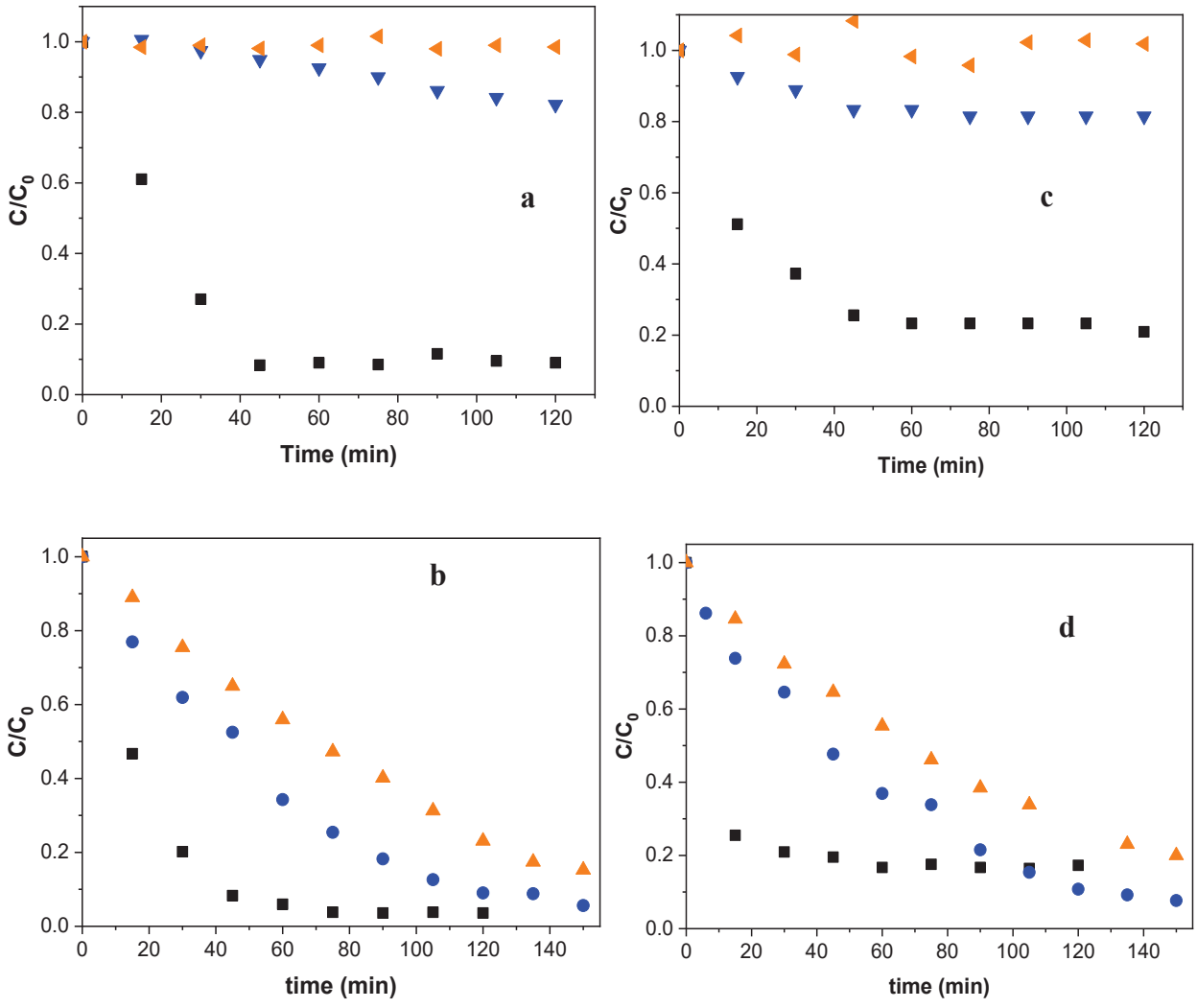

Figure VI.10. Comparison of the evolution of the concentration of (a,b) diclofenac and (c,d) salicylic acid, with respect to the initial concentration, with irradiation time using (a,c) ZnAlTi-LDH and (b,d) 5Fe/ZnAlTi as catalysts (5 $\mu mol_{contaminant}/dm^3$; 1 g_{sample}/dm^3).

Table VI.4. Diclofenac and salicylic acid removal by adsorption and photodegradation using ZnAlTi-LDH samples as catalysts.

1 g_{sample}/dm^3, 5 µmol/dm^3	***Diclofenac***		***Salicylic acid***	
Sample	Adsorption removal (%)	Total elimination (%)	Adsorption removal (%)	Total elimination (%)
Zn_6Al_2	93	91	40	79
$Zn_6Al_{1.5}Ti_{0.5}$	70	69	31	48
Zn_6AlTi	42	49	24	49
$Zn_6Al_{0.5}Ti_{1.5}$	17	18	15	19
Zn_6Ti_2	0	0	0	0
5Fe/Zn_6Al_2	93	96	40	83
5Fe/Zn_6AlTi	7	24	8	51
5Fe/$Zn_6Al_{0.5}Ti_{1.5}$	0	94 (time:150')	6	92 (time:150')
5Fe/Zn_6Ti_2	3	85 (time:150')	8	80 (time:150')

1 g_{sample}/dm^3, 50 µmol/dm^3	***Diclofenac***		***Salicylic acid***	
Sample	Adsorption removal (%)	Total elimination (%)	Adsorption removal (%)	Total elimination (%)
Zn_6Al_2	56	93	40	65
$Zn_6Al_{1.5}Ti_{0.5}$	53	91	24	66
Zn_6AlTi	16	58	32	51
$Zn_6Al_{0.5}Ti_{1.5}$	6	0	0	0
Zn_6Ti_2	0	0	0	0
5Fe/Zn_6Al_2	93	99	40	53
5Fe/$Zn_6Al_{1.5}Ti_{0.5}$	63	66	30	32
5Fe/Zn_6AlTi	63	65	25	32
5Fe/$Zn_6Al_{0.5}Ti_{1.5}$	0	8	5	15
5Fe/Zn_6Ti_2	0	5	1	10

When 5 wt.% iron was incorporated by impregnation into the surface of the materials (see Figure VI.10b for diclofenac and VI.10d for salicylic acid), the adsorption results for the two molecules using 5Fe/Zn_6Al_2 are practically the same as those obtained without the presence of impregnated Fe. In the case of 5Fe/$Zn_6Al_{0.5}Ti_{1.5}$ and 5Fe/Zn_6Ti_2, although the samples still had a percentage removal by adsorption of less than 10%, their degradation performance improved significantly, with removal percentages of more than 80%. The

addition of 5 wt.% impregnated iron has previously been proven to improve salicylic acid degradation (Khan and Smirniotis, 2008) by improving the characteristic electron-hole recombination of titanium. It has been reported that the induced photoexcitation can cause charge mobility and form photoactive defects in the case of LDH materials (Mantilla et al., 2011; Shao et al., 2011), and that the number of photoinduced centers could depend on the Me^{2+}/Me^{3+} ratio. *Xia et al.* (2013) and *Shao et al.* (2011) found high photocatalytic performances for the degradation of Rhodamine B and Methylene Blue on ZnTi-LDH materials synthesized with a 3:1 molar ratio. The presence of Fe^{3+} ions also played an important role in the degradation of phenol (Mantilla et al., 2010) and azo dyes (Mohapatra et al., 2012). Our results show that the Fe^{3+}/Ti^{3+} system is active in the photodegradation of diclofenac and salicylic acid under UV light conditions. As such, it is possible to propose a plausible photodegradation mechanism, as shown in Figure VI.11.

VI.3.2.2. ZnAlFe-LDH series with and without titanium

Overall, this series was shown to be less effective than ZnAlTi. The change in contaminant concentration in relation to the initial concentration (50 μM) of diclofenac and salicylic acid in the presence of 1g/dm^3 of catalyst is shown in Figures VI.12a and VI.12b, respectively.

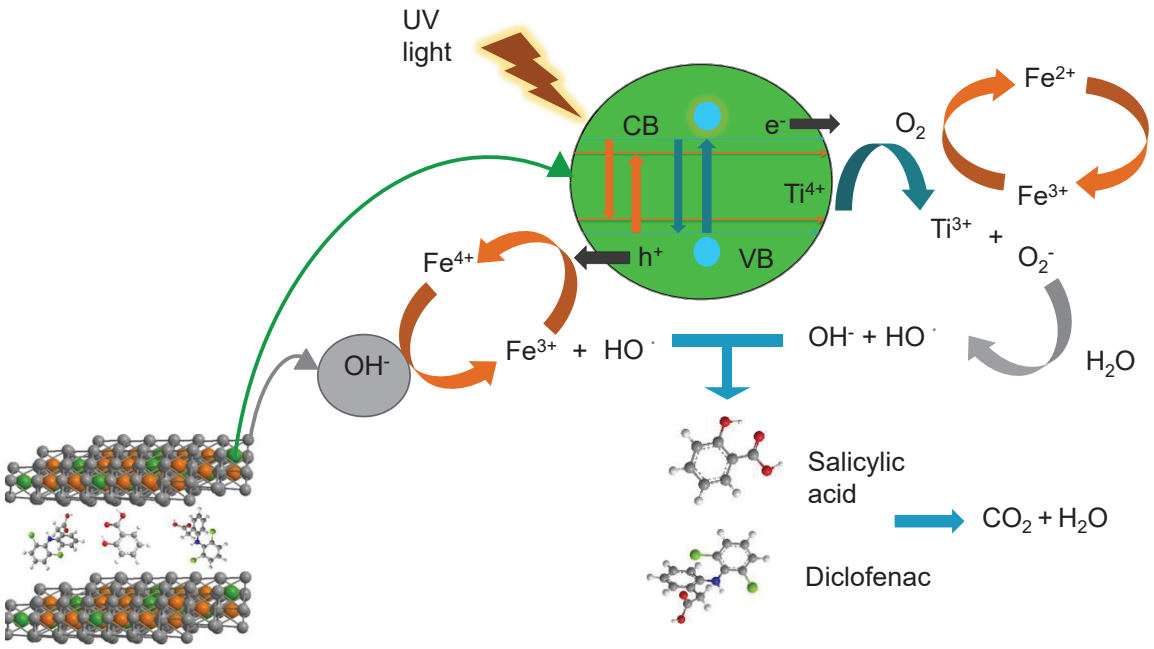

Figure VI.11. Schematic diagram showing the mechanism of the photocatalytic reaction taking place on the surface of Fe/ZnAlTi-LDH materials.

As in the case of the lower concentration, Zn_6Al_2 and $Zn_6Al_{1.33}Fe_{0.66}$ are much more effective at removing both contaminants than the other two samples (Zn_6Fe_2 and $Zn_6Al_{0.66}Fe_{1.33}$). The adsorption capacity of these materials was also investigated under the same experimental conditions. These results are included in Table VI.5. The results for diclofenac show that Zn_6Al_2 and $Zn_6Al_{1.33}Fe_{0.66}$ remove the 56% and 84% of the contaminant by adsorption. Zn_6Fe_2 and $Zn_6Al_{0.66}Fe_{1.33}$ do not result in adsorption or photodegradation.

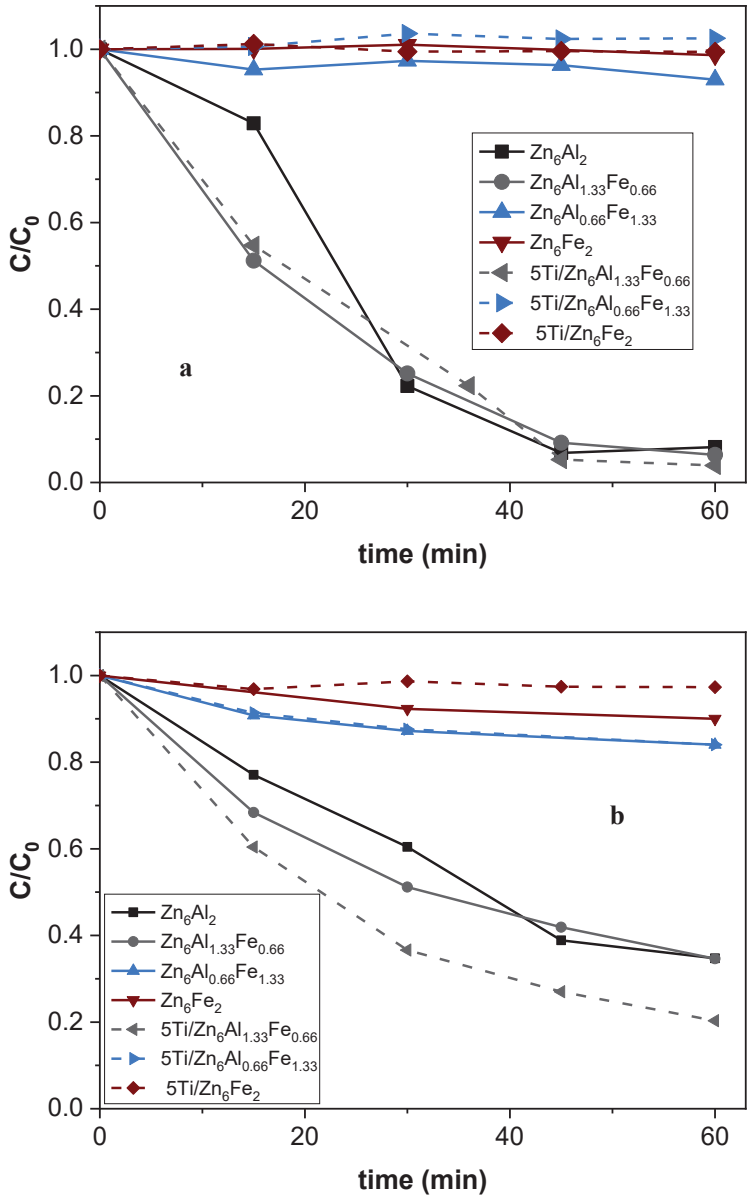

Figure VI.12. Comparison of the evolution of the concentration of (a) diclofenac and (b) salicylic acid, with respect to the initial concentration, with irradiation time using ZnAlFe-LDH catalysts. (50 $\mu mol_{contaminant}/dm^3$; 1 g_{sample}/dm^3).

The values for salicylic acid removal are 40% removal by Zn_6Al_2 and 59% by $Zn_6Al_{1.33}Fe_{0.66}$. The values for the total decrease of salicylic acid are also higher, thus leading us to believe that some photodegradation occurs. As in the case of diclofenac, salicylic acid is not adsorbed or degraded when Zn_6Fe_2 is used. The difference between these materials is the Fe content and the degree of crystallinity/layered structure. When increasing the Fe content and decreasing the degree of crystallinity/layered structure, the adsorption capacity of these materials is also decreased.

Table VI.5. Diclofenac and salicylic acid removal by adsorption and photodegradation using ZnAlFe-LDH samples as catalysts.

1 g_{sample}/dm^3, 50 µmol/dm^3	***Diclofenac***		***Salicylic acid***	
Sample	Adsorption removal (%)	Total elimination (%)	Adsorption removal (%)	Total elimination (%)
Zn_6Al_2	56	93	40	65
$Zn_6Al_{1.33}Fe_{0.66}$	84	94	59	65
$Zn_6Al_{0.66}Fe_{1.33}$	1	7	16	16
Zn_6Fe_2	1	1	7	10
5Ti/ $Zn_6Al_{1.33}Fe_{0.66}$	69	96	49	80
5Ti/ $Zn_6Al_{0.66}Fe_{1.33}$	2	0	11	16
5Ti/ Zn_6Fe_2	2	1	0	0

When 5 wt.% titanium was incorporated into the surface of the materials by impregnation (see Figure VI.12a for diclofenac and VI.12b for salicylic acid), the adsorption results for the two molecules using this series of catalysts was found to be practically the same as those obtained without the presence of impregnated Ti. In the case of $Zn_6Al_{1.33}Fe_{0.66}$, although the addition of 5 wt.% titanium prevents the contaminant from being adsorbed slightly, this is compensated by a better degradation and overall reduction of the salicylic acid concentration by 80%. Zn_6Al_2 was also impregnated with 5 wt.% titanium, although this only decreased the overall performance. In this case, the improvement in the degradation capacity did not compensate for the decrease in adsorption, and the concentration of diclofenac was double that of Zn_6Al_2 after 60 minutes, thus highlighting the importance of iron in the degradation process.

The reusability of Zn_6Al_2 and $5Ti/Zn_6Al_{1.33}Fe_{0.66}$ was tested over four cycles (see Figures VI.13a and b). These data were also used to investigate the kinetics of diclofenac degradation based on the Langmuir-Hinshelwood model (Xia et al., 2014):

$$r = -\frac{dC}{dt} = \frac{k_r K_{ad} C}{1 + K_{ad} C} \qquad \text{Eq. VI.1}$$

where r is the degradation rate, C the concentration of the organic compound, k_r the intrinsic rate constant and K_{ad} the adsorption equilibrium constant. In the case of a low adsorption and concentration of diclofenac, $K_{ad}C$ can be ignored and r can be expressed as:

$$r = k_r K_{ad} C = K_{app} C \qquad \text{Eq. VI.2}$$

Setting from the initial conditions ($t = 0$ and $C = C_0$):

$$ln \frac{C_0}{C} = K_{app} t \qquad \text{Eq. VI.3}$$

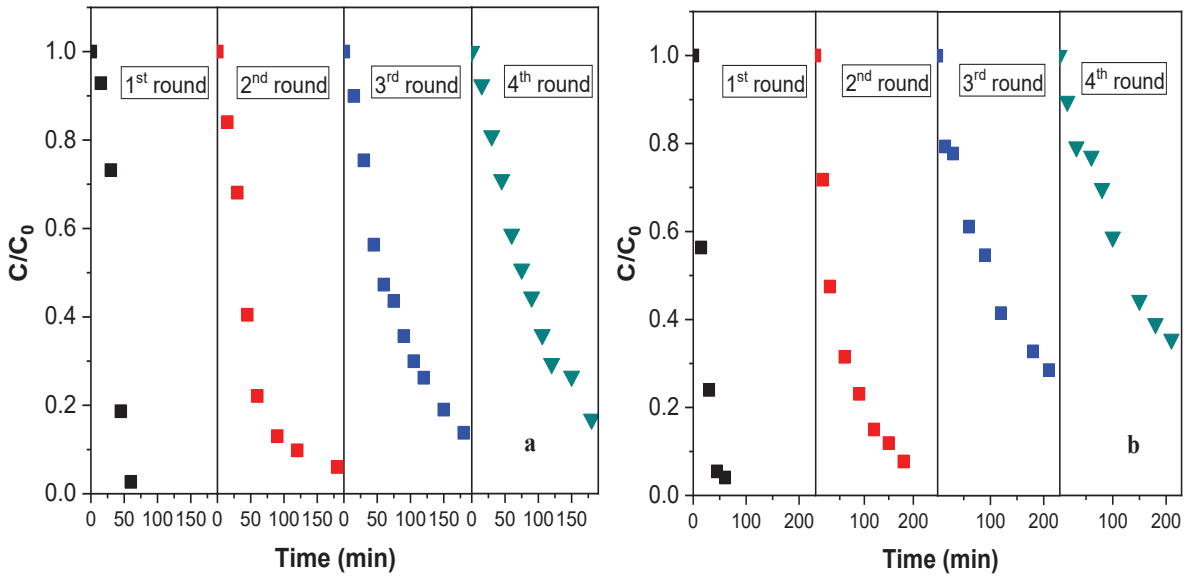

Figure VI.13. Comparison of the evolution of the concentration of diclofenac with irradiation time after several cycling runs. (a) 5Ti/$Zn_6Al_{1.33}Fe_{0.66}$, (b) Zn_6Al_2 (50 $\mu mol_{contaminant}/dm^3$; 1 g_{sample}/dm^3).

Table V1.6. Pseudo-first-order kinetic parameters for diclofenac photodegradation.

Catalyst		$t_{1/2}$ (min)	K_{app}
5Ti/$Zn_6Al_{1.33}Fe_{0.66}$	3rd round	56	0.011
	4th round	74	0.010
Zn_6Al_2	3rd round	103	0.006
	4th round	135	0.005

The first and second cycles for both samples presented a relevant amount of adsorption, thus making the assumption of Equation VI.2 impossible and giving poor adjustments to the pseudo-first-order kinetics of Equation VI.3. However, in the third cycle, adsorption was responsible for less than 10% of the decrease in diclofenac concentration for both samples. As such, the results for cycles 3 and 4 fitted well to pseudo-first-order kinetics. The reaction constant and $t_{1/2}$ for both samples, and the good fit of the results, are shown in Table VI.6. It can be seen that the K_{app} for 5Ti/$Zn_6Al_{1.33}Fe_{0.66}$ (0.011) is almost twice that of Zn_6Al_2 (0.006).

VI.4. CONCLUSIONS

The synthesis of hydrotalcite-type materials with the composition Zn-Al-Ti-Fe in which the aluminum used has been extracted from an industrial waste, namely a saline slag generated during the recycling of aluminum, has been reported. The ZnAl material presents a typical hydrotalcite structure, the crystallinity of which decreases as the amount of Fe or Ti increases due to partial substitution of Al. Thermal treatment at 673 K resulted in the formation of mixed oxides took place, with, ZnO, $ZnFe_2O_4$, Fe_3O_4, Fe_2O_3 and probably $ZnAl_2O_4$ being detected, depending on the composition of the sample. In all cases, the N_2 adsorption isotherms at 77 K were type II, and the BET specific surface areas were between 78 and 199 m^2/g.

The calcinated hydrotalcites with composition ZnAlTi and ZnAlFe have been studied as catalysts and catalyst supports, after impregnation with 5 wt.% Fe or Ti, in the photocatalytic degradation of diclofenac and salicylic acid, as examples of emerging contaminants, at 298 K and under UV light. The Fe/ZnAlTi catalysts showed the best catalytic behavior, although it was difficult to distinguish between the fraction removed by adsorption and the fraction photodegraded. To try to solve this problem, consecutive photodegradation cycles, in which the catalyst saturated with the pollutant molecule was used, were performed.

VI.5. REFERENCES

Balasamy, R.J., Tope, B.B., Khurshid, A., Al-Ali, A.A.S., Atanda, L.A., Sagata, K., Asamoto, M., Yahiro, H., Nomura, K., Sano, T., Takehira, K., Al-Khattaf, S.S., 2011. Ethylbenzene dehydrogenation over FeOx/(Mg,Zn)(Al)O catalysts derived from hydrotalcites: Role of MgO as basic sites. Appl. Catal. A Gen. 398, 113–122. https://doi.org/10.1016/j.apcata.2011.03.023

Benito, P., Guinea, I., Labajos, F.M., Rocha, J., Rives, V., 2008. Microwave-hydrothermally aged Zn,Al hydrotalcite-like compounds: Influence of the composition and the irradiation conditions. Microporous Mesoporous Mater. 110, 292–302. https://doi.org/10.1016/j.micromeso.2007.06.013

Carmona, E., Andreu, V., Picó, Y., 2014. Occurrence of acidic pharmaceuticals and personal care products in Turia River Basin: From waste to drinking water. Sci. Total Environ. 484, 53–63. https://doi.org/10.1016/j.scitotenv.2014.02.085

Carriazo, D., del Arco, M., García-López, E., Marcì, G., Martín, C., Palmisano, L., Rives, V., 2011. Zn,Al hydrotalcites calcined at different temperatures: Preparation, characterization and photocatalytic activity in gas–solid regime. J. Mol. Catal. A Chem. 342–343, 83–90. https://doi.org/10.1016/j.molcata.2011.04.015

Cavani, F., Trifirò, F., Vaccari, A., 1991. Hydrotalcite-type anionic clays: Preparation, properties and applications. Catal. Today 11, 173–301. https://doi.org/10.1016/0920-5861(91)80068-K

Chen, G., Qian, S., Tu, X., Wei, X., Zou, J., Leng, L., Luo, S., 2014. Enhancement photocatalytic degradation of rhodamine B on nanoPt intercalated Zn-Ti layered double hydroxides. Appl. Surf. Sci. 293, 345–351. https://doi.org/10.1016/j.apsusc.2013.12.165

Cheng, X., Huang, X., Wang, X., Sun, D., 2010. Influence of calcination on the adsorptive removal of phosphate by Zn–Al layered double hydroxides from excess sludge liquor. J. Hazard. Mater. 177, 516–523. https://doi.org/10.1016/j.jhazmat.2009.12.063

Cocheci, L., Lupa, L., Gheju, M., Golban, A., Lazău, R., Pode, R., 2018. Zn–Al–CO_3 layered double hydroxides prepared from a waste of hot-dip galvanizing process. Clean Technol. Environ. Policy 20, 1105–1112. https://doi.org/10.1007/s10098-018-1533-3

Cullity, B.D., 1978. Elements of X-ray Diffraction, Addison-Wesley series in metallurgy and materials. Addison-Wesley Publishing Company.

Das, N.N., Konar, J., Mohanta, M.K., Upadhaya, A.K., 2010. Synthesis, characterization and adsorptive properties of hydrotalcite-like compounds derived from titanium rich bauxite. React. Kinet. Mech. Catal. 99, 167–176. https://doi.org/10.1007/s11144-009-0120-3

Fang, L., Li, W., Chen, H., Xiao, F., Huang, L., Holm, P.E., Hansen, H.C.B., Wang, D., 2015. Synergistic effect of humic and fulvic acids on Ni removal by the calcined Mg/Al layered double hydroxide. RSC Adv. 5, 18866–18874. https://doi.org/10.1039/C4RA15406A

Ferrari, B., Paxéus, N., Giudice, R. Lo, Pollio, A., Garric, J., 2003. Ecotoxicological impact of pharmaceuticals found in treated wastewaters: Study of carbamazepine, clofibric acid, and diclofenac. Ecotoxicol. Environ. Saf. 55, 359–370. https://doi.org/10.1016/S0147-6513(02)00082-9

Fuentes, E.M., da Costa Faro, A., de Freitas Silva, T., Assaf, J.M., Rangel, M. do C., 2011. A comparison between copper and nickel-based catalysts obtained from hydrotalcite-like precursors for WGSR. Catal. Today 171, 290–296. https://doi.org/10.1016/j.cattod.2011.03.082

Galindo, R., López-Delgado, A., Padilla, I., Yates, M., 2014. Hydrotalcite-like compounds: A way to recover a hazardous waste in the aluminium tertiary industry. Appl. Clay Sci. 95, 41–49. https://doi.org/10.1016/j.clay.2014.03.022

Gil, A., Albeniz, S., Korili, S.A., 2014. Valorization of the saline slags generated during secondary aluminium melting processes as adsorbents for the removal of heavy metal ions from aqueous solutions. Chem. Eng. J. 251, 43–50. https://doi.org/10.1016/j.cej.2014.04.056

Gil, A., Arrieta, E., Vicente, M.A., Korili, S.A., 2018. Synthesis and CO_2 adsorption properties of hydrotalcite-like compounds prepared from aluminum saline slag wastes. Chem. Eng. J. 334, 1341–1350. https://doi.org/10.1016/j.cej.2017.11.100

Gil, A., Korili, S.A., 2016. Management and valorization of aluminum saline slags: Current status and future trends. Chem. Eng. J. 289, 74–84. https://doi.org/10.1016/j.cej.2015.12.069

Goh, K.H., Lim, T.T., Dong, Z., 2008. Application of layered double hydroxides for removal of oxyanions: A review. Water Res. 42, 1343–1368. https://doi.org/10.1016/j.watres.2007.10.043

Hadnadjev-Kostic, M., Vulic, T., Marinkovic-Neducin, R., Lončarević, D., Dostanić, J., Markov, S., Jovanović, D., 2017. Photo-induced properties of photocatalysts: A study on the modified structural, optical and textural properties of TiO_2–ZnAl layered double hydroxide based materials. J. Clean. Prod. 164, 1–18. https://doi.org/10.1016/j.jclepro.2017.06.091

Hosni, K., Abdelkarim, O., Frini-Srasra, N., Srasra, E., 2015. Synthesis, structure and photocatalytic activity of calcined Mg-Al-Ti-layered double hydroxides. Korean J. Chem. Eng. 32, 104–112. https://doi.org/10.1007/s11814-014-0199-8

José Dos Reis, M., Prévot, V., Leroux, F., Silvério, F., Valim, J.B., 2010. Dendrimer intercalation in layered double hydroxides. J. Porous Mater. 17, 443–451. https://doi.org/10.1007/s10934-009-9306-3

Khan, A., Smirniotis, P.G., 2008. Relationship between temperature-programmed reduction profile and activity of modified ferrite-based catalysts for WGS reaction. J. Mol. Catal. A Chem. 280, 43–51. https://doi.org/10.1016/j.molcata.2007.10.022

Kuwahara, Y., Ohmichi, T., Kamegawa, T., Mori, K., Yamashita, H., 2010. A novel conversion process for waste slag: Synthesis of a hydrotalcite-like compound and zeolite from blast furnace slag and evaluation of adsorption capacities. J. Mater. Chem. 20, 5052–5062. https://doi.org/10.1039/c0jm00518e

Lak, A., Simchi, A., Nemati, Z.A., 2012. Photocatalytic activity of TiO_2-capped ZnO nanoparticles. J. Mater. Sci. Mater. Electron. 23, 361–369. https://doi.org/10.1007/s10854-011-0396-8

Lambolez, L., Vasseur, P., Ferard, J.F., Gisbert, T., 1994. The Environmental Risks of Industrial Waste Disposal: An Experimental Approach Including Acute and Chronic Toxicity Studies. Ecotoxicol. Environ. Saf. 28, 317–328. https://doi.org/10.1006/eesa.1994.1056

Li, C., Wei, M., Evans, D.G., Duan, X., 2014. Layered Double Hydroxide-based Nanomaterials as Highly Efficient Catalysts and Adsorbents. Small 10, 4469–4486. https://doi.org/10.1002/smll.201401464

Liang, M., Kang, W., Xie, K., 2009. Comparison of reduction behavior of Fe_2O_3, ZnO and $ZnFe_2O_4$ by TPR technique. J. Nat. Gas Chem. 18, 110–113. https://doi.org/10.1016/S1003-9953(08)60073-0

Mantilla, A., Jácome-Acatitla, G., Morales-Mendoza, G., Tzompantzi, F., Gómez, R., 2011. Photoassisted Degradation of 4-Chlorophenol and p-Cresol Using MgAl Hydrotalcites. Ind. Eng. Chem. Res. 50, 2762–2767. https://doi.org/10.1021/ie1006883

Mantilla, A., Tzompantzi, F., Fernández, J.L., Góngora, J.A.I.D., Gómez, R., 2010. Photodegradation of phenol and cresol in aqueous medium by using Zn/Al + Fe mixed oxides obtained from layered double hydroxides materials. Catal. Today 150, 353–357. https://doi.org/10.1016/j.cattod.2009.11.006

McCafferty, E., Wightman, J.P., 1998. Determination of the concentration of surface hydroxyl groups on metal oxide films by a quantitative XPS method. Surf. Interface Anal. 26, 549–564. https://doi.org/10.1002/(sici)1096-9918(199807)26:8<549::aid-sia396>3.3.co;2-h

Miller, T.H., Bury, N.R., Owen, S.F., MacRae, J.I., Barron, L.P., 2018. A review of the pharmaceutical exposome in aquatic fauna. Environ. Pollut. 239, 129–146. https://doi.org/10.1016/j.envpol.2018.04.012

Miranda, L.D.L., Bellato, C.R., Milagres, J.L., Moura, L.G., Mounteer, A.H., de Almeida, M.F., 2015. Hydrotalcite-TiO_2 magnetic iron oxide intercalated with the anionic surfactant dodecylsulfate in the photocatalytic degradation of methylene blue dye. J. Environ. Manage. 156, 225–235. https://doi.org/10.1016/j.jenvman.2015.03.051

Mohammadi, M.R., Fray, D.J., 2010. Low temperature nanostructured zinc titanate by an aqueous particulate sol–gel route: Optimisation of heat treatment condition based on Zn:Ti molar ratio. J. Eur. Ceram. Soc. 30, 947–961. https://doi.org/10.1016/j.jeurceramsoc.2009.09.031

Mohapatra, L., Parida, K., 2016. A review on the recent progress, challenges and perspective of layered double hydroxides as promising photocatalysts. J. Mater. Chem. A 4, 10744–10766. https://doi.org/10.1039/c6ta01668e

Mohapatra, L., Parida, K., Satpathy, M., 2012. Molybdate/Tungstate Intercalated Oxo-Bridged Zn/Y LDH for Solar Light Induced Photodegradation of Organic Pollutants. J. Phys. Chem. C 116, 13063–13070. https://doi.org/10.1021/jp300066g

Murayama, N., Shibata, J., Sakai, K., Nakajima, S., Yamoto, H., 2009. Synthesis of Hydrotalcite-Like Materials from Various Wastes in Aluminum Regeneration Process. Resour. Process. 53, 6–11. https://doi.org/10.4144/rpsj.53.6

Naknam, P., Luengnaruemitchai, A., Wongkasemjit, S., 2009. Au/ZnO and Au/ZnO−Fe_2O_3 Prepared by Deposition−Precipitation and Their Activity in the Preferential Oxidation of CO. Energy & Fuels 23, 5084–5091. https://doi.org/10.1021/ef9004187

Nayak, S., Parida, K.M., 2018. Dynamics of Charge-Transfer Behavior in a Plasmon-Induced Quasi-Type-II p–n/n–n Dual Heterojunction in Ag@Ag_3PO_4/g-C_3N_4/NiFe LDH Nanocomposites for Photocatalytic Cr(VI) Reduction and Phenol Oxidation. ACS Omega 3, 7324–7343. https://doi.org/10.1021/acsomega.8b00847

Nayak, S., Pradhan, A.C., Parida, K.M., 2018. Topotactic Transformation of Solvated MgCr-LDH Nanosheets to Highly Efficient Porous MgO/$MgCr_2O_4$ Nanocomposite for Photocatalytic H_2 Evolution. Inorg. Chem. 57, 8646–8661. https://doi.org/10.1021/acs.inorgchem.8b01517

Nayak, S., Swain, G., Parida, K., 2019. Enhanced Photocatalytic Activities of RhB Degradation and H_2 Evolution from in Situ Formation of the Electrostatic Heterostructure MoS_2/NiFe LDH Nanocomposite through the Z-Scheme Mechanism via p–n Heterojunctions. ACS Appl. Mater. Interfaces 11, 20923–20942. https://doi.org/10.1021/acsami.9b06511

Parida, K.M., Baliarsingh, N., Patra, B.S., Das, J., 2007. Copperphthalocyanine immobilized Zn/Al LDH as photocatalyst under solar radiation for decolorization of methylene blue. J. Mol. Catal. A Chem. 267, 202–208. https://doi.org/10.1016/j.molcata.2006.11.035

Pérez-Fernández, V., Mainero Rocca, L., Tomai, P., Fanali, S., Gentili, A., 2017. Recent advancements and future trends in environmental analysis: Sample preparation, liquid chromatography and mass spectrometry. Anal. Chim. Acta 983, 9–41. https://doi.org/10.1016/j.aca.2017.06.029

Power, G., Gräfe, M., Klauber, C., 2011. Bauxite residue issues: I. Current management, disposal and storage practices. Hydrometallurgy 108, 33–45. https://doi.org/10.1016/j.hydromet.2011.02.006

Saber, O., Zaki, T., 2014. Carbon monoxide oxidation using Zn–Cu–Ti hydrotalcite-derived catalysts. J. Chem. Sci. 126, 981–988. https://doi.org/10.1007/s12039-014-0642-8

Santamaría, L., López-Aizpún, M., García-Padial, M., Vicente, M.A., Korili, S.A., Gil, A., 2020a. Zn-Ti-Al layered double hydroxides synthesized from aluminum saline slag wastes as efficient drug adsorbents. Appl. Clay Sci. 187, 105486. https://doi.org/10.1016/j.clay.2020.105486

Santamaría, L., Vicente, M.A., Korili, S.A., Gil, A., 2020b. Effect of the preparation method and metal content on the synthesis of metal modified titanium oxide used for the removal of salicylic acid under UV light. Environ. Technol. 41, 2073–2084. https://doi.org/10.1080/09593330.2018.1555285

Seftel, E.M., Puscasu, M.C., Mertens, M., Cool, P., Carja, G., 2014. Assemblies of nanoparticles of CeO_2–ZnTi-LDHs and their derived mixed oxides as novel photocatalytic systems for phenol degradation. Appl. Catal. B Environ. 150–151, 157–166. https://doi.org/10.1016/j.apcatb.2013.12.019

Shammas, N. (Ed.). (2010) Handbook of Advanced Industrial and Hazardous Wastes Treatment. Boca Raton: CRC Press.

Shannon, R.D., 1976. Revised Effective Ionic Radii and Systematic Studies of Interatomie Distances in Halides and Chaleogenides of Shannon & Prewitt Acta. Cryst. 32, 751–767.

Shao, M., Han, J., Wei, M., Evans, D.G., Duan, X., 2011. The synthesis of hierarchical Zn–Ti layered double hydroxide for efficient visible-light photocatalysis. Chem. Eng. J. 168, 519–524. https://doi.org/10.1016/j.cej.2011.01.016

Valente, J.S., Tzompantzi, F., Prince, J., Cortez, J.G.H., Gomez, R., 2009. Adsorption and photocatalytic degradation of phenol and 2,4 dichlorophenoxiacetic acid by Mg-Zn-Al layered double hydroxides. Appl. Catal. B Environ. 90, 330–338. https://doi.org/10.1016/j.apcatb.2009.03.019

Vulliet, E., Cren-Olivé, C., Grenier-Loustalot, M.F., 2011. Occurrence of pharmaceuticals and hormones in drinking water treated from surface waters. Environ. Chem. Lett. 9, 103–114. https://doi.org/10.1007/s10311-009-0253-7

Webb, P.A., Orr, C., Corporation, M.I., 1997. Analytical methods in fine particle technology. Micromeritics Instrument Corporation.

Xia, S.J., Liu, F.X., Ni, Z.M., Shi, W., Xue, J.L., Qian, P.P., 2014. Ti-based layered double hydroxides: Efficient photocatalysts for azo dyes degradation under visible light. Appl.

Catal. B Environ. 144, 570–579. https://doi.org/10.1016/j.apcatb.2013.07.060

Xia, S.J., Liu, F.X., Ni, Z.M., Xue, J.L., Qian, P.P., 2013. Layered double hydroxides as efficient photocatalysts for visible-light degradation of Rhodamine B. J. Colloid Interface Sci. 405, 195–200. https://doi.org/10.1016/j.jcis.2013.05.064

Yoldi, M., Fuentes-Ordoñez, E.G., Korili, S.A., Gil, A., 2019. Efficient recovery of aluminum from saline slag wastes. Miner. Eng. 140, 105884. https://doi.org/10.1016/j.mineng.2019.105884

Chapter VII

Other materials as drug adsorbents

VII.1. REMOVAL OF CAFFEINE AND DICLOFENAC FROM AQUEOUS SOLUTION BY ADSORPTION ON MULTIWALLED CARBON NANOTUBES

VII.1.1. INTRODUCTION

Emerging contaminants are defined as chemicals not currently subject to any discharge limitations or regulatory requirements and whose effects on human health and the environment are not yet sufficiently known. This type of contaminant includes a wide variety of compounds, such as pharmaceutical products, drugs, pesticides, personal care products and industrial additives (Richardson and Ternes, 2014), and some of them can be considered as anthropogenic markers for wastewater contamination (Gracia-Lor et al., 2017). Several methods can be applied to reduce the concentration of these types of contaminants in wastewater. Of these, adsorption processes on porous materials are simple to design and operate and do not contribute to the formation of undesirable by-products. As such, adsorption has been reported to be an effective treatment for removing organic compounds (Bolong et al., 2009).

Since their discovery, carbon nanotubes have generated a significant amount of research interest due to their high electrical conductivity, high specific surface area, and high mechanical, thermal and chemical stability (Gogotsi and Presser, 2013). These properties mean that, if used as fillers in nanocomposites, they can increase the mechanical, rheological and electrical properties of the resulting nanomaterials. For example, a better catalytic performance is observed in the case of Fenton-type catalysts combined with carbon nanotubes (Arshadi et al., 2016). To gain a better understanding of the mechanisms involved in the degradation of organic molecules, the interaction of carbon nanotubes used as fillers in catalysts for the adsorption of organic molecules as contaminants could be studied. In this regard, the use of carbon nanotubes as adsorbents in environmental pollution management, and in the particular case of the removal of organic contaminants, has gained interest in recent years (see Table VII.1). All these findings are a strong indication that carbon nanotubes are very interesting adsorbents for further study and development for use in environmental applications.

The chemicals considered in the present study are frequently found in wastewater and are also considered to be potential chemical markers of domestic wastewater contamination in surface waters. The concentration levels of these chemicals are in the range of μg-ng/dm^3 (Loos et al., 2009). To the best of our knowledge, despite the importance of the organic molecules considered in this work, studies of their adsorption using carbon nanotubes as adsorbents are very limited. Consequently, the objective of this work was to examine the effectiveness of commercial multiwalled carbon nanotubes for the removal of caffeine and diclofenac from aqueous solution at a concentration of up to 15 mg/ dm^3 by adsorption.

Table VII.1. Adsorption capacities (*q*) of organic molecules on carbon nanotubes.

Adsorbates	q (mg/g)	Reference
Acetic acid	6.5	(Özcan et al., 2013)
Atrazine	110.8	(Yan et al., 2008)
Bismarck brown R	32.15	(M. Kamil and Abdalrazak, 2014)
Carbamazepine	65	(Zhao et al., 2016)
Ciprofloxacoin	135	(Carabineiro et al., 2012)
Crystal violet	89.5	(Sabna et al., 2016)
Diclofenac	65	(Zhao et al., 2016)
Diclofenac	19.9	(Hu et al., 2017)
Diethyl phthalate	8.5	(Den et al., 2006)
Dimethyl phthalate	36	(Den et al., 2006)
Ibuprofen	186.5	(Cho et al., 2011)
Ibuprofen	33	(Zhao et al., 2016)
Methyl orange	52	(Yao et al., 2011)
2-(4-methylphenoxy)ethanol	172	(Patiño et al., 2015)
Nalidixic acid	196	(Patiño et al., 2015)
Oxalic acid	11.7	(Özcan et al., 2017)
Tetracycline	217	(Yu et al., 2014)
Thiamphenicol	25	(Zhao et al., 2016)
Trichloroethylene	83.3	(Naghizadeh et al., 2011)
Triclosan	434.7	(Cho et al., 2011)
Triclosan	19.7	(Hu et al., 2017)
Sulfamethoxazole	22	(Zhao et al., 2016)
Caffeine	4.2	This work
Diclofenac	7.3	This work

VII.1.2. EXPERIMENTAL PROCEDURE

VII.1.2.1. Materials

The multiwalled carbon nanotubes used as the adsorbent are commercial material obtained from Sigma-Aldrich. All chemical reagents were supplied by Sigma-Aldrich and used without further purification. The chemical structures and main characteristics of the organic molecules are shown in Table VII.2. The contaminant solutions were prepared using ultrapure water obtained with a Milli-Q apparatus (Millipore).

Table VII.2. General characteristics of the molecules used as adsorbates.

Characteristic	Caffeine	Diclofenac sodium
Structure	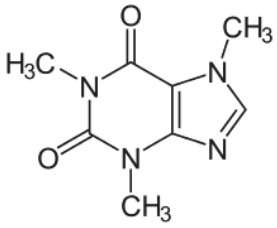	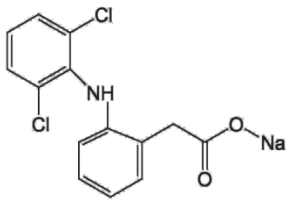
IUPAC name	3,7-Dihydro-1,3,7-trimethyl-1-H-purine-2,6-dione	Sodium;2-[2-(2,6-dichloranilino) phenyl] acetate
Chemical formula	$C_8H_{10}N_4O_2$	$C_{14}H_{10}Cl_2NNaO_2$
Molecular weight(g/mol)	194.19	296.15
λ_{max} (nm)	273	276
pK_a	10.4	4.15

VII.1.2.2. Characterization of the adsorbents

Determination of the point of zero charge (pH_{pzc}) indicates the net charge of the adsorbent surface in the solution. Thus, the net charge on the adsorbent surface is negative when the equilibrium pH of the solution is higher than the pH_{pzc} of the solid, whereas a positive net surface charge is observed when the equilibrium pH of the solution is lower than the pH_{pzc}. The pH_{pzc} of the carbon nanotubes used in the present study was determined according to a method described previously (Gil et al., 2011).

Textural analyses were based on nitrogen adsorption at 77 K using a static volumetric apparatus (Micromeritics ASAP 2010 adsorption analyzer). Prior to analysis, the adsorbent was degassed for 24 h at 473 K at a pressure of less than 0.133 Pa.

VII.1.2.3. Adsorption procedure

The adsorption kinetics were determined by performing a series of batch mode experiments. In each experiment, 10 cm^3 of aqueous solution with an initial concentration of 5, 10 or 15 mg/dm^3 was placed in a glass tube and mixed with 25, 50 or 100 mg of carbon nanotubes at pH 7. After shaking for a predetermined time, the suspension was filtered through 0.45 μm Durapore membrane filters and the concentration of the contaminant in the aqueous solution measured using a UV-Vis spectrometer (Jasco V-730). The absorbance was measured at the experimentally determined maximum absorbance wavelength and used to calculate the concentration of the contaminant remaining in solution. The quantity of organic compound adsorbed by the carbon nanotubes was calculated from the difference between the initial and remaining concentrations according to the following equation:

$$q_{t,e} = V \cdot (C_0 - C_{t,e}) / m \qquad \text{Eq. VII.1}$$

where C_0 and C_t (mg/dm^3) are the initial and final concentrations of organic compound in solution, respectively, V (cm^3) is the volume of the solution and m (g) is the adsorbent mass.

The equilibrium adsorption capacity of the adsorbent was determined by varying the initial concentration of the contaminant. In this case, 50 mg of adsorbent was added to a glass tube containing 10 cm^3 of solution with a concentration ranging from 0 to 50 mg/dm^3. After shaking for 2 h, the solution was separated from the solid by filtration and the remaining concentration determined by UV-visible spectrophotometry as in the case of the adsorption kinetics. The quantity of organic compound adsorbed per unit mass of adsorbent at equilibrium was determined according to equation VII.1, where C_e (mg/dm^3) is the concentration of that compound at equilibrium. All adsorption experiments were performed twice and the reported results are the average of these two measurements.

VII.1.3. RESULTS AND DISCUSSION

The nitrogen adsorption isotherm for the multiwalled carbon nanotubes used in this work was type II in the Brunauer, Deming, Deming and Teller (BDDT) classification (Gregg et al., 1967). The BET specific surface area was found to be 13 m^2/g, the total pore volume obtained at a relative pressure of 0.98 was 0.002 cm^3/g and the external specific surface area, as estimated using the *t*-plot method (Gregg et al., 1967), was 10 m^2/g. According to these results, these carbon nanotubes are a nonporous material. The pH_{pzc} value determined for the multiwalled carbon nanotube was 4.5. Moreover, the adsorbent had a negative charge as the equilibrium pH of aqueous solutions was higher than the pH_{pzc} value, thus meaning that electrostatic attractions between the negatively charged surface and the positively charged organic molecules could favor adsorption. However, the experimental results indicate that the effects of van der Waals and π-π interactions cannot be neglected (Hu et al., 2017). For example, (Zhang et al., 2011) attributed their experimental results for tetracycline adsorption on carbon nanotubes to non-electrostatic π-π dispersion interactions and hydrophobic interactions.

Various factors, such as adsorbent dose and initial organic compound concentration, may play an important role in the adsorption process. The adsorbent dose is an important parameter that strongly influences the process since adsorption capacity depends mainly on the specific surface area and the availability of binding sites on the solid. As such, various doses of multiwalled carbon nanotubes were used in this study, and the results are summarized in Figure VII.1. As the amount of adsorbent added to the contaminant solution increased from 25 to 100 mg, the adsorption capacity decreased from 3.21 to 1.41 mg/g in the case of caffeine, and from 3.32 to 1.36 mg/g in the case of diclofenac. This was probably the result of particle interactions, such as the partial overlapping or aggregation of adsorption sites, thus resulting in a reduction of the effective adsorbent surface area available to the organic molecules.

The adsorption process is also affected by the initial concentration and contact time. The evolution of adsorption with contact time is also shown in Figure VII.1 for various initial concentrations ranging between 5 and 15 mg/dm^3 and a fixed adsorbent dose of 50 mg. As can be seen, the equilibrium adsorption capacity of the carbon nanotubes increased with increasing organic compound concentration. This is probably due to the concentration gradient, which acts as the driving force to overcome the mass transfer resistance of the organic compound between the aqueous and solid phases. Under our experimental conditions,

a higher initial concentration provides a higher driving force for this mass transfer, thus leading to a higher adsorption capacity until saturation. Two stages were observed in the adsorption process: a very rapid initial adsorption over a few minutes (up to 15 min), followed by a longer period of much slower uptake. During the initial stage, adsorption was faster due to the large number of active sites available on the adsorbent and the interaction between the surface of the adsorbent and the organic molecule. The subsequent lower adsorption may be due to repulsive forces between the organic molecules already adsorbed on the solid surface and those in the bulk phase. Pseudo-first- and -second-order rate equations and the intra-particle diffusion model were tested to fit the experimental data (Gil et al., 2011). These types of kinetic modeling approaches are considered to indicate a simple relationship between the adsorption performance and operating conditions and show how the average adsorbent phase concentration (q) changes with adsorption time. The goodness-of-fit of these models to the experimental data was evaluated using the chi-squared test (χ^2) and the coefficient of determination (R).

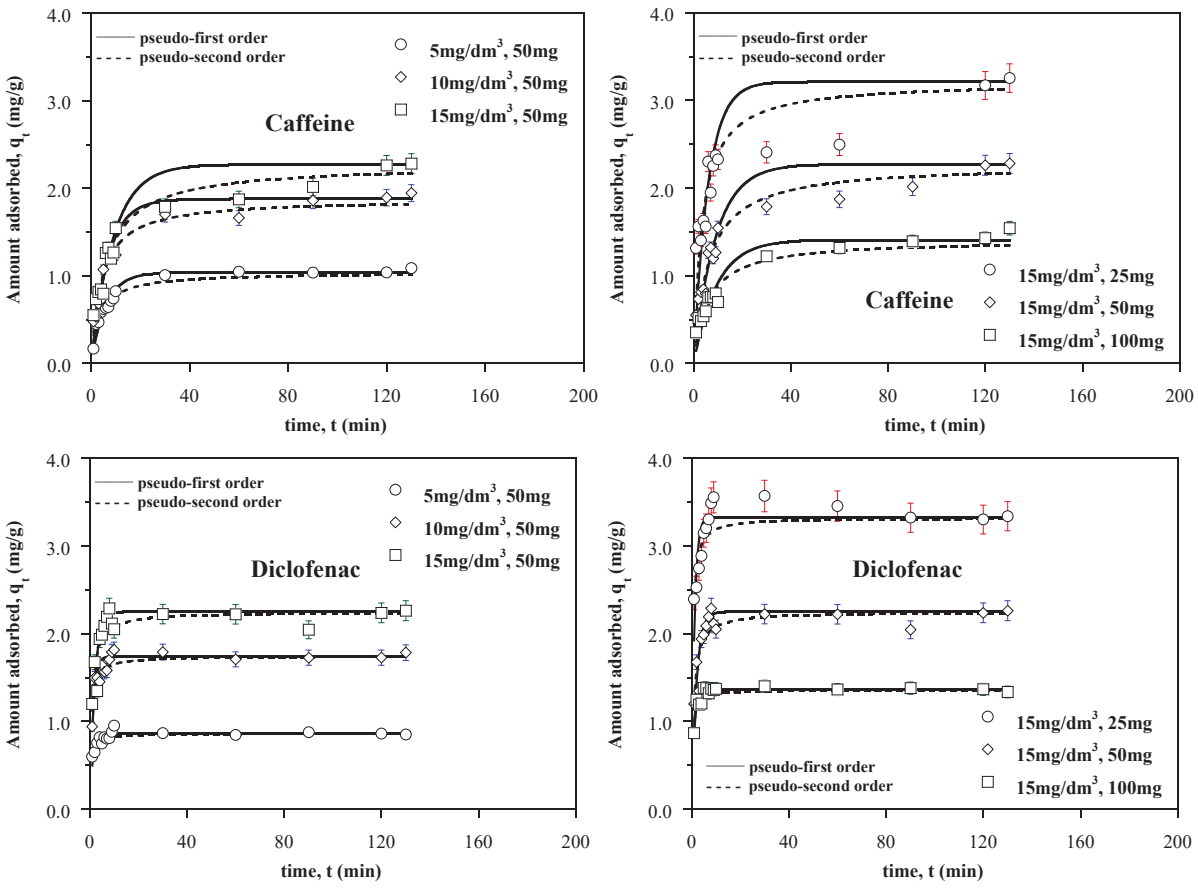

Figure VII.1. Kinetic adsorption data for caffeine and diclofenac on the multiwalled carbon nanotubes considering various compound concentrations and adsorbent amounts. T = 298 K. The lines represent a pseudo-first-order model (—) and a pseudo-second-order model (---).

The kinetic behavior results (see Figures VII.1 and VII.2, and Tables VII.3 and VII.4) indicate that adsorption can best be described as a pseudo-second-order process or that intraparticle diffusion is the rate-determining step. The suitability of these two models is related to a low initial concentration of the adsorbates (Haerifar and Azizian, 2013). In addition, although the first-order rate equation can describe the initial phase in the adsorption process, the adsorption data may deviate from the fitted curve as adsorption progresses. The second-order rate equation assumes that the adsorption process is controlled by a chemical mechanism. The k_2 values for diclofenac were found to be greater than those for caffeine (see Table VII.3), with the adsorption rate constant decreasing as the initial concentration of organic compound increased from 5 to 15 mg/dm^3.

A plot of the Morris–Weber relationship (Choy et al., 2004) for adsorption of the contaminants by the multiwalled carbon nanotubes is shown in Figure VII.2. As can be seen, the intra-particle diffusion of organic molecules within the carbon nanotubes occurs in two stages (Choy et al., 2004). The first linear part, which corresponds to the adsorption period

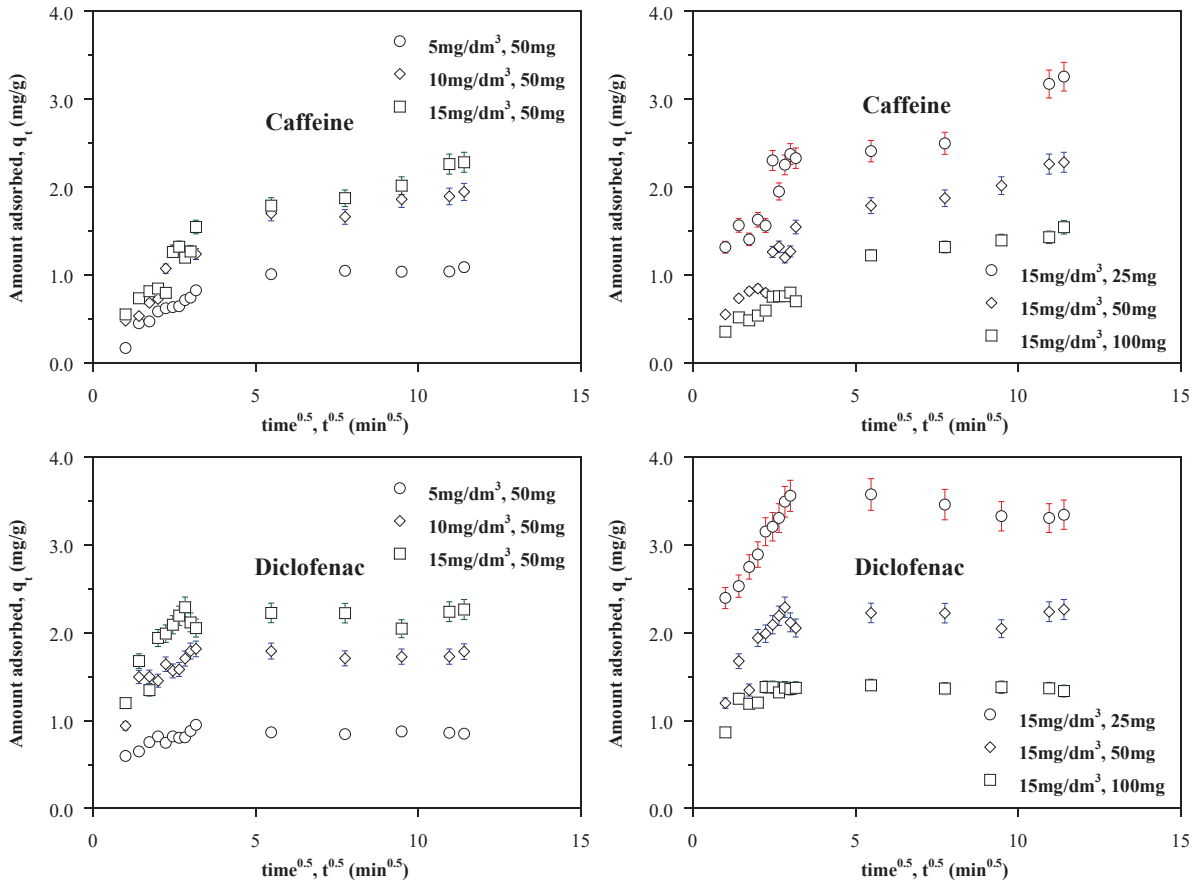

Figure VII.2. Intraparticle diffusion model for the adsorption of caffeine and diclofenac on the multiwalled carbon nanotubes considering various molecule concentrations and adsorbent amounts. T = 298 K.

Table VII.3. Pseudo-first- and -second-order parameters for the adsorption of caffeine and diclofenac by carbon nanotubes. T = 298 K[a,b].

	Caffeine	Diclofenac		Caffeine	Diclofenac
5 mg/dm^3 – 50 mg[c]			5 mg/dm^3 – 50 mg		
k_1 (1/min)	0.17	0.86	k_2 (g/mg·min)	0.29	2.62
χ^2	0.051	0.043	χ^2	0.034	0.028
R	0.97	0.79	R	0.98	0.87
10 mg/dm^3 – 50 mg			10 mg/dm^3 – 50 mg		
k_1 (1/min)	0.15	0.73	k_2 (g/mg·min)	0.13	1.02
χ^2	0.24	0.13	χ^2	0.16	0.12
R	0.96	0.89	R	0.98	0.90
15 mg/dm^3 – 50 mg			15 mg/dm^3 – 50 mg		
k_1 (1/min)	0.11	0.51	k_2 (g/mg·min)	0.074	0.55
χ^2	0.70	0.43	χ^2	0.29	0.34
R	0.92	0.85	R	0.97	0.88
15 mg/dm^3 – 25 mg			15 mg/dm^3 – 25 mg		
k_1 (1/min)	0.17	0.87	k_2 (g/mg·min)	0.091	0.74
χ^2	2.57	0.67	χ^2	1.29	0.51
R	0.68	0.80	R	0.86	0.85
15 mg/dm^3 – 100 mg			15 mg/dm^3 – 100 mg		
k_1 (1/min)	0.11	1.0	k_2 (g/mg·min)	0.12	2.07
χ^2	0.23	0.039	χ^2	0.15	0.067
R	0.95	0.92	R	0.97	0.86

[a] Pseudo-first-order equation model: $q_t = q_e \cdot (1 - \exp(-k_1 \cdot t))$, k_1 is the adsorption kinetic constant.

[b] Pseudo-second-order equation model: $q_t = \frac{k_2 \cdot q_e^2 \cdot t}{1 + k_2 \cdot q_e \cdot t}$, k_2 is the adsorption kinetic constant.

[c] Molecule concentration and adsorbent amount.

from 0 to 30 min, represents the external mass transfer or boundary layer diffusion and the rapid distribution of molecules onto the outer surface of the carbon nanotube. In contrast, the second linear part, which corresponds to the adsorption period from 30 to 90 min, represents the intra-particle diffusion and binding of molecules to the internal active sites of the adsorbent. The slope of the line (see Table VII.4) indicates the rate of the adsorption process, which decreases with contact time.

Table VII.4. Intraparticle rate parameters for the adsorption of caffeine and diclofenac by the multiwalled carbon nanotubes. T = 298 K[a].

	Caffeine	Diclofenac
5 mg/dm^3 – 50 mg [b]		
k'_3 (mg/g·min$^{0.5}$)	0.20	0.14
R	0.97	0.92
k''_3 (mg/g·min$^{0.5}$)	0.00080	0.0019
R	0.78	0.22
10 mg/dm^3 – 50 mg		
k'_3 (mg/g·min$^{0.5}$)	0.39	0.19
R	0.98	0.88
k''_3 (mg/g·min$^{0.5}$)	0.037	0.015
R	0.71	0.78
15 mg/dm^3– 50 mg		
k'_3 (mg/g·min$^{0.5}$)	0.48	0.42
R	0.98	0.995
k''_3 (mg/g·min$^{0.5}$)	0.056	0.0054
R	0.98	0.81
15 mg/dm^3– 25 mg		
k'_3 (mg/g·min$^{0.5}$)	0.73	0.61
R	0.97	0.993
k''_3 (mg/g·min$^{0.5}$)	0.15	0.0036
R	0.97	0.19
15 mg/dm^3 – 100 mg		
k'_3 (mg/g·min$^{0.5}$)	0.27	0.19
R	0.96	0.83
k''_3 (mg/g·min$^{0.5}$)	0.047	0.00080
R	0.96	0.14

[a] Intraparticle diffusion equation model: $q_t = k_3 \cdot t^{0.5}$, k_3 is the intraparticle diffusion rate constant. k'_3 is related to the first linear portion, from 0 to 30 min. k''_3 is related to the second linear portion, from 30 to 90 min.

[b] Molecule concentration and adsorbent amount.

The equilibrium adsorption isotherm is fundamental for describing the interactive behavior between solutes and adsorbents, as well as being a basic requirement in the design of adsorption systems (Azizian et al., 2009). In this study, the Freundlich, Langmuir and Toth isotherm equations were used to model the experimental data for caffeine and diclofenac. The resulting adsorption isotherms are presented in Figure VII.3. They can be seen to be characteristic L-2 type isotherms according to the Giles classification. This type of isotherm displays concavity towards the abscissa axis and is typical of a system in which the adsorbate has high affinity for the adsorbent (Giles et al., 1974). A monolayer formation is established.

The constants for the isotherm equations, as estimated by non-linear regression, are presented in Table VII.5. The goodness-of-fit of the models to the experimental data was evaluated using the chi-squared test (χ^2) and the coefficient of determination (R). Although all models describe the experimental results well, the Toth equation provides the best agreement between the theoretical and experimental data. This is in accordance with the results obtained in other studies involving the adsorption of organic compounds on activated carbons (Essandoh et al., 2015).

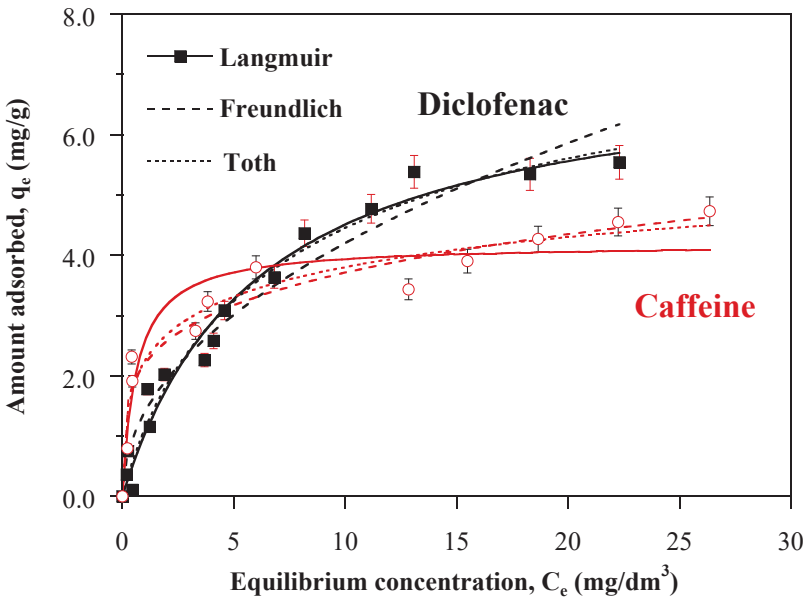

Figure VII.3. Experimental (symbols) and model (lines) isotherms for the equilibrium adsorption of caffeine and diclofenac on the multiwalled carbon nanotubes. Equilibrium time = 2 h, T = 298 K.

Table VII.5. Freundlich, Langmuir and Toth parameters for the adsorption of caffeine and diclofenac by the multiwalled carbon nanotubes. Equilibrium time = 2 h, T = 298 K.

	Caffeine	Diclofenac
Freundlich [a]		
q_F	2.20	1.39
m_F	4.4	2.1
χ^2	1.49	2.5
R	0.97	0.98
Langmuir [b]		
q_L (mg/g)	4.18	7.26
k_L (dm^3/mg)	1.59	0.16
χ^2	2.27	1.56
R	0.95	0.98
Toth [c]		
q_T (mg/g)	10.1	8.5
k_T (dm^3/mg)	93	0.18
m_T	0.21	0.77
χ^2	1.38	1.52
R	0.97	0.98

[a] Freundlich equation isotherm: $q_e = k_F \cdot C_e^{1/m_F}$

[b] Langmuir equation isotherm: $q_e = \frac{k_L \cdot q_L \cdot C_e}{1 + k_L \cdot C_e}$

[c] Toth equation isotherm: $q_e = \frac{k_T \cdot q_T \cdot C_e}{[1 + (k_T \cdot C_e)^{m_T}]^{1/m_T}}$

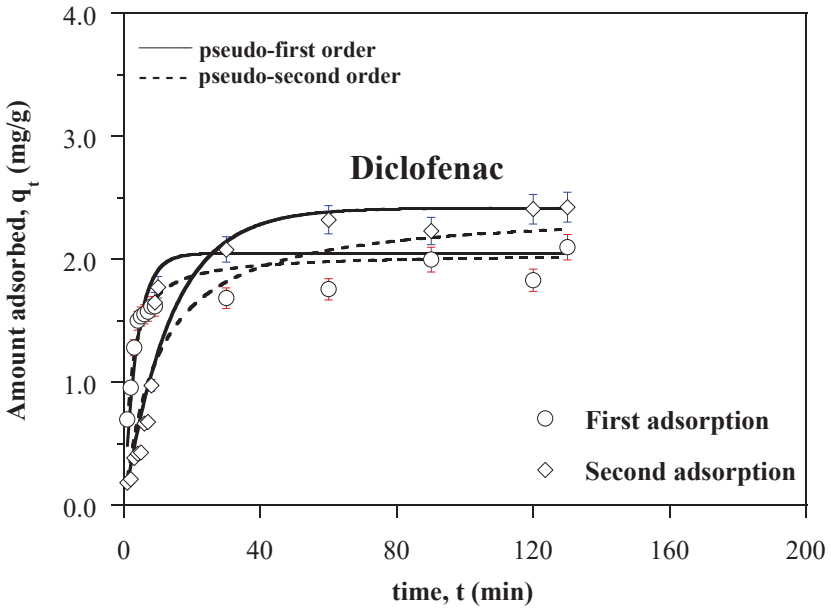

Figure VII.4. Reusability adsorption data for diclofenac on the multiwalled carbon nanotubes. 15 mg/dm^3 and 30 mg. T = 298 K. The lines represent a pseudo-first-order model (—) and a pseudo-second-order model (---).

In order to evaluate the reusability of the carbon nanotubes for diclofenac adsorption, the used adsorbent was separated from the solution by filtration and treated with 10 cm^3 of 0.1 mol/L HCl for 2 h to desorb the organic compound retained. The solid was then separated from the acid solution by filtration, washed well with deionized water, and dried in an oven at 333 K for 48 h before been reused in adsorption experiments. The amount of diclofenac adsorbed for each stage of reuse is shown in Figure VII.4.

VII.2. DICLOFENAC, CAFFEINE AND SOLKETAL REMOVAL FROM AQUEOUS SOLUTIONS USING ACTIVATED CARBON AND METAL ORGANIC FRAMEWORK AS ADSORBENTS

VII.2.1. INTRODUCTION

The search for an alternative to petroleum-based fuels started decades ago due to their limited availability, high impact on the environment and market fluctuation. Biodiesel has arisen as a great alternative to fossil fuel as it reduces chemical emissions such as unburned hydrocarbon (68%), polycyclic aromatic hydrocarbon (≈85%) and sulfur dioxide (100%) (Talebian-Kiakalaieh et al., 2018). It can be produced from many renewable sources such as plant oils, animal fat, waste cooking oil or photosynthetic algae (Monteiro et al., 2018). In addition to its greener nature, its physical properties, close to those of fossil diesel, make it a great substitute as the diesel engine and storage infrastructure do not need any modification (Tat and Van Gerpen, 1999). Biodiesel is produced from triglyceride in a transesterification process which results in a 90 wt.% methyl ester (biodiesel) and 10 wt.% glycerol as byproduct. Despite its promising characteristics, some challenges need to be overcome such as higher production costs when compared with fossil fuels, its refinement or the surplus of glycerol which has made the glycerol market price unstable (Anuar and Abdullah, 2016). Glycerol has been traditionally employed as additive in food, pharmaceuticals and tobacco (Bagheri et al., 2015). However, with the development of biodiesel production, finding alternative uses for glycerol is vital to ensure the sustainability of global production of biodiesel (Monteiro et al., 2018). Glycerol can be modified through different reactions such as esterification, acetalization and etherification (Bagheri et al., 2015; Timofeeva et al., 2017; Moreira et al., 2019). Among these derivatives ketals and acetals can be used as additives of gasoline and diesel fuel (Trifoi et al., 2016; Fatimah et al., 2019).

Solketal (2,2-dimethyl-1,3-dioxolane-4-methanol) has been revealed in recent years as one of the most interesting bioadditive due to its interesting properties. It improves cold flow

properties of diesel fuel and oxidation stability, gum formation and, specially, octane number of gasoline fuel (Mota et al., 2010). There is not much research performed regarding its toxicity: an aquatox fish test showed that solketal (LC50 = 3.162 ppm) had less environmental toxicity than methyl tertiary butyl ether, MTBE, a common fuel additive (LC50 < 1,000) (Nanda et al., 2014). *Maes et al.* (2012) studied solketal as solvent for zebrafish bioassays with results showing that embryos and larvae had problems tolerating it even at the lowest concentration (0.5%). Levels of 1% and above included developmental delay, impaired circulation and motility in embryos, and loss of posture and brain necrosis in larvae.

Being proven that solketal is not innocuous to water environment, a study of possible adsorbents in aqueous media in case of an oil spill needs to be carried out. The present study tests the effectiveness of two commercial adsorbents for the removal of solketal: a granular activated carbon (AC) and a metal organic framework (MOF). Two emerging contaminants (diclofenac sodium and caffeine) were also chosen for comparison purposes. The efficacy of several MOF for the adsorption of pharmaceutical compounds has been tested before (Lin et al., 2018; Luo et al., 2018; Van Tran et al., 2019) as well as that of AC (Bahamon and Vega, 2017; Alves et al., 2018; Delgado et al., 2019), however, to our best knowledge, their solketal sorption capacity is yet to be tested. Various kinetic and equilibrium models were assessed for the adsorption of these three organic molecules on the two adsorbents.

VII.2.2. EXPERIMENTAL PROCEDURE

VII.2.2.1. Materials and characterization techniques

The AC used in this work, Hydrodarco 3000, was kindly supplied by Cabot Corporation. This granular, acid-washed carbon is produced by steam activation of coal and has excellent adsorption capacity for organic molecules. The MOF, called Basolite A100, is a Sigma-Aldrich trademark for the MIL-53(Al) MOF. This adsorbent has a structure built up from infinite chains of corner-sharing $AlO_4(OH)_2$ octahedra connected through 1,4-benzenedicarboxylate ligands.

The chemical reagents used as adsorbates (caffeine, diclofenac sodium and solketal) were purchased from Sigma-Aldrich with purity above 97% and their chemical structures/physicochemical characteristics are displayed in Table VII.6.

N_2 physisorption was performed at 77 K with a Micromeritics ASAP 2010 adsorption analyzer. The samples (0.4 g) were degassed under vacuum before measurement at 423 K for

24 h. The specific surface area (S_{BET}) was evaluated by the BET method in the range between 0.05-0.20 of relative pressure. The external surface area (S_{ext}) and the micropore volumes ($V\mu p$) were also estimated using the *t-plot* method.

Table VII.6. Chemical structures/physicochemical characteristics of the adsorbates.

Name	Structure and characteristics	
Caffeine	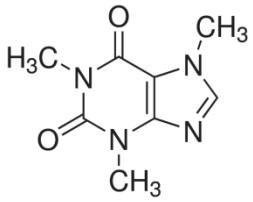	$C_8H_{10}N_4O_2$
		m=194.19
		pk_a=10.4
Diclofenac sodium	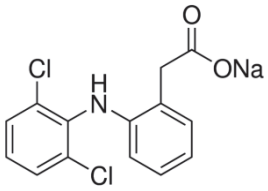	$C_{14}H_{10}Cl_2NNaO_2$
		m=296.15
		pk_a=4.15
Solketal	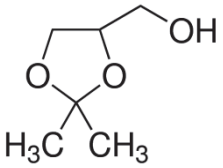	$C_6H_{12}O_3$
		m=132.16
		pk_a=14.20

VII.2.2.2. Adsorption procedure

The adsorption experiments of solketal, diclofenac and caffeine were carried out under batch adsorption conditions. Kinetic tests were performed to study both the effect of drug concentration and the adsorbent dose. In the case of diclofenac and caffeine, the effect of the drug concentration was studied by adding 20 or 75 mg of the adsorbent to 200 cm^3 solutions with several drug concentrations (10, 15 and 20 mg/dm^3). In the case of solketal, due to its low signal on the UV spectrophotometer, larger concentrations were chosen, 1.5 g of the adsorbent to a 50, 75 or 100 g/dm^3 solketal concentration. The adsorbent dose was examined by using various amounts of adsorbent 10, 20 and 30 mg (for diclofenac and caffeine with AC), 50, 75 and 100 mg (for diclofenac and caffeine with MOF) or 1, 1.5 and 2 g (for solketal) in a 200 cm^3 solution with a drug concentration of 15 mg/dm^3 or 75 g/dm^3, respectively. Experiments were performed with no pH modification and 298 K with samples being shaken in a stirring plate throughout the duration of the experiments. Samples of the

solution were taken at various time intervals until equilibrium was attained, up to 400 min. The contaminant concentration in the filtered solutions (0.45 μmol, Durapore) was determined by a Jasco V-730 UV–Vis spectrometer. Maximum adsorption wavelengths used were 276.5 nm for diclofenac, 273.5 nm for caffeine and 239 for solketal.

In order to estimate the amount of pollutant adsorbed by AC and MOF, the initial and remaining concentrations were subtracted, using Eq. VII.1. The kinetic modeling was studied using two different rate equations: pseudo-first (Eq. VII.2) and pseudo-second-order (Eq. VII.3). The experimental data was tested using OriginPro program (2018 version) in order to analyze the transport of organic molecules onto the adsorbent particles.

$$\frac{dq}{dt} = k_1(q_e - q_t) \qquad \text{Eq. VII.2}$$

$$\frac{dq}{dt} = k_2(q_e - q_t)^2 \qquad \text{Eq. VII.3}$$

where q_e is the amount of adsorbed solute at equilibrium and q_t at a time t (mg/g for diclofenac and caffeine and g/g for solketal), and k_1 and k_2 are the reaction rate constants of pseudo-first and pseudo-second-order, respectively.

The Weber-Morris linear representations for describing the kinetics of sorption at solid/solution interfaces controlled by intraparticle diffusion was also used (Plazinski and Rudzinski, 2009):

$$q_t = k_3 \cdot t^{0.5} \qquad \text{Eq. VII.4}$$

where k_3 (mg/g·min$^{0.5}$ or g/g·min$^{0.5}$) is the intraparticle-diffusion rate constant. Assuming constant diffusion through adsorbent pores (Khraisheh et al., 2002), if the Weber–Morris plot of q_t versus $t^{0.5}$ gives a straight line, this means that the sorption process is only controlled by intraparticle diffusion. In the same way, two or more steps influence the sorption process if the data exhibit multi-linear plots (Valderrama et al., 2008).

Intraparticle diffusion was also studied with a fractional approach to the equilibrium, used to estimate the effective diffusion coefficient (Urano and Tachikawa, 1991):

$$F(t) = \frac{C_0 - C_t}{C_0 - C_e} = \sqrt{1 - exp\left(-\frac{\pi^2 D t}{r^2}\right)} \qquad \text{Eq. VII.5}$$

where D (m^2/s) is the intraparticle-diffusion coefficient and r (m) is the particle size radius assuming a perfect sphere.

In order to study the adsorption capacity of both the MOF and AC on the three pollutants, equilibrium studies were also performed. Drug solutions of various concentrations (between 10 and 500 mg/dm^3 in the case of the drugs and between 10 and 500 g/dm^3 for solketal) were placed in 10 cm^3 glass tubes with either 6 mg of the adsorbent (AC) or 10 mg (MOF) and shaken for 7 h. Drug concentrations of the filtered samples were calculated with UV–visible spectrophotometry and using Eq. VII.1 (C_e, in either mg/dm^3 or g/dm^3, was the drug concentration at equilibrium). Various models can be considered to study the equilibrium experimental data and better understand the behavior between pollutants and adsorbents. Langmuir (Eq. VII.6) and Freundlich (Eq. VII.7) were chosen as two-parameter isotherms and Toth (Eq. VII.8) as three-parameter isotherm. Being first designed to describe gas-solid phase adsorption, Langmuir isotherm balances the relative rate of adsorption and desorption. It assumes monolayer adsorption onto a surface which contains a finite number of sites with uniform characteristics (Dąbrowski, 2001). The Freundlich isotherm was designated to be applicable to adsorption process that takes place in heterogeneous surfaces. The expression that the isotherm gives describes the surface heterogeneity as well as the active sites distribution and energies (Ramadoss and Subramania, 2018). The Toth isotherm is another empirical modification of the Langmuir equation with the purpose of reducing the difference between experimental data and predicted value of equilibrium data. This model is most valuable for the description of heterogeneous adsorption systems which satisfy both low and high end boundary of adsorbate concentration. The third parameter added, m_T, characterizes the heterogeneity of the adsorption system and when m_T, = 1 this equation reduces to Langmuir isotherm equation. If this parameter deviates further away from unity (1), then the system is said to be heterogeneous (Ayawei et al., 2017).

$$q_e = \frac{k_L \cdot q_L \cdot C_e}{1 + k_L \cdot C_e} \qquad \text{Eq. VII.6}$$

$$q_e = k_F \cdot C_e^{1/m_F} \qquad \text{Eq. VII.7}$$

$$q_e = \frac{k_T \cdot q_T \cdot C_e}{[1 + (k_T \cdot C_e)^{m_T}]^{1/m_T}} \qquad \text{Eq. VII.8}$$

where q_e (mg or g of adsorbate/g of adsorbent) is the amount adsorbed, C_e (mg or g/g) is the monolayer capacity, k_L is related to the adsorption capacity, k_F is the equilibrium constant, $1/m_F$ is the adsorption intensity (also indicates the heterogeneity of the adsorbate sites) and k_T is the Toth isotherm constant.

VII.2.3. RESULTS AND DISCUSSION

VII.2.3.1. Characterization of the adsorbents

The nitrogen adsorption-desorption data for samples at 77 K showed that the adsorption isotherm for AC was of type II in the Brunauer, Deming, Deming and Teller (BDDT) classification (S. J. Gregg and Sing, 1982) with an hysteresis loop of type IIIb in the Rouquerol et al. classification (Rouquerol et al., 1999), indicating that the adsorbent is a mesoporous material. The BET specific surface area of the AC was 578 m^2/g, with a 0.564 cm^3/g total pore volume, obtained at a relative pressure of 0.98. The t-plot method was used to estimate the external specific surface area and micropore volume, which were 159 m^2/g and 0.206 cm^3/g, respectively. MOF adsorption isotherm was also found to be of type II in the BDDT classification with a 465 m^2/g BET specific surface, a total 1.05 cm^3/g pore volume of and 0.13 cm^3/g micropore volume.

VII.2.3.2. Adsorption experiments

The adsorption process can be affected by several factors that play an important part; among them, the adsorbent dose and the initial concentration of adsorbate are of great influence in the final result.

In order to study the role of the adsorbent dose, various doses were studied depending on both the adsorbent and the adsorbate. With diclofenac and caffeine as adsorbates (15 mg/dm^3) and activated carbon, doses between 10 and 30 mg were studied. If solketal was the adsorbate, AC doses used ranked from 1 to 2 grams. The results are summarized in the first column of the Figure VII.5. It can be seen that the adsorption capacity of AC was similar for diclofenac and caffeine and much greater in the case of solketal were the AC adsorption capacity is expressed in g/g adsorbent. In MOF experiments, doses of 50, 75 and 100 mg of adsorbent on a 15 mg/dm^3 concentration of diclofenac or caffeine were analyzed and the same conditions for solketal than the AC. Results are shown in the first column of Figure VII.6. When MOF is used, its diclofenac adsorption capacity is greater than that of caffeine. As a whole, the adsorption capacity of MOF is in all cases lower than when AC is used as adsorbent. In all experiments the adsorption capacity in equilibrium decreased with an increasing amount of adsorbent dose. This result is likely due to particle interactions and aggregation of the adsorption sites which cause a decrease in the effective adsorbent surface area available to the organic contaminants.

To study the effect of the initial adsorbate concentration, various concentrations of the organic molecules were chosen between 10 and 20 mg/dm^3 for diclofenac and caffeine or between 50 and 100 g/dm^3 for solketal. The experiments were performed with a fixed amount of adsorbent, at 298 K, no pH modification and the equilibrium was achieved in less than 400 min. Results are shown in the second columns of Figure VII.5 for AC and Figure VII.6. for MOF.

In all experiments, a higher initial adsorbate concentration results in a higher adsorption capacity. This can be due to the fact that each adsorbent has the capacity to adsorb a fixed quantity of the pollutant, thus an increase in the adsorbate concentration produces an increase in the adsorption capacity until this amount is reached. Also, the concentration gradient, acting as a force that overcomes mass transfer resistance of the adsorbate between the aqueous and solid phases could be partially responsible. A higher initial concentration leads to a higher adsorption capacity as it provides a higher driving force.

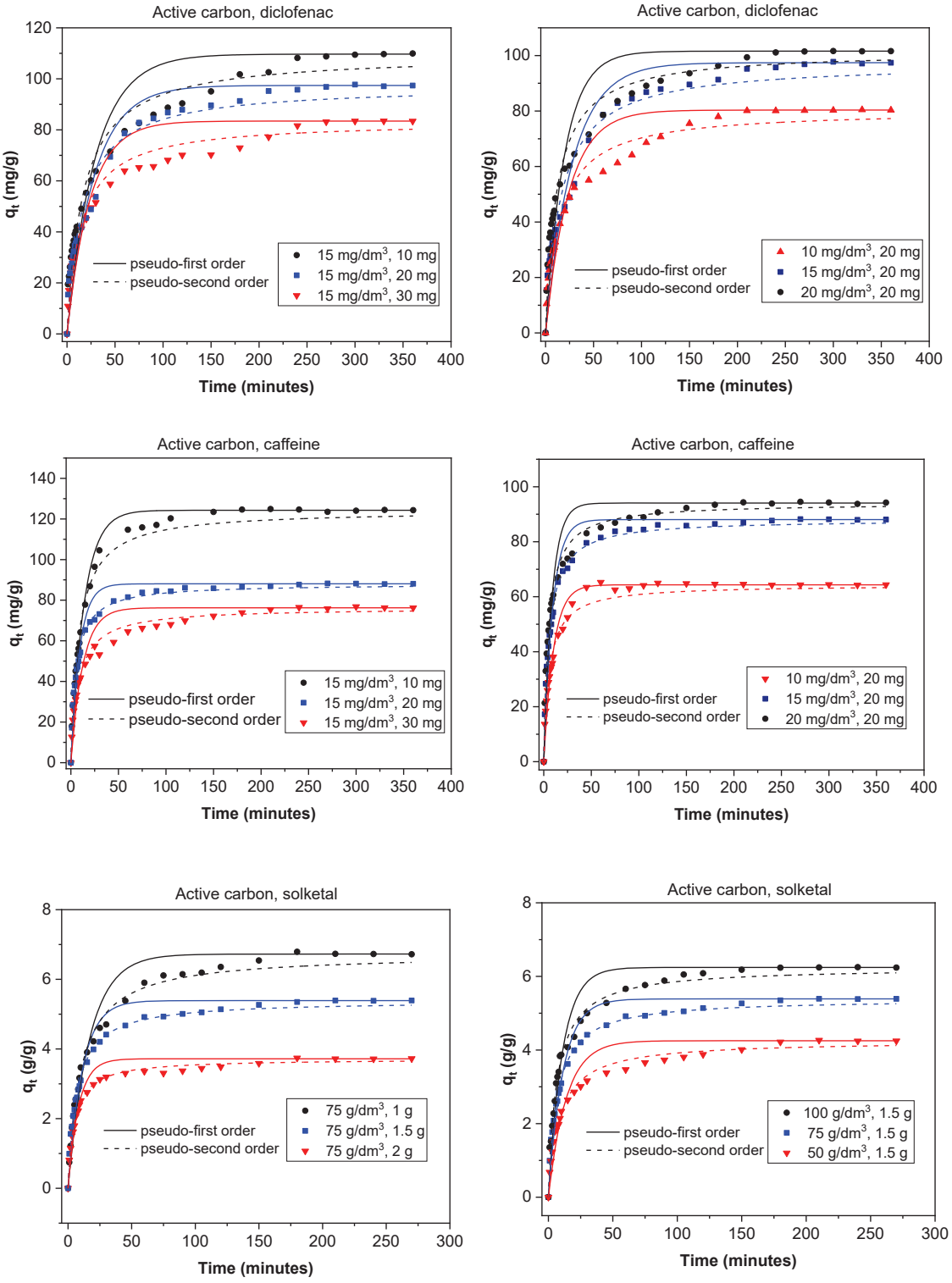

Figure VII.5. Kinetic adsorption data for diclofenac, caffeine and solketal on the AC considering various adsorbate concentrations and adsorbent amounts.

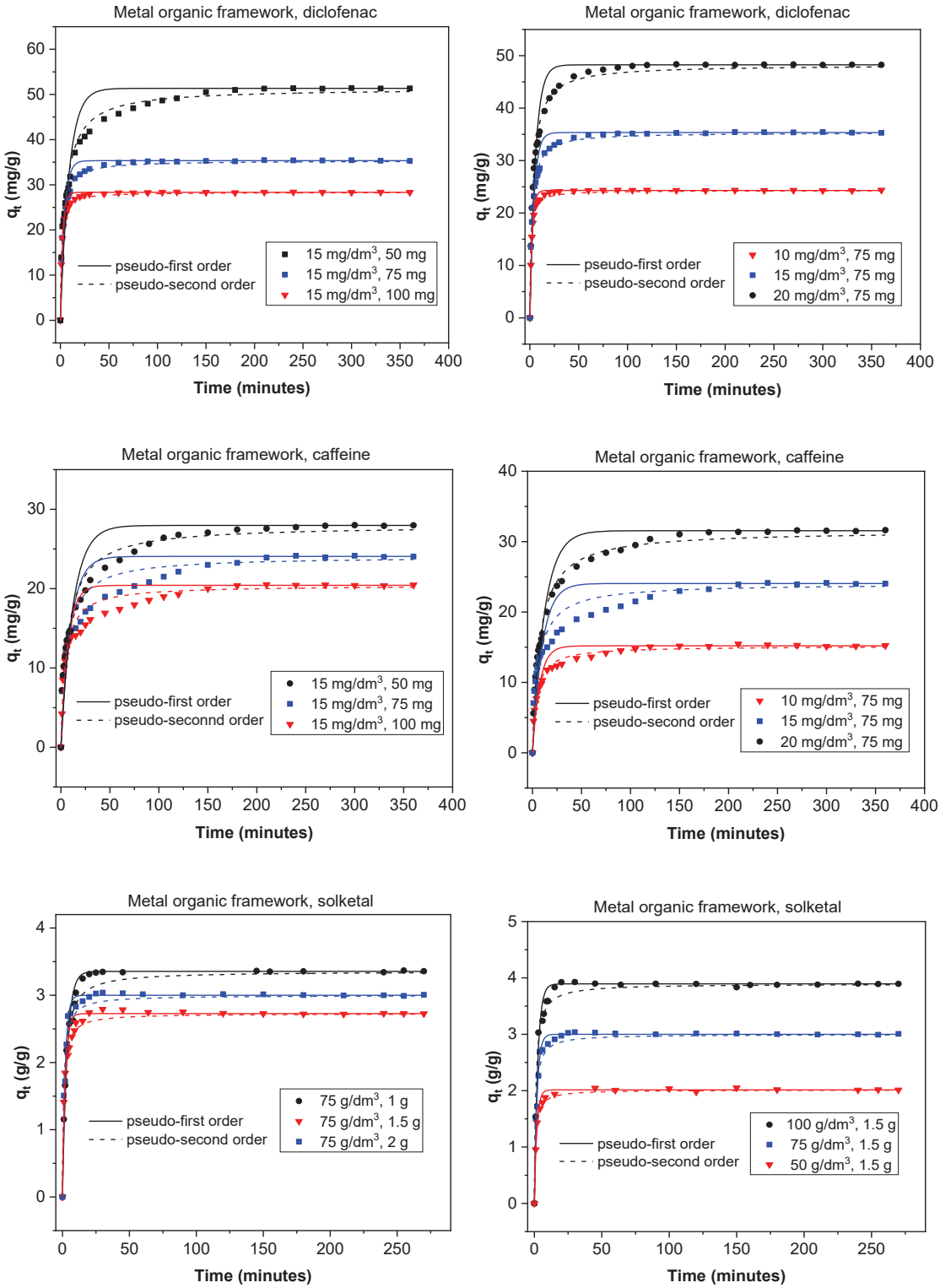

Figure VII.6. Kinetic adsorption data for diclofenac, caffeine and solketal on the MOF considering various adsorbate concentrations and adsorbent amounts.

VII.2.3.3. Kinetic models

The kinetic behavior of the adsorption processes is described in Tables VII.7 and VII.8 and Figures VII.5 and VII.6. The pseudo-second order linear reaction describes better the process in all cases. When AC is used as adsorbent (Table VII.7., Figure VII.5.), the adsorption rate is faster for solketal, as it has the highest values. The adsorption rate constant is similar for caffeine and diclofenac, although caffeine figures are slightly larger. An analysis of the changes as the adsorbate increases concentration from 10 mg/dm^3 to 20 mg/dm^3 shows no significant change in the k_2 values but a slight decrease. However, an increase in adsorbent mass from 10 to 30 mg reveals an increase on the adsorption rate constant. When MOF was used as adsorbent (Table VII.8., Figure VII.6), the adsorption rate was in general faster than for AC, as k_2 values are greater and equilibrium was achieved faster. A comparison between adsorbates shows again a much greater adsorption rate for solketal than the pharmaceutical compounds, which exhibit slightly larger k_2 values when diclofenac was tested as adsorbate than caffeine. An increase in the concentration of adsorbate shows a decrease in the adsorption rate constant and, as is also the case in AC results, the increase of adsorbent mass increments k_2 values.

As can be seen from Figures VII.5 and VII.6, equilibrium was achieved faster when MOF was used as adsorbent, although the amount adsorbed was always smaller. This is more obvious in the case of diclofenac and, specially, solketal where MOF has a very rapid initial adsorption in the first 20 min. The adsorption process is thus separated in two stages: an initial stage, short and with faster adsorption rate as there are a larger number of free and stronger active sites and a slower and longer uptake period in which repulsive forces appear between the already adsorbed organic molecules and the ones in the bulk phase preventing them from being adsorbed. This is further studied with the intraparticle diffusion of the organic molecules, Table VII.9. and Figure VII.7. The first slope of the process, k_3' represents the external mass transfer and the fast distribution of the organic molecules on the most superficial layer of the adsorbent.

Table VII.7. Pseudo-first and pseudo-second-order parameters for the adsorption of organic molecules by the activated carbon.

Sample		Pseudo-first order						Pseudo-second order				
		10 mg/dm^3 20 mg	15 mg/dm^3 20 mg	20 mg/dm^3 20 mg	15 mg/dm^3 10 mg	15 mg/dm^3 30 mg		10 mg/dm^3 20 mg	15 mg/dm^3 20 mg	20 mg/dm^3 20 mg	15 mg/dm^3 10 mg	15 mg/dm^3 30 mg
diclofenac	k_1 (1/min)	0.041	0.036	0.051	0.034	0.042	k_2 (1/min)	8.73E-4	6.48E-4	8.45E-4	5.43E-4	8.29E-4
	χ^2	1836	2044	3388	1372	2436	χ^2	439	823	815	1128	520
	R	0.95	0.96	0.93	0.93	0.93	R	0.99	0.99	0.98	0.98	0.99
caffeine	k_1 (1/min)	0.098	0.108	0.117	0.072	0.079	k_2 (1/min)	2.68E-3	2.10E-3	2.12E-3	9.61E-4	1.69E-3
	χ^2	319	943	1646	1096	1470	χ^2	216	101	199	533	240
	R	0.98	0.97	0.95	0.99	0.94	R	0.99	0.997	0.995	0.994	0.991
		50 g/dm^3 1.5 g	75 g/dm^3 1.5 g	100 g/dm^3 1.5 g	75 g/dm^3 1 g	75 g/dm^3 2 g		50 g/dm^3 1.5 g	75 g/dm^3 1.5 g	100 g/dm^3 1.5 g	75 g/dm^3 1 g	75 g/dm^3 2 g
solketal	k_1 (1/min)	0.072	0.089	0.092	0.060	0.12	k_2 (1/min)	0.027	0.027	0.024	0.014	0.054
	χ^2	4	3.7	5.8	6	1.75	χ^2	0.52	0.40	0.87	0.97	0.18
	R	0.95	0.97	0.97	0.97	0.96	R	0.993	0.997	0.995	0.996	0.996

Table VII.8. Pseudo-first and pseudo-second-order parameters for the adsorption of organic molecules by the metal organic framework.

Sample		Pseudo-first order						Pseudo-second order				
		10 mg/dm^3 75 mg	15 mg/dm^3 75 mg	20 mg/dm^3 75 mg	15 mg/dm^3 50 mg	15 mg/dm^3 100 mg		10 mg/dm^3 75 mg	15 mg/dm^3 75 mg	20 mg/dm^3 75 mg	15 mg/dm^3 50 mg	15 mg/dm^3 100 mg
diclofenac	k_1 (1/min)	0.044	0.245	0.178	0.011	0.041	k_2 (1/min)	0.040	0.014	6.94E-3	3.80E-3	0.032
	χ^2	14	130	263	593	40.4	χ^2	10.2	9.3	25	125	3.82
	R	0.991	0.97	0.97	0.94	0.98	R	0.993	0.996	0.997	0.99	0.998
caffeine	k_1 (1/min)	0.14	0.100	0.081	0.082	0.14	k_2 (1/min)	0.016	6.92E-3	4.31E-3	4.96E-3	0.011
	χ^2	46	254	177	220	140	χ^2	7.7	76	27.9	54	34
	R	0.95	0.87	0.96	0.93	0.90	R	0.991	0.96	0.994	0.98	0.98
		50 g/dm^3 1.5 g	75 g/dm^3 1.5 g	100 g/dm^3 1.5 g	75 g/dm^3 1 g	75 g/dm^3 2 g		50 g/dm^3 1.5 g	75 g/dm^3 1.5 g	100 g/dm^3 1.5 g	75 g/dm^3 1 g	75 g/dm^3 2 g
solketal	k_1 (1/min)	0.56	0.51	0.41	0.29	0.48	k_2 (1/min)	0.56	0.36	0.234	0.18	0.39
	χ^2	0.07	0.20	0.44	0.43	0.42	χ^2	0.032	0.27	0.30	0.29	0.09
	R	0.991	0.991	0.99	0.99	0.98	R	0.996	0.99	0.992	0.99	0.994

Table VII.9. Intraparticle rate parameters for the adsorption of organic molecules by the AC and MOF.

Sample		Active carbon					MOF				
		10 mg/dm^3	15 mg/dm^3	20 mg/dm^3	15 mg/dm^3	15 mg/dm^3	10 mg/dm^3	15 mg/dm^3	20 mg/dm^3	15 mg/dm^3	15 mg/dm^3
		20 mg	20 mg	20 mg	10 mg	30 mg	75 mg	75 mg	75 mg	50 mg	100 mg
diclofenac	K_3'(mg/g·min$^{0.5}$)	8.54	9.18	10.31	10.27	8.71	5.03	7.00	9.14	8.32	5.64
	R	0.99	0.99	0.97	0.99	0.99	0.80	0.94	0.96	0.97	0.89
	K_3''(mg/g·min$^{0.5}$)	1.99	1.64	2.00	2.94	2.02	0.01	0.12	0.27	0.71	0.03
	R	0.92	0.97	0.95	0.98	0.98	0.55	0.77	0.77	0.91	0.74
caffeine	K_3'(mg/g·min$^{0.5}$)	9.40	11.76	11.64	17.14	8.92	2.64	3.35	4.93	3.95	3.30
	R	0.99	0.96	0.94	0.98	0.95	0.97	0.93	0.99	0.97	0.91
	K_3''(mg/g·min$^{0.5}$)	0.12	0.51	0.77	0.77	1.13	0.19	0.51	0.52	0.52	0.35
	R	0.63	0.93	0.91	0.76	0.95	0.86	0.95	0.90	0.90	0.93
		50 g/dm^3	75 g/dm^3	100 g/dm^3	75 g/dm^3	75 g/dm^3	50 g/dm^3	75 g/dm^3	100 g/dm^3	75 g/dm^3	75 g/dm^3
		1.5 g	1.5 g	1.5 g	1 g	2 g	1.5 g	1.5 g	1.5 g	1 g	2 g
solketal	K_3'(g/g·min$^{0.5}$)	0.41	0.71	0.80	0.84	0.50	0.49	0.72	0.86	0.83	0.64
	R	0.97	0.97	0.96	0.98	0.97	0.90	0.92	0.92	0.97	0.92
	K_3''(g/g·min$^{0.5}$)	0.093	0.064	0.067	0.10	0.055	5E-4	0.002	0.001	0.002	0.002
	R	0.97	0.97	0.91	0.94	0.95	0.10	0.61	0.19	0.72	0.68

The second slope, k_3'', is related to the intraparticle diffusion into the more internal active sites of the adsorbent. As can be seen in Table VII.9, the second slope in the case of MOF is very small (especially in the case of diclofenac and solketal) as almost all the adsorbate uptake takes place in the first adsorption stage. However, AC adsorption processes have a non-negligible second slope. This could be related to a major number of internal active sites as AC has double the microscope volume of MOF. The adsorption process in porous adsorbents was also examined with the estimation of the effective diffusion coefficient by applying a fractional approach to the equilibrium, results shown in Table VII.10. The lower value of D/r^2, intraparticle diffusion, when AC was the adsorbent can indicate a slower uptake by the internal active sites which is related to a greater k_3'' value. MOF D/r^2 values are larger which facilitates the internal sites adsorption process. The general trend shows that as the adsorbent amount increases, so does the effective diffusion coefficient.

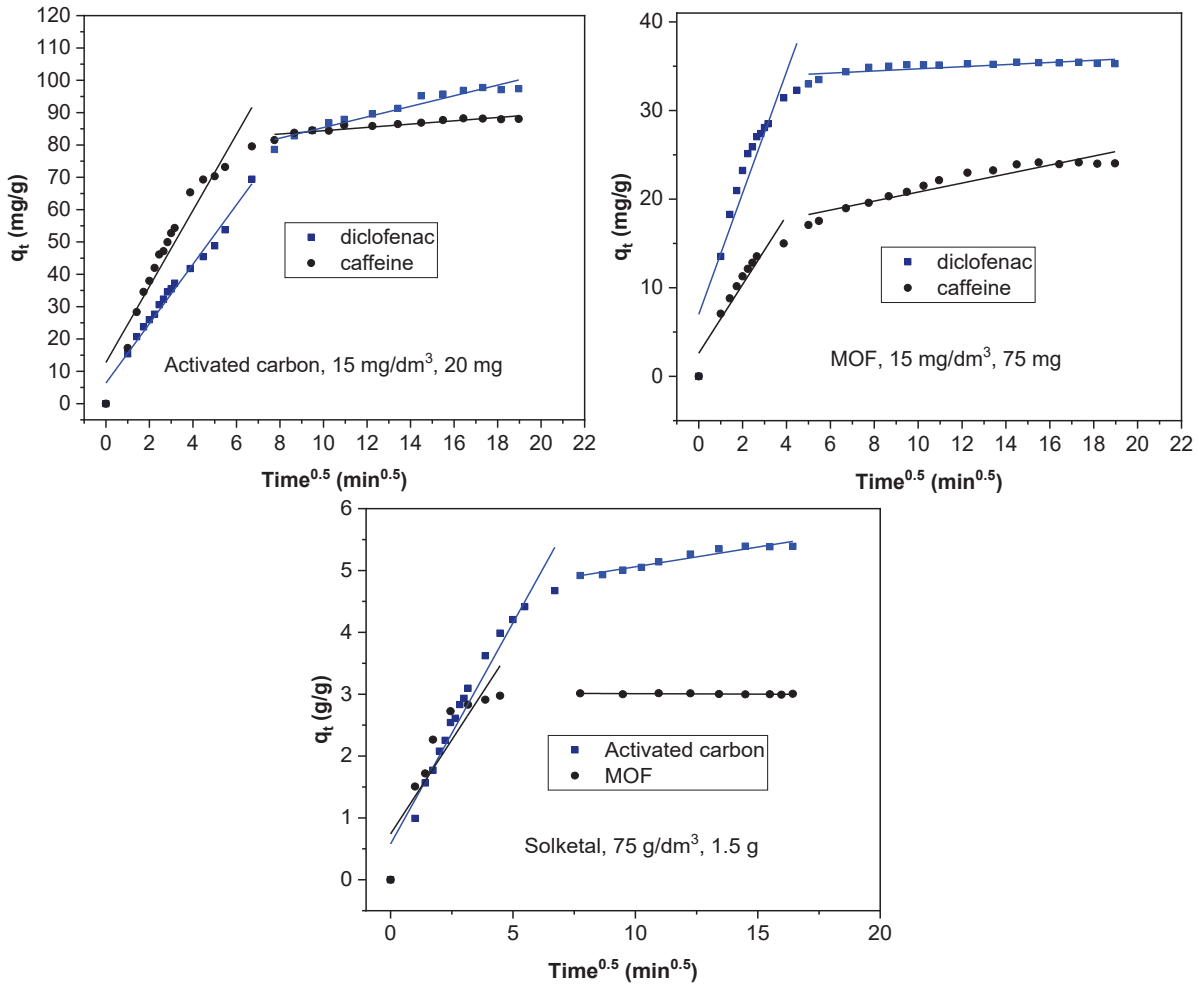

Figure VII.7. Intraparticle-diffusion model for the adsorption of organic molecules on the AC and MOF.

Table VII.10. Effective diffusion coefficients for the adsorption of organic molecules by the AC and MOF.

Sample		Active carbon					MOF				
		10 mg/dm^3	15 mg/dm^3	20 mg/dm^3	15 mg/dm^3	15 mg/dm^3	10 mg/dm^3	15 mg/dm^3	20 mg/dm^3	15 mg/dm^3	15 mg/dm^3
		20 mg	20 mg	20 mg	10 mg	30 mg	75 mg	75 mg	75 mg	50 mg	100 mg
diclofenac	D/r^2 (1/s)	2.66E-5	2.41E-5	3.26E-5	2.21E-5	2.56E-5	4.03E-4	2.08E-4	1.45E-4	7.85E-5	3.78E-4
	χ^2	0.031	0.020	0.050	0.038	0.064	0.0069	0.017	0.017	0.055	0.0096
	R	0.994	0.997	0.99	0.993	0.99	0.998	0.994	0.995	0.99	0.996
caffeine	D/r^2 (1/s)	7.61E-5	8.05E-5	8.55E-5	5.19E-5	5.21E-5	1.02E-4	5.97E-5	5.66E-5	5.38E-5	9.66E-5
	χ^2	0.008	0.015	0.042	0.014	0.066	0.052	0.17	0.024	0.058	0.15
	R	0.998	0.996	0.99	0.997	0.98	0.985	0.95	0.994	0.99	0.95
		50 g/dm^3	75 g/dm^3	100 g/dm^3	75 g/dm^3	75 g/dm^3	50 g/dm^3	75 g/dm^3	100 g/dm^3	75 g/dm^3	75 g/dm^3
		1.5 g	1.5 g	1.5 g	1 g	2 g	1.5 g	1.5 g	1.5 g	1 g	2 g
solketal	D/r^2 (1/s)	4.73E-5	6.35E-5	6.45E-5	4.15E-5	8.9E-5	4.95E-4	4.61E-4	3.72E-4	2.56E-4	3.88E-4
	χ^2	0.049	0.015	0.028	0.013	0.045	0.0057	0.014	0.012	0.0092	0.012
	R	0.99	0.996	0.993	0.998	0.99	0.997	0.993	0.995	0.996	0.996

VII.2.3.4. Adsorption isotherms

Adsorption isotherms were employed to represent the behavior between the organic molecules and adsorbents. Freundlich, Langmuir and Toth isotherms were adjusted to the experimental data for solketal, diclofenac and caffeine with AC and MOF as adsorbents. The results are represented in Figure VII.8. and the calculated constants for the equations are shown in Table VII.11. (AC) and Table VII.12. (MOF).

Table VII.11. Freundlich, Langmuir and Toth parameters for the adsorption by the AC.

	solketal	**diclofenac**	**caffeine**
Freundlich			
q_F	3.7	4.6	12.6
m_F	1.82	2.05	2.63
χ^2	726	449	3581
R	0.93	0.95	0.76
Langmuir			
q_L	83.7	68.4	82.8
k_L	0.013	0.021	0.058
χ^2	331	112	2128
R	0.97	0.99	0.86
Toth			
q_t	90.3	2122	79.6
K_t	0.013	0.27	0.37
m_T	0.66	0.13	0.61
χ^2	121	244	496
R	0.99	0.998	0.991

Table VII.12. Freundlich, Langmuir and Toth parameters for the adsorption by the MOF.

	solketal	**diclofenac**	**caffeine**
Freundlich			
q_F	2.57	6.13	7.87
m_F	1.76	2.60	2.41
χ^2	377	410	1428
R	0.91	0.91	0.78
Langmuir			
q_L	56.9	43.0	55.5
k_L	0.016	0.050	0.063
χ^2	189	109	833
R	0.96	0.98	0.88
Toth			
q_t	124.4	78.91	71.4
K_t	0.017	0.26	0.51
m_T	0.46	0.35	0.42
χ^2	219	170	401
R	0.99	0.998	0.99

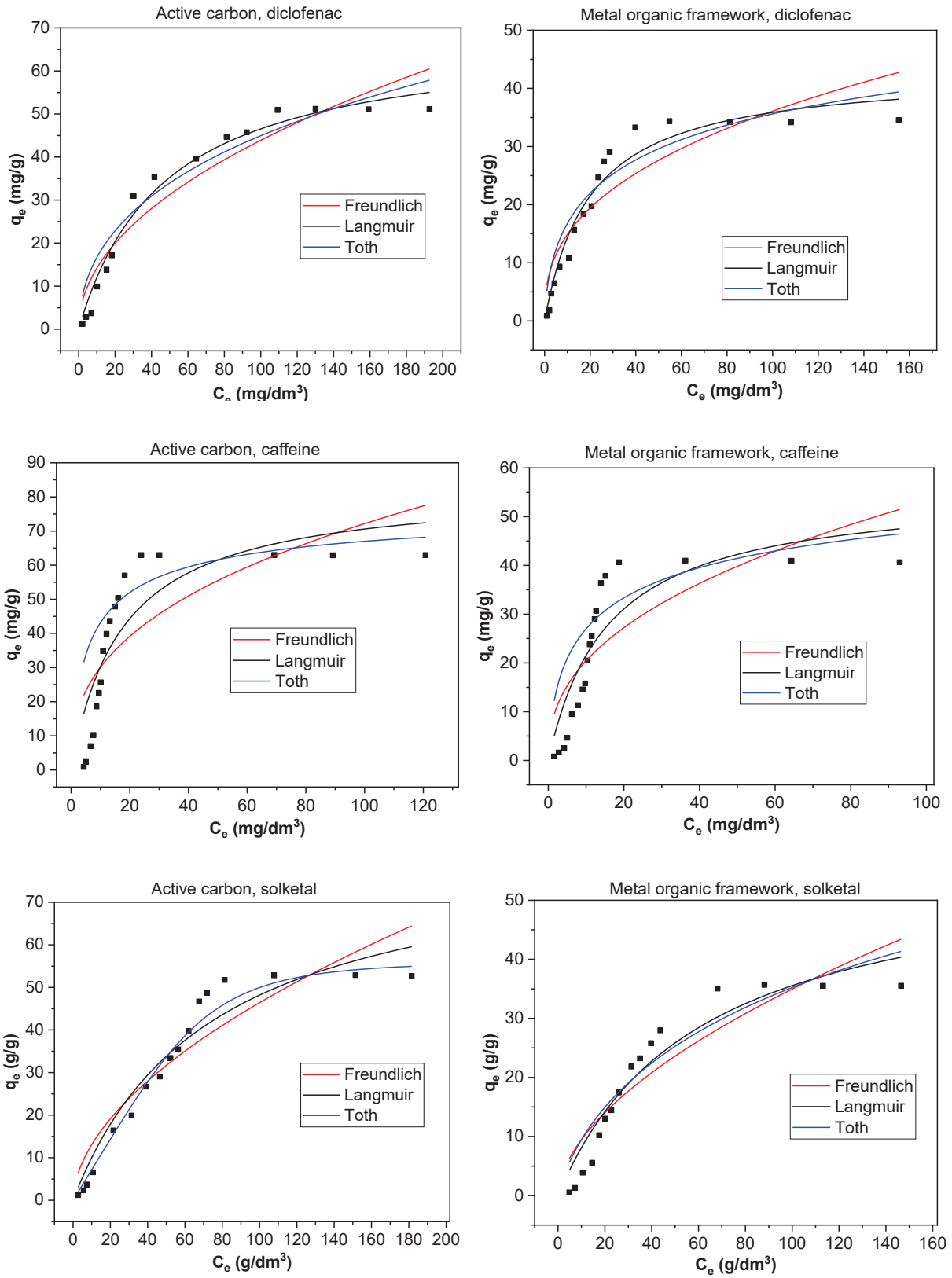

Figure VII.8. Experimental results (scatter) and isotherm adjustment to Langmuir, Freundlich and Toth models for diclofenac, caffeine and solketal adsorption on the AC (first column) and MOF (second column).

As defined by the Giles classification, the isotherms have an L-class shape, typical of systems with high adsorbate-adsorbent attraction (Giles et al., 1974). Of the three models tested, Toth equation gives the best adjustment to the results which makes sense as is an empirical modification of Langmuir equation to better fit the results. It is difficult to compare these results with other published works, as often only Freundlich and Langmuir are tested with the latter giving the best results for the analysis of pharmaceuticals, pesticides, herbicides and organic compounds in general (Delgado et al., 2019).

VII.3. CONCLUSIONS

In this work solketal adsorption, together with diclofenac and caffeine for comparison, has been tested as there was a lack of studies regarding its removal from water by adsorption. AC and MOF have been tested as adsorbents; AC gave the best results although MOF was faster in achieving equilibrium. The effect of various parameters, such as the adsorbent mass or initial concentration of pollutant was studied. Adsorption kinetics analysis revealed a better fit to pseudo-second-order model, the adsorption process was separated in two stages, AC gave a lower value in the intraparticle diffusion which may indicate a slower uptake by the internal active sites. Adsorption isotherms were also fitted to the experimental data, three parameter Toth equation gave better agreement between the experimental and theoretical data than Langmuir and Freundlich. Overall both adsorbents have been proven to be very effective for solketal adsorption.

Commercial multiwalled carbon nanotubes have been also used to adsorb caffeine and diclofenac, to remove them from aqueous solutions. The solid has a similar adsorption capacity for the two adsorbates, which can be explained by the low surface area accessible to the organic compounds. Equilibrium in the organic compound/carbon nanotube systems was usually reached after a contact time of 30 min. The experimental kinetic data were best described by the pseudo-second-order and intra-particle diffusion models.

VII.4. REFERENCES

Alves, T.C., Cabrera-Codony, A., Barceló, D., Rodriguez-Mozaz, S., Pinheiro, A., Gonzalez-Olmos, R., 2018. Influencing factors on the removal of pharmaceuticals from water with micro-grain activated carbon. Water Res. 144, 402–412. https://doi.org/10.1016/j.watres.2018.07.037

Anuar, M.R., Abdullah, A.Z., 2016. Challenges in biodiesel industry with regards to feedstock, environmental, social and sustainability issues: A critical review. Renew. Sustain. Energy Rev. 58, 208–223. https://doi.org/10.1016/j.rser.2015.12.296

Arshadi, M., Abdolmaleki, M.K., Mousavinia, F., Khalafi-Nezhad, A., Firouzabadi, H., Gil, A., 2016. Degradation of methyl orange by heterogeneous Fenton-like oxidation on a nano-organometallic compound in the presence of multi-walled carbon nanotubes. Chem. Eng. Res. Des. 112, 113–121. https://doi.org/10.1016/j.cherd.2016.05.028

Ayawei, N., Ebelegi, A.N., Wankasi, D., 2017. Modelling and Interpretation of Adsorption Isotherms. J. Chem. 2017, 11. https://doi.org/10.1155/2017/3039817

Azizian, S., Haerifar, M., Bashiri, H., 2009. Adsorption of methyl violet onto granular activated carbon: Equilibrium, kinetics and modeling. Chem. Eng. J. 146, 36–41. https://doi.org/10.1016/j.cej.2008.05.024

Bagheri, S., Julkapli, N.M., Yehye, W.A., 2015. Catalytic conversion of biodiesel derived raw glycerol to value added products. Renew. Sustain. Energy Rev. 41, 113–127. https://doi.org/10.1016/j.rser.2014.08.031

Bahamon, D., Vega, L.F., 2017. Pharmaceuticals removal from water effluents by adsorption in activated carbons using Monte Carlo simulations, Computer Aided Chemical Engineering. Elsevier Masson SAS. https://doi.org/10.1016/B978-0-444-63965-3.50451-7

Bolong, N., Ismail, A.F., Salim, M.R., Matsuura, T., 2009. A review of the effects of emerging contaminants in wastewater and options for their removal. Desalination 239, 229–246. https://doi.org/10.1016/j.desal.2008.03.020

Carabineiro, S.A.C., Thavorn-amornsri, T., Pereira, M.F.R., Serp, P., Figueiredo, J.L., 2012. Comparison between activated carbon, carbon xerogel and carbon nanotubes for the adsorption of the antibiotic ciprofloxacin. Catal. Today 186, 29–34. https://doi.org/10.1016/j.cattod.2011.08.020

Cho, H.-H., Huang, H., Schwab, K., 2011. Effects of Solution Chemistry on the Adsorption of Ibuprofen and Triclosan onto Carbon Nanotubes. Langmuir 27, 12960–12967. https://doi.org/10.1021/la202459g

Choy, K.K.H., Porter, J.F., Mckay, G., 2004. Intraparticle diffusion in single and multicomponent acid dye adsorption from wastewater onto carbon. Chem. Eng. J. 103,

133–145. https://doi.org/10.1016/j.cej.2004.05.012

Dąbrowski, A., 2001. Adsorption - From theory to practice. Adv. Colloid Interface Sci. 93, 135–224. https://doi.org/10.1016/S0001-8686(00)00082-8

Delgado, N., Capparelli, A., Navarro, A., Marino, D., 2019. Pharmaceutical emerging pollutants removal from water using powdered activated carbon: Study of kinetics and adsorption equilibrium. J. Environ. Manage. 236, 301–308. https://doi.org/10.1016/j.jenvman.2019.01.116

Den, W., Liu, H.-C., Chan, S.-F., Kin, K.T., Huang, C., 2006. Adsorption of phthalate esters with multiwalled carbon nanotubes and its applications. J. Environ. Eng. Manag. 16, 275–282.

Essandoh, M., Kunwar, B., Pittman, C.U., Mohan, D., Mlsna, T., 2015. Sorptive removal of salicylic acid and ibuprofen from aqueous solutions using pine wood fast pyrolysis biochar. Chem. Eng. J. 265, 219–227. https://doi.org/10.1016/j.cej.2014.12.006

Fatimah, I., Sahroni, I., Fadillah, G., Musawwa, M.M., Mahlia, T.M., Muraza, O., 2019. Glycerol to Solketal for Fuel Additive: Recent Progress in Heterogeneous Catalysts. Energies . https://doi.org/10.3390/en12152872

Gil, A., Assis, F.C.C., Albeniz, S., Korili, S.A., 2011. Removal of dyes from wastewaters by adsorption on pillared clays. Chem. Eng. J. 168, 1032–1040. https://doi.org/10.1016/j.cej.2011.01.078

Giles, C.H., Smith, D., Huitson, A., 1974. A general treatment and classification of the solute adsorption isotherm. I. Theoretical. J. Colloid Interface Sci. 47, 755–765. https://doi.org/10.1016/0021-9797(74)90252-5

Gogotsi, Y., Presser, V., 2013. Carbon nanomaterials. CRC press.

Gracia-Lor, E., Rousis, N.I., Zuccato, E., Bade, R., Baz-Lomba, J.A., Castrignanò, E., Causanilles, A., Hernández, F., Kasprzyk-Hordern, B., Kinyua, J., McCall, A.-K., van Nuijs, A.L.N., Plósz, B.G., Ramin, P., Ryu, Y., Santos, M.M., Thomas, K., de Voogt, P., Yang, Z., Castiglioni, S., 2017. Estimation of caffeine intake from analysis of caffeine metabolites in wastewater. Sci. Total Environ. 609, 1582–1588. https://doi.org/10.1016/j.scitotenv.2017.07.258

Gregg, S.J., Sing, K.S.W., Salzberg, H.W., 1967. Adsorption surface area and porosity. J.

Electrochem. Soc. 114, 279C-279C.

Haerifar, M., Azizian, S., 2013. Mixed Surface Reaction and Diffusion-Controlled Kinetic Model for Adsorption at the Solid/Solution Interface. J. Phys. Chem. C 117, 8310–8317. https://doi.org/10.1021/jp401571m

Hu, X., Cheng, Z., Sun, Z., Zhu, H., 2017. Adsorption of Diclofenac and Triclosan in Aqueous Solution by Purified Multi-Walled Carbon Nanotubes. Polish J. Environ. Stud. 26, 87–95. https://doi.org/10.15244/pjoes/63885

Khraisheh, M.A.M., Al-Degs, Y.S., Allen, S.J., Ahmad, M.N., 2002. Elucidation of controlling steps of reactive dye adsorption on activated carbon. Ind. Eng. Chem. Res. 41, 1651–1657. https://doi.org/10.1021/ie000942c

Lin, S., Zhao, Y., Yun, Y.S., 2018. Highly Effective Removal of Nonsteroidal Anti-inflammatory Pharmaceuticals from Water by Zr(IV)-Based Metal-Organic Framework: Adsorption Performance and Mechanisms. ACS Appl. Mater. Interfaces 10, 28076–28085. https://doi.org/10.1021/acsami.8b08596

Loos, R., Gawlik, B.M., Locoro, G., Rimaviciute, E., Contini, S., Bidoglio, G., 2009. EU-wide survey of polar organic persistent pollutants in European river waters. Environ. Pollut. 157, 561–568. https://doi.org/10.1016/j.envpol.2008.09.020

Luo, Z., Fan, S., Liu, J., Liu, W., Shen, X., Wu, C., Huang, Y., Huang, G., Huang, H., Zheng, M., 2018. A 3D stable metal-organic framework for highly efficient adsorption and removal of drug contaminants from Water. Polymers (Basel). 10, 12–18. https://doi.org/10.3390/polym10020209

M. Kamil, A., Abdalrazak, F.H., 2014. Adsorption of Bismarck Brown R Dye Onto Multiwall Carbon Nanotubes. J. Environ. Anal. Chem. 01. https://doi.org/10.4172/jreac.1000104

Maes, J., Verlooy, L., Buenafe, O.E., de Witte, P.A.M., Esguerra, C. V., Crawford, A.D., 2012. Evaluation of 14 Organic Solvents and Carriers for Screening Applications in Zebrafish Embryos and Larvae. PLoS One 7, 1–9. https://doi.org/10.1371/journal.pone.0043850

Monteiro, M.R., Kugelmeier, C.L., Pinheiro, R.S., Batalha, M.O., da Silva César, A., 2018. Glycerol from biodiesel production: Technological paths for sustainability. Renew. Sustain. Energy Rev. 88, 109–122. https://doi.org/10.1016/j.rser.2018.02.019

Moreira, M.N., Faria, R.P.V., Ribeiro, A.M., Rodrigues, A.E., 2019. Solketal Production from Glycerol Ketalization with Acetone: Catalyst Selection and Thermodynamic and Kinetic Reaction Study. Ind. Eng. Chem. Res. 58, 17746–17759. https://doi.org/10.1021/acs.iecr.9b03725

Mota, C.J.A., Da Silva, C.X.A., Rosenbach, N., Costa, J., Da Silva, F., 2010. Glycerin derivatives as fuel additives: The addition of glycerol/acetone ketal (solketal) in gasolines. Energy and Fuels 24, 2733–2736. https://doi.org/10.1021/ef9015735

Naghizadeh, A., Nasseri, S., Nazmara, S., 2011. Removal of trichloroethylene from water by adsorption on to multiwall carbon nanotubes. Iran. J. Environ. Heal. Sci. Eng. 8, 317–324.

Nanda, M.R., Yuan, Z., Qin, W., Ghaziaskar, H.S., Poirier, M.A., Xu, C.C., 2014. A new continuous-flow process for catalytic conversion of glycerol to oxygenated fuel additive: Catalyst screening. Appl. Energy 123, 75–81. https://doi.org/10.1016/j.apenergy.2014.02.055

Özcan, Ö., İnci, İ., Aşçi, Y.S., 2013. Multiwall Carbon Nanotube for Adsorption of Acetic Acid. J. Chem. Eng. Data 58, 583–587. https://doi.org/10.1021/je301064t

Özcan, Ö., İnci, İ., Aşçı, Y.S., Bayazit, Ş.S., 2017. Oxalic acid removal from wastewater using multi-walled carbon nanotubes: Kinetic and equilibrium analysis. J. Dispers. Sci. Technol. 38, 65–69. https://doi.org/10.1080/01932691.2016.1141688

Patiño, Y., Díaz, E., Ordóñez, S., Gallegos-Suarez, E., Guerrero-Ruiz, A., Rodríguez-Ramos, I., 2015. Adsorption of emerging pollutants on functionalized multiwall carbon nanotubes. Chemosphere 136, 174–180. https://doi.org/10.1016/j.chemosphere.2015.04.089

Plazinski, W., Rudzinski, W., 2009. Kinetics of adsorption at solid/Solution interfaces controlled by intraparticle diffusion: A theoretical analysis. J. Phys. Chem. C 113, 12495–12501. https://doi.org/10.1021/jp902914z

Ramadoss, R., Subramania, D., 2018. Adsorption of Chromium Using Blue Green Algae-Modeling and Application of Various Isotherms. Int. J. Chem. Technol. 10, 1–22. https://doi.org/10.3923/ijct.2018.1.22

Richardson, S.D., Ternes, T.A., 2014. Water Analysis: Emerging Contaminants and Current Issues. Anal. Chem. 86, 2813–2848. https://doi.org/10.1021/ac500508t

Rouquerol, F., Rouquerol, J., Sing, K., 1999. CHAPTER 5 - Adsorption at the Liquid–Solid Interface: Thermodynamics and Methodology, in: Rouquerol, F., Rouquerol, J., Sing. Academic Press, London, pp. 117–163. https://doi.org/10.1016/B978-012598920-6/50006-3

S. J. Gregg, Sing, K.S.W., 1982. Adsorption, Surface Area and Porosity. Auflage, Acad. Press 86, 957. https://doi.org/10.1002/bbpc.19820861019

Sabna, V., Thampi, S.G., Chandrakaran, S., 2016. Adsorption of crystal violet onto functionalised multi-walled carbon nanotubes: Equilibrium and kinetic studies. Ecotoxicol. Environ. Saf. 134, 390–397. https://doi.org/10.1016/j.ecoenv.2015.09.018

Talebian-Kiakalaieh, A., Amin, N.A.S., Najaafi, N., Tarighi, S., 2018. A review on the catalytic acetalization of bio-renewable glycerol to fuel additives. Front. Chem. 6, 1–25. https://doi.org/10.3389/fchem.2018.00573

Tat, M.E., Van Gerpen, J.H., 1999. The kinematic viscosity of biodiesel and its blends with diesel fuel. JAOCS, J. Am. Oil Chem. Soc. 76, 1511–1513. https://doi.org/10.1007/s11746-999-0194-0

Timofeeva, M.N., Panchenko, V.N., Krupskaya, V. V., Gil, A., Vicente, M.A., 2017. Effect of nitric acid modification of montmorillonite clay on synthesis of solketal from glycerol and acetone. Catal. Commun. 90, 65–69. https://doi.org/10.1016/j.catcom.2016.11.020

Trifoi, A.R., Agachi, P.Ş., Pap, T., 2016. Glycerol acetals and ketals as possible diesel additives. A review of their synthesis protocols. Renew. Sustain. Energy Rev. 62, 804–814. https://doi.org/10.1016/j.rser.2016.05.013

Urano, K., Tachikawa, H., 1991. Process development for removal and recovery of phosphorus from wastewater by a new adsorbent. II. Adsorption rates and breakthrough curves. Ind. Eng. Chem. Res. 30, 1897–1899. https://doi.org/10.1021/ie00056a033

Valderrama, C., Gamisans, X., de las Heras, X., Farrán, A., Cortina, J.L., 2008. Sorption kinetics of polycyclic aromatic hydrocarbons removal using granular activated carbon: Intraparticle diffusion coefficients. J. Hazard. Mater. 157, 386–396. https://doi.org/10.1016/j.jhazmat.2007.12.119

Van Tran, T., Nguyen, D.T.C., Le, H.T.N., Nguyen, O.T.K., Nguyen, V.H., Nguyen, T.T., Bach, L.G., Nguyen, T.D., 2019. A hollow mesoporous carbon from metal-organic framework for robust adsorbability of ibuprofen drug in water. R. Soc. Open Sci. 6.

https://doi.org/10.1098/rsos.190058

Yan, X.M., Shi, B.Y., Lu, J.J., Feng, C.H., Wang, D.S., Tang, H.X., 2008. Adsorption and desorption of atrazine on carbon nanotubes. J. Colloid Interface Sci. 321, 30–38. https://doi.org/10.1016/j.jcis.2008.01.047

Yao, Y., Bing, H., Feifei, X., Xiaofeng, C., 2011. Equilibrium and kinetic studies of methyl orange adsorption on multiwalled carbon nanotubes. Chem. Eng. J. 170, 82–89. https://doi.org/10.1016/j.cej.2011.03.031

Yu, F., Ma, J., Han, S., 2014. Adsorption of tetracycline from aqueous solutions onto multi-walled carbon nanotubes with different oxygen contents. Sci. Rep. 4, 5326. https://doi.org/10.1038/srep05326

Zhang, L., Song, X., Liu, X., Yang, L., Pan, F., Lv, J., 2011. Studies on the removal of tetracycline by multi-walled carbon nanotubes. Chem. Eng. J. 178, 26–33. https://doi.org/10.1016/j.cej.2011.09.127

Zhao, H., Liu, X., Cao, Z., Zhan, Y., Shi, X., Yang, Y., Zhou, J., Xu, J., 2016. Adsorption behavior and mechanism of chloramphenicols, sulfonamides, and non-antibiotic pharmaceuticals on multi-walled carbon nanotubes. J. Hazard. Mater. 310, 235–245. https://doi.org/10.1016/j.jhazmat.2016.02.045

SUMMARY AND CONCLUSIONS

In the present work, a new procedure for the recovery of aluminum present in saline slags generated during the secondary recycling processes of aluminum as adsorbent/photocatalyst of diclofenac and salicylic acid, as examples of emerging contaminants, has been reported. Results obtained have been extensively analyzed throughout the present study. Therefore, the main findings are briefly hereafter presented:

- The synthesis of a LDH series with various Me^{2+} (Co, Mg, Ni and Zn) with aluminum extracted from saline slags was performed. The LDH structure was achieved in all cases with differences between samples mainly due to Me^{2+} cations. Batch experiments were performed to analyze the adsorption capacity of the different LDH on diclofenac and salicylic acid, as example of emergent pollutants.
- Various adsorption and isotherm equation models were employed to study both the kinetic and equilibrium results and, in general, the removal of diclofenac was greater than that of salicylic acid.
- The main differences between the samples were due to their capacity to recover their LDH structure when rehydrated. Zn_6Al_2 and Mg_6Al_2 present the best adsorption results mainly due to their ability to recover their LDH structure when rehydrated. They showed higher adsorption capacity although it took longer for them to achieve equilibrium because of the time taken by both LDH to recover their structure when put in contact with water and/or the time taken by the drugs to enter the interlayer in those two samples.

- In Co_6Al_2 and Ni_6Al_2 samples, the adsorption is only external as the structure is not recovered in water, which implies lower adsorption capacity but bigger adsorption rate, the equilibrium is achieved faster.
- 1-Butanol conversion was also used as a means of acidity and basicity characterization and the results were compared with the adsorption performance of the samples in order to explain the results found. The adsorption capacities of the adsorbents correspond quite well to their acidic properties. Not so much in the case of the basic properties because the dehydrogenating capacity of the LDH samples is also affected by the redox properties of metals, Ni and Co.
- The effectiveness of the extraction process has been proven, as a comparison of LDH made from extracted aluminum versus LDH made from commercial aluminum was performed. Structural characterization and comparison of the two series has been made using powder X-ray diffraction (PXRD), Nitrogen physisorption at 77 K, Scanning electron microscopy (SEM), X-ray photoelectron spectroscopy (XPS) and Thermogravimetry measurements. Only minimum differences were found between the series. In addition, it should be noted the convenience of a basic extraction process that does not imply an extra use of sodium hydroxide in the overall production method, as it is no longer needed in the LDH synthesis.
- As Zn LDH had the best adsorption performance, it was chosen to synthesize a new series of LDH, in this case with Zn always as Me^{2+} and a combination, in different proportions, of Al^{3+}/Ti^{3+} as Me^{3+}. The adsorption capacities of these LDH were also tested for diclofenac and salicylic acid in both batch and fixed-

bed adsorption. The results showed that the adsorption capacity of the samples was better when less titanium was incorporated as Me^{3+}.

- The uncalcined and without Ti samples evidenced the presence of the typical hydrotalcite structure with a high crystallinity from the XRD analyses. As the amount of Ti increased, the crystallinity of the samples decreased appreciably. After calcination at 673 K, the hydrotalcite structure was destroyed and zincite (ZnO) was found. The textural properties, namely the specific surface area, decreased with the calcination temperature, related to the presence of amorphous mixed oxides, while increased when incorporating Ti into the structure from 78 to 199 m^2/g. By calcination of the samples at 673 K, these properties decreased due to the presence of amorphous mixed oxides. The presence of Ti in the LDH structure was confirmed by XPS analysis.
- The kinetic study of the adsorption process showed that 100-400 min were necessary for the emerging pollutants/hydrotalcites systems to reach the equilibrium. The hydrotalcites synthesized retained more diclofenac than salicylic acid (409 and 80 µmol/g, respectively), and the adsorption capacity was greater when Ti content in the adsorbents was lower. Zn_6Al_2 solid was very effective in retaining this type of organic pollutants.
- The adsorption capacities of different commercial adsorbents were also tested for comparison purposes. Carbon nanotubes were tested for the removal of caffeine and salicylic acid. On the other hand activated carbon and the MOF basolite A100 were tested for the removal of DL-1,2-Isopropylideneglycerol (used in the production of biodiesel as additive of glycerol); diclofenac and caffeine removal were also tested in batch adsorption.

- Overall, carbon nanotubes had a less effective adsorption of the contaminants followed by that of the metal organic framework. Activated carbon had very good adsorption results, comparable to those obtained with Zn_6Al_2 and Mg_6Al_2 in the case of diclofenac.
- For the study of photocatalysis, experiments with TiO_2 on its own were performed in advance. To prevent the TiO_2 from electron-hole recombination, anatase was synthesized and modified with different content (0.5-5wt.%) of Fe and Ag. Two different synthesis techniques were used (sol-gel and wet impregnation) to either dope (within the crystalline lattice) or impregnate the anatase with the metals.
- The results of PXRD show the crystalline structure of anatase, with no signals from dopants due to its low content or high dispersion on titanium dioxide. The textural analyses of the catalysts allowed to observe an increase of these properties when the sol-gel method was used. The surface and the volume of pores decrease when using the technique of wet impregnation. The degradation tests of salicylic acid indicate that doping the catalyst with iron can improve its effectiveness, while the largest performance was observed for the catalysts containing 5 wt.% Fe.
- These results were used for the tests performed with LDH as photocatalysts. The synthesis of hydrotalcite-type materials with the composition Zn-Al-Ti-Fe with aluminum extracted from an industrial waste were tested as photocatalysts for the removal of salicylic acid and diclofenac. The Zn-Al-Ti series performance was compared with the same series impregnated with 5wt.% of iron to prevent the electron-hole recombination of titanium obtaining better

results. In addition, another series $Zn^{2+}/(Fe+Al)^{3+}$ materials with and without 5 wt.% impregnated titanium (Ti^{4+}) are tested as catalysts for comparison.

- The ZnAl material presents a typical hydrotalcite structure, the crystallinity of which decreases as the amount of Fe or Ti increases due to partial substitution of Al. Thermal treatment at 673 K resulted in the formation of mixed oxides took place, with, ZnO, $ZnFe_2O_4$, Fe_3O_4, Fe_2O_3 being detected, depending on the composition of the sample. In all cases, the N_2 adsorption isotherms at 77 K were type II, and the BET specific surface areas were between 78 and 199 m^2/g.
- The Fe/ZnAlTi catalysts showed the best catalytic behavior, although it was difficult to distinguish between the fraction removed by adsorption and the fraction photodegraded. To try to solve this problem, consecutive photodegradation cycles, in which the catalyst saturated with the pollutant molecule was used, were performed.

Overall, these results show that the use of LDH as adsorbents/photocatalysts of emerging contaminants (pharmaceutical compounds) gives promising results although more research in this area is needed. In addition, this work proves that aluminum extracted from saline slags (used for the LDH synthesis) can be converted into an added-value product, as after the Al extraction process the saline slag becomes a non-hazardous material.